

Cover Page



Universiteit Leiden



The handle <http://hdl.handle.net/1887/19113> holds various files of this Leiden University dissertation.

Author: Martínez-Galarza, Juan Rafael

Title: Mid-infrared spectroscopy of starbursts : from Spitzer-IRS to JWST-MIRI

Date: 2012-06-19

Mid-Infrared Spectroscopy of Starbursts:
From Spitzer-IRS to JWST-MIRI

Mid-Infrared Spectroscopy of Starbursts: From Spitzer-IRS to JWST-MIRI

Juan Rafael Martínez Galarza

Thesis Universiteit Leiden - Illustrated - With summary in Dutch and Spanish - With references

ISBN/EAN 978-94-6182-123-2

Printed by Offpage.nl

Cover: The starburst galaxy IC 342 imaged by the Spitzer Space Telescope, Credit: NASA/JPL-Caltech/J. Turner (UCLA). Artist concept of JWST, Credit: NASA. An artist impression of IC 342 by Lara Versari.

Cover desing by Daniel Camilo Gómez

Mid-Infrared Spectroscopy of Starbursts: From Spitzer-IRS to JWST-MIRI

PROEFSCHRIFT

ter verkrijging van
de graad van Doctor aan de Universiteit Leiden,
op gezag van de Rector Magnificus prof. mr. P.F. van der Heijden,
volgens besluit van het College voor Promoties
te verdedigen op dinsdag 19 juni 2012
klokke 16.15 uur

door

Juan Rafael Martínez Galarza
geboren te Bogotá, Colombia
in 1981

Promotiecommissie

Promotor: Prof. dr. E. F. van Dishoeck

Co-promotor: Dr. B. Brandl

Overige Leden: Prof. dr. K. Kuijken

Prof. dr. F. Israel

Prof. dr. G. Wright

Prof. dr. M. A. Dopita

Dr. I. Kamp

Dr. B. Groves

The University of Edinburgh

Australia National University

Rijksuniversiteit Groningen

Max Planck Institut für Astronomie

Para mis padres, por regalarme este Universo.

*El brillo de las estrellas
es una noticia tardía, me dijiste,
esa luz que vemos no es sino un navío
de jaulas doradas
que guardan especies muertas.*

-Robert Max Steenkist

1	Introduction	1
1.1	Massive star formation and the history of the Universe	2
1.2	Starbursts systems	3
1.2.1	Definition of a starburst	4
1.2.2	Giant H II regions as the building blocks of starbursts	5
1.3	SED fitting of starbursts	11
1.3.1	χ^2 minimization	11
1.3.2	Bayesian approach	11
1.4	Future observations with the James Webb Space Telescope	12
1.4.1	JWST	12
1.4.2	Sensitivity	13
1.4.3	Spatial resolution	13
1.4.4	MIRI spectrometry	13
1.4.5	Starbursts and MIRI	14
1.5	This thesis	15
I	Bayesian SED Fitting of Starbursts	17
2	The physical conditions in starbursts derived from Bayesian fitting of mid-IR SEDs: 30 Doradus as a template	19
2.1	Introduction	20
2.2	The 30 Doradus region	21
2.2.1	Properties of the 30 Doradus region	22
2.2.2	The integrated mid-IR spectrum of 30 Doradus	24
2.2.3	Individual sources	24
2.3	Modelling the SEDs of starbursts	27
2.3.1	Literature on SED modelling	27
2.3.2	The physical concept behind the model	27
2.3.3	Model parameters	29

Contents

2.3.4	Attenuation by diffuse dust	31
2.4	Fitting routine	31
2.4.1	Probability Distribution Functions	31
2.4.2	Model priors	32
2.4.3	Uncertainties and model resolution	33
2.5	Results	35
2.5.1	Nebular lines ratios as age diagnostics.	36
2.5.2	Integrated spectrum	37
2.5.3	Individual sources	43
2.5.4	Age averaged case	46
2.6	Summary and conclusions	48
3	Ongoing massive star formation in NGC 604	51
3.1	Introduction	52
3.2	Data reduction and ancillary datasets	53
3.2.1	IRS data	54
3.2.2	IRAC photometry	56
3.2.3	PACS photometry	56
3.2.4	HST-WFPC2 F555W data	57
3.2.5	Chandra X-ray Observatory-ACIS data	57
3.3	Analysis	57
3.3.1	Distribution of the emission	58
3.3.2	Infrared spectra	61
3.3.3	Electron density	64
3.3.4	Hardness of the radiation field	67
3.3.5	[Si II] emission	70
3.3.6	H ₂ emission	71
3.3.7	SED modeling	72
3.4	Discussion	75
3.4.1	Notable sources	75
3.4.2	The evolutionary stage of NGC 604	76
3.4.3	Ongoing and triggered star formation in NGC 604	82
3.5	Conclusions	83
4	Outlook: recent star formation in nuclear starbursts	85
4.1	Introduction	86
4.2	Sample of galaxies	87
4.2.1	Selection criteria	87
4.2.2	Basic properties	88
4.2.3	Morphologies	90
4.2.4	Measurements from the literature	90
4.3	Results	92
4.3.1	MIR spectra of the selected galaxies	92
4.3.2	Bayesian fitting of the spectra	94

4.4	Discussion	97
4.4.1	Star formation rates	97
4.4.2	Pressure, compactness and their relation to massive clusters	98
4.4.3	Molecular gas content and feedback in starbursts	99
4.5	Summary and outlook	100
II MIRI Wavelength Calibration		103
5	Mid-infrared IFU spectroscopy from space: wavelength calibration of JWST-MIRI	105
5.1	Introduction	106
5.2	MIRI: an overview	107
5.2.1	The MIRI field of view on the sky	107
5.2.2	Integral field spectroscopy with MIRI	107
5.3	Setup and measurements	108
5.3.1	The MIRI Telescope Simulator (MTS)	108
5.3.2	Measurements	110
5.4	Analysis	111
5.4.1	Cube reconstruction	111
5.4.2	Etalon analysis	113
5.4.3	Fringing	116
5.4.4	Line shape and resolving power	120
5.5	Summary and outlook	122
6	The spectral properties of JWST-MIRI: calibration of the Flight Model	125
6.1	Introduction	126
6.2	Observations	127
6.2.1	The test campaign and the observational setup	127
6.2.2	Test data	128
6.2.3	Data reduction	129
6.2.4	Reduced data	131
6.3	Analysis	133
6.3.1	Wavelength characterisation	133
6.3.2	Uncertainties	140
6.4	Results and discussion	144
6.4.1	The resolving power of the MRS	144
6.4.2	Variations of R with wavelength and position in the field	145
6.4.3	Line shape and spectral ghosts	147
6.4.4	Wavelength stability	147
6.5	Summary	153
Bibliography		155

Contents

Nederlandse Samenvatting	161
Resumen en Español	169
Curriculum Vitae	177
Acknowledgements	179

The Spectral Energy Distributions (SEDs) of star-forming regions and starburst galaxies are unique tracers of the star formation processes in these environments, since they contain information on the escaping and processed photons emitted by newly formed massive stars. Understanding these internal processes is crucial in our physical interpretation of observations of unresolved star formation in the Universe. In the first part of this thesis, we study the physical conditions in resolved starburst regions using Bayesian fitting of their spatially integrated infrared SEDs, including both the thermal continuum and the atomic emission lines. We then apply the method to unresolved starburst to learn about their star formation physics. Our approach leads to robust constraints on physical parameters such as age, compactness, and amount of currently ongoing star formation in starburst, which are otherwise biased by model degeneracies, and allows us to link the resolved properties of giant H II regions to the star formation process at larger scales. In the second part of this thesis, we discuss the wavelength calibration of the next instrument to study the mid-infrared spectral properties of starbursts, with improved resolution and sensitivity: the mid-infrared instrument (MIRI), which will fly onboard the *James Webb Space Telescope* in 2018.

1.1 Massive star formation and the history of the Universe

The process through which large amounts of gas and dust in Giant Molecular Clouds (GMCs) are turned into crowded populations of stars with total masses of between $10^4 M_\odot$ and $10^6 M_\odot$ is a crucial problem in astrophysics. It is related to the structure of the Universe as we see it today, with all the complexity and beauty revealed by optical and infrared telescopes at scales ranging from the size of individual stars to the majestic structures of entire spiral galaxies. The most massive OB stars formed within these clusters affect the structure of galaxies through their radiative and mechanical input and through the chemical processing of the interstellar medium (ISM), thus influencing the evolution of the galaxy as a whole. The incidence of star formation in the evolution of galaxies was even more important at earlier times, when young gas-rich galaxies were in the process of assembling (Caputi et al. 2007). In fact, deep near-infrared surveys indicate that about 85% of all the baryonic mass that exists today in galaxies was formed in the last 9 billion years in massive star forming regions heavily embedded in thick layers of dust (Marchesini et al. 2009).

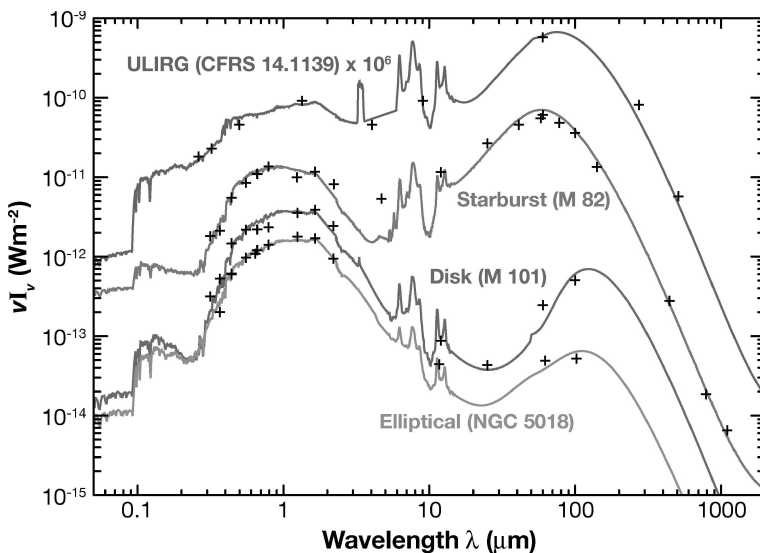
These facts highlight the importance of understanding the formation of massive star clusters both in the local and distant Universe, and their evolution during the first ~ 10 Myr of their existence, when the bulk of ultraviolet (UV) radiation from OB stars is emitted. Dedicated theoretical and observational efforts have been made to characterize the initial physical conditions for the formation of large stellar clusters in GMCs (see the review by Zinnecker & Yorke 2007, and references therein), and also the early stages of embedded clusters within these clouds (see for example Lada & Lada 2003, for a comprehensive review on embedded clusters in GMCs). As summarized in these reviews, most observational efforts have concentrated on tracing emission from: (a): the molecular gas that constitutes the fuel for the formation of massive stars, using submillimeter and radio observations of tracers of dense cores, such as HCO^+ ; and HCN and (b): thermal emission from dust particles heated by the intense radiation fields of young stars, using infrared imaging and spectroscopy.

In recent years, the study of the interaction between the radiation field of young OB stars formed within the cluster and the surrounding ISM, has benefited from new observations at mid-infrared and far-infrared observations, that complement previous optical and sub-millimeter surveys. It is now possible to sample the pan-chromatic spectral energy distributions (SEDs) of star-forming regions, from the UV to the far-infrared (FIR). These SEDs are dominated by the radiation field of OB stars that either escapes the birth cloud or is absorbed and processed by the gas and dust in the surrounding ISM. Because OB stars are short-lived, the SEDs provide information on the recent (< 10 Myr) star formation activity in these regions. In fact, for spatially unresolved objects, integrated SEDs are often the only diagnostic available to study their properties. The main goal of this thesis is the design of a robust method to derive physical information from the integrated SEDs of star-forming regions. Although we apply the method to regions with high specific star formation rates, the algorithms developed here should be suitable for any region whose

luminosity is dominated by star formation.

1.2 Starbursts systems

Star formation does not occur at the same rate everywhere in the local Universe. While most present day galaxies, including our Milky Way, have star formation rates (SFRs) of $\sim 1 M_{\odot} \text{ yr}^{-1}$ (Robitaille & Whitney 2010), a minority of local galaxies with similar stellar masses are undergoing bursts of star formation, and have SFRs of hundreds or even thousands of solar masses per year. While it is not entirely clear yet what triggers these *starbursts*, galaxy mergers have been proposed as a possible (but not unique) cause for the enhanced star formation (Sanders & Mirabel 1996). This is supported by the fact that the total contribution from luminous infrared galaxies to the cosmic SFR density is larger at higher redshifts, where collisions between galaxies were more common (Lagache et al. 2005). Fig. 1.1 shows the SEDs of different types of galaxies and provides evidence for the pronounced infrared emission from star-forming galaxies with respect to normal disk galaxies.



Lagache, G et al. 2005
Annu. Rev. Astron. Astrophys. 43: 727–68

Figure 1.1 The UV to FIR SEDs of different galaxy types, from elliptical dust-poor galaxies to Ultra Luminous Infrared Galaxies (ULIRGs). The crosses indicate photometry data, while the solid lines are SED models. Figure taken from Galliano (2004).

1.2.1 Definition of a starburst

The term *starburst* has been used by astronomers for about 40 years. The first reference in the scientific literature to *bursts* of star formation in galaxies comes from the seminal paper by Searle et al. (1973). In that paper, the authors claim that transient periods of enhanced star formation could be one possible explanation for the colors of certain galaxies, which were observed to be bluer than expected, indicating a young population of massive stars. Almost a decade later, (Weedman et al. 1981) used the term *starburst* for the first time, referring to the intense nuclear star formation activity in NGC 7714, as estimated using X-ray, optical and radio data. However, due to the broad interval of wavelengths at which massive star formation is detected, and to the equally spread range of bolometric luminosities of objects classified as starbursts ($10^8 L_\odot - 10^{12} L_\odot$), no formal definition of a starburst has been adopted, leading to confusion in the understanding of their nature.

Nevertheless, it is generally agreed that if such definition is to be adopted, it should be related to the following three factors: (i): The SFR of the galaxy or region, (ii): The amount of available gas to form stars, and (iii): The timescale of star formation as compared to the dynamical timescales of the system (e.g., galactic rotation period). A possible definition that includes these concepts was introduced by Heckman (2005). According to this definition, a starburst is a system in which the timescale t_{gas} for gas depletion is much shorter than the Hubble time. This can be written in an equation as

$$t_{\text{gas}} = M_{\text{gas}}/\text{SFR} \ll 1/H_0 \quad (1.1)$$

where M_{gas} is the mass of molecular gas in the system, measured for example using radio observations of molecular tracers such as CO, SFR is the star formation rate as estimated from optical or infrared diagnostics, and H_0 is the Hubble constant.

We can classify systems with different star formation intensities using this definition. For the Milky Way, $t_{\text{gas}} \sim 3$ Gyr, while for two well known local galactic mergers, M82 and Arp 220 (see Fig. 1.2), we have respectively $t_{\text{gas}}^{\text{M82}} \sim 20$ Myr and $t_{\text{gas}}^{\text{Arp220}} \sim 30$ Myr, as estimated from literature values for their masses and SFRs. This indicates that the latter two can be included in the category of starbursts. The definition is not exclusive of galaxies. A gas depletion timescale can also be used to classify star forming regions within galaxies, such as the 30 Doradus region in the Large Magellanic Cloud, for which $t_{\text{gas}}^{\text{30Dor}} \sim 10$ Myr.

A different approach considers the starburst bolometric luminosity, L_{SB} , as compared to the luminosity of the galactic host, L_G (Terlevich 1997). Bolometric luminosities are usually measured adopting template SEDs that are scaled according to available measurements, and then integrated within a certain wavelength range. According to this alternative definition, a galactic system is a starburst galaxy if $L_{\text{SB}} \gg L_G$. This approach avoids ambiguities arising from uncertainties in the total gas mas, but excludes in the definition star forming regions such as 30 Doradus.

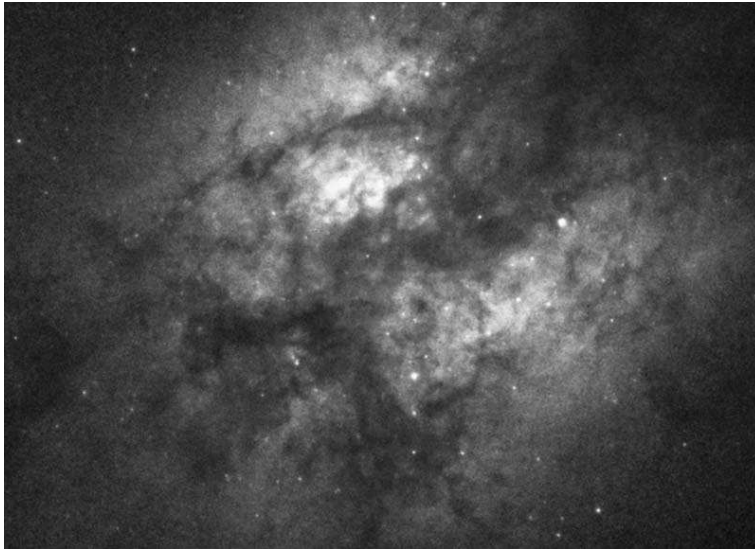


Figure 1.2 The starburst galaxy Arp 220 as seen by the *Hubble Space Telescope*. The bright blue spots are young clusters whose formation was triggered by the galactic collision. The light of many more clusters is obscured by large amounts of dust in the foreground. Image from Wilson et al. (2006).

1.2.2 Giant H II regions as the building blocks of starbursts

Behind the thick layers of gas and dust in starburst systems, stars form inside individual clouds with a distribution of masses set by the physical conditions of the molecular cloud before its collapse (see, for example Motte et al. 1998). The most massive (OB) stars in the resulting clusters are hot and luminous enough to ionize the surrounding gas, creating extensive H II regions (see, for example Shields 1990, for a review on H II regions). The ionized gas then tends to expand, dispersing the parental molecular cloud and creating a shock front into the surrounding neutral molecular gas. These so-called Giant H II Regions (GH II Rs) are thus the building blocks of starburst systems, not only because they represent the self-contained systems of star formation of which the starburst is made, but also because through their mechanical and radiative feedback, they alter the evolution of the starburst, setting a limit to the efficiency at which the molecular gas can be converted into stars (Krumholz et al. 2006). In Fig. 1.3 we show a simple schematic 2D view of an H II region.

Infrared bright clumps are usually observed in the vicinity of H II regions, and this has been generally associated with star formation triggered by the compressed gas as the expansion of the ionized region progresses (see Elmegreen 2011, and references therein).

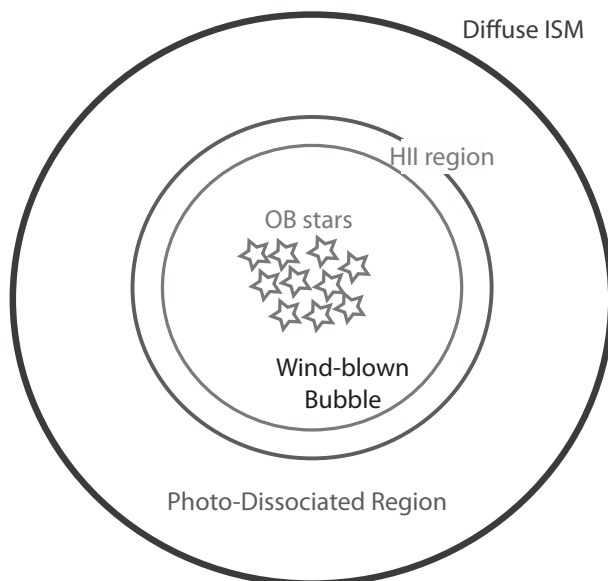


Figure 1.3 An schematic view of a symmetric H II region. The hot central stars expand, creating a cavity of shocked gas surrounded by a thin layer of ionized gas. Photons with energies below the ionization potential of the hydrogen atom process the surrounding molecular material, creating a photon-dominated region (PDR), that diffuses into the ISM. Figure by Brent Groves.

Possible evidence has been found of triggered intermediate-mass star formation in galactic regions of massive star formation, such as the RCW 34 region in the Vela Molecular Ridge (Bik et al. 2010). Nonetheless, not enough observational evidence for triggering of new massive stars has been collected, mainly due to weak indicators of ongoing massive star formation in galactic systems. It is in general difficult to judge whether very recent star formation events have taken place before or after the disturbance in pressure created by an expanding H II region. Triggering can be responsible for a significant contribution to the starburst activity, and hence quantifying it in the interior of star-forming regions is crucial in our understanding of these systems. In this thesis, we will quantify recent massive star formation in the vicinity of GH IIRs by fitting their integrated SEDs with a novel statistical method.

Infrared Observations of GH IIRs

Because massive star formation occurs in regions heavily enshrouded by dust, a significant fraction of their bolometric luminosity is emitted at infrared wavelengths, after UV photons from massive stars have been absorbed by dust particles and re-emitted as ther-

mal radiation (see Fig. 1.1). In fact, the total IR luminosity of a galaxy can be used as a tracer of its recent star formation history (Kennicutt 1998, Calzetti et al. 2010). Apart from the thermal continuum, several relevant features are observed at the wavelengths covered by recent infrared observatories including the *Spitzer Space Telescope* and the *Herschel Space Observatory*.

At mid-infrared (MIR) wavelengths ($5\ \mu\text{m}$ - $28\ \mu\text{m}$), the SEDs of starbursts are dominated by pronounced and broad emission features arising from bending and stretching mode transitions in Polycyclic Aromatic Hydrocarbons (PAHs) (Tielens 2008). These are molecules with carbon atoms arranged in a honeycomb structure of fused six-membered, aromatic rings with peripheral hydrogen atoms. These PAHs are present in the molecular photon-dominated regions (PDRs) that surround H II Regions. Atomic fine-structure emission lines from several highly ionized species including [Ar III], [S IV] and [Ne III] are also detected in the MIR and are important tracers of gas density, temperature and strength of the radiation field (Dopita et al. 2006c). Additionally, the prominent [Si II] line detected in the MIR spectrum of many galaxies traces either gas shocked by supernova explosions, or regions dominated by the X-rays in the stellar winds of massive stars. None of these species are present in low-mass star-forming regions, where the radiation fields are not as intense.

Fig. 1.4 illustrates the complexity of starbursts as revealed by their MIR spectra. Shown are the spectra of a sample of starburst galaxies taken with the Infrared Spectrograph (IRS) onboard *Spitzer*, which display a wide range in the strength of MIR features and continuum slopes (Brandl et al. 2006). Understanding how the underlying physics of star-forming regions relate to the observed spectral features is one of the goals of the present work.

Observations at even longer wavelengths allow a first order approach to the measurement of the average dust temperature and total amount of dust contained in starbursts (and hence of their evolutionary stage), by characterizing the peak and broadness of the thermal radiation bump observed at far-infrared (FIR) wavelengths. Although such physical quantities are biased by uncertainties in the SED models (dependence of dust emissivity on the composition, degeneracy between the spectral index β and the dust temperature), some general relations can be established between starburst activity and the overall shape of the SED.

In a recent comprehensive paper on star-forming galaxies using *Herschel* data, Elbaz et al. (2011) characterized the SEDs of a sample containing ~ 1800 galaxies, and concluded that they can be separated in two classes, according to their SED shapes. A majority of “main sequence” star-forming galaxies, with SFRs compared to that of the Milky Way and infrared bumps peaking $\sim 100\ \mu\text{m}$, and a minority of outliers whose SEDs peak at $\sim 70\ \mu\text{m}$ that the authors associate with objects undergoing compact starburst-like star formation. Relating their overall SEDs to the internal conditions of their individual GH IIRs is an important step in the understanding of the physical processes that lead to the formation of a starburst. In the chapters of this thesis we will show that it is possible to constrain the average physical parameters of H II regions by fitting the integrated SED of the starburst galaxy that hosts them.

The majority of starburst galaxies are distant and spatially unresolved by our current

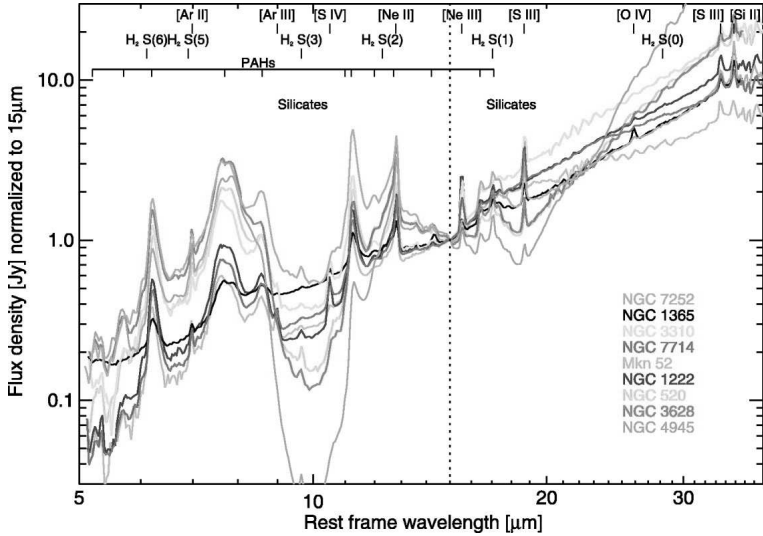


Figure 1.4 The MIR spectra of a sample of starburst galaxies, displaying a broad range of variation in the PAH strength, silicate absorption, slope continuum and atomic line emission. Some relevant MIR emission lines are indicated. Figure taken from Brandl et al. (2006).

instruments. Hence, in order to understand their internal properties, we rely almost exclusively on their integrated SEDs. Fig. 1.5 illustrates the situation, by showing the typical size of the galaxies whose SEDs are shown in Fig. 1.4 as compared to the size of the *Spitzer*-IRS slit. It is evident from the figure that most of the infrared emission from these objects is spatially unresolved. In the near future, the MIRI instrument for the *James Webb Space Telescope* (JWST) will move one step forward in resolution and sensitivity of mid-infrared observations (see in Chapters 5 and 6). However, even when MIRI comes online towards the end of the decade, resolved observations of individual GH π Rs at mid-infrared wavelengths will not be possible at distances larger than about 30 Mpc. In terms of the science presented in this thesis, this implies that the method developed here will remain a powerful and unique tool to study unresolved starburst beyond the Local Universe, long after the JWST mission has been completed.

Modelling of H π Rs and starbursts

From UV to submillimeter wavelengths, the emission properties of starbursts are dominated by the energetic photons emitted by massive stars younger than 10 Myr formed in OB associations and clusters (Kennicutt 1998). These photons are either directly observed as UV light or re-processed by gas and dust and re-emitted as atomic recombination lines or infrared thermal continuum. From the modelling point of view, this implies that the

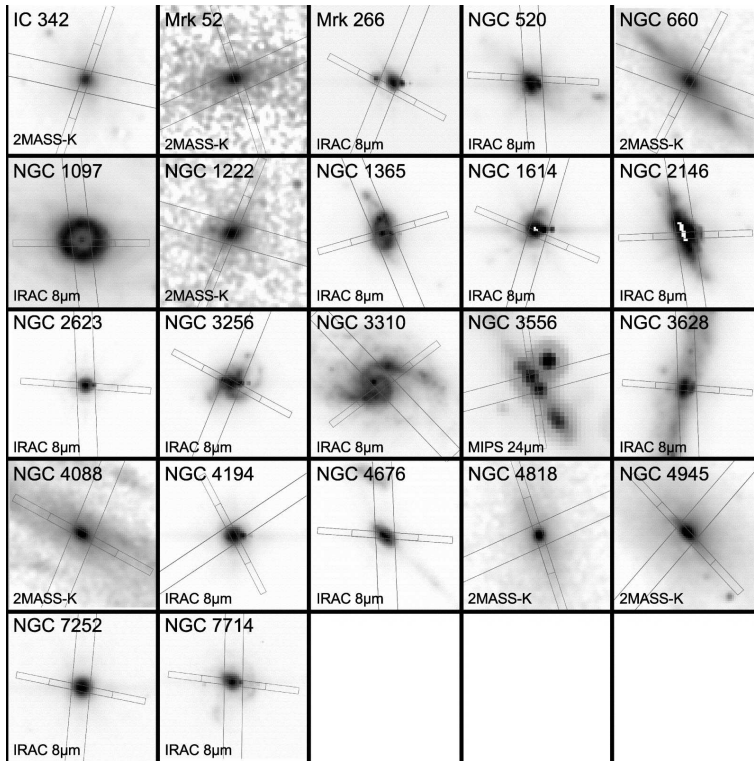


Figure 1.5 Positions of the *Spitzer*-IRS SL and LL slits overlplotted on IRAC $8\ \mu\text{m}$, MIPS $24\ \mu\text{m}$, or 2MASS K-band images for a sample of starburst galaxies. Figure taken from Brandl et al. (2006).

SED of a starburst is constructed from the linear combination of the SEDs of the individual GH nRs created by those clusters, and their surrounding molecular envelopes. To first approximation, the physical modelling of such regions needs to account for at least three main components:

1. The time-dependent radiation field emitted by the photospheres of a given population of stars, which provides the energetic input for the system. This is the stellar population synthesis.
2. The physics of the interaction between the stellar radiation and the surrounding ISM. This is the ionization, excitation and radiative transfer part of the analysis.
3. The dynamical evolution of the H II regions, which is driven by the competition between the radiation pressure that expands the H II region and the external ISM pressure that confines it.

1 Introduction

To first approximation, a galaxy is a collection of stars that ranges from low-mass stellar objects to the massive and luminous OB stars, with a given distribution of ages and metallicities. The so-called Initial Mass Function (IMF), describes the distribution of masses with which a stellar cluster is born, and sets many aspects of its subsequent evolution. Population synthesis is the art of creating a galactic SED as the sum of the spectra of these individual stars, by parametrizing the evolution of the system either as a function of age (Charlot & Bruzual 1991) or as a function of available thermonuclear fuel (Maraston 2005). Stellar synthesis models simplify the physical situation by assuming ensembles of single-age and single-metallicity stellar populations with a time-dependant mass distribution. The output of the stellar population synthesis is the radiation field that is later used as an input for the radiative transfer analysis.

In order to account for the entire UV to sub-millimeter spectral energy distribution of galaxies, the stellar spectra are only the first step. It is necessary to account for the absorption of stellar light by gas and dust particles present in the ISM, and for the cooling radiation of the gas, heated by the absorption of stellar photons and/or by the photoelectric heating and collisions with the dust. Although dust and gas are mixed within the ISM, the radiative transfer is usually done separately for each of these components, since they have different absorption and emission properties. While for most star-forming regions the gas is assumed to be atomic, in very dense regions such as AGN-dominated galaxies and very luminous starbursts, molecular gas can be responsible for significant absorption of stellar light. Full radiative transfer codes accounting for ionization and excitation such as *CLOUDY* (Ferland et al. 1998) and *Mappings III* (Groves et al. 2008) compute the absorption of EUV photons with energies $h\nu > 13.6$ eV, and their re-emission as hydrogen recombination lines or collisionally excited forbidden lines of other atomic species. Additionally, these codes compute the absorption and emission of dust particles, which are considered to be made of three different components: amorphous graphite grains, amorphous silicate grains and PAHs (Mathis et al. 1977, Draine 2011).

As the stellar populations ages, the ionized H II region expands driven by the mechanical input of stellar winds and supernovae in the clusters. A one-dimensional approach to compute the dynamical evolution of this expansion was proposed by Castor et al. (1975), and refined by Oey & Clarke (1997) to account for superbubbles created by clusters of OB stars rather than individual stars. Using their approach, it is possible to derive the evolution of the H II region radius as a function of only two parameters: the mechanical energy from stellar winds and supernovae as a function of time, which comes from the stellar synthesis analysis, and the density of the surrounding ISM, which provides the confining pressure against which the bubble expands. While this one-dimensional approach is a simplification of the more complex geometry of these systems, it provides values that can be directly compared with observations of expanding bubbles in the galaxy, such as the observed radii of such bubbles.

1.3 SED fitting of starbursts

One of the most common and wide-spread methods used in the last decade to determine the physical conditions of unresolved starbursts and of star-forming regions in general, is the fitting of observed SEDs using pre-calculated models like those described in the last section. This has been possible given major improvements in both physical models and the fitting procedures in recent years, as described in a comprehensive review by Walcher et al. (2011). By comparing the observed spectrum to predicted SEDs from models in which the physical conditions have been parametrized, one should be able to find a set of model parameters that better reproduce the data, given certain observational uncertainties, and hence derive probability distributions for the model parameters. Some of the important parameters to be constrained are the SFRs, age, compactness of the regions, mass contribution from young embedded objects, and PDR content.

1.3.1 χ^2 minimization

Most of the fitting techniques used today are based on χ^2 minimization routines that measure the difference between observed and predicted spectra in a bin-by-bin basis (along the frequency axis) and compare this difference to the observational error for each corresponding wavelength bin. It is then possible to obtain a distribution of χ^2 values for the model parameters by calculating this quantity across the full parameters space. It is assumed that the set of parameter values that minimize the χ^2 distribution is a good representation of the actual values of the physical quantities.

These minimization methods assume that the model parameters are fixed but unknown, and that the uncertainties in their determination are given by the *likelihood* of measuring certain values for the parameters assuming that the adopted models are a fair representation of reality. If the observational errors are distributed according to a Gaussian, this likelihood probability can be calculated as the exponential of the χ^2 distribution arising from the comparison between the possible outcomes of the models and the observed data, the *evidence*. In this respect, χ^2 minimization methods are *frequentist* in that they assume that the probability of a given model parameter having a certain value is determined by the spread in the results of applying a test (the SED fitting) to the measurement of a fixed parameter.

An important aspect of χ^2 minimization is that in order to provide reliable results, it requires a thorough mapping of the parameter space in order to avoid local shallow minima that can be misleading.

1.3.2 Bayesian approach

A more sophisticated, and philosophically different approach assumes that the model parameters are not fixed quantities, but random variables whose probability distribution functions (PDFs) are set, before any attempt of measurement has been made, by the belief of the scientist that the model parameters have certain values. These beliefs should

1 Introduction

be based on independent knowledge of the parameters, either from observations or theory, and constitute probability *priors* for the model parameters. In Bayesian inference, we measure the *posterior* probability distribution of a given parameter by updating its assumed prior probability in the light of new evidence. This evidence comes from new observations (the measured spectrum of a star-forming region, for example) and enters the calculation as the likelihood derived from the χ^2 minimization. The Bayes' theorem relates the posterior PDF to the likelihood and prior probabilities according to:

$$\text{posterior} = \text{likelihood} \times \text{prior} \times \frac{1}{N} \quad (1.2)$$

where N is a normalization factor that ensures that the posterior adds up to unity.

An advantage of Bayesian inference over frequentist methods is that it allows to update our previous knowledge on a particular model parameter using any new evidence on that particular parameter. Moreover, via the normalization constant, it accounts for the fact that SED fitting is nothing but a test, and as such it might detect things that do not exist (*false positives*) or fail to detect things that do exist (*false negatives*). Bayesian inference is, from the point of view of the author of this thesis, the right method to use when one is trying to calculate the probabilities of model parameters about which enough evidence has been collected prior to the measurements.

1.4 Future observations with the James Webb Space Telescope

The level of detail with which we can study the MIR SEDs of star-forming galaxies is limited by the sensitivity, angular resolution and spectral resolving power of our current spectroscopic observations. In particular, at wavelengths longer than $5 \mu\text{m}$, the spectra of star-forming galaxies located at distances larger than a few tens of Mpc are either dimmer than the current detection limits ($\sim 1 \text{ mJy}$ with *Spitzer*-IRS) or spatially unresolved by the beam size of the available imaging devices ($\sim 1''.7$ for *Spitzer*-IRAC at $8 \mu\text{m}$), with the exception of very bright objects. Moreover, the current spectral resolutions achieved at MIR wavelengths do not exceed values of $\lambda/\Delta\lambda \sim 600$. The sensitivity and angular resolution limitations can be overcome with a larger aperture telescope optimized for MIR wavelengths, which combined with state-of-the-art spectroscopic techniques, can also provide better spectral resolution.

1.4.1 JWST

Towards the end of the decade, a 6.5 m infrared-optimized telescope will be launched to the so-called Lagrange point No. 2, located at a distance of 150 million kilometers from the Earth, that offers a privileged observing location far from the thermal radiation of the Earth-Moon system. The *James Webb Space Telescope* (JWST) is a joint effort of three space agencies, namely NASA, ESA, and the Canadian Space agency and will constitute

1.4 Future observations with the James Webb Space Telescope

the next milestone in space-based infrared astronomy. With an effective collecting area 40 times as big as that of the *Spitzer* main mirror, it will reach unprecedented sensitivity at wavelengths ranging from $0.6\ \mu\text{m}$ to $29\ \mu\text{m}$ using four observing instruments: a $2.2' \times 4.4'$ field near-infrared camera, a near-infrared multi-object dispersive spectrograph with a field of view of $3.4' \times 3.4'$, a $2.2' \times 2.2'$ tunable filter imager and a mid-infrared instrument that will perform imaging, coronagraphy and integral field spectroscopy.

1.4.2 Sensitivity

The unprecedented dimensions of JWST imply that it will be able to perform observations two orders of magnitude more sensitive at MIR wavelengths as compared to the *Spitzer* Space Telescope, limited only by the thermal background from the telescope itself, and by the IR background from galactic cirrus. In fact, the telescope is designed to observe the light from the first stars that formed in the history of the Universe, at redshifts larger than $z \sim 13$ (Stiavelli 2010). To detect these sources, JWST needs to be able to measure photometric flux densities as low as 10^{-8} Jy for a point source, at the $10\text{-}\sigma$ level in a 10^4 s exposure. This means that the telescope has to operate at extremely low temperatures, close to 40 K, and even lower (~ 7 K) for the mid-infrared instrument (MIRI), whose solid state detectors require such operating temperature. In Fig. 1.6 we show a comparison in the limiting flux densities for several observatories including JWST (6.5 m aperture), *Spitzer* (0.85 m), HST (2.4 m), the Gemini Telescopes (8.2 m) and the SOFIA observatory (2.5 m).

1.4.3 Spatial resolution

The diffraction-limited beam size of JWST varies with wavelength from $0.063''$ at $2\ \mu\text{m}$ to $0.635''$ at $20\ \mu\text{m}$. The resolution elements are optimally sampled by at least 2 detector pixels. For comparison, the diffraction limit for the *Hubble* aperture is about $0.14''$ at $2\ \mu\text{m}$ and that of the *Spitzer* Space Telescope is $6.18''$ at $24\ \mu\text{m}$. Observing in the MIR thermal continuum, JWST will be able to resolve the size of typical giant H II regions, such as 30 Doradus (200 pc), at the distance of the Virgo cluster of galaxies.

1.4.4 MIRI spectrometry

The JWST-MIRI instrument will have integral field spectroscopy capabilities with resolving powers ranging from $R \sim 1000$ to $R \sim 4000$ between $5\ \mu\text{m}$ and $29\ \mu\text{m}$. Four spectrometer channels with nested fields of view (FOVs) will register the science target and the spectrometer optics will divide the FOVs into adjacent slices that will be aligned and then dispersed by a dedicated set of gratings. The maximum size of the FOV is $7.7'' \times 7.9''$. Both in terms of wavelength coverage and functionality, the MIRI spectrometer will be the natural successor to the *Spitzer*-IRS.

1 Introduction

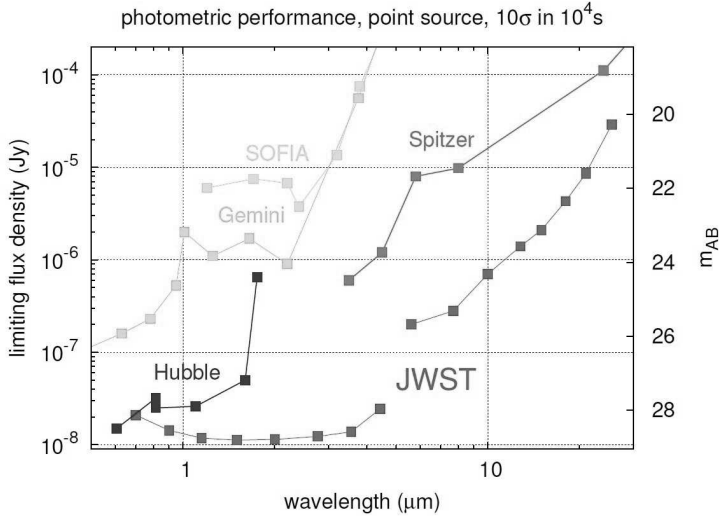


Figure 1.6 The faintest photometric flux of a point source that can be detected at 10σ in a 10^4 s integration, for different instruments observing at NIR and MIR wavelengths. JWST will be able to characterize the dimmest objects ever observed in the Universe. Credit: STScI.

1.4.5 Starbursts and MIRI

Several aspects of starbursts studies would greatly benefit from the large aperture of JWST, and from the imaging and spectroscopic capabilities of MIRI. In the Local Universe, at distances shorter than 30 Mpc, MIRI will be able to spatially resolve physical sizes of 45 pc (compared to about 300 pc resolved by previous infrared missions at the same distance), hence entering the domain of very compact nuclear starburst. We need MIRI to resolve this very inner regions of galactic nuclei, and to separated them from other galactic components or AGN. Additionally, MIRI will be able to penetrate through the dense layers of dust that obscures these nuclear starbursts. IFU spectroscopy of these regions will reveal with unprecedented spectral and spatial resolution several important features of the spectra that trace star formation, such as the PAH emission, and will allow detailed studies of the gas kinematics. Several MIR forbidden emission lines that are either dim or blended with other features will be readily detected. Some of those lines, such as the $[\text{O IV}]25.89\mu\text{m}$ and the $[\text{Ne V}]14.32\mu\text{m}$ can be used as discriminators between an active nucleus and a starburst nucleus.

At redshifts $z \sim 1$, the rest-frame near-infrared bands shift into the MIR wavelength range. MIRI will allow the measurement of stellar masses in intermediate z objects, based on their near-IR emission. The $\text{Pa}\alpha$ near-infrared line at $1.87\mu\text{m}$ shifts into the MIRI range for $z > 1.7$, allowing detailed kinematic studies of the ionized gas at kpc scales.

All together, these facts imply that more sensitive observations, with better angular resolutions, are needed to advance in the understanding of starbursts. MIRI will provide these observational capabilities.

1.5 This thesis

Unveiling the physical mechanisms that trigger and maintain events of enhanced star formation in galaxies along the history of the Universe is one of the most exciting challenges of modern astrophysics. In this thesis we will study the physical conditions in star-forming regions, such as age, total mass, star formation rates, PDR content, pressure, and amount of ongoing massive star formation, using their integrated spectral energy distributions as indicators. The goal is to understand how and to what extent specific physical conditions affect the infrared SEDs of these objects in order to develop a robust SED fitting method that can be easily applied to any unresolved starburst and, more importantly, obtain reliable results on their physical conditions and their relation to star formation. As we have seen above, even with the next generation infrared instruments, most distant starbursts will still be unresolved, and physical modelling thus remains a crucial tool for the near future. Hence, in **Part I** of this thesis we develop a Bayesian approach to fit the integrated SEDs of starbursts and their emission lines with physical models. We apply the resulting tool to the infrared spectra of well known calibrators, the giant star forming regions 30 Doradus and NGC 604, before we use it to interpret the spectra of more distant, unresolved starbursts.

There is a reason why this thesis has two parts. The next milestone in observational studies of starbursts will be the launch of JWST in 2018. We have discussed several aspects of how the improved sensitivity, angular and spectral resolution of JWST-MIRI are needed to advance in our knowledge of these objects, both in the local and high- z Universe. MIRI observations will be directly linked to the science and methods discussed in this work. Therefore, **Part II** of this thesis is dedicated to MIRI, its performance and ground calibration before integration with the other observatory instruments. We introduce the MIRI instrument, and describe the ground calibrations of its spectral properties. Based on test data obtained during the testing of the instrument in Europe, we derive its wavelength calibration, and compare our results to the requirements set by the science goals of the mission.

In **Chapter 2** we present our novel Bayesian tool to fit the spectra of starbursts. The fitting tool is applied to the *Spitzer* spectrum of the giant H II R 30 Doradus, a spatially resolved starburst. We find that our results are representative of this massive local starburst, and calibrate our tool using the wealth of literature information available for the region. Moreover, the model degeneracies are investigated. We discuss the importance of including the atomic nebular lines in the SED fitting in order to break these degeneracies. We show that emission from a significant amount of hot ($\sim 300\text{K}$) dust is needed to reproduce the SED of 30 Doradus.

Using a combination of observational and analytical tools, including the brand-new Bayesian algorithm and multi-wavelength observations, **Chapter 3** presents a comprehen-

sive analysis of the physical conditions in the second most massive star-forming region in the Local Group after 30 Doradus, the NGC 604 region in the M 33 galaxy. Several massive ($10^3 M_{\odot} - 10^4 M_{\odot}$) embedded clusters with diameters of about 15 pc are identified within the region, most likely the early stages of very recent star formation. These clusters account for about 8% of the total stellar mass in the region. Our results indicate that, while NGC 604 is a more evolved H II region, as compared to its largest sibling 30 Doradus, star formation in NGC 604 is still ongoing, triggered by the earlier bursts.

We conclude the first part of the thesis in **Chapter 4**, an outlook chapter that presents a pilot study showing the power of our Bayesian tool to investigate the properties of spatially unresolved starbursts. We provide some encouraging clues about the conditions for the formation of massive star clusters in these nuclear starbursts. If confirmed, this clues may imply that the most massive clusters have formed in gas-depleted regions. Moreover, they may imply that the gas-poor systems where massive clusters form have large luminosity contributions from very recent massive star formation. This can be interpreted as evidence of positive feedback from the inferred massive clusters. We propose a systematic study of a large sample of starburst SEDs, using the present method, to corroborate our findings.

Part II of the thesis is dedicated to the Mid-Infrared Instrument for JWST. A method for the wavelength calibration of the instrument, based on the use of synthetic etalon lines, fringing pattern and optical modelling is presented in **Chapter 5** and applied to data collected during the testing of MIRI's verification model (VM). Once the method has been calibrated and verified during VM testing, in **Chapter 6** it is fully applied to the Flight Model (FM) data acquired during the FM test campaign in 2011. This constitutes the only spectral calibration measurements of the instrument before its launch on 2018. The measured resolving power of MIRI over the entire wavelength range confirms the requirements and agrees with the predicted values for the resolving power from the optical model. Our results imply an improvement of at least one order of magnitude with respect to the resolving power of the *Spitzer*-IRS spectrometer low resolution orders, and at least a factor of 3 with respect to the resolving power of the IRS high resolution orders.

Part I

**Bayesian SED Fitting of
Starbursts**

CHAPTER 2

The physical conditions in starbursts derived from Bayesian fitting of mid-IR SEDs: 30 Doradus as a template¹

To understand and interpret the observed Spectral Energy Distributions (SEDs) of starbursts, theoretical or semi-empirical SED models are necessary. Yet, while they are well-founded in theory, independent verification and calibration of these models, including the exploration of possible degeneracies between their parameters, are rarely made. As a consequence, a robust fitting method that leads to unique and reproducible results has been lacking. Here we introduce a novel approach based on Bayesian analysis to fit the Spitzer-IRS spectra of starbursts using the SED models proposed by Groves et al. (2008). We demonstrate its capabilities and verify the agreement between the derived best fit parameters and actual physical conditions by modelling the nearby, well-studied, giant H II region 30 Dor in the LMC. The derived physical parameters, such as cluster mass, cluster age, ISM pressure and covering fraction of photodissociation regions, are representative of the 30 Dor region. The inclusion of the emission lines in the modelling is crucial to break degeneracies. We investigate the limitations and uncertainties by modelling sub-regions, which are dominated by single components, within 30 Dor. A remarkable result for 30 Doradus in particular is a considerable contribution to its mid-infrared spectrum from hot (≈ 300 K) dust. The demonstrated success of our approach will allow us to derive the physical conditions in more distant, spatially unresolved starbursts.

¹Based on: J.R. Martínez-Galarza, B. Groves, B. Brandl, G. de Messières, R. Indebetow and M. Dopita, 2011, *Astrophysical Journal*

2.1 Introduction

In theory, the spectral energy distribution (SED) of a galaxy contains a wealth of information about both its evolutionary history and current conditions. However, extracting this information is difficult and requires the use of physically based models. Nevertheless, SED fitting is a necessary process as many high redshift galaxies remain unresolved by our current instruments and any attempts to characterize the conditions and processes that lead to their starburst activities rely almost exclusively on their spatially averaged properties. These models of the integrated SEDs of galaxies currently cover a wide range of galaxy types, but are particularly dominated by models of Starburst galaxies (Galliano et al. 2003, Siebenmorgen & Krügel 2007, Takagi et al. 2003, Silva et al. 1998, Dopita et al. 2005, 2006b,c, Groves et al. 2008). The ultraviolet (UV) to far infrared (FIR) SED of these *Starbursts* is dominated by the energetic photons emitted by massive stars with typical lifetimes of less than 10 Myr.

In particular, the mid-infrared portion of the SED contains several important diagnostics that probe the physical conditions of starbursts. Observations of a set of marginally resolved starburst galaxies with the Spitzer Space Telescope show a broad range of mid-infrared properties, including different strengths of the polycyclic aromatic hydrocarbon (PAH) bands, thermal continuum slopes, depth of the silicate absorption features at $10\mu\text{m}$ and $18\mu\text{m}$ and intensity of nebular emission lines (Brandl et al. 2006, Bernard-Salas et al. 2009). All these signatures have contributions from different spatial regions, depending on the geometrical distribution of gas and dust with respect to the ionizing stars. For example, Beirão et al. (2009) reported on the presence of compact star forming knots around the nucleus of the starburst galaxy Arp 143, and similar star forming knots have been reported near the nucleus of NGC 253 (Fernández-Ontiveros et al. 2009). In other galaxies, such as M51, star formation spreads more uniformly over the galactic disk. The different distributions of gas, dust, and stars in galaxies affect the shape of the spatially integrated SED. Inversely, a sophisticated and well calibrated SED model should be able to recover the information on the local starburst conditions from the integrated SED.

A considerable amount of SED model libraries can be found in recent literature (see e.g. Walcher et al. 2011, for a comprehensive review on SED fitting). These models generally make assumptions on the internal physics of galaxies and predict the output SED as a function of certain model parameters, such as star formation rates (SFRs), metallicity (Z), and the interstellar medium (ISM) pressure, density, and temperature, among many others. SED fitting refers to the process of choosing from a particular library the model solutions that best reproduce the data. While finding the best-fit model via, for an example, a χ^2 minimization provides an estimate of the parameters, this method alone is insufficient to provide absolute parameter uncertainties. In order to obtain robust parameter estimates, including uncertainties, it becomes necessary to explore the whole parameter space and perform a statistical study of their correlations. We highlight four aspects that make this task difficult. First, the sensitivity of photometric and spectroscopic studies is limited not only by instrumental constraints, but also by more fundamental constraints such as shot noise in the case of weak sources. Hence, the robustness of SED fitting depends on the data quality and on sufficient data coverage. Second, degeneracies between model

parameters are common, especially when limited to a narrow spectral window (e.g., the mid-infrared). Third, independent determinations (from observations or theory) of the physical parameters against which we can confront our model results are rare for most starburst, hence making it difficult to calibrate the models. And last but not least, no robust fitting routine that leads to reproducible results has been established so far for the specific case of starburst spectra.

In this chapter we present a Bayesian fitting routine for the mid-infrared ($5 - 38 \mu\text{m}$) spectra of starbursts that can be extended to other wavelengths. We derive probability distribution functions (PDFs) for the model parameters, and study the implications on the physics of starbursts. To calibrate this routine we apply it to the mid-infrared spectrum of the 30 Doradus region in the Large Magellanic Cloud. The selection of this nearby starburst as a calibrator is natural, since its proximity ($\approx 53 \text{ pc}$) allows us to differentiate spatially resolved sub-regions of the giant H II region, and study their spectra separately. The well studied stellar populations, ionized gas, and dust content provide the necessary independent measurements to compare with SED fitting results.

Current spatial resolutions achieved with the mapping mode of the *Infrared Spectrograph* on board the Spitzer Space Telescope are of the order of a few arcseconds at $5 \mu\text{m}$ corresponding to a scale of about one parsec at the distance to 30 Doradus. Even the next generation spectrometer operating at these wavelengths, the *Mid Infrared Instrument* (MIRI), on board the 6.5 m James Webb Space Telescope, will not be able to resolve typical giant H II regions in galaxies located at distances larger than about 30 Mpc at a nominal wavelength of $15 \mu\text{m}$. This highlights the importance of understanding the integrated SEDs of these objects.

This chapter is structured as follows. In §2.2 we describe some general aspects of the 30 Doradus region, focusing on its stellar content and its physical properties, as obtained from HST and Spitzer observations, and we discuss the Spitzer-IRS spectral data that we model. In §2.3 we give a brief overview of the models we use to generate our grid of synthetic SEDs. In §2.4 we introduce our fitting routine and discuss the assumed priors and involved uncertainties. §2.5 presents the results of applying our fitting routine to 30 Doradus, discuss the implications of the model parameters and the physical interpretation of the mid-infrared SEDs. Finally, in §2.6 we summarize our main findings.

2.2 The 30 Doradus region

Our choice of 30 Doradus as a calibrator relies on three powerful reasons: *(i)* it is the largest giant H II region in the Local Group, *(ii)* it is well studied across the whole electromagnetic spectrum, and *(iii)* it is close enough to be well resolved into individual components. In this section we describe the general properties of 30 Doradus and the spectral data that we model.

2.2.1 Properties of the 30 Doradus region

30 Doradus is the most massive giant H II region in the Local Group. It is located 53 ± 3 kpc away (Feast & Catchpole 1997), in the north-east part of the Large Magellanic Cloud (LMC) and includes the stellar cluster NGC 2070, the cloud of ionized gas created by the ionizing radiation from NGC 2070 and dominated by its compact central core R136, and the photon-dissociated regions and molecular material associated with the star forming region. We show the complexity of the region in Fig. 2.1.

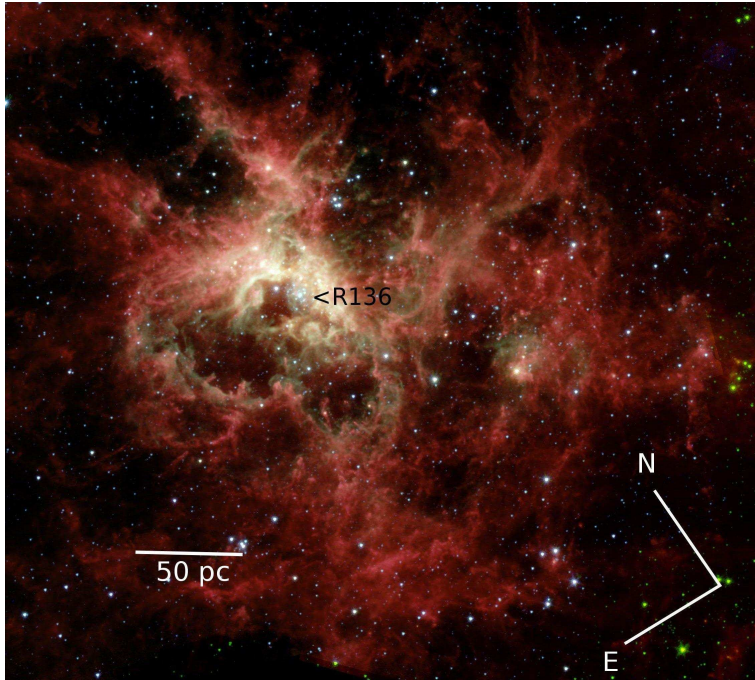


Figure 2.1 The 30 Doradus region imaged in the 4 Spitzer-IRAC channels. The filamentary structure and bubble-like cavities are evident. The ionized gas illuminated by R136 (green) is confined to a thin layer next to the PDR (red), where the PAH emission is found.

R136 is the most dense concentration of stars in the local group, with an estimated stellar mass of $2 \times 10^4 M_{\odot}$ contained within the innermost 5 pc (Hunter et al. 1995). The associated H II region has an $H\alpha$ luminosity of 1.5×10^{40} erg s^{-1} (Kennicutt 1984) and a far-infrared luminosity of $4 \times 10^7 L_{\odot}$ (Werner et al. 1978). Stellar winds, supernovae, and radiation pressure from the central cluster have excavated an expanding ionized bubble and created a complex filamentary structure (Fig. 2.1). This bubble, and other similar cavities in the region are filled with X-ray emitting gas at temperatures of $\sim 10^6$ K, as revealed by observations with the Chandra Space Observatory (Townsend et al. 2006). A

recent study of the optical emission lines shows no evidence of ionization by supernova-driven shocks found by a recent study (Pellegrini et al. 2010), and hence the dominant excitation mechanism in the 30 Doradus region is photoionization by the UV photons produced mainly in R136. This was corroborated by a comparison of observed IRS line fluxes with models of the mid-infrared lines (Indebetouw et al. 2009).

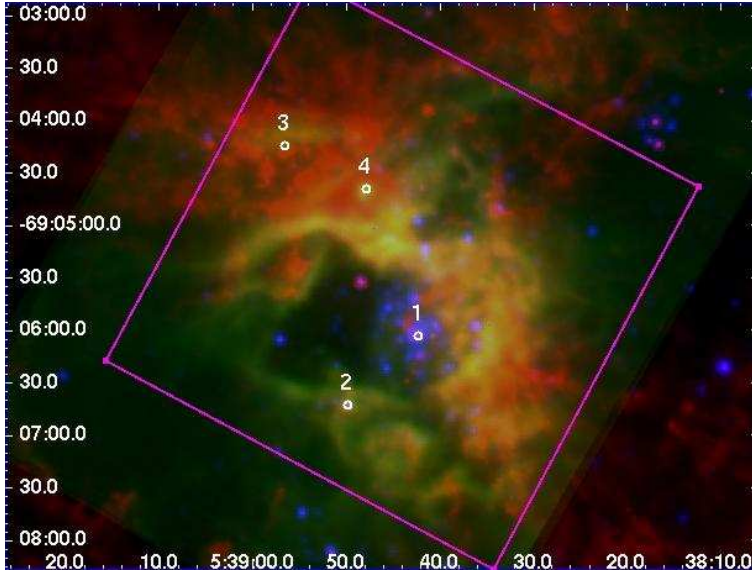


Figure 2.2 Multi-wavelength view of the 30 Doradus region. Red: IRAC $8\ \mu\text{m}$ image showing the PAH emission from the PDR region (c.f. 2.1). Green: $[\text{S IV}]10.5\ \mu\text{m}$ emission line map, constructed from the spectral map described in §2.2.2, tracing the distribution of highly ionized gas. Blue: Red continuum image showing the stellar continuum emission. White circles mark the positions of the individual spectra discussed in §2.2.3, and their sizes correspond to the size of one resolution element of the spectral map. The magenta square outlines the full IRS spectral map explored in this chapter. North is up and east is to the left.

Using HST spectroscopy, Walborn & Blades (1997) identified several non-coeval stellar populations in the 30 Doradus region, and classified them as follows: (i) a core-ionizing phase (R136), with an age of 2-3 Myr; (ii) a peripheral triggered phase, with an age of < 1 Myr (this population has also been identified using near infrared excess measurements, e.g. Maercker & Burton 2005); (iii) a phase of OB supergiants with an age of 6 Myr; (iv) the Hodge 301 cluster, $3'$ NW of R136, with an age of ≈ 10 Myr, and (v) the R143 OB association, with ages between 4-7 Myr.

An interesting aspect of 30 Doradus is its structure of bubbles and filaments. Observations of galactic and extragalactic H II regions have revealed expanding structures of ionized gas driven by stellar winds and supernova activity from the OB stellar population.

2 The physical conditions in starbursts derived from Bayesian fitting of mid-IR SEDs: 30 Doradus as a template

In the particular case of 30 Doradus, expanding supershells have been detected with diameters between 2 and 20 pc and expansion velocities of 100-300 km s⁻¹ (Chu & Kennicutt 1994).

The metallicity of 30 Doradus and of the LMC in general is sub-solar ($Z = 0.4 Z_{\odot}$) (Westerlund 1997). Due to this low metallicity environment, the dust-to-gas ratio in the LMC is about 30% lower than in the Milky Way (see review by Draine 2003, and references therein), and the system allows us to investigate the effect of UV radiation in lower metallicity environments as compared to our own galaxy.

For simplicity, in this chapter we refer to 30 Doradus as the region of ≈ 100 pc = 4.1 arcmin in diameter in projection centered in R136.

2.2.2 The integrated mid-IR spectrum of 30 Doradus

The Spitzer-IRS spectral data that we model here has been extensively discussed in Indebetouw et al. (2009), as part of the Spitzer General Observer Program *Stellar Feedback on Circumcluster Gas and Dust in 30 Doradus, the Nearest Super-Star Cluster*, (PID 30653, P. I. R. Indebetouw). It consists of four data cubes obtained by mapping the 30 Doradus region with the two low-resolution slits of the IRS (“short-low” and “long-low”) in each of their two spectral orders. For reference, the first order of the short-low (SL1) map covers an area of 116 pc \times 84 pc, and includes a significant portion of the 30 Doradus emission nebula. The wavelength coverage is between 5-38 μ m with a resolving power $R = \lambda/\Delta\lambda$, varying from 60 at the short wavelength end to about 110 at the long wavelength end. Exposure times were of the order of 150 s per slit position.

Spectra of chosen regions are extracted using the CUBISM software package (Smith et al. 2007). Once the sky subtraction has been performed, we extract individual spectra using a resolution element of 2×2 SL1 pixels for all orders. This corresponds to an angular resolution of 3.7 arcseconds, and a physical spatial resolution of roughly 1 pc at the distance to the LMC. To create the spatially integrated spectrum of 30 Doradus, we co-add the spectra of all individual resolution elements within an area of about 64 pc \times 63 pc (the magenta square in Fig. 2.2). We show the resulting integrated spectrum in Fig. 2.3. The integrated spectrum is dominated by emission from nebular lines and the thermal continuum, while the PAH emission is generally weak in the region.

Here we express all fluxes as νF_{ν} in units of erg s⁻¹. To convert from the MJy sr⁻¹ units from the IRS pipeline, we multiply the fluxes by the aperture area of 13.7 arcsec², and assume a distance to 30 Doradus (LMC) of 53 kpc (Feast & Catchpole 1997).

2.2.3 Individual sources

In Fig. 2.2 we have indicated four locations defined in Table 2.1, of which we show their respective spectra in Fig. 2.3. These locations include sources of different nature and were chosen to cover a broad range of physical conditions and spectral shapes. We model their spectra separately to study the validity of the models in environments which are dominated by either highly ionized gas or by embedded stars.

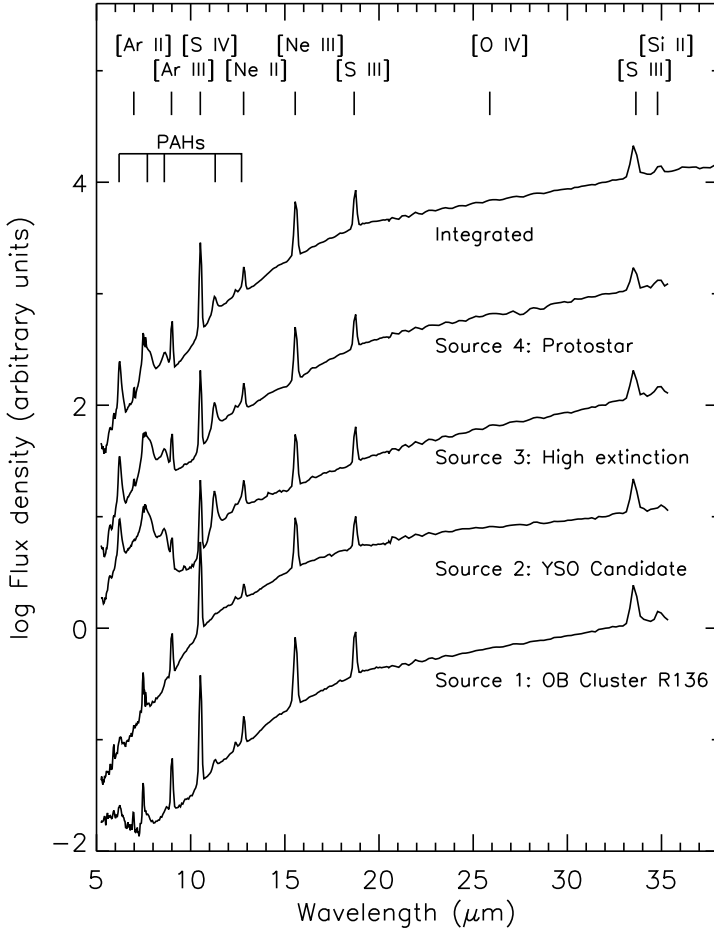


Figure 2.3 Integrated mid-infrared spectrum of 30 Doradus and spectra of sources described in §2.2.3 as labelled. All spectra are normalized to the flux at $30 \mu\text{m}$ and are shifted one decade in flux for comparison. The main spectral features are labelled.

Source 1 corresponds to the location of the young OB cluster R136. The emission here is dominated by UV and optical photons and shows little infrared emission from PAHs.

Source 2 is a YSO candidate selected from IRAC colors (Kim et al. 2007), according to the criterion suggested by Allen et al. (2004), about 1 arcminute southwest of R136, at the ionized southern edge of the main bubble-like structure, in a region with significant $[\text{S IV}]_{10.5 \mu\text{m}}$ emission. Its spectrum has a smooth thermal continuum with no sign of

2 The physical conditions in starbursts derived from Bayesian fitting of mid-IR SEDs:
30 Doradus as a template

Object	RA	Dec	Remarks
Source 1	5 ^h 38 ^m 42.3 ^s	-69° 06' 03.0''	R136
Source 2	5 ^h 38 ^m 49.7 ^s	-69° 06' 42.7''	YSO candidate
Source 3	5 ^h 38 ^m 56.5 ^s	-69° 04' 16.9''	High extinction ($\tau_{10\mu\text{m}} \approx 0.60$)
Source 4	5 ^h 38 ^m 48.30 ^s	-69° 04' 41.2''	Protostar, [S iv] emission

Table 2.1 Localized sub-regions in the 30 Doradus Spectral Map.

PAH emission, but with the typical nebular lines [Ne II]12.81 μm , [Ne III]15.56 μm , and [S III]18.71 μm .

Source 3 is a bright infrared source outside of the main bubble, to the north-west of the cluster. Its spectrum shows prominent PAH emission features and a deep silicate absorption feature at 10 μm .

Source 4 is an infrared source identified as a protostellar object by Walborn & Blades (1987), just outside the main bubble, north of R136. It coincides with a strong peak of [S IV] emission and is also an X-ray source. Lazendic et al. (2003) even consider this source to be a supernova remnant, but also point to its higher H α /H β ratio and the possibility of it being an H II region with an extinction higher than average.

In general, we observe that emission from all PAH bands is weak towards 30 Doradus as compared to other starburst systems (see, for example the starburst SED template in Brandl et al. (2006)). In particular, the 17 μm PAH complex generally associated with out-of-band bending modes of large neutral PAH grains (Van Kerckhoven et al. 2000, Peeters et al. 2004) is only marginally detected in our spectra. A remarkable result regarding this point is that the 17 μm complex is weaker towards source 3 than expected from the proportionality relations that have been empirically derived between different PAH bands (Smith et al. 2007). This proportionality implies that in starburst galaxies the equivalent width of the 11.3 μm feature is about twice the equivalent width of the 17 μm feature (Brandl et al. 2006). If this were to hold also for our source 3, we would expect a flux density of the 17 μm 20% higher than the thermal continuum at this wavelength. However, our data indicates an upper limit for the 17 μm emission of only 2% above the continuum level.

This suppression of the 17 μm band can have several interpretations. A possibility is that the PAH molecules are not neutral in this region of 30 Doradus. However, source 3 is outside of the main ionized bubble shown in Fig. 2.2, and hence we do not expect a high ionization state of the PAHs in this region. Metallicity variations could also account for a change in the relative strength of the 17 μm feature (Smith et al. 2007), but even in very low metallicity environments an extremely weak 17 μm would also imply a weak 11.3 μm feature, which we do not observe. We are left with the explanation of grain size effects. As mentioned, emission features between 15 μm and 20 μm are associated with large PAH grains, typically containing ≈ 2000 carbon atoms (Van Kerckhoven et al. 2000). Whether the conditions in 30 Doradus are unfavorable for the formation of large PAH grains is the matter of a subsequent paper.

2.3 Modelling the SEDs of starbursts

2.3.1 Literature on SED modelling

The simplest Spectral Energy Distribution models consider a starburst as a single spherical H II region surrounding a central ionizing cluster, use stellar synthesis for the stellar radiation and solve the radiative transfer for dust and gas in spherical geometry. These semi-empirical attempts use observations of specific objects, such as star-forming dwarf galaxies (Galliano et al. 2003) or nuclear starbursts (Siebenmorgen & Krügel 2007) to constrain the model parameters. They are successful in reproducing the photometry, and to some extent the IR spectra of these objects, but are limited to a narrow range of physical conditions (e.g., only two orders of magnitude in dust density). Fully theoretical models, such as the ones proposed by Takagi et al. (2003), make similar assumptions on geometry, dust properties and stellar synthesis, and cover a broader range of physical properties to model a larger sample of starburst galaxies, but ignore spatial variations of the parameters.

More sophisticated models consider the starburst as a collection of individual H II regions with different ages and environments, whose SEDs add up to produce the total galactic SED. In the GRASIL models, for example, each of these individual H II regions is assumed to have different physical properties (Silva et al. 1998). Unfortunately, they do not allow for the dynamical evolution of the expanding shell-like structures such as the ones we have described in §2.2.1. In the expanding mass-loss bubble scenario, the time-dependent radius and external pressure of the H II region are controlled by the mechanical luminosity from the newborn stars (Castor et al. 1975), and have a strong influence on the shape of the SED, as they control the gas and dust geometry (Groves et al. 2008).

None of the existing starburst models simultaneously accounts for both the multiplicity of H II regions in a starburst system and their time evolution as individual H II regions evolve as mass-losing bubbles. However, the models described in the series of papers Dopita et al. (2005), Dopita et al. (2006b), Dopita et al. (2006c) and Groves et al. (2008) (D&G models hereafter), represent a step forward in our theoretical description of starburst systems, by including these two aspects in a self-consistent way. Although these models have been successfully applied to the SEDs of a variety of objects, such as brightest cluster galaxies (BCGs) (Donahue et al. 2011), no systematic study of the model degeneracies have been presented. In the remainder of this section we briefly describe the underlying physics of the D&G models, emphasizing the aspects that are relevant for our discussion, and connect this description to the controlling model parameters. For a detailed description of the model, we refer the reader to the Dopita & Groves paper series.

2.3.2 The physical concept behind the model

The D&G models compute the SED of a starburst galaxy as the sum of the SEDs of individual expanding H II regions, averaged over ages younger than 10 Myr. By this age, over 95% of the total ionizing photons produced during the main sequence stage of the massive stars have been emitted (e.g. Dopita et al. 2006b) and the non-ionizing UV flux is

2 The physical conditions in starbursts derived from Bayesian fitting of mid-IR SEDs: 30 Doradus as a template

rapidly decreasing as the OB stars evolve off the main sequence into supernovae. Here we will test the applicability of the individual H II regions that constitute the building blocks of the models. Each individual giant H II region evolves in time as a bubble expanding into the surrounding ISM, driven by the stellar winds and supernova from the central cluster. The dynamical evolution is controlled by the equations of motion of the expanding bubble (Castor et al. 1975) and provides the instantaneous distance of the ionization front, dust and molecular gas with respect to the central cluster. The time-dependent expansion of this mass-loss bubble controls the temperature of the dust and the ionization state of the gas in the H II region, altering the shape of the SED.

The stellar synthesis code Starburst99 (Leitherer et al. 1999, Vázquez & Leitherer 2005) provides the stellar radiation field for a population of stars at a given age and metallicity. The energy output is normalized to a template cluster, whose mass is a free parameter of the models and can be scaled to any desired value. The stellar mass in the cluster is distributed according to a Kroupa IMF with a lower cutoff at $0.1 M_{\odot}$ and an upper cutoff of $120 M_{\odot}$ (Kroupa 2002). The photoionization code MAPPINGSIII (Groves 2004) provides a self consistent treatment of both the dust physics (photoelectric heating, dust absorption and emissivity properties, etc.) and the ISM physics, returning both line and continuum emission. The dust surrounding the cluster is considered to have contributions from three components: a population of carbonaceous grains with a power law size distribution; a population of silicate grains with the same size distribution; and a population of polycyclic aromatic hydrocarbon (PAH) molecules, whose emission is represented by a template based on IRS observations of NGC4676 and NGC7252, both interacting galaxies with strong PAH emission (Groves et al. 2008). Stochastic heating is taken into account, and the maximum grain size of the distribution is $a_{\max} = 0.16 \mu\text{m}$.

The radiative transfer is calculated for two physical situations. The first one considers the H II region only and follows the UV photons as they traverse the wind-blown bubble, heat the dust and ionize the atomic hydrogen until the boundary of the ionization front. The second one assumes a covering photo-dissociation region (PDR) around the H II region, with a hydrogen column density of $\log N(\text{H}) = 22.0 \text{ (cm}^{-2}\text{)}$ (an $A_V \approx 1 - 2$ at solar metallicity). The individual model SEDs are calculated at a discrete set of ages between 0 and 10 Myrs, with a resolution of 0.5 Myrs, and the final integrated SED is calculated as the age-averaged energy output of the process.

In §2.5 we will use both the integrated models and the single H II region models to interpret the observed integrated spectrum of 30 Doradus. This is equivalent to assuming two different approaches for the star formation history (SFH) of the region: an instantaneous burst of a given age, and a constant SFH over the last 10 Myrs. 30 Doradus, although dominated by the single star formation event that created R136, is neither morphologically nor spectroscopically a “single” H II region, and hence both of these simplifying assumptions should be tested to encircle the problem.

2.3.3 Model parameters

The global parameters that represent the general assumptions of the D&G models and that remain fixed by construction are those describing the overall geometry, the stellar IMF, the dust properties, and the PAH molecules. In the following we describe the parameters that are free to vary in the D&G models. To reduce our parameter space and focus our analysis, in our fitting process we will keep a few of these parameters constant based on previous knowledge of the region. The free parameters are: the starburst metallicity (Z), the ISM thermal pressure (P/k), the cluster mass (M_{cl}), the compactness (C), the PDR fraction (f_{PDR}), and the mass contained in embedded objects (M_{emb}).

Metallicity

We fix the value of this parameter to $Z \approx 0.4 Z_{\odot}$, which we consider a good average of several estimates using, for example, VLT observations of RR Lyrae star and Cepheid variables (Gratton et al. 2004) or modelling of chemical abundances in the LMC (Russell & Dopita 1992). Metallicity variations are expected for other extragalactic starburst environments, but the well established sub-solar metallicity of the LMC helps reducing the parameter space here.

ISM pressure

This parameter describes the ambient ISM pressure that opposes the expansion of the mass-loss bubble. From a comparison between FIR line ratios in a sample of star-forming galaxies measured with the Infrared Space Observatory (ISO) and PDR models by Kaufman et al. (1999), Malhotra et al. (2001) derived thermal pressures of the order of 10^5 K cm^{-3} . The spatial resolution achieved by ISO implies that, in most cases, this value corresponds to the thermal pressure averaged over the entire galaxy. While we acknowledge that $P_0/k = 10^5 \text{ K cm}^{-3}$ seems high for the average pressure of the LMC, we consider it a reasonable estimate near 30 Doradus, where gas densities have been boosted up by earlier star formation events. On the high pressure end, P_0/k is constrained by the pressure of the ionized X-ray emitting gas inside the bubble excavated by radiation pressure near R136, which has been estimated to be of the order of 10^6 K cm^{-3} (Wang 1999). We thus fix $P_0/k = 10^5 \text{ K cm}^{-3}$ in our models.

Cluster mass

The model SEDs scale in flux according to the total stellar mass contained in the star clusters. For an age-averaged model, averaged over the last 10 Myr, the scaling relates to the total mass of stars formed during that period of time, and hence the derived mass is interpreted as a star formation rate (SFR, in $M_{\odot} \text{ yr}^{-1}$), while for a model of a single cluster with a given age (our test case), the scaling relates to the cluster mass, M_{cl} . For all cases, however, it is assumed that stochastic effects within the IMF are limited, and that the stellar population samples the full range of stellar masses.

Compactness parameter

The D&G models introduce the compactness parameter, C , resulting from the combination of the ISM ambient pressure P and the cluster mass M_{cl} . This dimensionless parameter characterizes the distribution of the ISM with respect to the ionizing stars and is based on a constant heating flux input to the stars. Intuitively, it describes how close the dust is distributed to the ionizing stars as a function of the cluster mass and hence it controls the temperature distribution of the dust and the far-IR shape of the SED. C is proportional to the time-averaged cluster luminosity and inversely proportional to the time-averaged square of the swept-up bubble radius. As described in D&G, we can define the compactness as:

$$\log C = \frac{3}{5} \log \left(\frac{M_{\text{cl}}}{M_{\odot}} \right) + \frac{2}{5} \log \left(\frac{P/k}{\text{cm}^{-3} \text{ K}} \right) \quad (2.1)$$

where M_{cl} is the cluster mass, P is the ambient ISM pressure and k is the Boltzmann constant. The pressure parameter P/k relates to the ambient thermal pressure (or equivalently, the density) of the surrounding ISM.

PDR fraction f_{PDR}

As mentioned above, the D&G models explore two cases: a fully exposed H II region (i.e. the ISM ends at the ionization front), and an H II region that is completely covered by the PDR in projection, with $\log N(\text{H}) = 22 \text{ cm}^{-2}$. In reality, a star forming region will have a mix of both PDR emission and direct H II emission, which we approximate by the combination of the two extreme cases, parametrized by the fraction f_{PDR} :

$$F_{\nu}^{\text{HII+PDR}} = f_{\text{PDR}} F_{\nu}^{\text{PDR}} + (1 - f_{\text{PDR}}) F_{\nu}^{\text{HII}}, \quad (2.2)$$

where $F_{\nu}^{\text{HII+PDR}}$ is the monochromatic flux arising from the star forming region, while F_{ν}^{PDR} and F_{ν}^{HII} correspond respectively to the fluxes calculated for the PDR-fully covered case and the H II region-only case. $f_{\text{PDR}} = 0.0$ implies that there is no PDR material left around the ionized region, while $f_{\text{PDR}} = 1.0$ implies a fully PDR-covered H II region. In this fully-covered case, the PDR absorbs all of the non-ionizing UV continuum and re-radiates it at mid-infrared wavelengths.

Contribution from embedded objects

We expect a considerable contribution from a population of massive protostars to the mid-infrared SED of H II regions and starbursts, due to triggered and ongoing star formation. At the early stages of star formation, the young objects are in a protostar or Ultra-Compact H II phase, deeply buried in dust envelopes. From an observational point of view, and given the age resolution of the models, these two types of objects are indistinguishable. To account for them, the models include a population of UCHIIRs (Dopita et al. 2006a). In terms of the SED, these models add a component of hot dust at around $25 \mu\text{m}$. We parametrize this contribution by scaling it to the desired mass, M_{emb} .

2.3.4 Attenuation by diffuse dust

The models include an attenuation factor to account for additional absorption of UV light by foreground diffuse dust. This factor is important in the modelling of starburst galaxies, where there is significant diffuse material along the line of sight but not associated with the star-forming regions. The adopted extinction curve is derived by Fischera & Dopita (2005) and resembles a Calzetti extinction law, which is exponential. The incoming flux is corrected for extinction as: $F = F_0 e^{-\rho \sigma_{\text{att}}}$, where ρ is the column density of dust that gives a certain A_V , and σ_{att} is the dust attenuation cross section. Based on radio continuum observations, Dickel et al. (1994) find an extinction of $A_V = 1.1$ mag towards the 30 Doradus region. In a recent paper, Haschke et al. (2011) find a reddening towards 30 Doradus of $E(V-I) = 0.43$ mag, corresponding to a similar extinction. We expect individual sources to have higher extinction values within 30 Doradus, with individual protostars having values of A_V up to 4.0 magnitudes. Hence for consistency we use here an average value of $A_V = 2.0$.

2.4 Fitting routine

We introduce here a Bayesian fitting routine for the mid-infrared SED of a starburst, either individual starbursts such as 30 Doradus, or entire starburst galaxies. This routine can be easily extended to include other wavelength ranges, and can be used for any observed spectrum that is expected to be within the defined parameter space. We consider each model parameter as a random variable with an associated probability distribution function (PDF). Rather than just minimizing the χ^2 value to find the best fitting model, we solve for the probability distribution function of each of the model parameters.

In recent years, Bayesian analysis has been used in a number of different fields of astrophysics, where an attempt was made to reproduce a limited amount of data with multi-parameter models. Some of the applications of Bayesian methods in the determination of best fit parameters include photometric redshifts (Wolf 2009), observational cosmology (Kilbinger et al. 2010) and dusty tori around Active Galactic Nuclei (AGN) (Asensio Ramos & Ramos Almeida 2009).

2.4.1 Probability Distribution Functions

We fit the integrated spectrum of 30 Doradus and the individual locations in Table 2.1 using a grid of the D&G models parametrized by the quantities described in §2.3. In determining the best fit we use χ^2 -minimization, where the reduced χ^2 is given by

$$\chi_{\text{red}}^2 = \sum_{i=1}^N \frac{(F_i - f(p_0, \lambda_i))^2}{\text{DOF} \times \sigma_i^2}, \quad (2.3)$$

with the sum performed over all wavelength bins λ_i . The size of these bins is fixed by the wavelength resolution of the models. F_i is the measured flux for each wavelength

Parameter	Range	Resolution	Remarks
Age	0 – 10 Myr	0.5 Myr	
$\log C$	3.5 – 6.5	0.5	
f_{PDR}	0.0 – 1.0	0.05	
M_{stars}	2 orders of magnitude	0.13 dex	Adjusted to total flux density
M_{emb}	0.8 orders of magnitude	0.05 dex	Adjusted to total flux density

Table 2.2 Values adopted by the model parameters.

bin, f is the model-predicted flux at certain wavelength λ_i for a given set of parameters p_0 , σ_i is the observational error for F_i , and DOF is the number of degrees of freedom, namely the total number of wavelength bins minus the number of free parameters in the model. Minimizing χ^2 gives us the best fit values for the parameters, but tells us very little about the uncertainties in the model and the parameter degeneracies. However, by exploring the χ^2 surface over the range of parameters we can explore these degeneracies and the robustness of the returned parameters.

If the errors in the parameters can be described using a Gaussian distribution, the Bayes theorem states that the probability distribution function (PDF) for a given parameter or group of parameters (p_0) can be recovered from the reduced χ^2 distribution:

$$P(p_0) = \sum_{p \neq p_0} e^{-1/2 \chi_{\text{red}}^2}, \quad (2.4)$$

The resulting distribution, called the *posterior* distribution for that parameter, is the product of the *likelihood* distribution and a modulating probability distribution that includes any available a priori knowledge about the parameter, that comes from previous observations, theory, or the experimental setup. This modulating probability distribution is called the *prior* distribution. We refer to the adopted prior distributions as the priors of our study.

2.4.2 Model priors

Initially, we introduce bounded uniform priors for all parameters of the D&G model. The bounds introduced in our priors are predominantly constrained by theory, with some constraints from observations. We use a grid of 9×10^5 model outputs to cover the broad range of physical conditions in starbursts. Table 2.2 summarizes the resulting sampling for this study, the parameter ranges and their resolutions.

The range of ages is constrained by the typical main sequence lifetime of an early type star. For the compactness parameter C the limits are related to our knowledge of star-forming regions: values below $\log C = 3.5$ would imply very diffuse ($n \approx 10^4/T$) ISM or stellar clusters, far lower than expected for starburst regions, while values exceeding $\log C = 6.5$ would lead to very compact and massive clusters. The values of stellar mass in

the cluster, M_{cl} , and the mass contribution from embedded objects, M_{emb} are selected on a logarithmic scale depending on the total mid-infrared flux as measured in the spectra. The fraction of PDR material, f_{PDR} , ranges from a completely PDR-free starburst ($f_{PDR} = 0.0$) to a situation where the H II region is completely hidden by the PDR ($f_{PDR} = 1.0$).

2.4.3 Uncertainties and model resolution

Sources of observational error

There are three types of errors contributing to the total uncertainty of the measured flux densities:

- The absolute flux calibration. Using model stellar atmospheres, Decin et al. (2004) find that the 1σ uncertainties on the absolute IRS flux calibration are $\approx 20\%$ for the SH and LH modules and $\approx 15\%$ for the SL and LL modules. With regard to the modelling this error is similar to an uncertainty in the distance to the object, and affects mainly luminosity-based estimates, such as the derived SFR or stellar mass.
- The relative flux calibration. This refers to response variations within the given spectral range, often from one resolution element to the next one and is the equivalent of a “flat field”. From the typical differences between spectra of high signal-to-noise, taken at two different locations within the same slit, we estimated this uncertainty to be about 5%. With regard to the modelling this error limits the weight that can be given to individual spectral features, and is thus a fundamental limitation to the achievable accuracy.
- Systematic errors due to the specific observing conditions. This uncertainty includes observational jitter, drifts and source (de-)centering, which may lead to a wavelength dependent change in the overall SED slope. It also includes the amount of radiation that is external to the source of interest but picked up by the slit, e.g., from the diffuse interstellar radiation field or another nearby source.

Flux calibration of a slit spectrum can assume that the source is a point source, and multiply by the fraction of the point source outside of the slit, which corresponds to a wavelength-dependent “slit loss correction factor”. Alternately one can assume that the intrinsic distribution of emission is spatially flat, so the same amount of light is lost from the slit as re-enters it from a neighbouring point on the sky. *CUBISM* assumes the latter. Neither extreme is correct, and it results in a systematic flux uncertainty that scales nonlinearly with brightness.

In addition, many adjacent spectral features, measured with the low resolution IRS modules, will be blended together. This is most evident for the blending of the [Ne II] $12.81\ \mu\text{m}$ line and the $12.7\ \mu\text{m}$ PAH feature. Some of these systematic uncertainties vary in time, location on the slit and wavelengths, and are extremely hard to quantify. Hence, we do not attempt to quantify them but we need to keep these additional uncertainties in mind.

Furthermore, many distinct spectral features, such as the nebular emission lines, contain information on the physical conditions of the ISM which is complementary to the information that can be derived from the dust continuum. One might thus consider assigning these distinct wavelengths a larger weight (i.e., smaller error) in the fitting with respect to the more numerous continuum bins. However, these line fluxes are difficult to model very accurately, and a larger weight combined with some mismatch between observed spectrum and model may dominate the χ^2 -minimization routine and lead to an incorrect local maximum in the PDF.

One could also consider a very sophisticated fitting procedure where each resolution element gets its unique uncertainty (i.e., weight) assigned, taking all the above mentioned error contributions. However, we consider this approach practically impossible to reach our main goal, namely the provision of a reliable modelling procedure that yields reproducible results. From the above arguments it is evident that any total uncertainty (which will be used as weight in the χ^2 fitting) has to be larger than the error in the relative flux calibration, but will likely be smaller than the absolute flux uncertainty. Our tests have shown that a flux uncertainty of 10% for all IRS resolution elements leads to meaningful and robust results. Hence, we adopt an error of 10% per IRS resolution element.

However, the above stated values only hold for the Bright Source Limit (BSL) of the IRS, which corresponds to a S/N ratio of about 10 (*IRS Instrument Handbook*). For dim sources with $S/N < 10$, statistical variations in the number of detected photons (i.e., shot noise) dominate the uncertainties, and our 10% uncertainty estimate no longer holds. Other noise sources, such as noise from the detector read out and dark current come into play, and we need a more conservative error estimate. For all spectral resolution elements with $S/N < 10$ we use the RMS variations of the spectrum between adjacent positions in the spectral map. For each location we extract the spectra of the four nearest resolution elements. From these five locations we calculate the average and RMS deviations for each spectral resolution element, and replace our standard 10% uncertainty for the BSL by the RMS value for that spectral element.

Data rebinning

There is a difference between the wavelength bin size of the models and the resolution element of the Spitzer-IRS. The resolving power of the IRS ranges between 60-110, and hence a typical resolution element is of the order of $0.1 \mu\text{m}$. In contrast, for the models we have a wavelength step size that increases logarithmically with wavelength, and varies from $0.05 \mu\text{m}$ at $5 \mu\text{m}$ to $1 \mu\text{m}$ at $40 \mu\text{m}$, but includes local variations to resolve important line features. Therefore, we have re-binned the IRS spectral data to match the lower spectral resolution of the models, by averaging the fluxes of the data bins corresponding to the same model bin. The uncertainty of the resulting bins, on the other hand, are calculated as the square root of the quadratic addition of the uncertainties of the original IRS resolution elements. This propagation of error with the binning also prevents the uncertainties in the long-wavelength bins to dominate the fit.

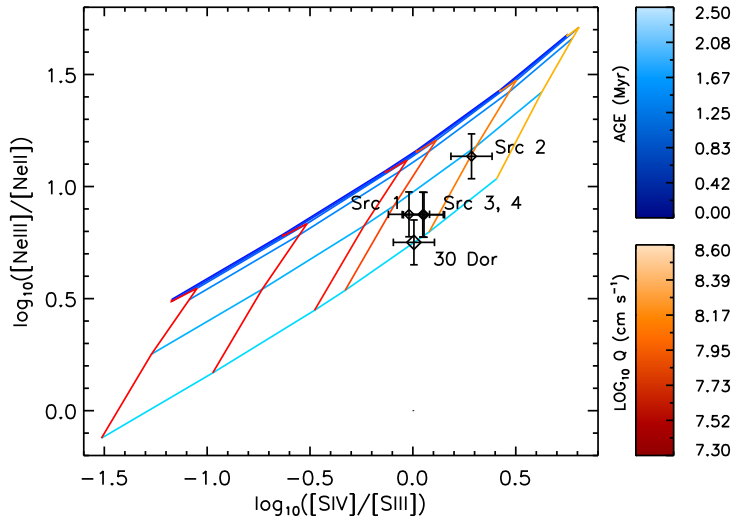


Figure 2.4 Measured mid-infrared nebular line ratios overplotted on a grid of starburst models from Levesque et al. (2010) that include a single H II region only. The parameters of the model are the age of the stellar cluster, and the ionization parameter, Q (the ratio of ionizing photon density to gas density), as labelled on the color-bars to the right.

2.5 Results

In this section we present and discuss the results of our fitting routine applied to the integrated spectrum of 30 Doradus, and subsequently also to selected subregions within 30 Dor. The latter have been added (see also sections 2.3 and 5.3) to probe the validity and limitations of our starburst models on regions whose spectra are dominated by one type of source (e.g., an OB cluster or a protostar).

In the following subsection we compare the results on the integrated starburst spectrum of 30 Dor, using three different approaches: (i) fitting all resolution elements of the entire $5 - 38\mu\text{m}$ spectrum, (ii) fitting the continuum bins only, i.e., excluding the fine-structure emission lines, and (iii) deriving the stellar ages from the IRS high resolution lines only. We will show how sensitive the results depend on the spectral information provided. We then compare the best fit results on the integrated 30 Dor spectrum with the results on the subregions. Finally, we discuss how the results would change if we would not assume a single age burst but an age averaged model.

2.5.1 Nebular lines ratios as age diagnostics.

The collection of emission lines in the mid-infrared wavelength range of the IRS are sensitive diagnostics of ages of massive OB stars and to the hardness of the radiation field. They have the advantage of suffering little from obscuration and hence allow us to probe the conditions of deeply buried regions. In particular, the $[\text{Ne III}]15.5\mu\text{m}/[\text{Ne II}]12.8\mu\text{m}$ and the $[\text{S IV}]10.5\mu\text{m}/[\text{S III}]18.7\mu\text{m}$ line ratios are good diagnostics of the ionization state of the gas, and hence provide a good constraint on the age of the ionizing cluster through measuring the hardness of the radiation field (see e.g. Groves et al. 2008).

By using the ratios of the nebular emission lines, we can provide useful constraints on the ionization state and age of the central cluster, and thus break the present degeneracies. In the particular case of 30 Doradus, we have measurements of the line fluxes with both the low resolution orders (*lores* hereafter) and the high resolution orders (*hires* hereafter) of the IRS. The *lores* lines have a larger flux uncertainty, and hence a good consistency check is to compare the results we get from the routine with results derived from the *hires* lines.

We use the *hires* nebular line fluxes presented in Leboutteiller et al. (2008) as a reference for the estimation of cluster age and ionization parameter and compare the results with what we obtain from the SED fitting for the four individual sources of Table 2.1. These line ratios are plotted in Fig. 2.4 superimposed on to a grid of models by Levesque et al. (2010) (created using the ITERA program of Groves & Allen 2010). These are essentially the same as the D&G models, and use both the Starburst99 and MAPPINGSIII codes with similar assumptions about the gas. However, the Levesque et al. (2010) models use a much simpler geometry (namely plane-parallel instead of spherical), demonstrating much more clearly how the degeneracy between the hardness of the radiation field (i.e. stellar cluster age) and the ionization parameter, Q (the ratio of the ionizing photon density to gas density), is broken using four strong mid-infrared emission lines. The dependence of the line ratios on these two parameters has also been noted by Morisset et al. (2004). Our comparison between the measured line ratios and the predictions from the Levesque models indicate ages between 2.0-2.5 Myr for all four positions.

The sample of sources in Leboutteiller et al. (2008) includes five more locations in the 30 Doradus region, apart from our four selected sources. Assuming that the measured line fluxes in these sources are representative of the overall conditions in the cluster, we estimate the line ratios for the whole region from the luminosity-weighted average line fluxes: $\log_{10}[\text{Ne III}]/[\text{Ne II}]_{30\text{Dor}} = 0.75$ and $\log_{10}[\text{S IV}]/[\text{S III}]_{30\text{Dor}} = 0.005$. We also plot this average value in Fig. 2.4. The result indicates an age of 2.5 Myr.

In Table 2.3 we list the ages derived from the Leboutteiller et al. *hires* line ratios as compared to the ages derived from the SED fitting in two cases: (a) fitting the emission lines and (b) excluding the emission lines. The reason to perform the fit using the continuum only is two-fold. First, we want to check the consistency of the results for our individual sources, which can not be treated as isolated H II regions, since their ionization states are affected by other external sources. Second, as we have already stated, while the line ratios can be reasonably estimated by the models, the *lores* equivalent widths of the lines are predicted with a lower degree of accuracy by the D&G models.

Source	SED fit with lines [Myr]	SED continuum [Myr]	Line ratios [Myr]
1	7.5	2.0	2.0-2.5
2	10.0	2.5	1.5-2.0
3	8.0	2.5	2.0-2.5
4	0.5	2.0	2.0-2.5
30 Dor	3.0	5.0	2.5

Table 2.3 Ages of individual sources

The results show that for the individual sources, the ages derived from the continuum-only fit are consistent with the high resolution measurements from Fig. 2.4 and with the independent measurements of the overall age of the region. On the other hand, including the unresolved lines in the fit for these individual sources leads to age estimates which are in disagreement with all the other methods, with a tendency to overestimate the ages.

The lowres line ratios imply age estimates that are not significantly different from the hires results and hence the mentioned disagreement should be interpreted in terms of the limitations of the integrated H II region D&G models to reproduce the continuum and the line emission for *individual* sources. Nonetheless, for the integrated spectrum, the derived age from the emission line fit is consistent with the high resolution measurements and with the literature, as expected for a self-contained region for objects of which class the models were intended.

Based on this results, for the integrated spectrum of 30 Dor we run the fitting routine including the emission lines. For the individual sources, however, we do not attempt to fit the low resolution lines and fit only the continuum. Also for the individual sources, to include the information contained in the high resolution line measurements, we modify the prior probability distribution for the ages from those listed in Table 2.2 to use a Gaussian distribution centered a 2.5 Myrs with a dispersion of 1.5 Myrs. This suppresses weights solution with older ages down, further constraining the parameters.

2.5.2 Integrated spectrum

Best fit

We show the resulting best fit from our code to the integrated spectrum of 30 Doradus in Fig. 3.9, with the residuals of the model fit to the observations shown in the lower panel. The quality of the fit is remarkable, with most of the spectral features in the mid-infrared spectral range successfully reproduced. This is a significant improvement from broad band photometry SED fitting, where only a few data points were fitted to constrain an equal number of parameters.

The individual contributions from the unobscured H II region, the PDR, and embedded populations are explicitly plotted in Fig. 3.9. The residuals in the bottom panel indicate

that the model fits the observations within the uncertainties for most of the IRS wavelength range, but underestimate the fluxes near $15 \mu\text{m}$. This feature is most likely due to an overabundance of small silicate grains within the assumed dust model, and is dominated by the embedded star model.

The sulphur lines at $10.5 \mu\text{m}$ and $18.3 \mu\text{m}$ appear as underestimated by our best fit model. This could be possibly due to abundance and/or pressure variations (see Dopita et al. 2006c), and we can only argue here that for the assumed abundances and ISM pressure, the fit in Fig. 3.9 represents the best case in the prediction of line ratios. The mid-infrared continuum is dominated by the embedded population, especially for $\lambda > 10 \mu\text{m}$ with the PDR contributing mainly to the PAH fluxes and the continuum slope at the long wavelength end of the spectral range. The H II region and PDR are responsible for most of the emission lines.

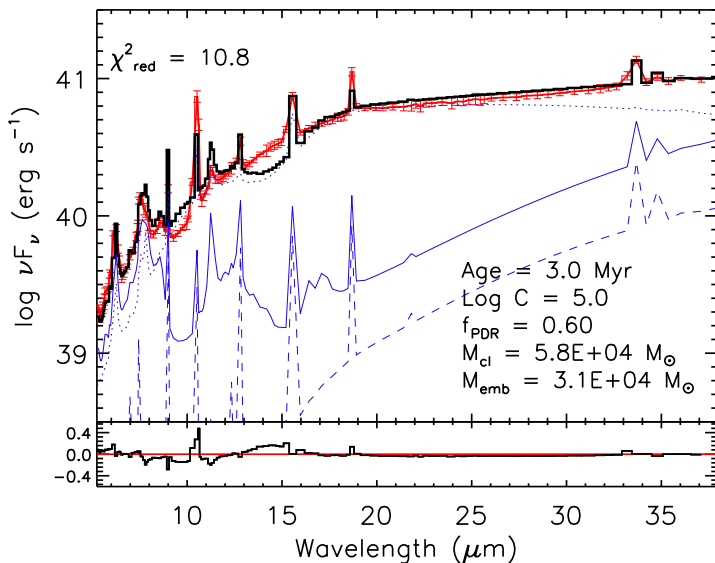


Figure 2.5 Best fit to the integrated IRS spectrum of 30 Doradus. *Red*: Observed spectrum rebinned to the model resolution with error bars for each bin. *Black*: best fit SED. *Dashed blue*: “Naked” H II region contribution. *Solid blue*: PDR and obscured H II region contribution. *Dotted blue*: Embedded object contribution. The best fit values and reduced χ^2 are indicated. Residuals are shown in the lower panel, in the same logarithmic units.

Interpretation of the results for the integrated spectrum

The normalized PDFs for the model parameters are shown in Fig. 2.6, for the priors as listed in Table 2.2 (dotted lines), and for the modified probability distribution of ages

Parameter	Age-unconstr.	Age-constr.	Literature
Age (Myr)	$3.0^{+5.5}_{-0.5}$	$3.0^{+1.5}_{-1.5}$	≈ 3 (Hunter et al. 1995)
$\log C$	$5.0^{+1.5}_{-1.0}$	$5.0^{+0.2}_{-1.0}$	
f_{PDR}	$0.6^{+0.4}_{-0.1}$	$0.6^{+0.4}_{-0.1}$	
$\log M_{\text{cl}} (M_{\odot})$	$4.8^{+0.7}_{-0.1}$	$4.8^{+0.2}_{-0.2}$	4.7 (R136) (Hunter et al. 1995)
$\log M_{\text{emb}} (M_{\odot})$	$4.47^{+0.08}_{-0.02}$	$4.47^{+0.08}_{-0.02}$	

Table 2.4 Best fit to the integrated spectrum of 30 Doradus

described earlier (dashed lines). The best fit values marked by vertical lines and the 1σ uncertainties indicated by the horizontal line pattern. We list the best-fit values, with the uncertainties corresponding to each case, in Table 2.4.

From the dark-shaded and dotted PDFs in Fig. 2.6 it is evident that several of the parameters appear to be very broad or even unconstrained. The reason for this can be clearly seen when we plot 2D PDFs for selected pairs of parameters in Fig. 2.7 (i.e. collapsing the χ^2 space down to two parameters). These show degeneracies between certain model parameters, indicating that, at least in the IRS wavelength range, these parameters affect the SED shape in a similar way. If one or both of these parameters can be constrained using other information, such as from other wavelengths, the 1D PDFs should become narrower, and the parameters better constrained.

In order to understand these degeneracies we need to look carefully at the 2D probability maps and link the resulting distributions to the effect that each parameter has on the spectrum. There is an age-compactness-cluster mass degeneracy revealed by two different set of parameters that provide a good fit to the observed SED. The first panel of Fig. 2.7 clearly shows the resulting two-peak distribution on the probability distribution for the total cluster mass-age subspace. These two parameters, as well as compactness, have a similar effect on the mid-infrared continuum as they vary across the grid: they scale the continuum flux by certain multiplicative factor.

The age-mass component of this degeneracy is not surprising: as compared to a cluster of certain mass and age, a less massive cluster is dimmer at Spitzer wavelengths, but the same holds true for an older cluster. IRS continuum fitting alone is incapable of distinguishing between these two parameters, as can be seen from the two-peak distribution. However, we have more information contained in the nebular lines. In particular, older clusters show less nebular emission, as the ionizing radiation strongly decreases with age. Including the lines in the fit breaks the age-mass degeneracy and enables us to select, between the two possible solutions, the one that best reproduces the measured line ratios. The best fit in Fig. 3.9 corresponds to this best solution.

The two peaks of the compactness-age degeneracy are clearly seen in the PDF maps, as shown in the second panel of Fig. 2.7. This degeneracy implies that both a young cluster with small compactness or an old cluster with high compactness lead to similar fits of the observed spectra, provided that the cluster mass also adjusts. This is shown in the

2 The physical conditions in starbursts derived from Bayesian fitting of mid-IR SEDs:
 30 Doradus as a template

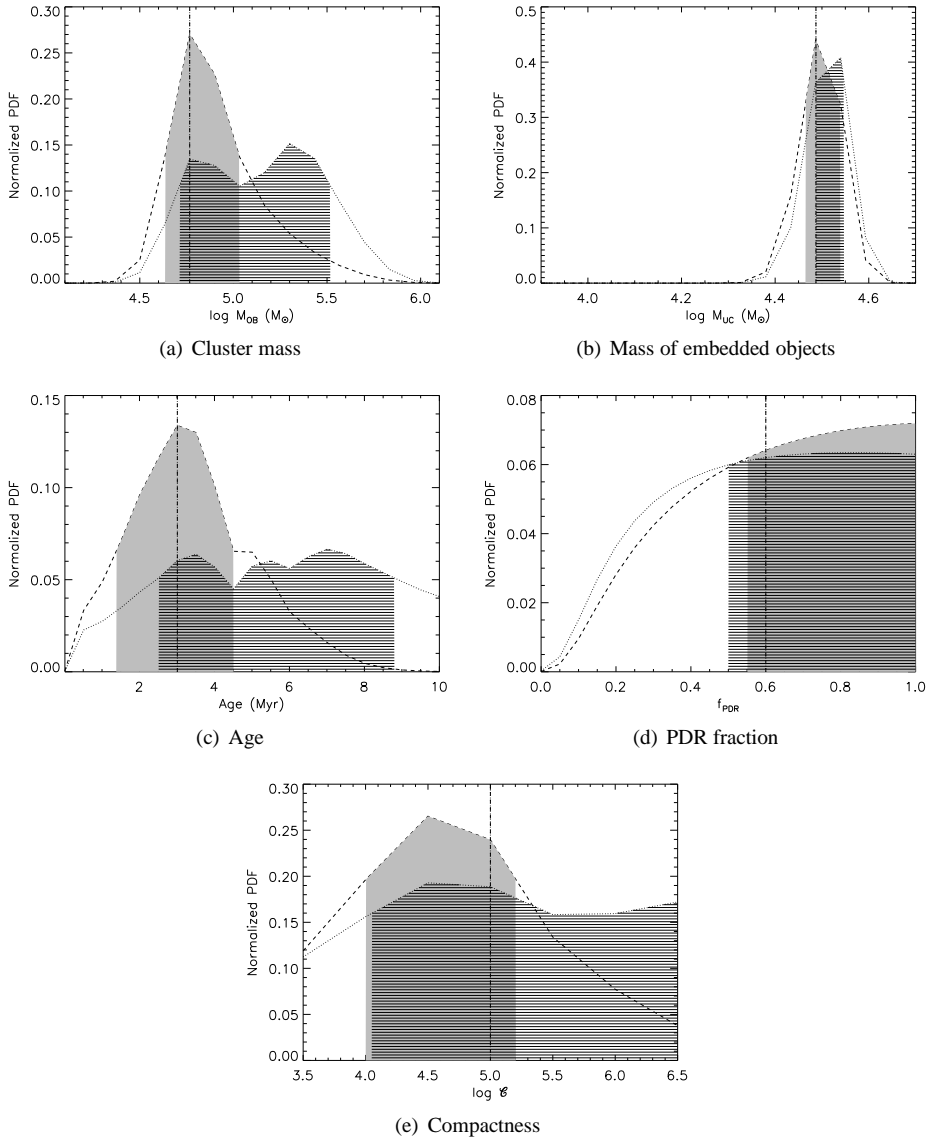


Figure 2.6 Probability distribution functions of the model parameters when fitted to the integrated spectrum of 30 Doradus, for two cases. *Dotted line*: uniform priors described in Table 2.2. *Dashed line*: Modified prior distribution for age, as defined in §2.5.1. The shaded areas correspond to the $1\text{-}\sigma$ integrated probabilities, while the vertical lines indicate the best-fit values.

central panel of Fig. 2.7. In this case, the emission lines are less sensitive to the variations of the two parameters together, since both the age of the cluster and the compactness affect the line ratios. However, once the age has been determined from the line ratios, the compactness probability distribution also shrinks and selects only one of the possible solutions for compactness.

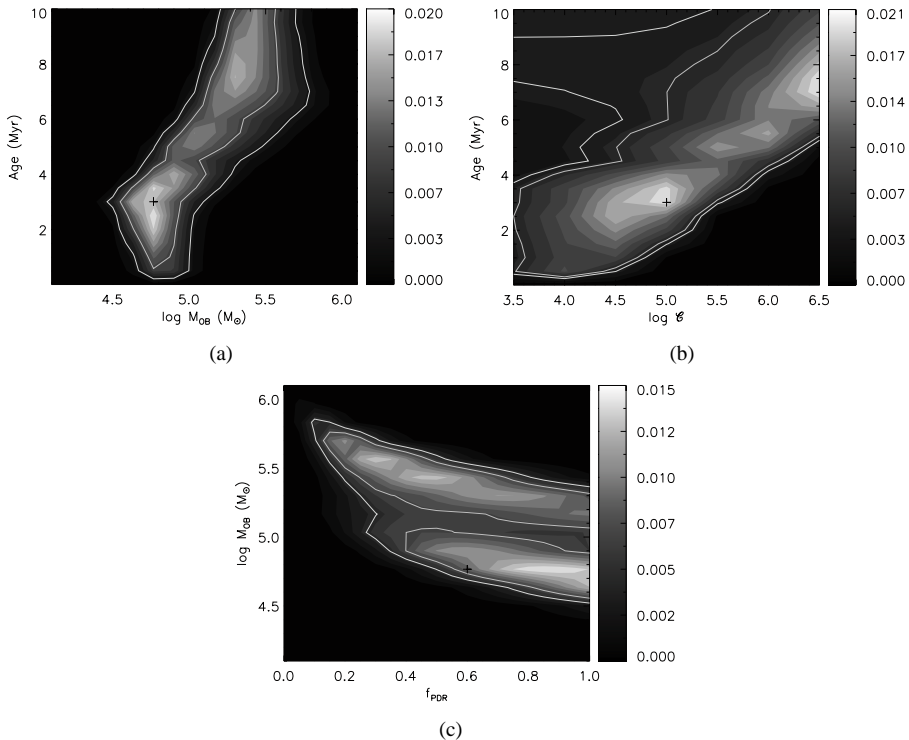


Figure 2.7 Two-dimensional PDFs for selected pairs of parameters showing the model degeneracies. The grey scale contours indicates normalized probability. The cross symbols mark the best-fit values while the white line contours indicate the $1\text{-}\sigma$ and 90% confidence levels.

Panel (c) of Fig. 2.7 shows a degeneracy between cluster mass and PDR fraction. The two strips correspond to the two peaks of the age-mass-compactness degeneracy, while the smooth diagonal variation corresponds to the PDR fraction-cluster mass degeneracy. This degeneracy arises from the fact that the PDR region that covers the H II region contributes mostly PAH emission, but also adds thermal dust continuum that in the models scales up with the PDR fraction. The emission lines are not of great help in breaking this degeneracy, since their relative fluxes are almost insensitive to variations in PDR content and total mass. In this particular point, thus, we can only do better if we include data from other wavelengths.

2 The physical conditions in starbursts derived from Bayesian fitting of mid-IR SEDs:
 30 Doradus as a template

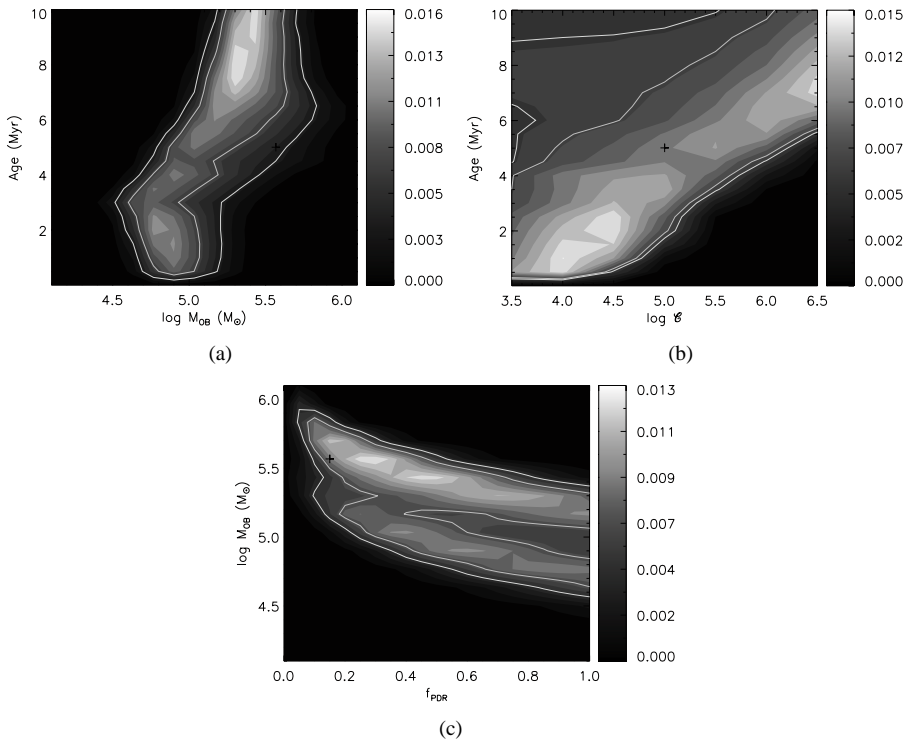


Figure 2.8 Two-dimensional PDFs for selected pairs of parameters, when only the continuum has been fitted. The grey scale contours indicates normalized probability. The cross symbols mark the best-fit values while the white contour lines indicate the 1- σ and 90% confidence levels.

To assess the importance of the line ratios in the constraining of the parameters and the break of the age-compactness-mass degeneracy, in Fig. 2.8 we plot the PDFs for the same parameter pairs, but this time after only the continuum has been fitted. A quick comparison between the two cases reveals that the inclusion of the lines not only selects one of the two degenerate peaks, but also helps the best fit values to converge towards the absolute maximum of the PDF. This is particularly evident for the mass-age degeneracy, where the continuum-only fit favors an older age solution, while the inclusion of the lines shifts the probability maximum to an age that is in agreement with independently measured values.

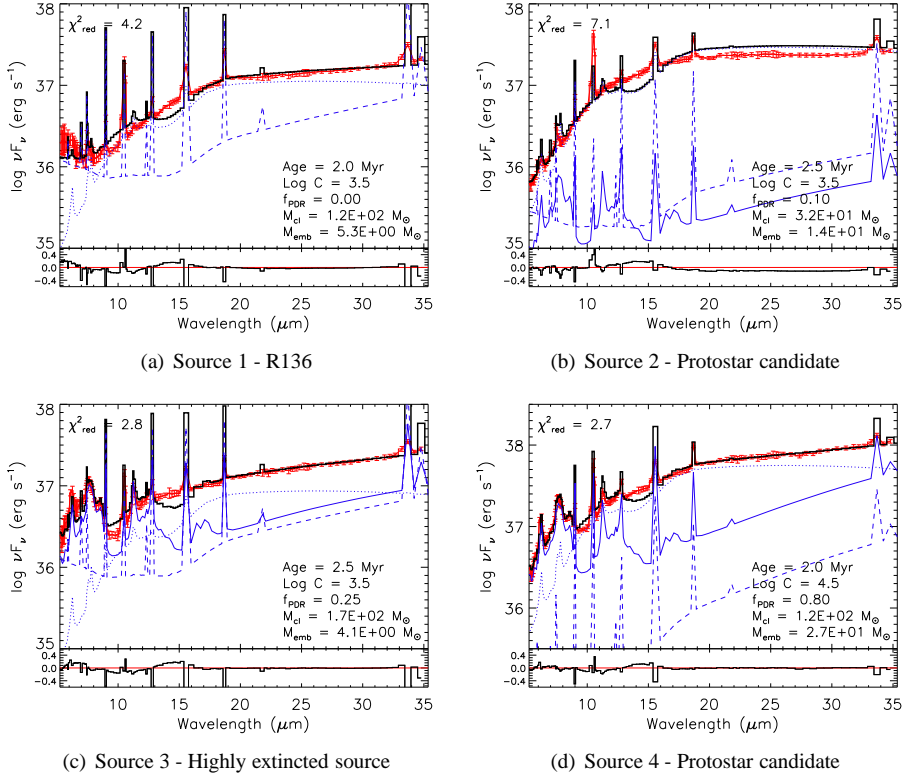


Figure 2.9 Best fit models for the individual positions, excluding the emission lines from the fit and with the age distribution constrained by the line ratio analysis. The color code is the same as for Fig. 3.9.

2.5.3 Individual sources

As noted before, any complex starbursting system is likely to cover a wide range of object types and physical conditions, from individual protostars and luminous UCHIIRs to OB clusters, loose stellar associations, PDRs and the diffuse ISM. To investigate the range of conditions for which our starburst models still yield accurate results, we have chosen four subregions that probe these “extreme” cases where one of these components is expected to dominate the mid-infrared spectrum, based on detection of, for example, infrared excess or X-ray emission. These sources are the OB cluster R136 with little dust obscuration, an H II region which shows high extinction along the line of sight (source 3), and two compact objects, which are luminous protostellar candidates (sources 2 and 4).

We fit the continuum spectra of those subregions and include the emission line ratios as a modified probability of the ages, as described in §2.5.1. While we do not expect to

2 The physical conditions in starbursts derived from Bayesian fitting of mid-IR SEDs:
30 Doradus as a template

	Source 1	Source 2	Source 3	Source 4
t (Myr)	$2.0^{+2.0}_{-1.0}$	$2.5^{+2.0}_{-1.5}$	$2.5^{+2.5}_{-1.0}$	$2.0^{+2.5}_{-1.0}$
$\log C$	$3.5^{+1.0}_{-0.0}$	$3.5^{+0.5}_{-0.0}$	$3.5^{+0.5}_{-0.0}$	$4.5^{+0.5}_{-0.5}$
f_{PDR}	$0.00^{+0.40}_{-0.00}$	$0.10^{+0.50}_{-0.05}$	$0.25^{+0.70}_{-0.00}$	$0.80^{+0.20}_{-0.35}$
$\log M_{\text{cl}}$ (M_{\odot})	$2.1^{+0.0}_{-1.1}$	$1.5^{+0.0}_{-0.6}$	$2.2^{+0.2}_{-0.5}$	$2.1^{+0.4}_{-0.2}$
$\log M_{\text{emb}}$ (M_{\odot})	$0.73^{+0.12}_{-0.03}$	$1.13^{+0.07}_{-0.03}$	$0.61^{+0.14}_{-0.06}$	$1.43^{+0.12}_{-0.08}$

Table 2.5 Best fit parameters for individual positions in 30 Dor

get a very good fit on these types of sources with the general starburst models, we want to verify that the crucial parameters are qualitatively still constrained within reasonable limits, according to the respective physical condition probed by the individual sources.

Best fits to the spectra of individual sources

We have seen that in the case of the integrated spectrum, fitting the emission lines along with the continuum greatly helps in breaking the model degeneracies. However, as discussed in §2.5.1 and summarized in Table 2.3, this is not the case for the individual sources, where the fitting of unresolved lines leads to age estimates which are in disagreement with the continuum-only fit and with the line ratio analysis, for reasons that are described in §2.5.1. Hence, we do not include the emission lines in the SED fitting of the individual sources. Furthermore, we modify the age prior to include only ages that are consistent with the high-resolution line ratios, within the uncertainty limits set by the comparison of the line ratios and the Levesque models. In each case, instead of the uniform prior distribution of probability for the age, we use a Gaussian PDF centered at 2.0 Myr with an uncertainty of 1.5 Myr.

The resulting best-fit SEDs are shown in Fig. 2.9. The resulting best fit parameters and $1-\sigma$ ranges derived from the PDFs are shown in Table 2.5.

Interpretation of the results for individual sources

All of our spectra show significant flux densities in the $10 \mu\text{m}$ range. This continuum emission is indicative of hot dust at $T \approx 300 \text{ K}$, which is typically associated with proto-stars, but not exclusively. It may also include emission from dust close to slightly more evolved stars, as well as hot dust in between stars of a cluster, and dense clumps in the H II region that cannot be modelled by the simple uniform H II region model of D&G. We account for all these contributions by what we have called the embedded component. Fig. 3.9 shows that this component dominates the emission of 30 Doradus at mid-infrared wavelengths.

In fact, our attempts to fit the integrated spectrum of 30 Doradus without including this embedded component have proven unsuccessful, and hence, it is one of our main

results that this component of “embedded objects” is necessary to fit the observed spectra for $\lambda > 10 \mu\text{m}$. Qualitatively, this interpretation looks quite plausible: the two positions that coincide with the location of YSO candidates (sources 2 and 4) have the higher relative mass contribution from the embedded component, with 30% and 20% of the total mass contained in embedded objects, respectively. The corresponding contributions from embedded mass in R136 and the highly extinguished source are 5% and 2%, respectively (Table 2.5). However, we need to keep two issues in mind:

First, while we associate this component with a recently formed star, strictly speaking it is not entire due to protostars and UCHIRs, for the reasons given above. Hot dust in starbursts may also be found in other environments and, hence, the amount of “embedded objects” derived from our fits can only be considered as an *upper limit* on the amount of protostars and UCHIRs.

Second, the contribution of this embedded component to the total emission at $\lambda > 10 \mu\text{m}$ may be surprisingly high but is not unreasonable. This is illustrated in Figs. 2.9(a) and 2.9(b), which show the fits to source 1 (R136, the main cluster) and source 2 (a protostar, or group of protostars). While M_{cl} (stars + H II region + PDR ensemble) is at least one order of magnitude larger in the case of R136 than in the embedded region, the contribution of the embedded component is much higher for the protostar in comparison, and so are the observed flux densities over most of the IRS spectral range. While R136 contributes most of the stellar mass, much less massive components described as “embedded objects” contribute the majority of the mid-IR flux.

In other words, the fact that the integrated flux in 30 Doradus is dominated by this embedded component does not imply that there is a similar mass contribution from this embedded component. In fact, our derived mass contribution of embedded objects to the stellar mass of 30 Doradus is about 35%. Furthermore, despite the uncertainty in the nature of the embedded component, we will show in section 5.4 that the star formation rate in 30 Dor derived from our modelling approach does *not* overestimate the “true” star formation rate as derived from integrated panchromatic SEDs that include the far-IR. Additionally, the application of our routine to starburst galaxies shows that this component of embedded objects does not dominate the mid-infrared emission for these galaxies, as it does for 30 Doradus.

Our results in Table 2.5 indicate that source 4 has a higher compactness as compared to the other individual sources. High values of $\log C$ are expected in compact starbursts with high surface brightness, where dust is in close proximity to intense UV fields. Source 4 is a very bright and compact source of [S IV] $10.5 \mu\text{m}$, indicating the presence of highly ionized gas probably near a hard UV source, and, as pointed out in §2.2.3, is also a bright X-ray source that has even been considered as a supernova remnant candidate. No other location in our spectral map shares these characteristics as an individual source. On the other hand, low compactness is derived for sources where the simultaneous presence of bright stars and dust can be inferred, as it is the case of sources 1, 2 and 3.

We conclude that, even though our models are not intended to model these individual sources, we can nonetheless learn from the compactness parameter, as defined in §2.3.2, by comparing the results of the routine applied to them. The routine is capable of constraining the proximity of luminous sources and hot dust. We have derived a relatively

high compactness for 30 Doradus itself with $\log C = 5.0$, which is consistent with the luminous cluster in its center surrounded by nearby ridges of dust.

A comparison of the values for f_{PDR} in Table 2.5 with the spectra in Fig. 2.3 indicates that, as expected from the construction of the models, a high covering fraction is generally associated with strong PAH features. We show here that source 2, where a YSO has been identified via infrared excess, has little associated PAH emission, whereas source 4, which also shows infrared excess and has been associated with a YSO, shows significant PAH emission. The presence of PAH emission in the line of sight towards embedded objects might depend on the evolutionary stage of the YSO, i.e., on the optical thickness of the envelope. If UV photons from a young, massive protostar manage to escape the embedded region and create a PDR around the YSO, then we expect to detect PAH emission. In some cases, like source 3, where the deep silicate feature typical from highly embedded objects is accompanied by high line ratios indicative of an ionizing source, the PAH emission can even dominate over the embedded component. No significant PDR emission is inferred from the fit to R136. This is consistent with the expected absence or low abundance of PDR material very close to the ionizing cluster.

There are two important caveats that we must consider in the interpretation of the PDR covering fraction. First, we have not included here emission from diffuse dust, not associated with the starburst (i.e. heated by the interstellar radiation field); this adds both cold dust and PAH emission. Second, there exists a degeneracy between the covering fraction of PDR material and the cluster mass in the mid-infrared (right panel of Fig. 2.7), due to the fact that PDR regions not only add PAH emission, but also continuum emission at longer wavelengths. This translates in the apparent mismatch between the PDFs and the best fit values for these two parameters in Table 2.5.

2.5.4 Age averaged case

The degeneracy found for the integrated spectrum of 30 Doradus that leads to the two possible solutions of an old, massive cluster or a young cluster with a smaller mass is indicative that not even 30 Doradus can be considered as a single coeval stellar population. As described in the introduction, a number of spectroscopically identified populations have been identified in 30 Doradus, and the fact that the continuum is compatible with two different sets of parameters leads us to the conclusion that a simple, single-age approach might be inaccurate even for our benchmark H II region. Thus we also carry out the SED fitting using an age-averaged model.

We have fitted the integrated spectrum of 30 Dor using the age-average model described in §2.3.2, where the SED is integrated over the 0–10 Myr lifetime of the ionizing stars. In this case, the cluster age is no longer a free model parameter, and we can interpret the absolute flux scaling as the SFR instead of a single cluster mass. We keep the ISM pressure (P/k) and the metallicity (Z) fixed to the same values as for the single age case. The best fit parameters we calculate in this way must be interpreted as average values over the time span covered by the models. Fig. 2.10 shows the resulting best fit to the data with the age-average model, and Table 2.6 lists the best-fit parameters with the associated

Parameter	Best fit
$\log C$	$5.0^{+0.0}_{-1.0}$
f_{PDR}	$1.00^{+0.00}_{-0.45}$
$\log \text{SFR}_{\text{eff}} (M_{\odot} \text{ yr}^{-1})$	$-2.05^{+0.35}_{-0.05}$
f_{emb}	$3.20^{+0.64}_{-0.40}$

Table 2.6 Best fit to the integrated spectrum of 30 Doradus with age-average model.

uncertainties derived from the PDFs.

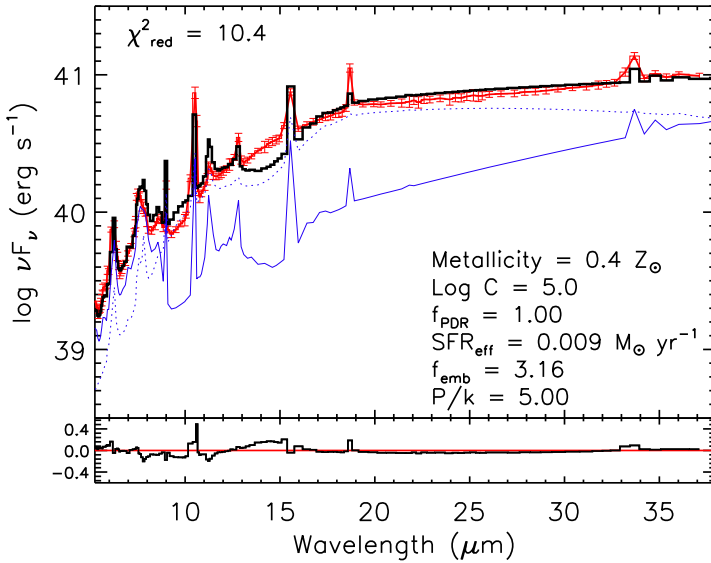


Figure 2.10 Best fit to the integrated IRS spectrum of 30 Doradus using the age-average model. The color code is the same as in Fig. 3.9.

Here we use the parameter f_{emb} instead of M_{emb} . It refers to the ratio of mass contained in embedded objects to the mass of main sequence stars for objects younger than 10 Myr, and hence it is related to the amount of currently ongoing star formation. In other words, f_{emb} gives the fraction of embedded/UCHII luminosity-weighted contribution that we have to add to the SED to fit the observed spectrum. If $f_{\text{emb}} = 0.0$, there is no current star formation happening, whereas if $f_{\text{emb}} = 1.0$, half of the massive stars formed over the last million year are still in a embedded state. Since this contribution is integrated over a period of 1 Myr only, adding embedded objects also implies that the average SFR has to be modified according to:

$$\text{SFR}_{\text{eff}} = \text{SFR} + \frac{f_{\text{emb}}}{f_{\Delta t}} \text{SFR} \quad (2.5)$$

where SFR_{eff} is the effective SFR that accounts for the additional population of embedded objects, and $f_{\Delta t}$ is the ratio of the total time over which the starburst has been modelled (10 Myr) and the estimated duration of the embedded phase (1 Myr). For our best fit case, we get $\text{SFR} = 0.007 M_{\odot} \text{ yr}^{-1}$ and $f_{\text{emb}} = 3.2$, which implies that among the stars younger than 1 Myr, there are about three times more embedded objects than main sequence objects. Hence, the effective SFR is $\text{SFR}_{\text{eff}} = \text{SFR} + 0.32 \times \text{SFR} = 0.009 M_{\odot} \text{ yr}^{-1}$.

The LMC has a SFR of $0.1 M_{\odot} \text{ yr}^{-1}$ (Whitney et al. 2008). Keeping in mind that this is only a lower limit estimate, given the incompleteness of any YSO catalogue, our result implies that between 3% and 10% of the star forming activity of the LMC takes place in the 30 Doradus region. To see how this compares to estimates of the SFR in 30 Doradus from single photometric measurements, we compare the IRAS flux at $25 \mu\text{m}$ for the entire LMC to the $64 \text{ pc} \times 63 \text{ pc}$ area from which we have extracted the spectrum of 30 Dor. The total flux density from the LMC at $25 \mu\text{m}$ is $7520 \pm 1100 \text{ Jy}$ (Israel et al. 2010). From our integrated spectrum (Fig. 2.3), we derive a monochromatic flux density of $1739 \pm 174 \text{ Jy}$ for the same wavelength, which corresponds to 24% of the total LMC flux density. Assuming this wavelength directly traces star formation, it suggests that our value is close, but may be underestimated by a factor of two.

The compactness and fraction of PDR results are consistent in both the single age case and the age average case.

2.6 Summary and conclusions

Significant progress in our understanding of starburst systems has been made over the past decades, both on the observational and theoretical side. A huge amount of spectral data on star forming regions and starburst galaxies has been collected with ISO, Spitzer and the Herschel Space Telescopes, complemented by a considerable library of SED models that predict the energy output of starbursts as a function of wavelength.

However, SED fitting of starburst has mainly focused on maximum likelihood methods, which generally overlook degeneracies between physical parameters and lead to results that are not unique. Furthermore, these ad hoc approaches often depend on some hidden assumptions that make the results reproducible. In this chapter, we presented a routine to fit the SEDs of starbursts based on the models proposed in the series of papers Dopita et al. (2005), Dopita et al. (2006b), Dopita et al. (2006c) and Groves et al. (2008). We verified the accuracy and limitations of our approach by comparison between the model fit results and the known properties of the well-studied, prototypical giant H II region 30 Doradus. Our main findings are:

- Our modelling procedure is able to fit a broad range of continuum slopes, PAH intensities, and emission lines. Although we have only used the mid-infrared spectra for the calibration, the method can be easily expanded to other wavelength ranges.

- We have verified the validity of our approach by comparison with the well studied 30 Doradus region. The derived physical parameters, such as cluster mass, cluster age, ISM pressure and PDR content, are in good agreement with the known properties of this nearby starburst.
- We have provided a detailed study of the model degeneracies in the mid-infrared window of the spectrum, and have shown that the best fit values to the continuum shape are driven by a triple luminosity-age-compactness degeneracy that, in general, leads to multiple “best fits”.
- The inclusion of emission lines in the analysis breaks this degeneracy. It is expected that the addition of other wavelength ranges would further constrain the model parameters. In particular, the precise location of the peak of the dust emission in the far-infrared is crucial to constrain the compactness parameter. Herschel spectroscopy, as well as MIPS and PACS photometry, play an important role here.
- We provided meaningful results to the model-defined compactness parameter C , introduced by Groves et al. (2008), and linked them to the proximity of ionizing sources and hot dust.
- We have shown that modelling the SED of a typical starburst region requires a component of heavily embedded objects (massive YSOs and UCHIIRs) which dominate the mid-infrared continuum slope. The derived mass fraction of this embedded component can be interpreted as an upper limit to the amount of current star formation, since there are other dust heating mechanisms not included in the models.
- We found a degeneracy between the total stellar mass and the relative amount of PDR material, f_{PDR} , as both will contribute to the dust continuum. This degeneracy may lead to uncertain mass estimates and can only be resolved with additional data at longer wavelengths, e.g. from Herschel.
- Generally, two critical assumptions in all starburst models are the age and duration of the burst. Our “local” template 30 Doradus nicely illustrates the typical complexity of a starburst with both, the presence of a luminous, coeval cluster (R136), and strong evidence for continuous star formation across the region. Hence, we have also used an age-average model of continuous star formation for comparison. This model delivers values for compactness and PDR contribution that are consistent with those derived from the single age models. For 30 Doradus we derive a contribution of approximately 10% to the total SFR of the LMC.

Now with a robust and well-tested modelling and fitting routine in hand, we plan to apply this approach to more distant giant H II regions and starburst galaxies. The lack of spatially resolved data on e.g., more distant ULIRGs and sub-millimeter galaxies requires reliable and well calibrated models to derive the physical conditions in these starbursts. The novel fitting procedure presented in this chapter constitute the next step in starburst modelling and puts such studies on solid grounds.

CHAPTER 3

Ongoing massive star formation in NGC 604¹

NGC 604 is the second most massive H II region in the Local Group, thus an important laboratory for massive star formation. Using a combination of observational and analytical tools that include *Spitzer* spectroscopy, *Herschel* photometry, *Chandra* imaging and Bayesian Spectral Energy Distribution (SED) fitting, we investigate the physical conditions in NGC 604, and quantify the amount of massive star formation currently taking place. We derive an average age of 4 ± 1 Myr and a total stellar mass of $1.6_{-1.0}^{+1.6} \times 10^5 M_{\odot}$ for the entire region, in agreement with previous optical studies. Across the region we find that the X-ray field destroys small aromatic molecules and excites the emission of [Si II]. Within NGC 604 we identify several individual bright infrared sources with diameters of about 15 pc and luminosity weighted masses between $10^3 M_{\odot}$ and $10^4 M_{\odot}$. Their spectral properties indicate that some of these sources are embedded clusters in process of formation, which together account for $\sim 8\%$ of the total stellar mass in the NGC 604 system. The variations of the radiation field strength across NGC 604 are consistent with a sequential star formation scenario, with at least two bursts in the last few million years. Our results indicate that, while NGC 604 is a more evolved H II region as compared to its largest sibling 30 Doradus, star formation in NGC 604 is still ongoing, triggered by the earlier bursts.

¹Based on: J.R. Martínez-Galarza, D. Hunter, B. Groves and B. Brandl, 2012, Submitted to ApJ

3.1 Introduction

Despite their importance in the structure and evolution of galactic systems, via strong radiative and mechanical input into the surrounding interstellar medium (ISM), our understanding of massive star formation regions remains poor, both on observational and theoretical grounds. From an observational point of view, a number of reasons make the study of massive star formation a challenging topic in astrophysics, as pointed out in the comprehensive review on the issue by Zinnecker & Yorke (2007). Regions of massive star formation are highly embedded in thick layers of dust during the crucial early stages of their existence. In addition, these early stages are short-lived, leaving little time for the study of their evolution. Another problem is the lack of spatial resolution in the observations. Most of extragalactic giant star forming regions are often contained within a single pixel. Finally, most massive stars form in close proximity to each other, and their mutual influence via gravitational interaction, powerful outflows, supernova events and strong winds contributes to the complexity of the problem.

Observations of nearby star forming regions provide an excellent laboratory for the study of a particular aspect of this interaction, namely the triggering of new star formation events by gas compression resulting either from a ionization shock front created by the radiation field of a previous generation of stars, or by the supersonic shocks of a supernova event. In the classical theory by Elmegreen & Lada (1977), an ionization front compresses an adjacent layer of molecular gas and heats it, producing a gravitational instability that will eventually result in a new generation of stars. In order to test this and other theories of triggered star formation, it is important to unequivocally determine and quantify the amount of currently ongoing star formation in Giant H II Regions (GH II Rs), and its relation to the ionizing radiation from previous generations of stars.

After 30 Doradus, NGC 604 is the second most massive GH II R in the Local Group. Located in the Triangle Galaxy (M33) at a distance of 0.84 Mpc (Freedman et al. 1991), it harbors several associations of massive stars distributed across an area of about 200 pc on the side, dominated by a cluster containing ~ 200 OB stars (Hunter et al. 1996). These associations have excavated a complex system of filaments and cavities of ionized material surrounded by photon-dominated regions (PDRs) and molecular gas (see, for example Relaño & Kennicutt 2009, for a discussion on the spatial distribution of emission in the region). Optical studies reveal an age of the region between 3 and 5 Myr (Hunter et al. 1996, González Delgado & Pérez 2000) and a total stellar mass of $(3.8 \pm 0.6) \times 10^5 M_{\odot}$. Individual CO molecular clouds have been detected with sizes between 5 and 29 pc and with masses of between $0.8 \times 10^5 M_{\odot}$ and $7.4 \times 10^5 M_{\odot}$ (Miura et al. 2010). Relaño & Kennicutt (2009) have carried out a photometric multi-wavelength study of NGC 604 and derived an average extinction in the line of sight towards NGC 604 of $A_V = 0.30$ and a stellar mass of about $(5.7 \pm 0.4) \times 10^5 M_{\odot}$ for the region, not too far from the mass estimate of Eldridge & Relaño (2011).

Several attempts have been made to quantify the total amount of ongoing massive star formation in NGC 604. Using near-infrared (NIR) observations with the *Hubble Space Telescope* (HST), Barbá et al. (2009) identify several sources that coincide spatially with radio-peak structures, and argue that this is suggestive of their star-forming nature. More

recently, Fariña et al. (2012) report the discovery of sources with near infrared excess within the infrared-bright ridges surrounding the ionized gas, and associate them with Massive Young Stellar Objects (MYSO). Relaño & Kennicutt (2009) argue that the reddening observed towards some prominent sources in the region can be explained by the existence of foreground molecular material, but they do not rule out the possibility of those sources being embedded sites of star formation. The use of infrared spectrophotometry combined with physical modeling provides a powerful tool to distinguish between foreground extinction and embedded star formation, which complements the photometric methods that use near-infrared colors as discriminators between the two cases, and could be.

In this chapter we perform a comprehensive analysis of the physical conditions in NGC 604 in the context of its evolutionary status, and investigate the presence of ongoing massive star formation in the region. We use infrared spectral and photometric data from the *Spitzer* and *Herschel* Space Telescopes, complemented with archival X-ray and optical data, as well as a set of analytical tools to interpret them. We report the discovery of individual infrared knots whose derived masses are consistent with them being stellar cluster in process of formation. This is also supported by Bayesian fitting of the Spectral Energy Distribution (SED) of the region, which points to the presence of a significant component of embedded objects in the region. We derive line emission and continuum maps of NGC 604 and use them to assess the variations in radiation field strength, ionization levels and extinction across the GH nR, and find that our results are consistent with a sequential star formation history in the last ~ 4 Myr. We also discuss some additional findings regarding the role of X-ray emission in the enhancement of both [Si II] atomic emission and $17\ \mu\text{m}$ PAH emission.

The chapter is structured as follows. In §3.2 we present the IRS data and describe the data reduction to obtain the maps and the spatially integrated spectrum of NGC 604. §3.3 describes the resulting maps and spectra, as well as the tools used to extract physical information from the observations. In §3.4 we discuss the results of our analysis in terms of the current evolutionary stage of NGC 604 and the presence of ongoing star formation in the region. We conclude with a summary of our main results in §3.5.

3.2 Data reduction and ancillary datasets

Most of our analysis will be based on *Spitzer* Infrared Spectrograph (IRS) (Houck et al. 2004) data of a region encompassing the bulk of infrared emission from NGC 604. However, to provide more robust constraints on the physics of the region, we also use complementary photometry from the *Spitzer* Infrared Array Camera (IRAC) (Fazio et al. 2004) and from the *Herschel Space Observatory* Photodetector Array Camera and Spectrometer (PACS) (Poglitsch et al. 2010). Additionally, we use archival *Hubble Space Telescope-Wide Field and Planetary Camera 2* and *Chandra X-ray Observatory-ACIS* images.

3.2.1 IRS data

The *Spitzer* Infrared Spectrograph (IRS) provides unprecedented spatial resolution and sensitivity as compared to any previous mid-IR spectroscopic observations of the NGC 604 region. The spectral resolving power ranges from $R \sim 60$ at short wavelengths to $R \sim 120$ at the long-wavelength edge. The sensitivity is about 100 times better than that of the spectrometer onboard the *Infrared Space Observatory* (ISO), while the spatial resolution is a factor of 10 larger. The wavelength coverage of the IRS ranges from about $5 \mu\text{m}$ to about $38 \mu\text{m}$.

IRS observations of the NGC 604 region were obtained in January 2006 using the IRS mapping mode for spectroscopy, which consists of the acquisition of slit spectra using a grid of positions around a central target. These observations were part of the program *Comparative Study of Galactic and Extragalactic H II Regions* (P. I. J. Houck). Only the low resolution modules short-low (SL1, SL2) and long-low (LL1, LL2) of the IRS were used for this set of observations. For the SL modules, 12 slit pointings were made with each of the two spectrometer orders covering an area on the sky of about $55'' \times 40''$, which corresponds to a physical scale of about $225 \text{ pc} \times 160 \text{ pc}$ at the distance of NGC 604 (see Fig. 3.1). The slice width for the SL modules is $3''.6$, corresponding to a pixel scale of $1''.85 \text{ px}^{-1}$ (7.5 pc px^{-1}). For the LL modules, the slice width is $10''.5$, which corresponds to a pixel scale of $5''.08 \text{ px}^{-1}$ (20.5 pc px^{-1}) and 6 pointings were made with each order to cover an area of about $720 \text{ pc} \times 205 \text{ pc}$.

In addition to the spectral map with the IRS low resolution modules (lores data hereafter), we also use IRS staring mode observations of three specific locations within the region using the high resolution modules of the spectrometer (hires data here after). For these modules the wavelength coverage is shorter (between 9.9 and $38.0 \mu\text{m}$), but the resolving power is significantly higher ($R \approx 600$). The locations of the staring mode observations are within the area of the spectral map and correspond approximately to the positions of the peaks of $8 \mu\text{m}$ emission, associated with PAH emission, as discussed later. The high resolution slits are wider than their low resolution counterparts ($4''.7$ and $11''.1$ for the short-high and long-high orders respectively) and therefore their spectral apertures are also larger than the spatial resolution elements of the spectral maps.

Extraction of the spectra

For the staring mode data, the Spitzer Science Center Tool IRSCLEAN was used to remove cosmic rays and then SMART v.8.0 was used with the full aperture mode for extended sources, based on the size of the slits compared to the source NGC 604, which is large enough to be considered extended. The observation cycles were co-added and the sky background removed using an additional off-source background exposure taken as part of the campaign. We have applied a scaling factor to the fluxes extracted in the long-high (LH) module to match the overlap region in the short-high (SH) module. This is an aperture correction to account for the larger size of the LH slit with respect to the SH slit. The scaling factors for the LH spectra towards fields A, B and C are 0.28, 0.41 and 0.41 respectively (see Fig. 3.2).

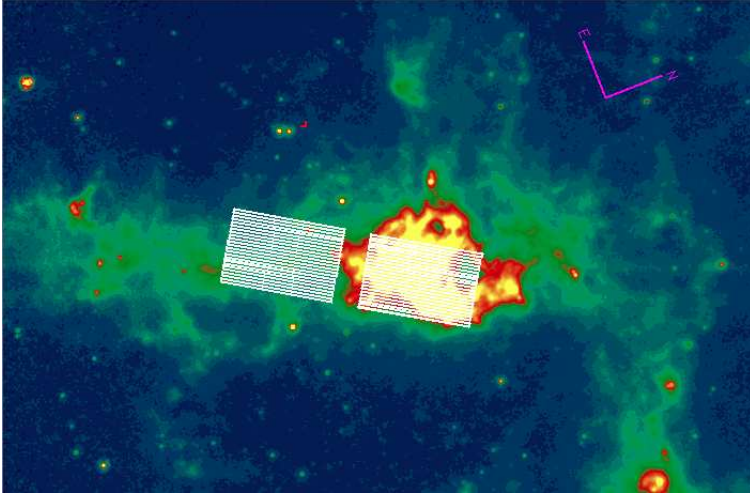


Figure 3.1 The target and background slit pointings superimposed on the IRAC $8\ \mu\text{m}$ image of NGC 604. The green structure near the H II region is part of the spiral arm structure of M33. See text for a discussion on the flux levels.

For the spectral map, we extracted the spatially integrated spectrum of the region for all four IRS orders using an extraction aperture corresponding to the SL coverage of the map (see Fig. 3.2), which includes the bulk of the IR emission of NGC 604. Some of the extended filamentary structure of the region, which is one order of magnitude dimmer than the peaks of emission, is left outside this area. The low surface brightness of these filaments and the bubble-like geometry that we will assume when modeling the region implies that this will be unimportant for the purposes of the present analysis. The background subtraction was performed using the order of the SL and LL modules that was not centered at the source during the corresponding exposure. The software package CUBISM (Smith et al. 2007) performs the data cube build-up once the background and the correct slit pointings have been provided. The background levels are not exactly the same for the low resolution and high resolution modules. The reason is that the orientation of opposite orders of the slit is different for different modules. In the case of the low resolution modules, the background picks up some emission from M33's spiral arm (See Fig. 3.1). This is our best estimate for the sky levels in the SL modules. For reference, the measured IRAC $8\ \mu\text{m}$ flux levels on the spiral arm ($\sim 10\ \text{MJy sr}^{-1}$) are only 20% higher than the sky level outside the arm ($\sim 8\ \text{MJy sr}^{-1}$), and correspond to about 7% of the peak of $8\ \mu\text{m}$ emission in the region.

Spectra can be extracted from each spatial pixel of the resulting data cube. The spatially integrated spectrum over the entire aperture is obtained by summing up the individual spectra of all resolution elements. We use the same extraction area for all modules and orders using the tools provided by CUBISM to make sure that the final spectrum for each order corresponds to the same physical region.

In addition to the spectrum of the integrated region, we have extracted the lores spectra of individual sources that we discuss in §3.3.1. For this extraction we use an aperture of a single SL pixel ($1''.85$). The CUBISM software allows us to extract the spectra in the LL spectral module with this small aperture, by scaling down the fluxes of the larger LL pixels to the SL sizes. This is equivalent to applying a scaling factor to match the different orders of IRS spectra, and introduces additional flux uncertainties in the long wavelength modules, where the PSF is not well sampled. Nonetheless, we consider this scaling a good approximation of the actual fluxes at smaller scales, since the SL pixels are not sufficiently small to resolve the sources, and the LL pixels are not large enough to include more than one source.

By selecting a single pixel aperture, we have chosen to lose some spatial information on the individual sources, because a single pixel samples only half of the PSF FWHM, and in exchange we avoid off-source flux contamination. More important than a full sampling of the PSF for our analysis, are the variations of the PSF with wavelength, that might introduce artifacts in the measured spectral features. Using calibration data, Pereira-Santaella et al. (2010) characterized the PSF variations with wavelength for the IRS reconstructed PSFs. Apart from an undulating behavior of the PSF size with wavelength, that they attribute to alignment issues and to the reconstruction algorithm used, they compute variations of less than 10% on the PSF FWHM for the SL module. This is, as we will see in §3.2, below the observational errors in our data. The PSF of the LL module is affected by fringing and is difficult to characterize.

3.2.2 IRAC photometry

As part of the same Spitzer program, IRAC maps of the NGC 604 region were obtained with the camera filters with nominal wavelengths at $3.6\ \mu\text{m}$, $4.5\ \mu\text{m}$, $5.8\ \mu\text{m}$ and $8\ \mu\text{m}$. The pixel scale for these maps is $1.2\ \text{arcsec px}^{-1}$, and they cover an area of about $5' \times 9'$, several times larger than the area covered by the spectral map. For the purpose of this chapter we have extracted the integrated flux of each map within a rectangular aperture area equal to the extraction area of the IRS spectral map. We perform this extraction using the FUNTOOLS package for the SAO *ds9* software. The sky background is estimated from the map by measuring the flux in a box of the same size as the map, but shifted to the west, to an area where no source emission is observed. In Table 3.1 we list the measured photometry. The listed uncertainties correspond to absolute flux calibration uncertainties ($\sim 3\%$), which are derived for point sources taking several systematic effects into account, as described in Reach et al. (2005).

The IRAC maps provide a sharper view of the region at specific wavelengths, and will allow the identification of interesting sources.

3.2.3 PACS photometry

Imaging maps of the host galaxy M33 have been obtained with the Herschel PACS instrument using the green ($100\ \mu\text{m}$) and red ($160\ \mu\text{m}$) filters as part of the HERM33ES

Wavelength [μm]	Flux [Jy]
3.6	0.067(0.002)
4.5	0.062(0.002)
5.8	0.322(0.010)
8.0	0.922(0.028)

Table 3.1 Integrated IRAC photometry of NGC 604.

Herschel key project (Kramer et al. 2010). The maps were obtained with a slow scan speed of 20 arcsec s^{-1} , and cover a total area of about $70' \times 70'$. Here we use the integrated photometry of an area of the PACS maps equivalent to the size of the IRS spectral maps (bottom panel of Fig. 3.2). The pixel sizes are $3''.2$ for the green band and $6''.4$ for the red band, or about 2 and 4 times the IRS-SL pixel size. The obtained fluxes, integrated over the entire area of the map, are $F_{100\mu\text{m}} = 39.7 \pm 4.0 \text{ Jy}$ and $F_{160\mu\text{m}} = 30.1 \pm 3.0 \text{ Jy}$. The 10% uncertainty comes from a combination of absolute calibration errors, uncertainties associated with differences in the PSF at $100 \mu\text{m}$ and $160 \mu\text{m}$ and different pixel sizes in the two bands that lead to aperture uncertainties. The rms noise levels of the PACS maps are 2.6 mJy px^{-2} and 6.9 mJy px^{-2} .

3.2.4 HST-WFPC2 F555W data

We use the optical images obtained at $0.55 \mu\text{m}$ with the *Hubble* WFPC2 using the F555W filter, described in Hunter et al. (1996). At angular resolutions of $0''.1$, this optical map reveals the location of the massive ionizing clusters that provide the radiative input for the NGC 604 system.

3.2.5 Chandra X-ray Observatory-ACIS data

We use archival data from the *Advanced CCD Imaging Spectrometer* (ACIS) onboard the *Chandra X-ray Observatory*. The data were taken as part of the Chandra proposal “The Giant Extragalactic Star-Forming Region NGC 604” (Proposal ID 02600453, P.I. F.Damiani), and consist of a soft (0.5-1.2 keV) X-ray image of the entire nebula, with an exposures time of 90 ks. The pixel scale is $1'' \text{ px}^{-1}$.

3.3 Analysis

We analyse the multi-wavelength observations described above using a set of analytical and statistical tools that are based on physical models of the region, and that we will describe shortly. The models compute the radiative transfer of the UV radiation as it traverses the ionized gas and molecular material around the H II region. They also compute

the dynamical evolution of its the expanding H II region. We use these tools to derive physical properties of the region, such as dust temperatures, total stellar mass, hardness of the radiation field and ionization state of the gas. In this section we present the obtained maps and spectra and describe the analytical tools that we use.

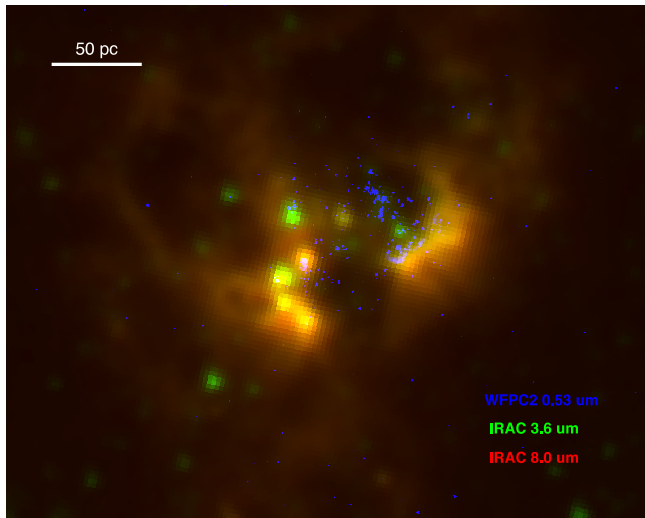
3.3.1 Distribution of the emission

Overall distribution

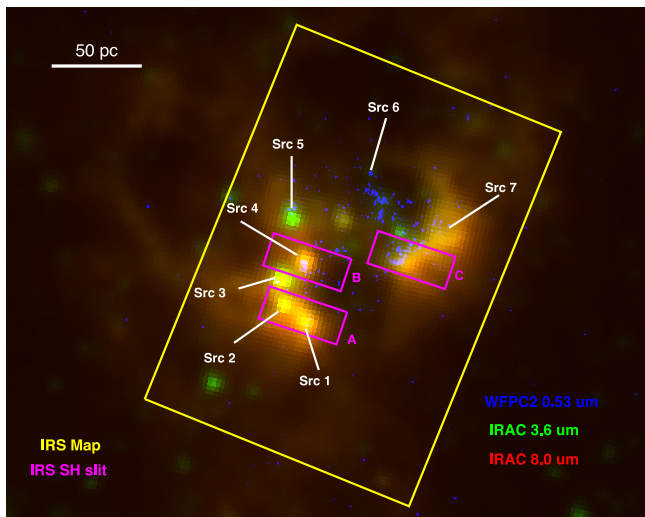
In Fig. 3.2(a) we show a three-color map of NGC 604 composed from the $3.6\ \mu\text{m}$ and $8.0\ \mu\text{m}$ IRAC channels together with the WFPC2 image at $0.55\ \mu\text{m}$. The blue channel shows the photospheric emission from young massive stars, most of which belong to the dense clustered structure labelled as “cluster A” by Hunter et al. (1996). Other, more spread stellar associations are seen next to the bright lobes of infrared emission. The $8\ \mu\text{m}$ emission traces warm dust and the $7.7\ \mu\text{m}$ PAH feature, and hence the location of the PDRs, while the $3.6\ \mu\text{m}$ traces a combination of the $3.3\ \mu\text{m}$ PAH feature, very hot dust and photospheric emission from stellar populations older than 10 Myr. The filamentary and shell-like structure of the region observed at optical wavelengths is also visible in the mid-infrared.

Relaño & Kennicutt (2009) have shown that the $8\ \mu\text{m}$ emission delineates the H α shells in the boundaries between cavities. Most of the infrared emission in our maps comes from two lobes oriented in a SE-NW direction and that constitute the bulk of the emission at the IRAC bands. These lobes coincide with the edges of two main cavities observed in the region (cavities B1 and B2 in Tüllmann et al. (2008)), with diameters of approximately 50 pc each (see Fig. 3.2). They also coincide with the position of bright radio knots identified by Churchwell & Goss (1999). Within these cavities sits the majority of the luminous stars observed by HST (blue stellar sources in Fig. 3.2). An exhaustive X-ray study of the region carried out by Tüllmann et al. (2008) showed that the distribution of high energy photons inside these cavities is consistent with them being shaped by the mass loss and radiative pressure of about 200 OB stars. The eastern portion of NGC 604, on the other hand, seems to be an older part of the system, with X-ray emission consistent with a more evolved population.

The two lobes have similar surface brightness at $8\ \mu\text{m}$, but they show differences in their morphology. At the IRAC wavelengths, the SE lobe shows a series of subcondensations, some of which are notably brighter at $3.6\ \mu\text{m}$, while the NW lobe shows a more uniform distribution of emission. CO maps of the region reveal several molecular clouds in the region, with a CO-bright cloud peaking near the SE infrared lobe and extending southwards, and a dimmer and smaller cloud peaking near the NW lobe (Wilson & Scoville 1992). A number of MYSO candidates have been identified along these two lobes as sources with NIR excess (see, for example Fariña et al. 2012). By combining observational and SED modelling tools, in this chapter we will provide additional evidence that supports the star formation scenario, and quantifies its contribution to the total stellar mass in the region.



(a)



(b)

Figure 3.2 (a) Three-color Hubble/Spitzer map of NGC 604. The IRAC 8 μm band traces the PDR material, while the 3.6 μm band traces both PAH and photospheric emission from young stars. The WFPC2 image shows the location of the hot massive stars. (b) the same map with superimposed apertures of the IRS slits and labels for seven sources of interest based on their IRAC colors. We discuss these sources in the text and indicate their location in the map. The yellow rectangle corresponds to the extraction window for the IRS map and for the photometry, while the smaller magenta boxes show the location of the IRS SH slit for the high resolution observations. North is up, east is to the left.

3 Ongoing massive star formation in NGC 604

Source	RA	Dec
Src 1	1h34m33.43s	+30°46'48.50''
Src 2	1h34m33.67s	+30°46'51.01''
Src 3	1h34m33.70s	+30°46'54.86''
Src 4	1h34m33.43s	+30°46'57.11''
Src 5	1h34m33.56s	+30°47'03.00''
Src 6	1h34m32.73s	+30°47'09.32''
Src 7	1h34m31.99s	+30°46'59.95''
A	1h34m33.6s	+30°46'51''
B	1h34m33.6s	+30°46'58''
C	1h34m32.4s	+30°46'59''

Table 3.2 Coordinates of the sources with extracted lores.

Individual sources.

In Fig. 3.2(b) we show again the three color map of with the superimposed extraction area for the lores spectral map and the location of the short-high IRS slits for the hires observations listed in Table 3.2. The extraction area for the spectral map includes the bulk of the emission in the IRAC bands and the stellar cluster. We have selected 7 individual sources of interest in the spectral map, including the well defined subcondensations that are visible in the IRAC images. These sources are indicated in Fig. 3.2(b), with their positions listed in Table 3.2. Sources A and B of the hires observations coincide with selected sources of the lores map. Specifically, source A includes sources 1 and 2, while source B includes source 4. Source C does not include any of the selected lores targets, but belongs to the NW infrared lobe, and is close to source 7. Also, sources A, B and C correspond to radio sources B, A and C, respectively, of Churchwell & Goss (1999), while source 6 is slightly shifted from the cluster A of Hunter et al. (1996).

We have fitted Gaussian profiles to the flux distribution of the observed subcondensations to investigate their spatial extension of the PAH emitting regions. Our fits reveal that they have projected diameters of about $3''.6$ at $8\ \mu\text{m}$ as measured from the FWHM of the Gaussian fits. The diffraction-limited resolution of the IRAC camera at this wavelength is $1''.71$, and hence we conclude that the subcondensations are spatially resolved at $8\ \mu\text{m}$, having a diameter of at least two IRAC resolution elements. At the distance of NGC 604, their projected sizes correspond to physical diameters of about 15 pc, and hence they are comparable to the size of a typical giant molecular cloud.

Source	$F_{15\mu\text{m}}$ [MJy sr ⁻¹]	$F_{30\mu\text{m}}$ [MJy sr ⁻¹]	$F_{15\mu\text{m}}/F_{30\mu\text{m}}$
Src 1	102.8(10.3)	432.1(43.2)	0.238(0.034)
Src 2	65.4(6.5)	310.4(31.0)	0.211(0.030)
Src 3	95.8(9.6)	582.8(58.3)	0.164(0.023)
Src 4	95.9(9.6)	447.5(44.8)	0.214(0.030)
Src 5	25.8(2.6)	258.5(25.9)	0.100(0.014)
Src 6	10.1(1.0)	99.2(9.9)	0.101(0.014)
Src 7	113.5(11.4)	493.9(49.4)	0.230(0.033)
NGC 604	16.8(1.7)	100.93(10.1)	0.166(0.023)

Table 3.3 Continuum slopes of the SED for all seven sources and the region as a whole.

3.3.2 Infrared spectra

Extracted spectra

In Fig. 3.3 we show the IRS spectra of the integrated region and the selected sources of Table 3.2. The vertical axis is in units of flux density (νF_ν), and we have scaled them for the purpose of direct comparison. The integrated spectrum of NGC 604 has prominent PAH emission and some of the nebular lines detected are from species such as [Ar III], [Ne III], [Ne II], [S IV], [S III] and [Si II]. The thermal continuum increases monotonically in the IRS range.

Fig. 3.4 shows the high resolution spectra of the staring mode targets. The wavelength coverage of the hires modules is smaller than the lores case, from $\sim 10 \mu\text{m}$ to $\sim 37 \mu\text{m}$, but the higher spectral resolving power allows the resolution of lines not seen in the lores spectra, such as the lines resulting from pure rotational transitions of molecular hydrogen, H₂S(2) at $12.3 \mu\text{m}$ and H₂S(1) at $17.0 \mu\text{m}$. These lines are usually hard to detect on top of a strong continuum, due to the fact that they arise from quadrupolar rotational transitions, which are intrinsically weak.

Continuum emission

In order to characterize the spectral slope of the thermal continuum, we measure the flux densities at $15 \mu\text{m}$ and $30 \mu\text{m}$ using a range of wavelengths around the corresponding central wavelength containing about 20 resolution elements ($14.75 \mu\text{m}$ - $15.25 \mu\text{m}$ for the $15 \mu\text{m}$ measurement and $29.5 \mu\text{m}$ - $30.5 \mu\text{m}$ for the $30 \mu\text{m}$ measurement), and we calculate the ratio $F_{15\mu\text{m}}/F_{30\mu\text{m}}$ for each source as well as the integrated spectrum. The spectral slopes give an indication of the dust temperature. Higher values of $F_{15\mu\text{m}}/F_{30\mu\text{m}}$ are associated with a hotter component of the dust, whereas lower values of this ratio indicate colder dust temperatures. We list the measured slopes in Table 3.3.

3 Ongoing massive star formation in NGC 604

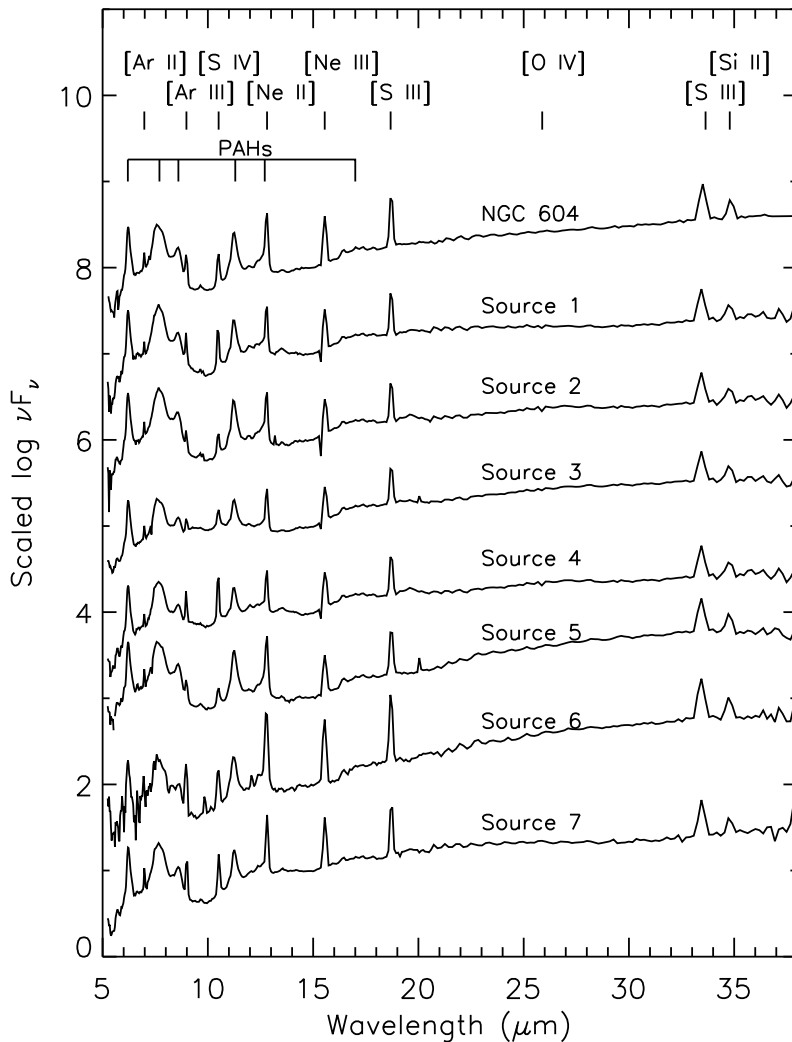


Figure 3.3 IRS spectra of the integrated NGC 604 region and the individual sources listed in Table 3.2. The position of some prominent mid-infrared fine structure lines are indicated, as well as the location of the PAH bands. The small feature seen at $\sim 20 \mu\text{m}$ in sources 3 and 5 is an artifact from the data reduction.

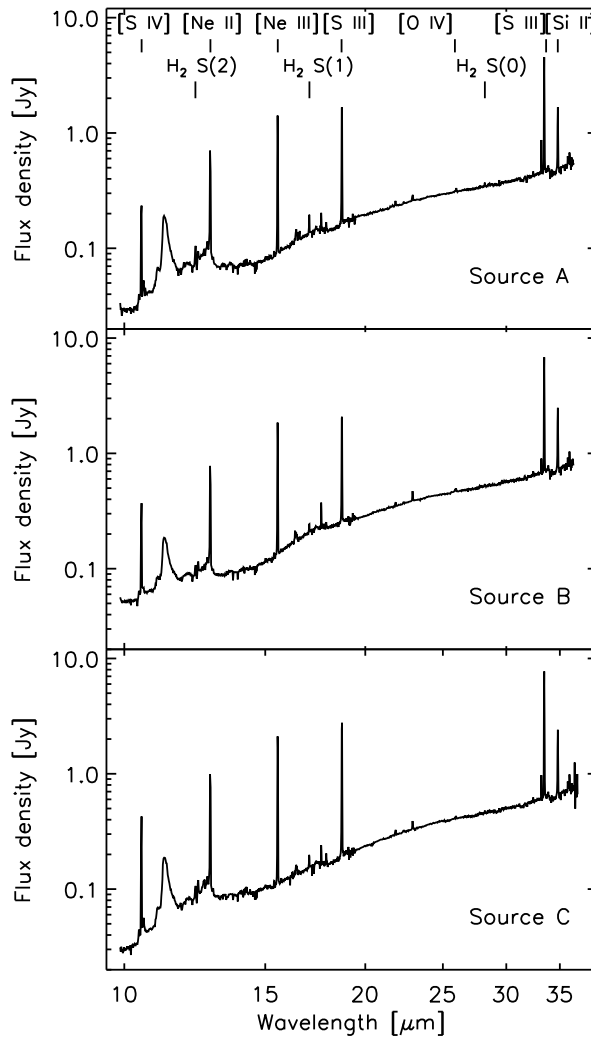


Figure 3.4 High resolution spectra of the three locations labeled A, B and C in Fig. 3.2. The prominent nebular and molecular hydrogen lines are indicated.

PAH emission

We have measured the strengths of the individual PAH features using the PAHFIT tool (Smith et al. 2007), which decomposes the IRS spectrum in individual contributions from dust thermal continuum, PAH features and fine-structure lines, as well as rotational lines of molecular hydrogen. In Table 3.4 we list the measured continuum-subtracted strengths of the different PAH components. The $7.7\ \mu\text{m}$ strength was obtained by adding the PAHFIT $7.4\ \mu\text{m}$, $7.6\ \mu\text{m}$ and $7.8\ \mu\text{m}$ features. Similar combinations of the $11.2\ \mu\text{m}$ and $11.3\ \mu\text{m}$ strengths for the $11.3\ \mu\text{m}$ feature and the $16.4\ \mu\text{m}$, $17.0\ \mu\text{m}$, $17.4\ \mu\text{m}$ and $17.9\ \mu\text{m}$ for the $17\ \mu\text{m}$ feature were performed.

In general, the ratios between PAH features remain constant for all sources. An interesting exception is the ratio of the $\text{PAH}_{17\mu\text{m}}$ feature to the sum of all other PAH features, ΣPAH ($\Sigma\text{PAH} = \text{PAH}_{6.2\mu\text{m}} + \text{PAH}_{7.7\mu\text{m}} + \text{PAH}_{8.6\mu\text{m}} + \text{PAH}_{11.3\mu\text{m}}$). This ratio peaks strongly towards source 3, which is also a local peak of soft X-ray emission. In Table 3.5 we list the $\text{PAH}_{17\mu\text{m}}/\Sigma\text{PAH}$ ratio and the Chandra-ACIS soft X-ray fluxes for our sources. For the ACIS fluxes we assume a nominal 20% uncertainty, based on Chandra catalogues of point sources such as Servillat et al. (2008).

Nebular line emission

Fine-structure emission lines are an important diagnostic of the physical conditions in star-forming region. Their strengths and ratios constrain physical parameters such as the hardness of the radiation field, gas density, or the presence of shocked gas. In the mid-IR, several forbidden lines are observable from species such as $[\text{Ne II}]$, $[\text{Ne III}]$, $[\text{S III}]$ and $[\text{S IV}]$. In Table 3.6 we list the continuum-subtracted nebular line strengths in NGC 604, as measured with the PAHFIT tool, which performs Gaussian fits to the nebular lines.

We have also measured the continuum-subtracted line strengths in the hires data for targets A, B and C in the right panel of Fig. 3.2. We have fitted Gaussian profiles to the lines, this time using the built-in tool for that purpose included in the SMART software. We show the resulting line strengths in Table 3.7.

Two of the most prominent lines are $[\text{S IV}]10.5\ \mu\text{m}$ and $[\text{Ne II}]12.8\ \mu\text{m}$. Fig. 3.5 shows continuum-subtracted maps of these two lines, and illustrates the regions from where the line emission originates. At the resolution of the maps there is spatial coincidence between the peaks of line emission and the infrared sources we have identified. Sources of particularly bright line emission are sources 1, 4 and 7. The localized nature of the emission allows investigations of the physical conditions in the individual sources.

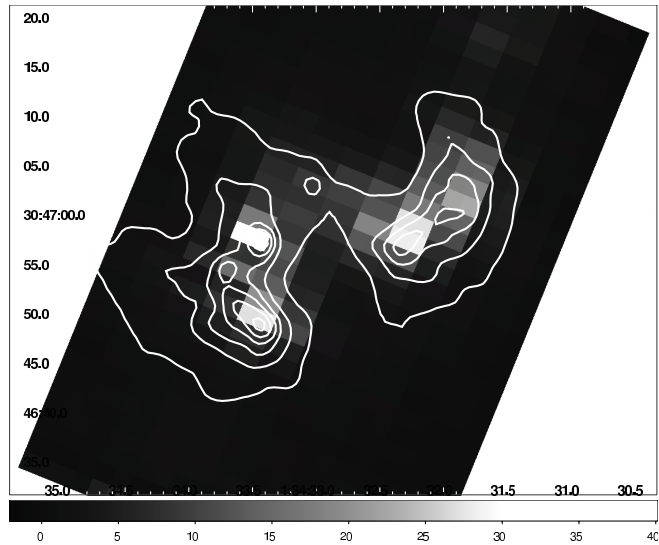
3.3.3 Electron density

The ratio of two lines of the same ionization state of a single species, emitted from levels with similar excitation energies, can be used as a tracer of the electron density n_e (Rubin et al. 1994). We use the $[\text{S III}]18.7\ \mu\text{m}/[\text{S III}]33.6\ \mu\text{m}$ to investigate the electron densities in the NGC 604 region, based on the lores line ratios. We use the lores data rather than the

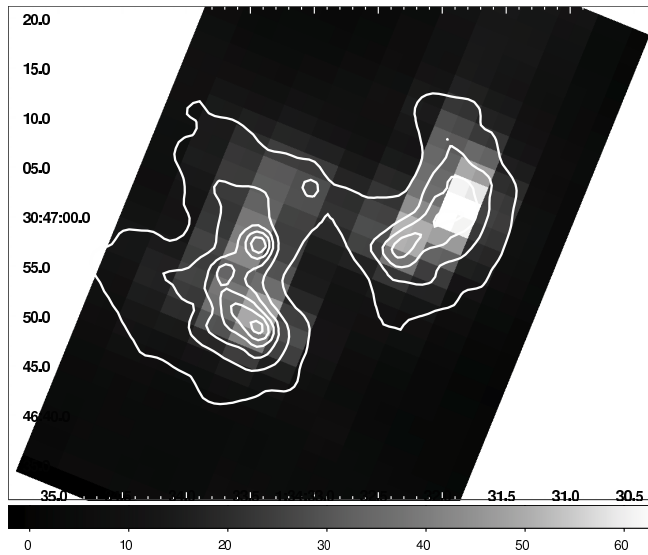
Source	$\text{PAH}_{6.2\mu\text{m}}$ $10^{-6} \text{ W m}^{-2} \text{ sr}^{-1}$	$\text{PAH}_{7.7\mu\text{m}}$ $10^{-6} \text{ W m}^{-2} \text{ sr}^{-1}$	$\text{PAH}_{8.6\mu\text{m}}$ $10^{-6} \text{ W m}^{-2} \text{ sr}^{-1}$	$\text{PAH}_{11.3\mu\text{m}}$ $10^{-6} \text{ W m}^{-2} \text{ sr}^{-1}$	$\text{PAH}_{17\mu\text{m}}$ $10^{-6} \text{ W m}^{-2} \text{ sr}^{-1}$
Src 1	2.56(0.10)	7.96(0.54)	1.28(0.12)	1.33(0.16)	0.85(0.26)
Src 2	1.76(0.07)	5.49(0.38)	0.87(0.09)	1.07(0.11)	0.73(0.17)
Src 3	1.24(0.07)	2.82(0.33)	0.51(0.09)	0.83(0.14)	1.15(0.24)
Src 4	1.51(0.07)	4.25(0.35)	0.64(0.09)	0.76(0.13)	0.88(0.23)
Src 5	0.93(0.03)	2.42(0.19)	0.50(0.04)	0.52(0.05)	0.24(0.07)
Src 6	0.14(0.01)	0.48(0.03)	0.06(0.01)	0.11(0.01)	0.06(0.03)
Src 7	1.64(0.08)	5.14(0.41)	0.91(0.10)	1.04(0.14)	0.26(0.07)
NGC 604	0.40(0.02)	1.16(0.09)	0.19(0.02)	0.25(0.03)	0.11(0.04)

Table 3.4 PAH feature strengths.

3 Ongoing massive star formation in NGC 604



(a)



(b)

Figure 3.5 Continuum-subtracted line emission in NGC 604, in units of MJy sr^{-1} . (a) $[\text{Siv}]10.5\mu\text{m}$ emission has well defined peaks near sources 1, 4 and C. (b) $[\text{Ne II}]$ peaks near source 7. The white contours are IRAC $8\mu\text{m}$ emission.

Source	PAH _{17μm}/(ΣPAH)}	$F_{X_{\text{soft}}}$ [10^{-9} erg cm $^{-2}$ s $^{-1}$]
Src 1	0.065(0.020)	0.84
Src 2	0.079(0.019)	1.37
Src 3	0.213(0.047)	3.70
Src 4	0.123(0.033)	2.50
Src 5	0.055(0.016)	1.64
Src 6	0.076(0.038)	1.65
Src 7	0.030(0.002)	0.91
NGC 604	0.055(0.020)	-

Table 3.5 Ratio of PAH 17 μ m to the sum of all other PAH features.

hires data because the two [S III] lines are measured at similar spatial resolutions in the lores data, while for the hires data they are measured in two different apertures ([S III]18.7 falls on the SH module, while [S III]33.6 falls in the LH module).

The [S III]18.7 μ m/[S III]33.6 μ m ratios calculated from Table 3.6 are very uniform in the region, varying from 0.51 to 1.02, with the highest value near source 7, in the NW infrared lobe. These values are very close to the low density limit discussed in Dudik et al. (2007) (their Fig. 9), and hence our data provide only upper limits for the electron densities. Using the Dudik et al. (2007) diagram, we derive upper limits for the electron densities between $\log n_e = 1.5 \text{ cm}^{-3}$ and $\log n_e = 2.5 \text{ cm}^{-3}$ in the region.

3.3.4 Hardness of the radiation field

We investigate the hardness of the radiation field in the region by looking at the line ratio [S IV]10.5 μ m/[Ne II]12.8 μ m. The use of these two lines has an observational motivation. The two lines are within the SL wavelength range and hence have the same spatial scale and pixel size, which is not the case for the [Ne III]/[Ne II] ratio. The ionization potential required to produce [Ne II] is only 21.6 eV, while it takes 34.8 eV to ionize [S III] to obtain [S IV]. Hence, the ratio between these two ionic species traces the hardness of the radiation field, which can be interpreted in terms of stellar ages, with [Ne II] tracing star formation activity during the last 10 Myr and [S IV] tracing massive stars born in the last 4-6 Myr. In Fig. 3.6 we show the corresponding line ratio map obtained from the spectral cube. Note that the color scale of the map is in logarithmic units.

The mid-IR line ratios do not only depend on the hardness of the radiation field. They also depend on the ionization state of the gas, that can be parametrized using the ionization parameter Q (the ratio of the ionizing photon density to gas density). In Martínez-Galarza et al. (2011) (MG11 hereafter) we have used the hires line ratios as derived from the measurements done in Lebouteiller et al. (2008), and combined them with the radiative transfer models in Levesque et al. (2010) using the interactive ITERA software (Groves & Allen 2010), to break the degeneracy between age and ionization parameter in the particular case of the 30 Doradus region. We found in that

3 Ongoing massive star formation in NGC 604

Source	[Ar II]6.9 μm $10^{-7} \text{ Wm}^{-2}\text{sr}^{-1}$	[Ar III]8.9 μm $10^{-7} \text{ Wm}^{-2}\text{sr}^{-1}$	[S IV]10.5 μm $10^{-7} \text{ Wm}^{-2}\text{sr}^{-1}$	[Ne II]12.8 μm $10^{-7} \text{ Wm}^{-2}\text{sr}^{-1}$
Src 1	0.58(0.19)	2.05(0.33)	3.07(0.42)	4.61(0.64)
Src 2	0.60(0.17)	0.58(0.16)	0.84(0.14)	2.89(0.40)
Src 3	0.59(0.14)	0.90(0.34)	1.54(0.28)	3.18(0.39)
Src 4	0.48(0.16)	2.05(0.31)	4.02(0.53)	3.39(0.52)
Src 5	0.51(0.08)	0.47(0.09)	0.32(0.06)	1.85(0.19)
Src 6	0.15(0.02)	0.35(0.04)	0.25(0.03)	1.28(0.11)
Src 7	0.93(0.21)	2.59(0.35)	2.68(0.45)	6.80(0.86)
NGC 604	0.17(0.04)	0.29(0.06)	0.34(0.04)	1.04(0.11)
Source	[Ne III]15.5 μm $10^{-7} \text{ Wm}^{-2}\text{sr}^{-1}$	[S III]18.7 μm $10^{-7} \text{ Wm}^{-2}\text{sr}^{-1}$	[S III]33.7 μm $10^{-7} \text{ Wm}^{-2}\text{sr}^{-1}$	[Si II]34.8 μm $10^{-7} \text{ Wm}^{-2}\text{sr}^{-1}$
Src 1	4.83(0.67)	6.41(0.91)	6.64(1.13)	2.54(0.76)
Src 2	2.81(0.40)	3.53(0.54)	4.29(0.76)	1.74(0.53)
Src 3	3.84(0.47)	5.66(0.83)	7.90(1.40)	3.29(0.96)
Src 4	4.08(0.48)	5.37(0.79)	6.52(1.13)	2.57(0.76)
Src 5	1.15(0.13)	2.21(0.23)	4.37(0.72)	1.90(0.47)
Src 6	1.02(0.11)	1.65(0.01)	2.34(0.01)	0.90(0.01)
Src 7	7.02(0.94)	9.10(1.30)	8.90(1.11)	3.15(0.74)
NGC 604	1.04(0.10)	1.57(0.01)	1.90(0.01)	0.77(0.01)

Table 3.6 Fine structure line fluxes as extracted from the lores data.

study that the [Ne III]15.5 μm /[Ne II]12.8 μm and the [S IV]10.5 μm /[S III]18.7 μm ratios in 30 Doradus are compatible with starburst ages ≤ 3.0 Myr and ionization parameters $8.0 \text{ cm s}^{-1} \leq \log Q \leq 8.6 \text{ cm s}^{-1}$.

We perform a similar analysis for NGC 604. In Fig. 3.7 we plot the ratios computed from Table 3.6 as compared to a set of Levesque et al. (2010) models with the sub-solar metallicity of NGC 604 ($Z = 0.4Z_{\odot}$) and low electron density ($n_e = 10 \text{ cm}^{-3}$), in accordance with the low density regime inferred from the line ratios. The overall line ratios are indicative of an age of between 4 and 4.5 Myr. Differences in age and ionization parameter between the sources can be inferred from the plot. Sources 1 and 4 have larger ionization parameters and older ages, while sources 2,3 and 7 have line ratios consistent with younger ages. The IRS map resolution is not enough to resolve the sources individually, and hence some confusion between the emission line from different sources is expected. Nevertheless, the trend towards younger ages inferred from Fig. 3.7 for the brightest IR sources is a good indication of recent star formation activity in those locations.

Using the hires line fluxes we also measure the strength of the radiation field in sources A, B and C with the parametrization of Beirão et al. (2006), which uses the [Ne III]/[Ne II] to estimate the strength as the product of the field intensity and the field hardness:

Source	[S IV]10.5μm $10^{-20} \times W \text{ cm}^{-2}$	[Ne II]12.8μm $10^{-20} \times W \text{ cm}^{-2}$	[Ne III]15.5μm $10^{-20} \times W \text{ cm}^{-2}$	[S III]18.7μm $10^{-20} \times W \text{ cm}^{-2}$	[S III]33.7μm $10^{-20} \times W \text{ cm}^{-2}$	[Si II]34.8μm $10^{-20} \times W \text{ cm}^{-2}$
Src A	1.63(0.36)	3.71(0.14)	4.24(0.08)	4.54(0.12)	5.54(0.07)	1.85(0.09)
Src B	2.24(0.22)	4.24(0.24)	5.52(0.12)	5.49(0.12)	9.03(0.09)	2.76(0.09)
Src C	2.60(0.46)	5.77(0.24)	6.63(0.02)	7.29(0.18)	10.08(0.09)	2.71(0.11)

Table 3.7 Fine structure line fluxes as extracted from the hires data.

3 Ongoing massive star formation in NGC 604

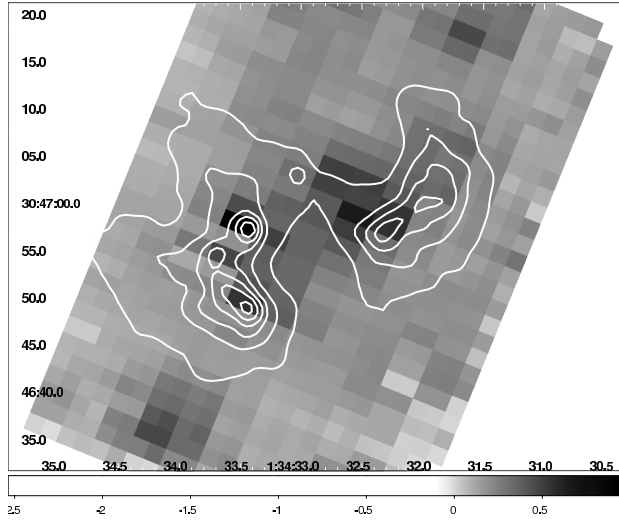


Figure 3.6 The $\log([S\text{ IV}]10.5\mu\text{m}/[Ne\text{ II}]12.8\mu\text{m})$ ratio in NGC 604 as derived from the spectral map. For reference, the IRAC $8\mu\text{m}$ contours (white) are superimposed. We use the measured ratios to estimate the hardness of the radiation field towards specific locations (see text).

$$\left(F_{[Ne\text{ II}]12.8\mu\text{m}} + F_{[Ne\text{ III}]15.6\mu\text{m}}\right) \times \frac{F_{[Ne\text{ III}]15.6\mu\text{m}}}{F_{[Ne\text{ II}]12.8\mu\text{m}}} \quad (3.1)$$

We get a radiation field strength of $9.1 \times 10^{-20} \text{ W cm}^{-2}$, $12.7 \times 10^{-20} \text{ W cm}^{-2}$ and $14.25 \times 10^{-20} \text{ W cm}^{-2}$ for sources A, B and C respectively.

3.3.5 [Si II] emission

Most of the lines listed in Table 3.6 are from regions with ionized hydrogen gas. The exception is [Si II], which originates in a variety of environments including H II regions, but also X-ray dominated regions (Maloney et al. 1996), high density PDRs (Kaufman et al. 2006) and regions of shocked gas, where heavy elements are returned to the gas phase. It is in general hard to pin down the physical mechanism for the emission of [Si II]. We investigate this in NGC 604 by looking at a possible correlation between the ratio [Si II]/[Ne II] and the ratio of PAH emission at $17\mu\text{m}$ to all other PAH features together. We plot the relation between these two ratios in Fig. 3.8. In §3.4.2 we discuss this finding in the context of several possible scenarios for the emission of [Si II].

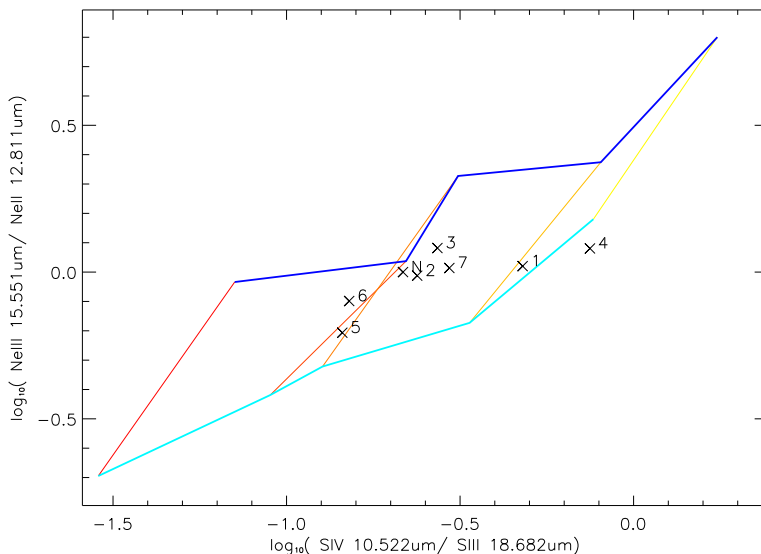


Figure 3.7 Comparison of the line ratios in NGC 604 with the Levesque et al. (2010) models. The $[\text{Ne III}]15.5\mu\text{m}/[\text{Ne II}]12.8\mu\text{m}$ ratio is plotted versus the $[\text{S IV}]10.5\mu\text{m}/[\text{S III}]18.7\mu\text{m}$ ratio. Data points from Table 3.6 are overplotted to the grid of models, that cover a range of ages from 4 Myr (blue) to 4.5 Myr (cyan) and a range of ionization parameters from $4 \times 10^7 \text{ cm s}^{-1}$ (yellow) to $4 \times 10^8 \text{ cm s}^{-1}$ (red). The line ratio for the integrated map is indicated by “N”.

3.3.6 H₂ emission

Additional diagnostics on the physical conditions in NGC 604 come from the molecular hydrogen lines arising from pure rotational transitions at $12.27 \mu\text{m}$ (0-0 S(2)) and $17.03 \mu\text{m}$ (0-0 S(1)), which we detect (although marginally in the case of the $12.27 \mu\text{m}$ line) in the hires modules of the IRS in sources A, B and C. Using the same procedure as for the nebular lines, we fit Gaussian profiles to the H₂ rotational lines and estimate their strengths. In Table 3.8 we list the measured line strengths.

H₂ temperatures can be calculated from the ratio of the two detected line strengths listed in Table 3.8, using a general method (see, for example the Appendix of Brandl et al. 2009). This method holds under the following assumptions: (i) the gas is in local thermodynamic equilibrium (LTE); (ii) the hydrogen rotational lines are optically thin; (iii) the critical densities for the lines are $< 10^3 \text{ cm}^{-3}$ and (iv) the two states of the H₂ molecule, ortho-H₂ and para-H₂, exist in a ratio of 3 to 1. From the Boltzmann statistics that describe the distribution of energy states for the H₂ molecule and the relation between the line strength and the H₂ column density, it can be shown that the excitation temperature is given by:

3 Ongoing massive star formation in NGC 604

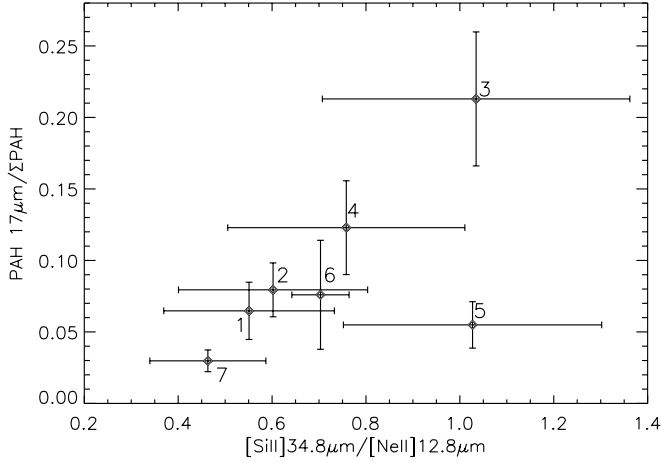


Figure 3.8 The $[\text{Si II}]/[\text{Ne II}]$ ratio plotted against the ratio of $\text{PAH}_{17\mu\text{m}}$ strength to the strength of all other PAH features, for our sources. Error bars in both quantities are shown.

Source	$\text{H}_2 \text{ S}(2)12.27\mu\text{m}$ [$10^{-20} \times \text{W cm}^{-2}$]	$\text{H}_2 \text{ S}(1)17.03\mu\text{m}$ [$10^{-20} \times \text{W cm}^{-2}$]	T_{ex} [K]
Src A	0.19(0.15)	0.20(0.01)	520
Src B	0.13(0.15)	0.13(0.02)	540
Src C	0.16(0.04)	0.14(0.01)	490

Table 3.8 H_2 rotational lines.

$$T_{\text{ex}} = \frac{E_2 - E_1}{k \ln \left(C \frac{\lambda_1 F_1}{\lambda_2 F_2} \right)} \quad (3.2)$$

where E_1 and E_2 are the energies of the involved levels, k is the Boltzmann constant, C is a constant dependent on the ratio of Einstein coefficients and statistical weights, λ_1 and λ_2 are the rest-frame wavelengths of the observed lines, and F_1 and F_2 their respective integrated line fluxes. We list the computed temperatures in Table 3.8.

3.3.7 SED modeling

In MG11 we have presented a Bayesian fitting tool to study the infrared SEDs of star-forming systems. The tool is based on a grid of the Dopita & Groves models (D&G models hereafter), which are thoroughly described in a series of papers (Dopita et al. 2005, 2006b,c, Groves et al. 2008). Here we briefly describe the tool and then apply it to

the observed infrared SED of NGC 604 in §3.4.2, including both the IRS spectrum and the PACS photometry, to derive statistically meaningful values for the following physical parameters of the region: cluster age and stellar mass, compactness, fraction of total mass contained in embedded objects and fraction of the luminosity arising in photon-dominated regions.

Physics

The D&G models combine stellar synthesis, radiative transfer, dust physics and self-consistent dynamical evolution of individual H II regions to simulate the UV to sub-millimeter spectral energy distributions (SEDs) of star-forming regions, including thermal emission from dust and PAHs, and nebular line emission. Using all the available spectral information, for a given metallicity (Z) and ambient interstellar pressure (P_0/k), the fitting tool computes probability distribution functions (PDFs) for key model parameters such as stellar cluster age (t_{cl}), cluster mass (M_{cl}), compactness (C), fraction of the total luminosity arising in the PDRs (f_{PDR}) and the mass contribution from a component of young embedded objects that we model as Ultra Compact H II Regions (M_{emb}).

We have defined these parameters in Chapter 2. Of relevance here is the definition of C . This parameter is proportional to the product $M_{\text{cl}}^{3/5} (P_0/k)^{2/5}$, and sets the evolution of dust temperature with time. If L_* is the luminosity of the cluster and R_{HII}^2 is the radius of the H II region, then C parametrizes the incident heating flux, L_*/R_{HII}^2 and controls the position of the far-IR bump of the SED for a given value of P_0/K . Intuitively, the compactness provides a measure of how close the dust particles are to a stellar heating source of certain luminosity. It is important to realize that, for a given compactness, different physical diameters of the sources are expected, depending on the luminosity of the central cluster. This parameter is thus only weakly related to the physical size of the sources.

Priors

Bayesian inference allows to include any previous evidence on the values of the model parameters in the calculation of the posterior probability distribution (the PDF). Here we use flat, bounded priors for all the model parameters, with boundaries set by observational and theoretical studies of star-forming regions, as discussed in MG11. We assume solar metallicity and adopt a thermal pressure of the surrounding ISM of $P_0/k = 10^5 \text{ K cm}^{-3}$.

The assumption on ISM pressure is supported by measurements of far-IR line ratios from the ISO satellite on a sample of star-forming galaxies (Malhotra et al. 2001). The metallicity of NGC 604 has been measured to be about half-solar (Magrini et al. 2007). However, our experiments show that only the solar metallicity models in our grid are able to reproduce the observed ratio of PAH strength to continuum emission at $100 \mu\text{m}$ in NGC 604. The discrepancy is most likely due to the specific PAH template used in the D&G models, which is an empirical template based on observations of starburst galaxies. The choice of metallicity does not only affect the PAH emission strength. At far-IR

3 Ongoing massive star formation in NGC 604

wavelengths, the change in dust column and mechanical luminosity of the starburst with metallicity produces a slight shift and a broadening of the far-IR bump. While this implies an additional degeneracy with the compactness parameter, the additional errors introduced in the determination of C are smaller than our chosen step size for the compactness grid, which is 0.5.

χ^2 Weighting

In MG11 we have included a discussion of the observational uncertainties involved in measuring the IRS fluxes, which include absolute and relative flux calibrations and systematic errors due to specific observing conditions. Based on that discussion, for fitting purposes we have adopted a uniform uncertainty of 10% across the IRS wavelengths, which also implies a uniform weighting for all data points in the fitting.

The χ^2 minimization procedure described in MG11 has been slightly modified here to ensure that the χ^2 minimization is not dominated by the IRS range, which has many more resolution elements, as compared to only two data points at 100 μm and 160 μm from PACS. Each bin contributes to the χ^2 with a weight that is proportional to the bin size in the logarithmic wavelength space. The bin size is set by the resolution of the models in the IRS range and by the wavelength separation between data points for the PACS data. This results in a weighting function that increases uniformly in the IRS range so that the bins at the short wavelength end (around 5 μm) have about half the weight of those at 35 μm and about 0.25 times the weight of the PACS bins. In section §3.4.2 we apply this tool to the observed SED of NGC 604.

Color correction of PACS photometry

The D&G models compute the monochromatic flux densities for each wavelength bin. However, the flux densities measured by the PACS filters at 100 μm and 160 μm are not monochromatic. They are the integrated flux densities over certain wavelength ranges, as modulated by the filter response function. Before we compare the model fluxes to the observed PACS photometry, it is necessary to evaluate the errors introduced by this difference. To do so, we adopt the method described in da Cunha et al. (2008) to predict the flux density of a source when observed using a given filter. According to their approach, the flux density for any filter is:

$$F_{\nu}^{\lambda_0} = \frac{\lambda_0^2}{c} C_{\nu_0} \frac{\int d\lambda F_{\lambda} \lambda R_{\lambda}}{\int d\lambda C_{\lambda} \lambda R_{\lambda}} \quad (3.3)$$

where

$$\lambda_0 = \frac{\int d\lambda \lambda R_{\lambda}}{\int d\lambda R_{\lambda}} \quad (3.4)$$

is the effective wavelength of the filter response R_{λ} , c is the speed of light and C_{λ} is a calibration spectrum that depends on the photometric system used for the calibration. In

the case of the PACS photometer, the calibration spectrum is constant ($C_{\lambda}\lambda = \text{constant}$), which simplifies the calculations. Using this method, and the filter response curves available at the Herschel Science Center, we have computed effective wavelengths for the PACS filters at $L_0^{100} = 102.6\ \mu\text{m}$ and $L_0^{160} = 167.2\ \mu\text{m}$, and we estimate that the difference between the monochromatic and filter fluxes in the models are $< 1\%$ for the PACS green filter ($100\ \mu\text{m}$) and $\sim 9\%$ for the PACS red filter ($160\ \mu\text{m}$). These uncertainties are within the 10% observational errors.

3.4 Discussion

3.4.1 Notable sources

The most striking morphological characteristic of the sources labelled 1-7 in Fig. 3.2 is that most of them (sources 1-5) are well defined, individual infrared-bright knots. Sources 1, 2, 7 and 4 are, in that order, the strongest sites of PAH emission, as shown in Table 3.4. They are also associated with less steep continuum slopes, as shown in Table 3.3. This implies a component of emission from warm (300 K) dust that peaks at about $15\ \mu\text{m}$, in the vicinity of sources with strong $8\ \mu\text{m}$ emission. These regions are the locations where most of the MYSO candidates have been identified by Fariña et al. (2012) using NIR photometry.

Source 2

This source, located in the SE lobe, is bright in all IRAC bands but has no optical, $H\alpha$ or FUV counterpart. In addition, it has one of the strongest silicate absorptions at $10\ \mu\text{m}$ as shown in Fig. 3.3, and it is very close to the peak of one of the CO clouds reported in Wilson & Scoville (1992). Using HST data, Maíz-Apellániz et al. (2004) derived an extinction map for the region. They found a strong peak of extinction at the location of source 2, which is consistent with its relatively strong silicate absorption. Compared with all the other sources, nebular emission towards this source is weak (Table 3.6). Its high optical extinction, bright PAH emission and spatial coincidence with a reservoir of molecular gas makes of source 2 a very good candidate for a site of embedded star formation.

Source 5

From the $F_{15\mu\text{m}}/F_{30\mu\text{m}}$ ratios listed in Table 3.3, we infer that Source 5 has the coldest dust temperature among our sources. Its $[\text{S IV}]10.4/[\text{S III}]18.7$ and $[\text{Ne III}]15.5/[\text{Ne II}]12.8$ line ratios derived from Table 3.6 are both the lowest among our sources and the PAH features listed in Table 3.4 are weaker towards this source, compared with all the other well defined IR knots. The combination of cold dust, low ionization state, soft radiation field (as traced by the line ratios), and weak emission from PDRs are indicative of a more evolved stage

3 Ongoing massive star formation in NGC 604

for this particular source. In fact, source 5 is located near the boundary between the active star-forming western and quiescent and older eastern hemisphere of NGC 604, as catalogued by Tüllmann et al. (2008). Source 5 is also brighter than all the other sources at $3.6 \mu\text{m}$. This band traces the $3.3 \mu\text{m}$ PAH feature, very hot dust and photospheric emission from stellar populations older than 10 Myr, but since the continuum slope is not indicative of hot dust and the PAH emission is weak towards this source, the most plausible explanation for the excess at $3.6 \mu\text{m}$ is the presence of stars older than 10 Myr.

Source 7, Source 4 and Source 1

Source 7, located in the NW infrared lobe, shows the strongest nebular line emission among our sources (Table 3.6). This source is very close to a bright ridge of photospheric optical emission from a nearby group of young stars (see Fig. 3.2). The higher electron density near the NW lobe is consistent with the strong nebular lines measured near source 7 and with the enhanced $H\alpha$ emission observed in this same area of NGC 604 (see, for example, Fig. 2 in Relaño & Kennicutt (2009)), and implies a higher ionization state. This source is most likely the location of the youngest main sequence stars of the cluster. This is supported by our measurements of the radiation field strength in the neighbouring source C, where we have measured a stronger radiation field using Eq. 3.1, relative to the other sources.

The $[\text{S IV}]/[\text{Ne II}]$ ratio map of Fig. 3.6 peaks at source 4, which has a relatively weaker radiation field. This suggests an enhanced radiation field hardness near this location, where we have also measured a warm dust component from the spectral continuum slope (Table 3.3). Another location with relatively hard radiation field is source 1. The Relaño & Kennicutt (2009) study of the region reveals enhanced $H\alpha$ emission in sources 1, 4 and 7. However, the eastern part of NGC 604, where sources 1 and 4 are located, has a higher optical extinction traced by the Balmer optical thickness ($\tau_{\text{Bal}} \sim 1.2$), as compared with the surrounding average extinction ($\tau_{\text{Bal}} = 0.2 - 0.3$) (Maíz-Apellániz et al. 2004). The $[\text{S IV}]10.5\mu\text{m}$ falls on the broad silicate absorption feature near $10 \mu\text{m}$, and this leads to an underestimation of the $[\text{S IV}]/[\text{Ne II}]$ ratio in regions of high extinction. Although this does not affect our general picture about the radiation hardness, larger $[\text{S IV}]/[\text{Ne II}]$ ratios and hence younger ages might be expected in sources 1 and 4 from extinction corrected $[\text{S IV}]/[\text{Ne II}]$ ratios.

Finally, the $[\text{S IV}]10.5\mu\text{m}/[\text{Ne II}]12.8\mu\text{m}$ ratio is sensitive not only to the cluster age, but also to the gas density. However, at the relatively low electron densities measured in the region ($\log n_e \approx 1.5 - 2.5 \text{ cm}^{-3}$), we do not expect the measured line ratios to be significantly affected.

3.4.2 The evolutionary stage of NGC 604

Fig. 3.9 shows the best fit to the observed integrated SED of NGC 604 (IRS + PACS) using the Bayesian tool described in §3.3.7. Also, in Fig. 3.10 we show the resulting PDFs, covering the totality of our parameter space, and in Table 3.9 we list the associated best

Parameter	Best fit value	Eldridge & Relaño (2011)
t_{cl} (Myr)	$4.0_{-1.0}^{+1.0}$	> 4
$\log C$	$5.5_{-0.5}^{+0.5}$	
f_{PDR}	$0.5_{-0.2}^{+0.3}$	
M_{cl} ($10^5 M_{\odot}$)	$1.6_{-1.0}^{+1.6}$	$(3.8 \pm 0.6) \times 10^5$
M_{emb} ($10^4 M_{\odot}$)	$1.2_{-0.1}^{+1.3}$	
f_{emb}	0.075	

Table 3.9 Best fit to the integrated spectrum of NGC 604. Parameters listed are, from the top: the cluster age, the compactness, the fraction of total luminosity arising in PDR regions, the stellar mass of the cluster, the mass contained in embedded objects, and the ratio of embedded to stellar mass.

fit parameters and uncertainties, with the values for t_{cl} and M_{cl} determined independently by Eldridge & Relaño (2011) using several methods, including optical SED fitting. We also include f_{emb} , the ratio of mass contained in young embedded objects (M_{emb}) to stellar mass in the cluster (M_{cl}). This Bayesian fit, as well as the other spectral features discussed above, provide a wealth of information about the physics and the evolutionary stage of NGC 604.

A remarkable fact is highlighted by a comparison between the PDFs shown in Fig. 3.10 and those obtained for 30 Doradus and shown in in Fig. 2.7. The distribution of probability over the parameter space considerable shrinks in the case of NGC 604. In particular, the PDFs of Fig. 3.10 do not show the bi-modal degeneracies that are evident in Fig. 2.7. The improvement is related to the inclusion of the *Herschel* data in the analysis. Far-infrared observations greatly help constraining model parameters such as the compactness, thus breaking this degeneracy. Nevertheless, as we have seen in Chapter 2, in the degenerate case the Bayesian tool chooses the solution that better represents the conditions in a regio, using the information from the nebular lines. Therefore, although data at longer wavelengths further constrain the model parameters, the best fit parameter obtained using mid-IR data only remain practically unchanged.

Dust temperature and compactness

The thermal continuum, PAH emission and line emission are well reproduced by the best fit. The combined IRS and PACS data are consistent with a far-IR SED peaking at approximately $70 \mu\text{m}$, which indicates an effective dust temperature of ~ 40 K. Using multi-wavelength photometry of a sample of H II regions in the Magellanic Clouds, Lawton et al. (2010) show that the infrared SEDs of most of these regions peak at $70 \mu\text{m}$. Our result indicates that this average dust temperature is not unique of “local” H II regions, but also applies to at least one relatively more distant region.

We have stated that the compactness parameter controls the incident heating flux

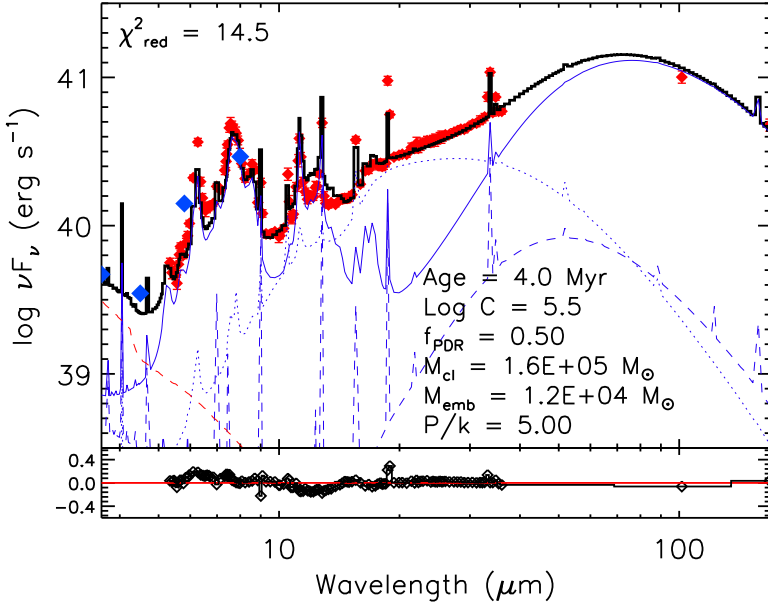


Figure 3.9 Best fit model to the integrated SED of NGC 604. The IRS and PACS data are shown as red diamonds, and the IRAC photometry as blue diamonds. The solid line is the best fit model. Also shown are the contributions from pure H II region emission (dashed blue), PDR (solid blue), embedded population (dotted blue) and photospheric emission from stars older than 10 Myr (dashed red). Residuals are shown in the bottom panel.

L_*/R_{HII} as a function of age of the H II region. From our given set of best fit parameters it is then possible to derive an incident heating flux (see Fig. 3 in Groves et al. 2008). We obtain an incident flux of $\log(L_*/R_{\text{HII}}) = 0.65 \text{ erg s}^{-1} \text{ cm}^{-2}$ for our best fit values of compactness and age. The bolometric luminosity of the cluster can be obtained from integration of the best fit SED, and gives approximately $6.0 \times 10^{41} \text{ erg s}^{-1}$, which allows us to solve for the effective radius of the H II region. We obtain $R_{\text{HII}} \sim 120 \text{ pc}$. This value corresponds to the scale of the larger filaments observed in NGC 604 (Fig. 3.2). This agreement between a model-derived quantity and a measurable observable demonstrates the capabilities of our Bayesian approach to obtain valuable physical information when applied to unresolved star forming regions.

Stellar mass

The total stellar mass of $1.6_{-1.0}^{+1.6} \times 10^5 M_{\odot}$ that we estimate with the SED fitting is in agreement with the value derived by Eldridge & Relaño (2011) and indicates a total stellar mass similar to that of the 30 Doradus region, for which we find a total stellar mass of

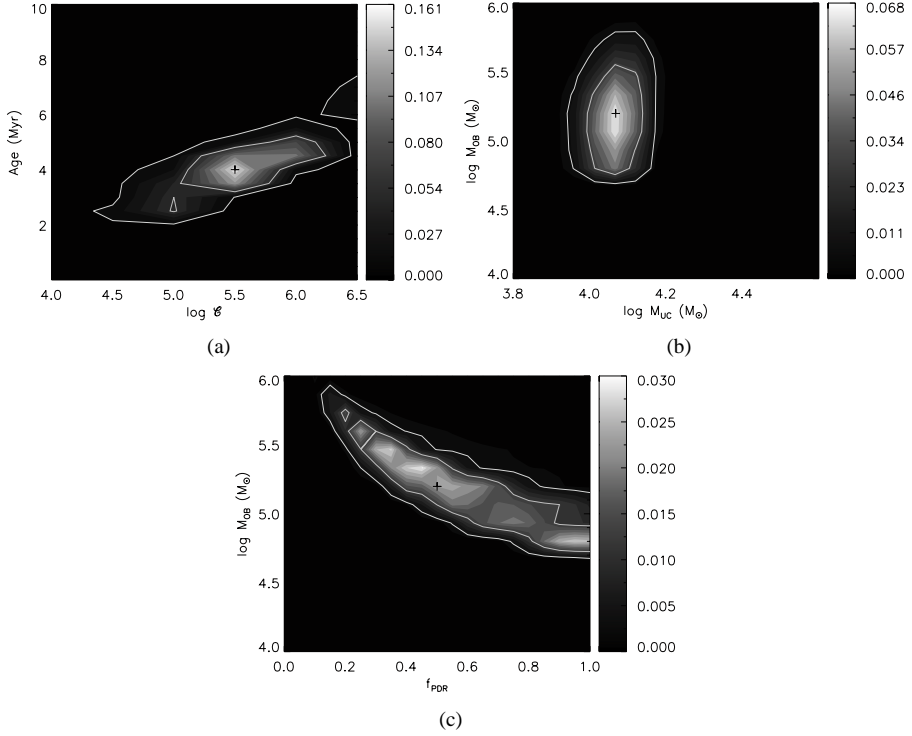


Figure 3.10 Two-dimensional PDFs for selected pairs of parameters covering the totality of the parameter space. The pairs shown are: (a) $\log C - t_{\text{cl}}$, (b) $\log M_{\text{emb}} - \log M_{\text{cl}}$ and (c) $f_{\text{PDR}} - \log M_{\text{cl}}$. The grey scale contours indicates the normalized probability. The cross symbols mark the best-fit values while the white contour lines indicate the 1- σ and 90% confidence levels.

$0.63^{+0.37}_{-0.23} \times 10^5 M_{\odot}$ in MG11. In general, the total stellar mass in 30 Doradus is larger than in NGC 604. Our result indicates a slightly lower mass for 30 Doradus which may be due to the fact that the physical projected area covered in our 30 Doradus map is smaller than the projected area of the map presented in this chapter.

We observe in Fig. 3.10(c) the same degeneracy between cluster mass and fraction of the total luminosity from PDRs that we found for 30 Doradus in Chapter 2. We have argued that the reason for this degeneracy is the fact that both the the PDR and the pure H II region spectra contribute to the dust thermal continuum. An increase in PAH from emission is accompanied by an increase in the overall infrared luminosity. This also renders the additional far-infrared data insufficient to solve this degeneracy. At optical wavelengths, where the emission from PDR is significantly different from that of an H II region, are needed to settle the issue. Nevertheless, the degeneracy between M_{cl} and f_{PDR} implies that the the Bayesian fitting tool based on the D&G models can find solutions that

3 Ongoing massive star formation in NGC 604

fit both the optical and infrared mass estimates found by Eldridge & Relaño (2011) and Relaño & Kennicutt (2009) respectively.

Age of the region

The fraction of total mass contained in embedded objects measured here for NGC 604 ($f_{\text{emb}} \sim 0.08$) is smaller than that measured for 30 Doradus in MG11 ($f_{\text{emb}} \sim 0.53$). This is a clear suggestion of an evolutionary difference between these two regions, and points towards 30 Doradus being younger than NGC 604.

Additionally, the age of $\sim 4 - 5$ Myr derived with our fitting method is consistent with the study of the line ratios that we presented in §3.3.4 and agrees well with the studies by Eldridge & Relaño (2011) and Hunter et al. (1996). Statistically, and assuming that the majority of the stars in NGC 604 were born in a single star formation event, our result also supports the generally accepted view that NGC 604 is a more evolved star-forming region than its more luminous counterpart 30 Doradus, for which we have derived an age of ~ 3 Myr using the same method in MG11.

PDR content

Although the fraction of total luminosity arising in PDRs is degenerate with the total cluster mass, as shown in Fig. 3.10, our result from SED fitting suggests that at least half of the energy output from NGC 604 is generated in PDRs, the other half arising in ionized regions closer to the cluster stars. The presence of a luminous PDR in NGC 604 is consistent with the findings of Heiner et al. (2009), who find considerably high amounts of atomic hydrogen ($N_{\text{HI}} \sim 2.0 \times 10^{21} \text{ cm}^{-2}$), and associate them with the photodissociation of H_2 in a dense ($n \sim 500 \text{ cm}^{-3}$) PDR.

Molecular hydrogen in NGC 604

The H_2 temperatures calculated using Eq. 3.2 and the measured strengths for sources A, B and C are all close to 500 K. Due to the large uncertainties in the H_2 line fluxes we do not study in detail the temperature variations. We only take these values as indicative of the average temperature of the warm gas. For a given value of the molecule angular momentum, the total number of hydrogen molecules is proportional to the strength of the line. Our results on the H_2 S(1) line, which has smaller error bars (Table 3.8), indicate that warm molecular hydrogen is more abundant towards source A, which has the strongest H_2 lines. Source A is near to the peak of CO emission reported in Wilson & Scoville (1992).

Despite some disagreements on the specific conversion factor that should be used, it is generally assumed that CO is a good tracer of cold molecular hydrogen. Our results hence support the co-existence of a warm and a cold phase of molecular hydrogen near source A. The warm component is usually associated with regions heated by interstellar shock waves (Gautier et al. 1976). These regions emit a rich spectrum of rovibrational

and pure rotational H_2 emission. Although these emissions are only marginally detected in the present work, the improved sensitivity of the Mid-Infrared Instrument (MIRI) for JWST will allow a better estimation of the amount of shocked gas in star-forming regions.

Selective destruction of small PAHs

The $17\ \mu\text{m}$ PAH feature is generally associated with out-of-band bending modes of large PAH molecules, containing ≈ 2000 C-atoms (Van Kerckhoven et al. 2000). Table 3.5 shows that the relative strength of this feature scales with the X-ray flux. If we adopt the PAH size argument, this implies that it is the ratio of large to small PAH molecules that scales with the X-ray field. In fact, Fig. 3.11 shows that source 3, which shows the largest enhancement of the $17\ \mu\text{m}$ PAH feature among our sources, coincides with a peak of soft X-ray emission. Soft X-ray emission from massive stars can be associated with shocked stellar winds or magnetically confined gas near the wind base, near the stellar coronae (Cassinelli & Swank 1983).

The dissociation of PAH molecules by X-rays has been discussed in Micelotta et al. (2010). They argue that not all X-ray photon absorptions by PAH molecules lead to photodissociation and estimate that after a second electron has been ejected by the PAH molecule via the Auger effect, the molecule is left with an internal energy of 14-35 eV, enough to dissociate small (50 C-atoms) PAHs, but possibly insufficient to dissociate larger molecules. They leave the question of large PAH survival open. Our observations suggest that, at least in the particular case of source 3, X-ray emission from massive stars may be responsible for the dissociation of small PAH molecules, creating an enhancement of the $17\ \mu\text{m}$ feature.

The origin of the [Si II] emission

Fig. 3.8 is suggestive of a correlation between the enhancement of [Si II] and the enhancement of $17\ \mu\text{m}$ PAH emission at scales of tens of parsecs. Despite the relatively large uncertainties in both the PAH ratio and the [Si II]/[Ne II] ratio, the figure indicates clearly that the enhancement of the PAH $17\ \mu\text{m}$ feature scales with the relative strength of the [Si II] emission, with the exception of source 5, which lies outside this correlation. This result suggests a common underlying physical mechanism for the enhancement of both features. We have shown in Table 3.5 that the regions of strongest $17\ \mu\text{m}$ PAH emission also correspond to regions of enhanced X-ray emission. Based on the triple correlation between $\text{PAH}_{17\mu\text{m}}$ emission, [Si II] emission, and soft X-ray flux, we argue that absorption of ambient X-rays may be linked to both the destruction of small PAH molecules and the excitation of [Si II], and produces the correlation observed in Fig. 3.8

As we have pointed out, source 5 is an outlier of this correlation: it shows a relatively large [Si II]/[Ne II] ratio, but very moderate $\text{PAH}_{17\mu\text{m}}/\Sigma\text{PAH}$ ratio. It also lies in a region of low X-ray flux, near the edge between the western, active star-forming hemisphere of NGC 604 and the quiescent eastern region where most of the Wolf-Rayet stars are located (Drissen et al. 2008). In this part of NGC 604, the X-ray luminosity is most likely

3 Ongoing massive star formation in NGC 604

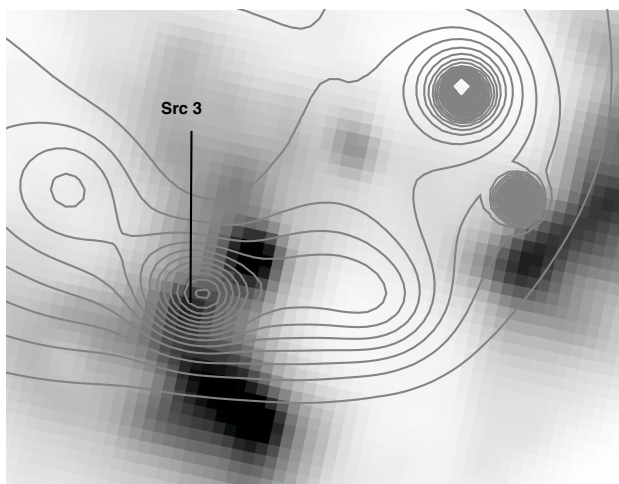


Figure 3.11 Soft X-ray emission in NGC 604. The black and white image is the IRAC $8\ \mu\text{m}$ emission. The line contours correspond to the ACIS image. Source 3 coincides with a local peak of X-ray emission, with a flux of $3.7 \times 10^{-9}\ \text{erg cm}^{-2}\ \text{s}^{-1}$.

powered by the SNe activity of an older event of star formation Tüllmann et al. (2008). Based on these facts, we speculate that the $[\text{Si II}]/[\text{Ne II}]$ ratio for this source is enhanced due to the presence of shocked gas rather than X-ray induced. Although no supernova remnants (SNRs) have been identified in the eastern hemisphere, this is not surprising, since such objects expanding into a low-density gas are hard to detect (Chu & Mac Low 1990).

3.4.3 Ongoing and triggered star formation in NGC 604

Until now, a clear-cut answer on whether or not there is ongoing massive star formation in NGC 604 has been lacking. Although there has been suggestive evidence of embedded star formation in NGC 604 (Fariña et al. 2012, Relaño & Kennicutt 2009) from IR excess studies, a reliable measure of its contribution to the total cluster mass has not been obtained.

In §3.4.1 we have discussed the IR-bright subcondensations that we detect in the IRAC maps. At the distance of NGC 604 it is unlikely that they are individual massive young stellar objects. A fit to their SEDs (shown in Fig. 3.3) using for example the D&G models, reveals that they are consistent with stellar masses between $10^3 M_{\odot}$ and $10^4 M_{\odot}$, given the uncertainty in the determination of the stellar mass shown in Fig. 3.10(b). This implies that all together they account for at least a few percent of the stellar mass in NGC 604. We have pointed out that the line ratios measured towards some of those clumps, namely sources 2, 3 and 7, are consistent with younger ages than the rest of the sources. Although

the timescales for the dissipation of dusty envelopes around star-forming clusters can be as long as 10 Myr in regions of high density, the low electron density that we have inferred in §3.3.3 implies that NGC 604 is a rather diffuse region. Consequently, we do not believe that sources 2, 3 and 7 are evolved clusters. The presence of these young, massive, IR-bright clusters, some of which have deep silicate absorption features, is a clear indication of significant massive star formation currently taking place in NGC 604.

Additional evidence that supports this scenario comes from our SED fitting analysis. We have shown in Fig. 3.9 and Table 3.9 that a warm ($T \sim 300$ K) component of dust arising in MYSO (that in the D&G frame we model as Ultra Compact H II Regions) is necessary to reproduce the observed SED of NGC 604 at mid-IR wavelengths. As we have pointed out, the required fraction of mass in embedded objects is considerably smaller than that derived for 30 Doradus in MG11, and comparable to the individual sum up of the cluster masses.

In an evolutionary context, sequential star formation in NGC 604 is a plausible scenario to explain our observations. This idea has been explored by other authors before. Based on submillimeter observations of the CO ($J = 3 - 2$)/CO ($J = 1 - 0$) ratio, Tosaki et al. (2007) report the existence of a dense ridge of molecular gas that surrounds the main cluster in NGC 604 and extends in the SE-NW direction, closely following the location of our bright IR lobes. To explain their results, they adopt an scenario in which the compression of molecular gas by the mechanical input from the main cluster (the first generation of stars) has triggered a second generation of stars near the NW infrared lobe. The strong radiation field that we observe close to sources C and 7, where main sequence stars are clearly observed, supports the existence of this second generation of highly ionizing stars. Furthermore, the results discussed in this subsection indicate that massive star formation is currently taking place within the SE lobe of NGC 604, even further away from the main cluster, where we have identified the IR-bright subcondensations of Fig. 3.2, some of which are heavily enshrouded by dust (e.g., source 2). This suggests the existence of a third generation of stars forming in the region, the last chapter in a sequential star formation process that started ~ 4 Myr ago.

3.5 Conclusions

We have investigated the physical conditions and quantified the amount of ongoing massive star formation in the star forming region NGC 604. We used a combination of observational and modeling tools, including infrared spectrophotometry and Bayesian SED fitting of Spitzer and Herschel data. Here are our main findings:

1. We have identified several individual bright infrared sources along the luminous PDRs that surround the ionized gas in NGC 604. These sources are about 15 pc in diameter and have luminosity weighted masses between $10^3 M_{\odot}$ and $10^4 M_{\odot}$.
2. The deep $10 \mu\text{m}$ silicate absorption feature, mid-IR continuum slope and atomic line ratios towards some of these sources indicate that they are young embedded systems, and most likely the sites of ongoing massive star formation in NGC 604.

3 Ongoing massive star formation in NGC 604

Some of them (i.e. source 2) are also associated with gas reservoirs as traced by CO maps. This is in agreement with previous studies that found evidence of embedded star formation in the region.

3. This massive star formation scenario is supported by Bayesian fitting of the integrated spectrum (lines+continuum) of NGC 604 constructed from *Spitzer*-IRS and *Herschel*-PACS observations. Our results indicate that embedded star formation can account for up to 8% of the total stellar mass in NGC 604.
4. The spectral fitting also implies an age of 4.0 ± 1.0 Myr for the region, a total stellar mass of $\sim 1.6 \times 10^5 M_{\odot}$ and an average dust temperature of ~ 40 K. These results are in agreement with independent measurements of these quantities using optical broad band photometry.
5. We measure a stronger than average radiation field near our sources 7 and C. This result is consistent with the sequential star formation scenario adopted in Tosaki et al. (2007), in which a second generation of main sequence stars has formed near this sources, triggered by the mechanical input from the first generation, 4 Myr old main cluster.
6. We find a positive correlation between the strength of the $17 \mu\text{m}$ PAH feature, the enhancement of the [Si II]/[Ne II] emission and the strength of the X-ray field towards our sources. We propose that X-rays are responsible for both the excitation of [Si II] and the enhancement of the $17 \mu\text{m}$ feature via selective destruction of large PAH molecules.
7. Our detection of molecular hydrogen in the region indicates gas excitation temperatures of ~ 500 K in NGC 604, and a slightly larger abundance of H_2 near source A, which correlates well with the location of a bright CO cloud reported in Wilson & Scoville (1992).
8. The physical parameters derived for NGC 604, such as its age and fraction of total mass contained in embedded objects indicate that this region is a more evolved H II region, as compared to its larger sibling 30 Doradus, that we have studied in MG11 using the same Bayesian method employed here. Nevertheless, star formation in NGC 604 is still ongoing, triggered by the earlier bursts.

Acknowledgements

The authors want to thank M d ric Boquien and the HERM33ES team for kindly providing the PACS photometry of NGC 604. This chapter would not have been possible without the hospitality of all the astronomical community at the Lowell Observatory.

Outlook: Recent star formation in nuclear starbursts¹

In this outlook chapter we carry out a pilot study on the modelling of spectral energy distributions (SEDs) of unresolved starbursts in the Local Universe. We apply our Bayesian SED fitting tool to the MIR spectra of a small sample of starburst galaxies, in order to investigate differences in their physical properties and recent star formation histories (SFHs). Our robust method finds significant differences in the recent SFHs of the studied objects. For example, we find that in our small sample of targets, the most massive, recently formed clusters were born in regions with comparatively less intense SFRs, where the molecular gas is depleted. Moreover, we find that these gas-poor systems show the largest contribution from very recent (< 1 Myr) massive star formation, which might be indicative of positive feedback from the inferred massive clusters, at the end of a more quiescent period of star formation in these systems. Our pilot study is encouraging, although the small size of the sample does not yet allow for the formulation of general trends. We thus propose a systematic study of a large sample of starburst SEDs, using the present method, to corroborate our findings.

¹J.R. Martínez-Galarza, B. Groves, B. Brandl, in preparation.

4.1 Introduction

A considerable number of nearby galaxies show increased rates of star formation per unit of stellar mass, as compared to the Milky Way. Their bolometric luminosities are dominated by the UV radiation field of young massive stars formed within the last 10: Myr, the product of a fast gas depletion process. These *starbursts* (Weedman et al. 1981) are often related to galactic mergers, but their nature and triggering mechanism has not been fully established. Since massive star formation occurs in regions heavily enshrouded by dust, starburst have very high infrared luminosities, the product of the processing of stellar UV light by dust particles in the interstellar medium (ISM). The incidence of these star formation-powered, very luminous galaxies increases with cosmic distance and at redshifts beyond $z \sim 1$, the most luminous members of this class account for most of the cosmic star formation rate (SFR) density (Elbaz & Cesarsky 2003). Furthermore, infrared emission from dust accounts for about half of the bolometric luminosity of the Universe (Dole et al. 2006). Thus, the study of the infrared properties of starbursts, both near and far, and its relation to their internal physics, is crucial in the understanding of massive star formation throughout cosmic history.

Fitting the observed integrated SEDs of starbursts using predictions from theoretical models is an elegant way to relate measured observables to the internal physics of these systems. A systematic application of a reliable fitting method to a selection of starburst galaxies can provide clear answers to the questions of what triggers starbursts and how they relate to the internal physics and local conditions of the ISM. This information is instrumental on the interpretations of distant systems for which only unresolved information is available. The MIR portion of the starburst SEDs is of particular relevance for several reasons. First, for distant, obscured objects only data at mid-infrared and far-infrared wavelengths are available. Also, the effects of extinction are much less significant at infrared wavelengths and allow a more accurate determination of SFRs, in contrast with ultraviolet (UV) determination methods, which require extinction corrections of a factor of ~ 10 , as pointed out in Sargsyan & Weedman (2009). The same authors have shown that infrared discovered starbursts are not dustier than starbursts discovered using other wavelength regimes, thus minimizing selection effects.

SED fitting has another advantage over monochromatic SFR diagnostics: it does not only quantify recent star formation in galaxies, but it also constrains the plausible values of other physical parameters involved in the process of star formation. While monochromatic, MIR diagnostics have been successful in measuring the SFRs in galaxies (Calzetti et al. 2005, Relaño et al. 2007, Alonso-Herrero et al. 2006, Rieke et al. 2009), they have provided little insight into the reasons for the enhanced star formation in starbursts. However, SED fitting should be applied with care, because of the many degeneracies that arise both from observational errors and intrinsic inter-dependencies of the model parameters. Also, a successful method should use as much information as possible from the integrated SEDs, including the nebular line fluxes that are instrumental in the determination of physical conditions such as ionization state of the gas and the ISM pressure. So far, a statistically robust method for fitting the SEDs of galaxies, including both thermal continuum and nebular lines, has been lacking.

In this outlook chapter we investigate the physics of star formation in a small selection of starburst galaxies from Brandl et al. (2006) (B06 hereafter), with different morphologies and infrared luminosities. For this purpose we apply the fitting tool presented in Chapter 2 to the MIR spectra of the nuclear regions of these galaxies to obtain robust constraints of the SFRs, compactness, ISM pressure, and amount of currently ongoing massive star formation in these galaxies, in a similar way as we did for the NGC 604 star forming region in Chapter 3. In §4.2 we present the basic parameters of the selected galaxies and discuss their morphologies. We continue with a description of their mid-infrared spectra and the results of the fitting process in §4.3. In §4.4 we discuss our results and show our main findings in terms of the differences in the recent SFHs of the starbursts in the sample. We summarize our results in §4.5.

4.2 Sample of galaxies

4.2.1 Selection criteria

The sample of starburst galaxies presented in B06 includes both “pure” starbursts as well as objects with a weak contribution to the dust heating from active galactic nuclei. They also cover a broad range of metallicities, from sub-solar to supra-solar metallicities. Additionally, while most of them show evidence of mergers or some type of interaction with near companions, at MIR wavelengths some of them appear as single nuclei, while others clearly show the presence of more than one nucleus, and one of them appears as a circum-nuclear star-forming ring. For the present study, we have selected a sub-sample of this group of starbursts, composed of five objects that comply with two selection criteria: (*a*) the contribution from an AGN to the luminosity of the nucleus is nonexistent or marginal, and (*b*) their metallicities are close to the solar value ($0.8Z_{\odot} \leq Z \leq 1.4Z_{\odot}$). The second criterion helps us reduce the parameter space investigated with our models and allows us to focus on specific parameters such as compactness, ISM pressure, and amount of embedded star formation.

The variations of MIR spectral properties with metallicity have been studied by several authors, both from observations and theory. For example, in a study of the SINGS sample of galaxies (Kennicutt et al. 2003), Draine et al. (2007) have measured the PAH index q_{PAH} (the percentage of dust mass contributed by PAHs) as a function metallicity, and found a bi-modal distribution of the q_{PAH} s values, with $q_{\text{PAH}} \sim 1\%$ for galaxies $12 + \log_{10}(\text{O}/\text{H}_{\text{gas}}) < 8.1$, and $q_{\text{PAH}} \sim 3.5\%$ for galaxies $12 + \log_{10}(\text{O}/\text{H}_{\text{gas}}) > 8.1$. This reflects in stronger PAH features in metal-rich galaxies. From the point of view of physical modelling, we expect metallicity to affect the MIR spectra of starbursts in several ways (Groves et al. 2008). First, there is an intrinsic change in the stellar radiation field with metallicity. Also, different metal abundances result in variations in the temperature and line emission from ionized regions, and of course, there is also a change in the grain composition with metallicity, which results in different effective dust temperatures and a resulting change in the MIR and FIR thermal continuum.

By selection, none of the galaxies has an AGN contribution to their internal energy.

4 Outlook: recent star formation in nuclear starbursts

Although B06 do not find a systematic difference between “pure” starbursts and galaxies with a weak contribution from AGNs for most of their galaxies, some differences are expected. The high energy photons and strong radiation field related to dust and gas heating by an active nucleus prevent the formation of PAH molecules or destroy them rapidly, and hence these features tend to be weak in AGN dominated galaxies. Also, the spectral slope can be used as a discriminator between starbursts and AGN activity, as first noticed using IRAS data (e.g. Wang 1992). In the following subsections we briefly describe some general properties of our sample galaxies.

4.2.2 Basic properties

In Table 4.1 we list the basic properties of the galaxies studied here. We want to emphasize the fact that, even though they all have similar infrared luminosities, they are different in many other aspects, such as their molecular gas content (the fuel for star formation), surface brightness, and galactic host morphology. They are also located at a broad range of distances, which directly affects their surface brightness and also the fraction of the total flux that falls within the *Spitzer*-IRS spectrometer slit in the B06 study. This also means that not in all cases the measured spectra corresponds to the nuclear region only. For the more distant objects, the larger structure of the host galaxy fits within the spectrometer slit. The selected galaxies are shown in Fig. 4.1 as they appear at mid-IR wavelengths

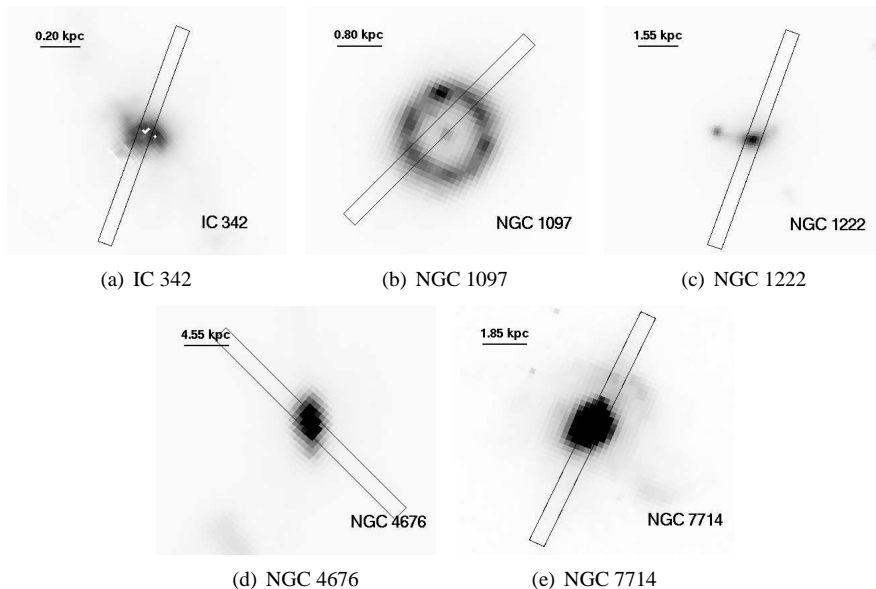


Figure 4.1 IRAC 8 μm images of our selected galaxies, with the IRS short-low slit over-imposed for comparison.

Table 4.1 Properties of sample galaxies.

Name	α	δ	D^a [Mpc]	$\log(L_{\text{IR}})^a$ [L_{\odot}]	Z^b [Z_{\odot}]	M_{mol}^c [M_{\odot}]	SFR^d [$M_{\odot} \text{ yr}^{-1}$]	$\log(M_*)^e$ [M_{\odot}]
IC 342	3 46 48.51	+68 05 46.0	4.6	10.17	0.80	1.0×10^7	1.87	7.0
NGC 1097	2 46 19.08	-30 16 28.0	16.8	10.71	1.38	1.3×10^9	5.0	9.0
NGC 1222	3 08 56.74	-02 57 18.5	32.3	10.60	1.07	$< 10^8$	6.8	5.1
NGC 4676	12 46 10.10	+30 43 55.0	94.0	10.88	1.17	5.0×10^9	15.8	~ 7.0
NGC 7714	23 36 14.10	+02 09 18.6	38.2	10.72	1.17	$< 10^8$	6.0	6.9

^a Distances and IR luminosities taken from B06.

^b Metallicities are taken from Leboutteiller et al. (2011), except for IC 342 and NGC 1097, whose metallicities have been taken from Crosthwaite et al. (2001), and Dors et al. (2008), respectively.

^c Molecular gas masses taken from Israel & Baas (2003), Gerin et al. (1988), Chini et al. (1992), Yun & Hibbard (2001) and Smith & Struck (2001), respectively.

^d Star formation rates taken from the KINGFISH website, Hummel et al. (1987), Brandl et al. (2006), Mineo (2011) and Gonzalez-Delgado et al. (1995).

^e Stellar masses taken from Schinnerer et al. (2008), Quillen et al. (1995), (Beck et al. 2007), de Grijs et al. (2003), and González Delgado et al. (1999).

4.2.3 Morphologies

Although they are all classified as nuclear starbursts, the galaxies in our sample have a variety of morphologies and luminosities. For most of the galaxies, the morphology is due to ongoing or recent mergers or galactic collisions. The star-forming ring in the nucleus of NGC 1097 is clearly resolved at $8\ \mu\text{m}$ while in the other galaxies the IR emission is more compact. The scaling of the orders has been performed accordingly, as described in B06. Here we are interested in studying if there is a clear relation between the nucleus morphology, the measured spectra, and the underlying physics of star formation.

4.2.4 Measurements from the literature

IC 342

The face-on late-type barred spiral IC 342 belongs to the Maffei Group of galaxies and harbors a nuclear starburst powered by the infall of molecular gas via the spiral bar. The inner 400 pc of IC 342 have roughly the same infrared luminosity and stellar mass as the inner 400 pc of the Milky Way (Lebrón et al. 2011). Early CO and [C I] measurements showed that the molecular gas is strongly concentrated in the nucleus of this galaxy, with surface gas densities of $\sim 70\text{ M}_{\odot}\text{pc}^{-2}$ (Israel & Baas 2003). These authors also report that at least half of the molecular gas is associated with hot photon-dominated regions (PDR) in the nuclear region. Negative feedback from the nuclear starburst on the star formation has been reported in Schinnerer et al. (2008), who claim that the efficiency of gas inflow towards the nucleus via the bar is reduced by the effect of stellar winds and supernovae. This is in agreement with the recent detection of depleted very dense gas near the sites of recent star formation (Meier et al. 2011), which indicate a high star formation efficiency. Using X-ray data, Mak et al. (2011) have recently detected supernova remnant activity near the nuclear starburst.

NGC 1097

NGC 1097 is a barred spiral galaxy with a weak active nucleus (Phillips et al. 1984). It has been known for several decades now that there is a star-forming ring-like structure with a diameter of $\sim 1\text{ kpc}$ that surrounds the nuclear region. This ring is rich in molecular gas, and has a sub-structure of azimuthal, very compact clumps that are bright at infrared wavelengths, with estimated masses of the order of 10^7 M_{\odot} (Walsh et al. 1986). Models of the star formation activity in the ring indicate that it is better explained by an instantaneous burst of star formation that occurred 6-7 Myr ago (Kotilainen et al. 2000). Recent star formation has also been detected at very small distances ($< 10\text{ pc}$) from the active nucleus (Storchi-Bergmann et al. 2005), but evidence has been gathered that even in this very central region star formation, rather than the central engine, is responsible for the dust heating (Mason et al. 2007). More recently, Herschel observations have shown that more than 60% of the FIR thermal emission from dust in NGC 1097 comes from the central

ring (Sandstrom et al. 2010), which has a total molecular mass of $\sim 1.3 \times 10^9 M_{\odot}$ (Gerin et al. 1988). FIR cooling lines are indicative of ionized gas densities between $150\text{-}400 \text{ cm}^{-3}$, and a strong radiation field near the ring clumps (Beirão et al. 2010). Although such star-forming rings are common to many galaxies, it is not yet clear what the triggering mechanism is for such structures.

NGC 1222

NGC 1222 is a spheroidal galaxy with a nuclear starburst whose SFR is about 4 times that of the host galaxy (Petrosian & Burenkov 1993). This object has been recognized as a peculiar galaxy due to its bright MIR nebular emission lines and spectral properties, that resemble those of a dwarf metal-poor galaxy. In fact, NGC 1222 has the highest deduced upper limit for the stellar mass in solar-metallicity galaxies, between $40 M_{\odot}$ and $100 M_{\odot}$ (Beck et al. 2007). Another peculiarity has to do with its low content of molecular mass, for which only upper limits have been detected (Elfhag et al. 1996). Beck et al. (2007) also speculate that the peculiarities of this galaxy are due to a double merger with two nearby companions. The ionization state of the gas in the nuclear region is compatible with a stellar population containing 1.4×10^5 O stars, that are contained within a region of size < 500 pc. The starburst is characterized by a high ISM gas density ($\log n = 4.1 \text{ cm}^{-3}$), compared to other starbursts, as determined using FIR emission lines (Malhotra et al. 2001).

NGC 4676

This interacting pair of galaxies has been popularly known as “the Mice”, and it is classified as an early stage merger in the Toomre sequence (Toomre 1977). Here we analyze the spectrum of the northern galaxy (NGC 4676A), which contains most of the PAH and CO emission in the system. In fact, NGC 4676A shows a peculiar variation of the PAH feature ratios, with a $\text{PAH}_{7.7\mu\text{m}}/\text{PAH}_{11.3\mu\text{m}}$ decreasing toward the nucleus, indicating a deficit of ionized PAHs in the center with respect to neutral PAHs (Haan et al. 2011). This is even more surprising given the fact that no weak active nucleus has been identified in the central region of this galaxy. Using NIR spectroscopy, Chien et al. (2007) find evidence for a young (< 6 Myr) stellar population in the nucleus of this northern galaxy, which is indicative of a recent starburst. This is in agreement with starburst-driven galactic winds outflowing along the minor axis of the galaxy, as revealed by *Chandra* X-ray observations (Read 2003). The nuclear region is characterized by a compact ($R < 2$ kpc) molecular complex that contains $\sim 20\%$ of the total molecular mass, which is estimated to be $M_{\text{H}_2} \sim 5 \times 10^9 M_{\odot}$ and have a density of $N_{\text{H}_2} \sim 6 \times 10^{22} \text{ cm}^{-2}$ in the central region (Yun & Hibbard 2001).

NGC 7714

This peculiar spiral was the first galaxy to be designated as a *starburst* (Weedman et al. 1981), and has since become a prototype for these systems. It has a nearby interacting

4 Outlook: recent star formation in nuclear starbursts

post-starburst companion (NGC 7715) with which it had a close, off-center encounter between 100 and 200 Myr ago (Struck & Smith 2003). Its star formation activity is heavily concentrated in the nucleus, though it also shows star-forming regions across the deformed galactic disk. The strong nuclear $H\alpha$ emission, bright PAH features and weak silicate absorption features (Gonzalez-Delgado et al. 1995, Brandl et al. 2004) suggest that the nuclear activity is powered by an unobscured starburst with a total mass of $\sim 10^7 M_{\odot}$, while the weak $[\text{Fe II}]$ emission (Matsuoka et al. 2011) and strong star formation-triggered bipolar winds traced by X-ray observations (Taniguchi et al. 1988) seem to rule out the presence of an AGN in the nucleus of the galaxy. Like NGC 1222, this galaxy also shows strong forbidden lines, compatible with a population of $\sim 2 \times 10^4$ O stars (Smith et al. 1997). Modelling of the UV spectrum gives an age of 5 Myr for the nuclear starburst (González Delgado et al. 1999), but evidence for an older population (15-50 Myr) in the same region has also been found (Lançon et al. 2001). Taniguchi et al. (1988) estimate a total mass of ionized gas of $1.9 \times 10^6 M_{\odot}$.

4.3 Results

4.3.1 MIR spectra of the selected galaxies

Fig. 4.2 shows the IRS spectra of our sample galaxies. A comprehensive description and analysis of the spectral features, including PAH emission, nebular lines and thermal continuum can be found in B06. Of relevance here is the fact that not all the wavelength range shown in the figure is covered by a single order (and hence by a single slit) of the spectrometer, and hence a scaling factor is necessary to match the orders together. As discussed in the B06, the IRS short-low (SL) fluxes were scaled up to match the IRS long-low (LL) slit fluxes, which are measured with a larger slit (only the small SL slit is shown in Fig. 4.1). The motivation for this choice, in the case of the nuclear starbursts discussed here, is that the mismatch is due to some nuclear flux missed by the SL slit, and not to unrelated extended flux. Hence, scaling the SL fluxes up accounts for this missing nuclear flux, and the resulting spectra represent the true integrated starburst flux. We will discuss this further in §4.4

The selected galaxies sample a fair range of spectral shapes. The most remarkable differences have to do with the relative strength of the PAH features with respect to the thermal continuum, the depth of the $9.7 \mu\text{m}$ silicate absorption feature and the intensity of the nebular lines. NGC 4676 has by far the strongest PAH emission and also the deepest silicate absorption, in contrast with NGC 7714, which has relatively weak PAHs and very little silicate absorption. These two objects only seem to represent the extremes between a heavily obscured and an unobscured starburst, although they are both the product of an interaction and have a similar age (5-6 Myr). The ionization of higher atomic states in the gas, as traced by the strength of the $[\text{Ne III}]15.5\mu\text{m}$ and $[\text{S IV}]10.5\mu\text{m}$ nebular line emission, is high in NGC 1222 and undetected in IC 342 and NGC 1097. The slope of the dust thermal continuum, measured in B06 using the $F_{15\mu\text{m}}/F_{30\mu\text{m}}$ ratio, is steeper for NGC 4676, and decreases in the following order: NGC 7714, NGC 1222, IC 342 and

NGC 1097.

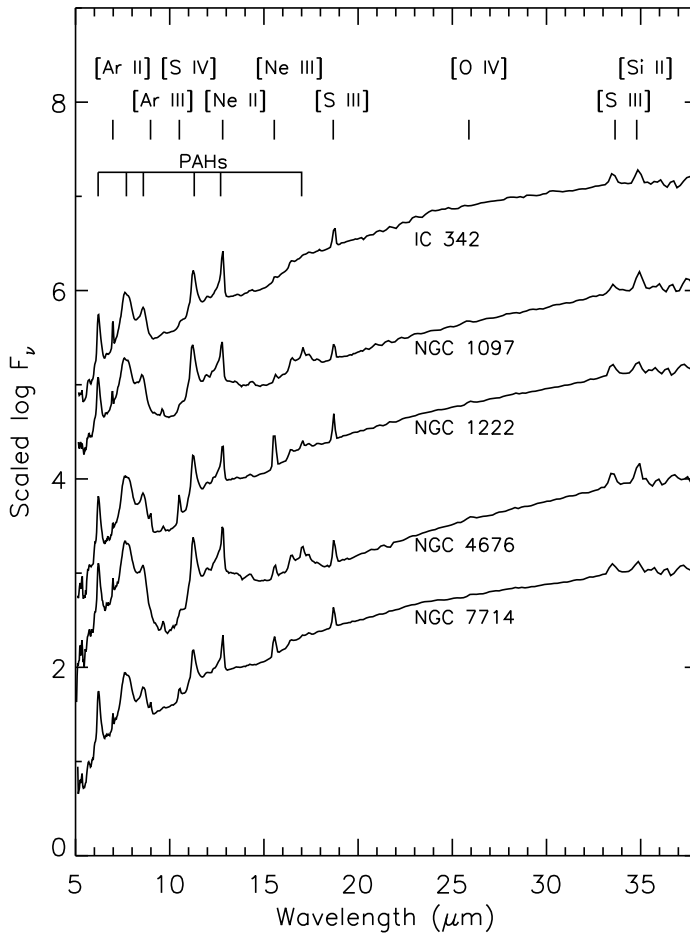


Figure 4.2 Mid-infrared spectra of our selected galaxies. All spectra are normalized to the flux at $30 \mu\text{m}$ and shifted one decade in logarithmic flux for comparison. The main spectral features are labelled.

4.3.2 Bayesian fitting of the spectra

General remarks

In order to investigate if there are fundamental differences in the physics of the interstellar medium between the galaxies in our sample, we applied the Bayesian fitting tool described in Chapters 2 and 3 to the spectra shown in Fig. 4.2. The tool provides a fit to the spectra, and robust constraints for the physical parameters on the models. We have used the age-averaged version of the galactic SEDs, which assumes a constant SFH over the last 10 Myr, as described in §2.5.4 of this thesis. Our assumption of a constant star formation history rather than an instantaneous burst of star formation is supported by several facts. First, while the SFR of the systems studied here are dominated by recent starbursts, there is also evidence for an age spread in the systems, as we have seen in §4.2. Rather than one or a few instantaneous star formation bursts, a continuous enhanced SFR over the last million years seems a more physical explanation for the age spread. Second, since the fixed size of the IRS slit translates into different physical scales at the distances of the galaxies, we cannot guarantee that, although dominating, the emission from the nuclear region is the only component of the spectra. Finally, we have seen in Chapter 2 that not even a single Giant H II Region such as 30 Doradus can be modelled assuming a single instantaneous burst, and hence a time-averaged approach seems more reasonable for distant counterparts of 30 Doradus.

The physical parameters studied here are the SFR, the compactness (C), the fraction of the total luminosity emitted in PDR regions (f_{PDR}), the ISM ambient pressure (P_0/k) and the mass contribution of young, embedded objects (f_{emb}), that accounts for very recent star formation in the systems. Additionally, it is possible to account for variations in the extinction, which at MIR wavelengths affects the depth of the $9.7 \mu\text{m}$ silicate absorption feature. We have described these parameters in §2.3.3. Here we will only remind the reader that in the age-averaged models used in the present chapter, these parameters represent the physical conditions in individual H II regions within the starbursts, averaged over the last 10 Myr. We have seen in Chapters 2 and 3 that these parameters are well constrained, and their derived values and uncertainties are robust. More importantly, we have shown that their values are related to the evolutionary stage of the H II regions, and hence they provide information on the physics that regulate the star formation in starbursts. By relating the derived parameters to the morphology and observables of these systems, we will learn about the local conditions in individual H II regions and the overall star formation characteristics of the starbursts.

Far-infrared photometry has been obtained for some of the galaxies in our sample using the Photodetector Array Camera and Spectrometer (PACS) instrument onboard the *Herschel Space Observatory*, but it is unfortunately not yet publicly available. Nevertheless, as we have seen in §3.4.2, while the *Herschel* data provides better constraints to the parameters, the best-fit estimates obtained with our tool remain unchanged when far-infrared data are included.

Name	$\log C$	f_{PDR}	f_{emb}	SFR $M_{\odot} \text{ yr}^{-1}$	$\log P_0/k$ K cm^{-3}
IC 342	$6.5^{+0.0}_{-0.5}$	> 0.80	$0.94^{+0.17}_{-0.38}$	$0.74^{+0.17}_{-0.03}$	> 7.0
NGC 1097	$5.0^{+0.5}_{-0.5}$	> 0.90	$0.25^{+0.19}_{-0.08}$	$5.18^{+0.77}_{-0.47}$	> 7.5
NGC 1222	$6.0^{+0.5}_{-0.5}$	> 0.80	$1.40^{+0.17}_{-0.53}$	$4.65^{+1.66}_{-0.38}$	> 5.0
NGC 4676	$5.0^{+0.5}_{-0.5}$	> 0.90	< 0.20	$21.23^{+3.89}_{-1.28}$	> 7.5
NGC 7714	$6.0^{+0.5}_{-0.5}$	> 0.75	$1.76^{+0.89}_{-0.44}$	$7.38^{+2.62}_{-0.62}$	> 6.5

Table 4.2 Best fit values for the model parameters in the galaxy sample. The uncertainties as derived from the Probability Distribution Functions (PDFs) are indicated.

Best fit parameters and uncertainties

In Fig. 4.3 we show the best fit models after applying the Bayesian tool to the spectra shown in Fig. 4.2, and in Table 4.2 we list the best fit parameters and their derived uncertainties.

The uncertainties are obtained from the $1\text{-}\sigma$ contours of the derived posterior probability distribution functions (PDFs), in the same fashion as they were derived in Chapters 2 and 3. The best fits shown in the figure emphasize the variation in the contributions from different components to the integrated spectra of our sample galaxies. In particular, the contribution from hot dust arising near the embedded objects, modelled here as Ultra Compact H II Regions (dotted blue line in the figure) varies considerably from galaxy to galaxy. The galaxy spectra are dominated by the PDR component, over the pure H II component, that contributes very little in all cases, although the uncertainties are larger for IC 342 and NGC 7714. The derived SFRs range from a Milky Way value for IC 342 up to 20 times the galactic value in NGC 4676, the northern galaxy of the Mice. For the ISM thermal pressure we can only establish lower limits, since the mid-IR spectrum is not very sensitive to this parameter. Only the nebular lines constrain P_0/k , which falls near the high pressure end for most of our galaxies, those with the lowest limits being NGC 1222 and NGC 7714.

An interesting fact is that galaxies with weak PAH emission, such as NGC 1222 and NGC 7714 do not necessarily imply a small contribution from PDR regions. In fact, as we have noticed, all galactic spectra are dominated by a PDR-like component and the best fit model gives f_{PDR} close to unity for all but one of the galaxies. An increase in the level of the MIR thermal continuum, for example by adding the embedded component, can result in a relatively weaker PAH emission. However, the derived uncertainties do show that the lower limits to the PAH contribution tend to be smaller for galaxies that show weak PAH emission.

Another important difference has to do with the depth of the $9.7 \mu\text{m}$ silicate absorption feature, which is a measure of the extinction towards these galaxies. As we have mentioned, this can be related to the inclination at which we observe the galaxy, or simply to

4 Outlook: recent star formation in nuclear starbursts

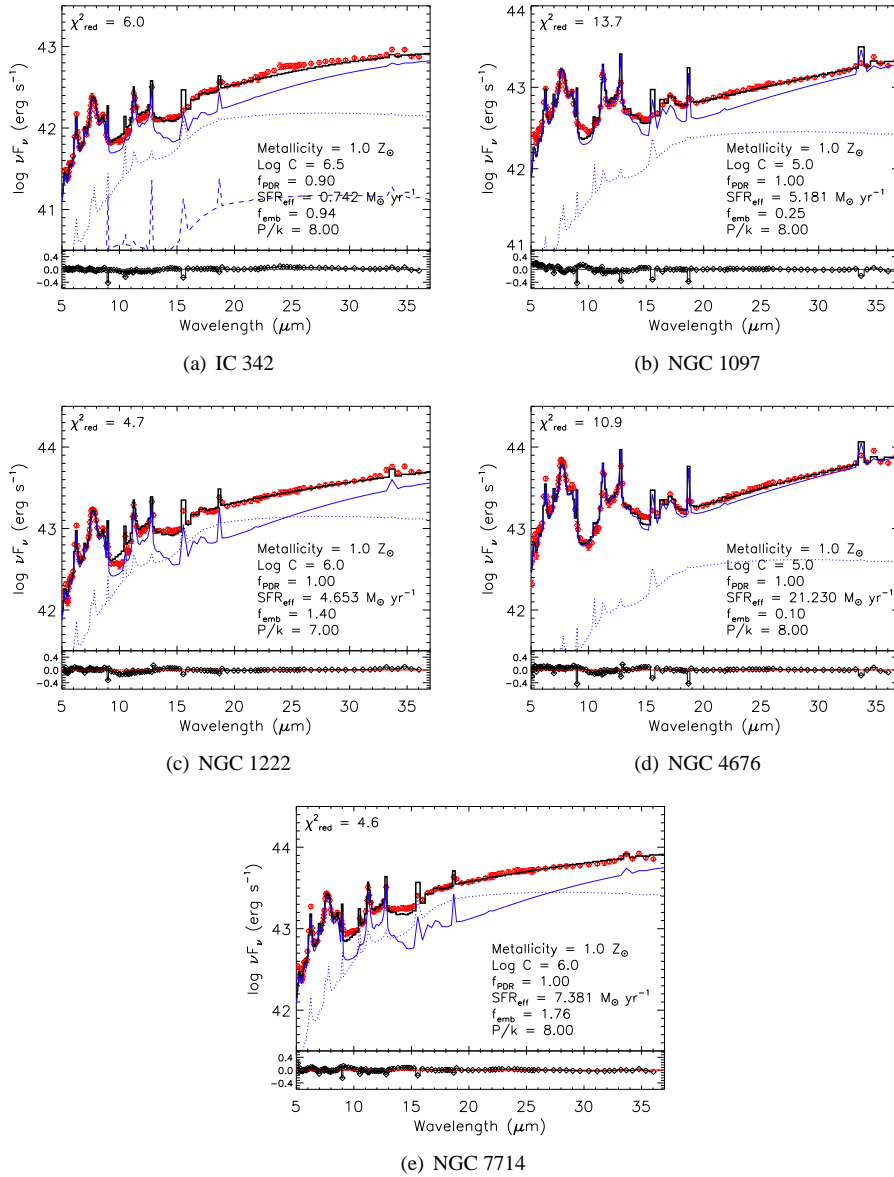


Figure 4.3 Best fit to the IRS spectra of our selected galaxies. Shown are the IRS data (red), best fit SED (solid black), and the different contributions of the resulting SED: the H II region (dashed blue), the PDR region (solid blue), and the embedded populations (dotted blue). The residuals are indicated in the lower panel.

the total column density of dust between us and the source. To account for the variations on the extinction we adjust the value of the dust column density, ρ_{dust} , to reproduce the shape of the silicate absorption feature. For all galaxies, a value of ρ_{dust} corresponding to an optical extinction of $A_V = 1.0$ gives a good fit to the silicate feature, except for NGC 4676, for which a higher value of extinction ($A_V = 4.0$) is needed to reproduce the spectra.

Fig. 4.3 and Table 4.2 indicate that spectral differences in the MIR translate into variations in the physical conditions in starbursts of similar metallicities. In B06, the authors showed that in spite of the spectral differences, some average properties are common to all starburst galaxies, and produced an average “template” starburst spectrum. Here, we adopt a different perspective. We quantify the differences in the spatially unresolved spectra of the nuclear regions and relate them to variations in the local physical conditions of the ISM. This will allow us to investigate what physical parameters have an impact on the star formation activity of starbursts.

4.4 Discussion

Although the galaxies in our sample are all nuclear starbursts, with no significant contributions from AGNs, our results indicate that they have a broad range of physical conditions. Some of the observed differences may be related to geometrical effects unresolved by the spectrometer slit, such as orientation (mainly galaxy inclination) and size. However, it is unlikely that the pronounced differences seen in the MIR spectra of these galaxies is related to inclination effects, because very high optical depths would be necessary to affect the MIR emission in these objects. In a theoretical study by Jonsson et al. (2010), using the same physical models on which our Bayesian tool is based, the authors show that the effect of galactic inclination on the MIR SED is very small, with the only noticeable effect being a change in the $9.7 \mu\text{m}$ silicate absorption feature for very inclined galaxies. Moreover, we have also discussed in §4.3 the fact that the spectra have been scaled to match the flux of the entire region contained within the LL slit. Since the galaxies are located at different distances, this region is not always restricted to the galactic nucleus. Nevertheless, we assume that in all our objects the observed spectrum is dominated by the central starburst.

We are therefore confident that the measured differences in the spectral shapes of these objects are related to the physics of the stars and the ISM in the starbursts, with only a small dependence in geometry. In the following we interpret our findings in terms of the relation between the observed trends in the best fit parameters and the overall characteristics of the starbursts.

4.4.1 Star formation rates

In general our estimates for the SFRs agree with the literature values listed in Table 4.1. The galaxies with the most intense star formation activity in our sample are NGC 4676

4 Outlook: recent star formation in nuclear starbursts

and NGC 1097. Although we derive a SFR of only $5.2 M_{\odot} \text{ yr}^{-1}$ for the latter, it is worth remembering that the IRS LL slit only covers a fraction of the 1 kpc star-forming ring, and hence our estimation is only a lower limit. Assuming a uniform star formation azimuthally distributed in the ring, the actual SFR for this starburst might be two or three times larger, and hence comparable to that of NGC 4676. These two galaxies have the highest nuclear molecular gas masses in the sample, and in both cases the nuclear molecular mass accounts for at least 20% of the total molecular gas in the host galaxies. In the remaining galaxies the molecular masses are at least one order of magnitude lower, and in the cases of NGC 1222 and NGC 4676 only upper limits have been detected.

Our estimate of the SFR is based on the integrated luminosity of the best fit SED, and as a pan-spectral diagnostic, it is more accurate than star formation diagnostics that use a single feature (e.g., the PAH emission at $7.7 \mu\text{m}$), to estimate the total luminosity. The resulting SFRs, are correlated with the total molecular masses measured towards the nuclei. This agrees well with the star formation laws in which the SFR scales proportionally to the molecular gas content (Kennicutt 1998), and does not seem to depend much on the geometry of the nucleus. By far, IC 342 is the starburst nucleus with the lowest SFR. The amount of molecular gas in this galaxy has been estimated to be $1.0 \times 10^7 M_{\odot}$, lower in comparison with NGC 1097 and NGC 4676. However, it hosts a high concentration of molecular gas in the central region (Israel & Baas 2003). IC 342 is the only galaxy on the sample that is not visibly affected by interactions with nearby companions. Our result of more intense starbursts in interacting systems would support an scenario in which galactic collisions are more efficient than other mechanisms in bringing the starburst gaseous fuel together.

4.4.2 Pressure, compactness and their relation to massive clusters

We have discussed in previous chapters the relevance of the compactness parameter C in controlling the dust temperature in H II regions as a function of time, and its corresponding impact on the SED. This arises from the fact that, as the H II region evolves, the cluster mass (M_{cl}) and the ISM external pressure P_0/k combine to set the temporal evolution of the heating flux, as parametrized by the cluster luminosity divided by the square of the H II region radius, $L_{\text{cl}}/R_{\text{HII}}^2$. From equation 2.1, we know that the compactness parameter is proportional to the product $M_{\text{cl}}^{0.6} * P_0/k^{0.4}$. This implies that to keep compactness constant, an increase in the cluster mass must be counteracted by a decrease in ISM pressure.

Our results in Table 4.2 point to an inverse correlation between the measured compactness and pressure for our sample galaxies. Those galaxies with higher compactness are also those with lower values of P_0/k , and vice-versa. If this trend is confirmed in a larger sample of objects, it would have implications in our interpretation of the compactness. According to the definition of the compactness, to keep a high C at their low ISM thermal pressures, NGC 1222 and NGC 7714 should have a significantly higher average cluster mass as compared to NGC 1097 and NGC 4676, which also have significantly higher SFRs over the last 10 Myr. Altogether, this indicates that, even if NGC 1222 and

NGC 7714 are not forming the largest amounts of stars, they might be forming the most massive star clusters. Interestingly, as discussed in §4.2, and shown in Fig. 4.2, these two galaxies show strong nebular lines that indicate the presence of particularly massive stars.

Let us speculate in the context of the possible scenarios for the formation of massive stars. If the presence of very massive stars in the starbursts where we infer the largest average cluster masses is confirmed, this would support an scenario of competitive accretion, which requires massive stars to form in clustered environments. The reason is that competitive accretion predicts an explicit relation between the mass of a cluster and the most massive star in that cluster (m_{\max}), with $M_{\text{cl}} \propto m_{\max}^{1.5}$ (Bonnell et al. 2004). In contrast, the core accretion model of star formation allows for massive stars to form in relative isolation. Our method can thus be combined with reliable diagnostics of the presence of very massive stars in clusters to test proposed models of massive star formation. Because of the small sample size of this pilot study, however, this is a very speculative statement, and further evidence is needed, part of which can be obtained by applying the present method to a larger sample of starbursts.

4.4.3 Molecular gas content and feedback in starbursts

NGC 1222 and NGC 7714 are also peculiar in their low molecular gas content, with only upper limits detected. IC 342 also has molecular gas mass two orders of magnitude below NGC 1097 and NGC 4676. Their low molecular content is also consistent with the lower upper limits that we have derived for their luminosity contribution from PDR regions. While this correlates well with their comparatively lower SFRs (in fact, IC 342 has the lowest SFR in the sample), the reason for the depletion of molecular gas in these starbursts is not clear. Negative feedback has been reported as a possible cause for this depletion by some authors in the particular case of IC 342 (Meier et al. 2011, Schinnerer et al. 2008). According to these authors, dense gas in IC 342 gets dispersed in the presence of an expanding H II region, and the influence of the negative feedback process can be such that it considerably diminishes the gas flow from the bar that feeds the star formation activity, thus quenching further star formation. Negative feedback from the massive clusters inferred in NGC 1222 and NGC 7714 can explain their low gas contents, not only from the expansion of H II regions, but also aided by the strong stellar winds from massive stars, and supernova activity.

However, a striking characteristic is that both NGC 1222 and NGC 7714 have the largest inferred contribution from young embedded objects, with f_{emb} being at least 6 times larger for these systems than for NGC 1097 and NGC 4676 (Table 4.2). We have described the interpretation for this parameter in §2.5.4. Briefly, it refers to the mass ratio of embedded to non-embedded stars that are younger than 1 Myr. If $f_{\text{emb}} = 0.0$, embedded objects no longer exist in the clusters, whereas if $f_{\text{emb}} = 1.0$, half of the massive stars formed over the last million year are still in a embedded state. Our results indicate that in NGC 1222 and NGC 7714, about 60% of the young (< 1 Myr) massive stars are still in an embedded phase, while only 25% of the stars of similar age are still embedded in NGC 1097, and even less in NGC 4676. For IC 342 the fraction is about 50%.

4 Outlook: recent star formation in nuclear starbursts

Does this apparent enhanced activity of recent massive star formation in NGC 1222 and NGC 7714 contradict their low molecular mass content? Not necessarily, for two main reasons. First, the CO surveys on which the molecular gas determination is based do not necessarily trace the very dense regions where massive stars form, which have column densities of the order of 10^{24} cm^{-2} . Second, the timescales for gas depletion in the nuclear regions are longer than the age difference between the young embedded stars and the massive main sequence stars formed over the last 10 Myr. Therefore, even if gas has been depleted over periods longer than 10 Myr, very recent events of star formation are possible (via triggering, for example) from the same primordial molecular gas cloud that formed the ionizing sources. Once again, this is an scenario that requires a more significant statistical sample of galaxies before any strong conclusions are drawn.

4.5 Summary and outlook

The MIR spectra of starbursts contain a wealth of information about recent star formation activity in galaxies, in particular in those with nuclear starbursts. In the pilot study presented in this chapter we have applied our Bayesian SED fitting tool to the MIR spectra of a small sample of galaxies whose star formation activity is dominated by nuclear starbursts. We have chosen a sample of objects with solar metallicities, in order to investigate metallicity-independent differences in their physical properties. Our Bayesian method gives robust best fit values and uncertainties to the physical parameters of these starbursts.

Overall, starbursts share some common spectral features that include PAH emission, silicate absorption at $9.7 \mu\text{m}$, strong thermal continuum and nebular forbidden lines from atomic species, as discussed in B06. Our results show that, despite these general similarities, significant differences in the recent star formation histories of nuclear starbursts can be derived from their MIR spectra, and related to their overall properties. Our exploratory study points to a relation between the star formation rate, the gas content, and the presence of massive stars in these systems. While the SFRs in the studied starbursts correlate well with the measured mass of molecular gas, the starburst with the highest SFRs in our sample do not host the most massive derived star clusters. Instead, in our sample the most massive clusters that formed during the last 10 Myr are from starbursts with less intense SFRs, where the molecular gas is depleted, like NGC 1222 and NGC 7714. This relation requires further confirmation. Interestingly, we also find that these gas-poor systems show the largest contribution from very recent ($< 1 \text{ Myr}$) massive star formation. Further evidence needs to be collected to investigate if feedback from the inferred massive clusters is responsible for the triggering of these new events of star formation.

We have shown in the preceding chapters the power of Bayesian SED fitting in the interpretation of spectral observations at MIR and FIR wavelengths. We have calibrated our tool using the well known nearby massive star formation regions 30 Doradus and NGC 604, and then applied it to the spectra of a small sample of starburst galaxies. We have shown the potential of the tool in the interpretation of these starburst spectra. Our results provide the first hints to interesting trends in the physical parameters of these systems

and their relation to the condition of the ambient ISM. These hints can be at the base of our understanding of starbursts, but require further confirmation. The next step is to apply the Bayesian tool to a larger sample of galaxies in order to provide statistical significance to these trends. A natural candidate sample is the Great-Observatories All-Sky LIRG Survey (Armus et al. 2009, GOALS), which includes imaging and spectroscopy data from several space-based observatories, and is unique regarding the large number of observations and their wavelength coverage. In particular, it contains *Spitzer*-IRS spectroscopy of a sample of 202 galaxies including many Luminous Infrared Galaxies (LIRGs), many of which also have available *Herschel* data. A systematic study of these objects with our method will provide some answers to the long-standing questions regarding the nature of starbursts.

Part II

MIRI Wavelength Calibration

Mid-infrared IFU spectroscopy from space: wavelength calibration of JWST-MIRI¹

In 2018 a new integral field unit (IFU) spectrometer will fly to space onboard the *James Webb Space Telescope* (JWST), as one of the components of its *Mid-Infrared Instrument* (MIRI). With an approximate wavelength coverage from $5\ \mu\text{m}$ to $29\ \mu\text{m}$ and a field of view ranging from $3.7'' \times 3.7''$ to $7.9'' \times 7.9''$ depending on the wavelength, this medium resolution spectrometer (MRS) will study the infrared sky at spatial scales 10 times smaller, sensitivities 100 times larger and spectral resolution 5 times better than its natural predecessor, the *Infrared Spectrograph* (IRS) onboard the *Spitzer Space Telescope*. In this chapter we present a method for the ground wavelength calibration of the MRS. We test our method using data collected during testing of the Verification Model (VM) of the instrument, and obtain a first calibration of one of the spectrometer sub-channels. We compare our results with predictions from optical models and combine them with a study of the fringing pattern created within the detector substrate, to verify some of the spectroscopy requirements set by JWST's science goals. We demonstrate the reliability of our method and show compliance with the spectral resolution requirements for the studied sub-channel. In Chapter 6 we apply our method to the full wavelength range of the Flight Model of the instrument.

¹Partially based on: J.R. Martínez-Galarza, A. M. Glauser, A. Hernán-Caballero, R. Azzollini, A. Glasse, S. Kendrew, B. Brandl and F. Lahuis, 2010, SPIE Proceedings, San Diego.

5.1 Introduction

The powerful capabilities of the *James Webb Space Telescope* (JWST) at mid-infrared wavelengths ($5\ \mu\text{m}$ - $29\ \mu\text{m}$) have been widely recognized by the astronomical community. Practically all of the JWST science themes will greatly benefit from observations extending into the thermal infrared. For example, at redshifts where the first light sources in the history of the Universe are expected to form ($z > 8$), several spectral features from evolved stellar populations have shifted into wavelengths beyond the JWST near infrared instruments, making it necessary to observe at MIR wavelengths to distinguish between real “first light” sources and sources with older stellar populations. Before JWST, observations in this spectral range have been limited to apertures below 1 meter, and to spectral resolving powers of $R \sim 600$, both limits imposed by the capabilities of the *Spitzer Space Telescope*. As we have pointed out in Chapter 1, the larger aperture size of JWST (6.5 m) implies a sensitivity 100 times larger than Spitzer in the wavelength range $5\ \mu\text{m}$ - $10\ \mu\text{m}$.

As the only mid-infrared instrument onboard the JWST, MIRI will provide multiple configurations that include wide-field imaging and photometry, coronagraphy between $10\ \mu\text{m}$ and $27\ \mu\text{m}$, low-resolution ($R \sim 100$) slit spectroscopy between $5\ \mu\text{m}$ and $10\ \mu\text{m}$ and medium resolution integral field spectroscopy with a velocity resolution of $\sim 100\ \text{km s}^{-1}$ ($R = 1000 - 3000$) between $5\ \mu\text{m}$ and $28.5\ \mu\text{m}$. The instrumental requirements for all these capabilities are set by the science goals of the mission and can be separated into two main aspects: diffraction limited image quality and high sensitivity. With a main aperture of 6.5 m, JWST has diffraction limits at $10\ \mu\text{m}$ and $20\ \mu\text{m}$ of $0''.317$ and $0''.645$ respectively, with a pixel size on the MIRI detectors of $0''.11$. This guarantees a fully sampled diffraction limit for $\lambda > 7\ \mu\text{m}$, which has not been achieved by previous observatories at the same wavelengths. As for the sensitivity, the goal is to ensure that the noise level is set by the thermal infrared background from cosmic sources, and the telescope itself. This requires high photon conversion efficiency and, of particular relevance for the present chapter, spectral and spatial resolutions that match the potential scientific targets.

The sensitivity requirements can only be achieved with an instrument that operates at very low temperatures, and hence MIRI is the only one of the JWST instruments that is cooled to a temperature of 7 K, considerably lower than the 40 K operational temperature of the telescope. The MIRI cooler is hybrid, and uses a Joule-Thomson adiabatic cooler precooled by a multi-stage Pulse Tube Cooler (Banks et al. 2008). This configuration allows remote cooling, which is necessary to place the instrument far from the warm parts of the cooling system. Because of this low-temperature operation, MIRI has to be tested in a cryochamber that simulates the operational conditions.

In this chapter we present spectral data obtained during testing of the Verification Model (VM) of the instrument, an almost exact copy of the instrument that will actually fly with JWST in 2018. We design a method to perform the wavelength calibration of the MRS, and apply it to the test data for one of the instrument sub-bands. We derive a wavelength range and spectral resolution for this sub-band, and compare them with predictions from optical models of the instrument. We demonstrate that our method is reliable and able to provide wavelength calibration within the required uncertainties, even

within the limitations of the VM hardware. The method provides us with a powerful tool to measure the wavelength calibration of the MRS across the full wavelength-range, once the Flight Model (FM) becomes available. We perform the full wavelength calibration in Chapter 6.

The chapter is structured as follows. In §5.2 we introduce the medium resolution spectrometer (MRS), and indicate some generalities of its functionality. In §5.3 we describe the spectrometer setup during VM testing, and present the resulting measurements. Since the wavelength calibration is tightly related to the spatial information of the IFU, we start §5.4 with a description of the algorithms for the reconstruction of the datacubes. We also describe the method used to perform wavelength calibration, and its application to channel 1C. Finally, we discuss fringing, resolving power and the instrumental line shape. We summarize our results in §5.5.

5.2 MIRI: an overview

5.2.1 The MIRI field of view on the sky

The field of view of MIRI on the sky is divided in different regions, each dedicated to one of the instrument functionalities. It has a $75'' \times 113''$ field of view for the imager, a $30'' \times 30''$ field of view with a Lyot coronagraph that operates at $23 \mu\text{m}$, three 4-Quadrant Phase Mask Coronagraphs, each with a field of view of $24'' \times 24''$ and operating at $10.7 \mu\text{m}$, $11.4 \mu\text{m}$, and $15.5 \mu\text{m}$, a $5'' \times 0''.6$ slit for low resolution spectroscopy and four nested fields of view for the IFU spectrometer. These are offset from the field of view containing the imager, coronagraphs and low resolution slit, as we show in Fig. 5.1. We also show in Fig. 5.1 how the focal plane looks like on the three MIRI detectors.

5.2.2 Integral field spectroscopy with MIRI

The MRS is composed of two main optical components. The spectrometer pre-optics (SPO) (Wells et al. 2004) separate the incoming beam in 4 spectral channels by the use of dichroics, and divide the field of view of each channel using slicing mirrors. The spectrometer main-optics (SMO) (Kroes et al. 2010), consist of three sets of diffraction grating mechanisms that divide each MRS channel in three sub-bands (short, medium and long wavelengths) and record the resulting spectrum on two MRS detectors (Ressler et al. 2008). In Table 5.1 we list all the nominal sub-bands of the MRS, with their respective nominal wavelength ranges and the number of MRS slices.

Each of the two MRS detectors registers the dispersed spectrum of two channels simultaneously. In Fig. 5.2 we show schematically how a particular field of view is divided by the slicing mirrors for each channel and, and then dispersed into the detector. In Table 5.2 we provide some relevant numbers regarding the size of the FOV and the spatial sampling for each channel.

5 Mid-infrared IFU spectroscopy from space: wavelength calibration of JWST-MIRI

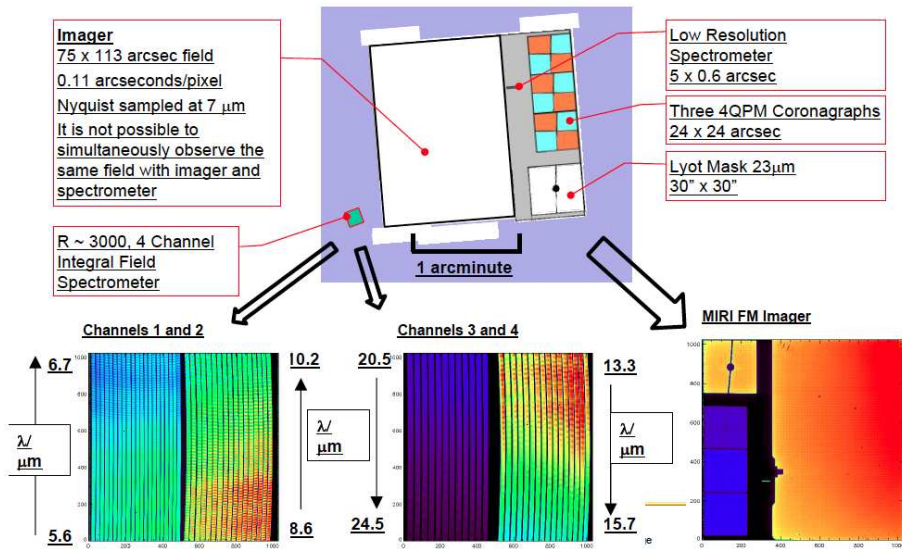


Figure 5.1 The MIRI FOV on the sky and on the detectors. The sizes of the different fields of view is indicated. Courtesy of the MIRI European Consortium.

For the MRS, specific requirements to accomplish the proposed science include a field of view of at least 3 arcseconds and the capability of image reconstruction within 10% of the diffraction limit. On the spectral side, the MRS is required to have a resolving power $R > 2400$ for $5 \mu\text{m} < \lambda < 10 \mu\text{m}$, $R > 1600$ for $10 \mu\text{m} < \lambda < 15 \mu\text{m}$ and $R > 800$ for $15 \mu\text{m} < \lambda < 27 \mu\text{m}$, and the wavelength determination accuracy should be of 10% the size of the resolution element at all wavelengths. Also, spectral ghosts are expected to be of less than 1% measured as the brightness of an unresolved line fitted to a ghost image relative to the brightness of the primary line. Finally, wavelength stability is expected to the level of 5% of the resolution element size.

5.3 Setup and measurements

5.3.1 The MIRI Telescope Simulator (MTS)

To provide the Verification Model with an input signal, a MIRI Telescope Simulator (MTS) (Belenguer et al. 2008) has been developed by INTA. Its main purpose is to provide a test beam for MIRI similar to the one that will be delivered by JWST under flight conditions. Light from a 800 K blackbody is collimated and passed through a variable aperture system and then through the desired filter before a diffuser spreads the beam and makes the illumination uniform. A $100 \mu\text{m}$ pinhole on the extended source target provides

Subchannel	Wavelength Range μm	No. of Slices	FOV arcsec^2
1A	4.87-5.82	21	3.7×3.7
1B	5.62-6.73	21	3.7×3.7
1C	6.49-7.76	21	3.7×3.7
2A	7.45-8.90	17	4.5×4.7
2B	8.61-10.28	17	4.5×4.7
2C	9.94-11.87	17	4.5×4.7
3A	11.47-13.67	16	6.1×6.2
3B	13.25-15.80	16	6.1×6.2
3C	15.30-18.24	16	6.1×6.2
4A	17.54-21.10	12	7.9×7.7
4B	20.44-24.72	12	7.9×7.7
4C	23.84-28.82	12	7.9×7.7

Table 5.1 Nominal characteristics of the MRS subchannels

Channel	Across slice sampling [arcsec]	Along Slice sampling [arcsec]	Across slice Inst. FOV [arcsec]	Along Slice Inst. FOV [arcsec]
1	0.18	0.20	3.7 (21)	3.7
2	0.28	0.20	4.5 (17)	4.7
3	0.39	0.25	6.1 (16)	6.2
4	0.64	0.27	7.9 (12)	7.7

Table 5.2 The spatial sampling and instantaneous FOVs of all MRS channels. The third column indicates in parenthesis the number of slices in which the FOV is divided.

the point-source capabilities. This point source can be scanned across the MIRI FOV. An imaging subsystem then sends the light to the MIRI FOV through a set of focusing and folding mirrors.

The MTS was meant to project a point source onto the FOV of MIRI, as well as an extended uniform illumination. Due to some mechanical issues during the manufacturing of the MTS, it was not possible to properly focus the point source, and hence its Point Spread Function (PSF) was significantly distorted. Additional mechanical issues prevented us to illuminate the entire MIRI field of view with the extended source mode. Unfortunately, the non-illuminated area includes the FOVs of the four MRS channels. The MTS is also equipped with several narrow-band filters, etalons to provide synthetic spectral lines in the full range, and a mask to produce dark images. It also has two cutoff filters, a long wavelength pass (LWP) and a short wavelength pass (SWP) filter. The MTS etalons are Fabry-Perot interferometers that produce synthetic spectral lines at specific wavelengths by interference of two reflected wave fronts. The pattern of this etalon lines can be resolved by the MRS.

5 Mid-infrared IFU spectroscopy from space: wavelength calibration of JWST-MIRI

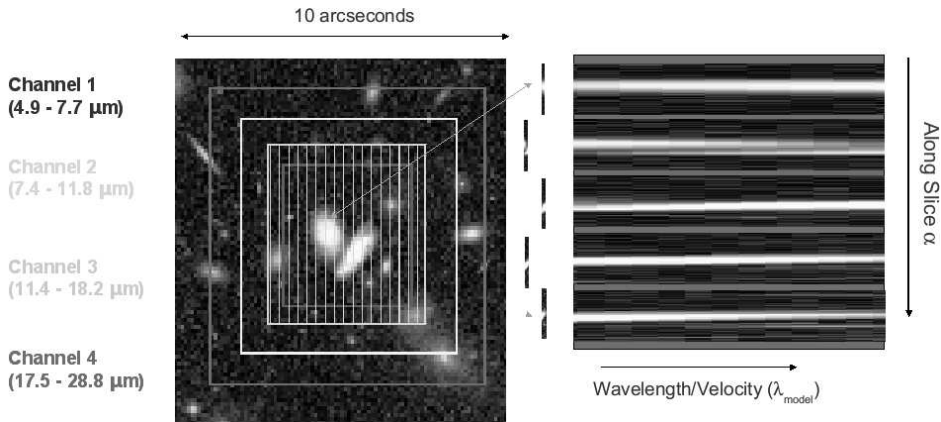


Figure 5.2 IFU spectroscopy. The slicing of the FOV is performed by the spectrometer pre-optics and arranged in an output format, for each of the four nested FOVs (left). Light is dispersed by first-order gratings and forms a spectrum on the detector (right).

5.3.2 Measurements

Using the setup described in the previous section we have taken MRS spectra of the etalon lines for the different available subchannels. Since full illumination of the MRS field of view was not possible, we used the out-of-focus point source to illuminate two regions of the MRS field of view. Full illumination of the MRS FOV will be possible during FM testing. For each of those etalon exposures we also took a background image by moving the point source out of the image field and taking an exposure of the same duration. Additionally, for each of the two point source positions we took exposures using the MTS LWP filter, and the 800 K blackbody continuum, without any filters. The LWP exposures are crucial to fulfil our goal, since the filter cutoff provides an absolute wavelength reference for the calibration. This cutoff wavelength falls within the range of channel 1C, and hence we use this channel for the present analysis.

The MIRI detectors have two standard readout patterns: Fast Mode and Slow Mode. Fast Mode reads the full array every 2.775 seconds, and Slow Mode performs the same operation every 27.105 seconds. The slow mode is preferred for long exposures ($> \sim 10\text{s}$), in order to reduce the data volume. The exposure parameters used in the present study are listed in Table 5.3.

Fig. 5.3 shows the resulting detector signal for channels 1C and 2C for an etalon exposure. The slices into which the FOV has been divided are arranged along the horizontal axis, while the vertical direction corresponds to the dispersion axis. Each of the vertical 'slices' on the detector plane is then the spectrum of one spatial slice of the FOV. The etalon lines are clearly visible as dots more or less equally spaced along the dispersion axis. They are not present in all the spatial slices, since not all the FOV was illuminated,

NFrames	40
NInt	1
Readout	SLOW
Int. Time	120 sec
VAS %	100

Table 5.3 Exposure parameters.

as mentioned. Optical distortions within the MRS are evident as a curvature of the spectrum. We expect these distortions to produce an observable variation in the position of equal- λ points as we move in the along-slice (spatial) directions.

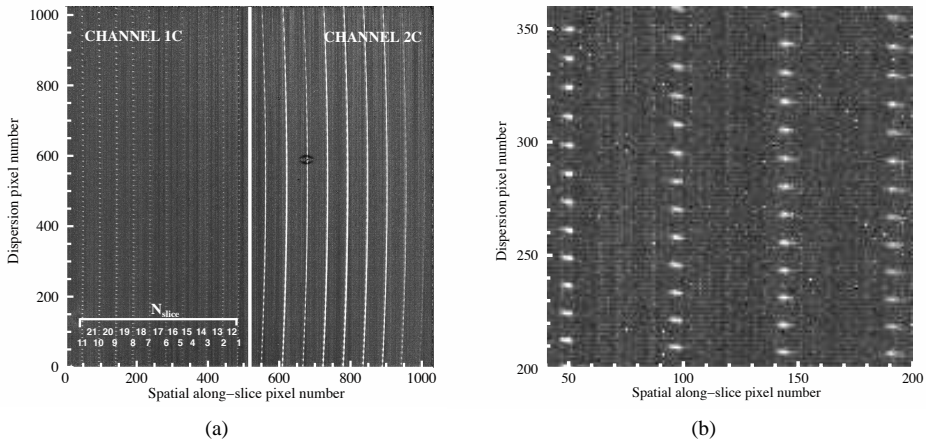


Figure 5.3 *Left*: An etalon exposure using the MRS for channels 1C and 2C. The horizontal axis corresponds to the spatial along-slice direction, while the vertical axis corresponds to the dispersion direction. The slice numbers are indicated. *Right*: Detail of the same etalon exposure. Etalon lines appear as little blobs aligned along the dispersion axis.

5.4 Analysis

5.4.1 Cube reconstruction

In an IFU spectrometer like the MRS, the spectral and spatial information are closely related, because the FOV of each channel is optically sliced, re-aligned, and then dispersed by the gratings to generate the image spectra of Figs. 6.3, 6.4 and 6.6. Hence, although the main focus of this and the following chapters is the wavelength calibration, a brief discussion on the datacube reconstruction algorithm is necessary before we describe the

5 Mid-infrared IFU spectroscopy from space: wavelength calibration of JWST-MIRI

analysis in detail. The algorithm builds the datacube from the flat-fielded slope image, and it has been implemented in the DHAS software. The resulting cube has two spatial dimensions, corresponding to sky coordinates, and a wavelength dimension.

In Fig. 5.4 we illustrate the basic concept of the cube reconstruction. The IFU level 3 data shows close-to-parallel stripes that correspond to the spectra of each of the slices in which the FOV is divided. The three dimensions of the cube are the along-slice direction, α , the across-slice direction, β , and the wavelength direction, λ . Because of the optical distortions as the light traverses the spectrometer optics, this reconstruction is not straightforward.

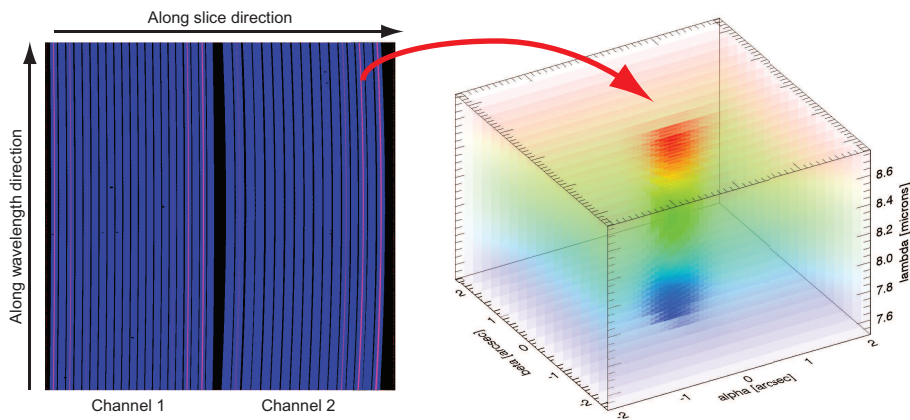


Figure 5.4 A schematic view of the cube reconstruction from raw IFU data. The two-dimensional information from the raw data (left) is transformed into the three-dimensional structure (right).

The earlier stage of the calibration is based on the optical models that trace the rays between the astronomical object in the sky plane and the positions on the detector, as a function of wavelength. Using these models, a map is produced between the corners of each of the 1024×1024 detector pixels (x, y) , and the sky coordinates (α, β) and wavelength (λ) . These maps are a first guide to rebin the detector pixels into the cube space.

These transformation maps also allow for global variations in the alignment of the slices between the optical model and the as-built instrument, that will result in variations of the α coordinate as a function of β . Using test images of the focal plane obtained during testing, it is possible to measure these offsets by determining the slice center in these images from the slice edges, and then compare them with the model predictions. Fig. 5.5 shows and explains the principle of this correction.

This method is not perfect, because it relies on the assumption of symmetric edges of the slices, and hence additional offsets of the observed α coordinate with respect to the models were observed during the testing. These additional offsets were corrected using the totality of the dataset to measure the spatial distortions, but this is outside the scope

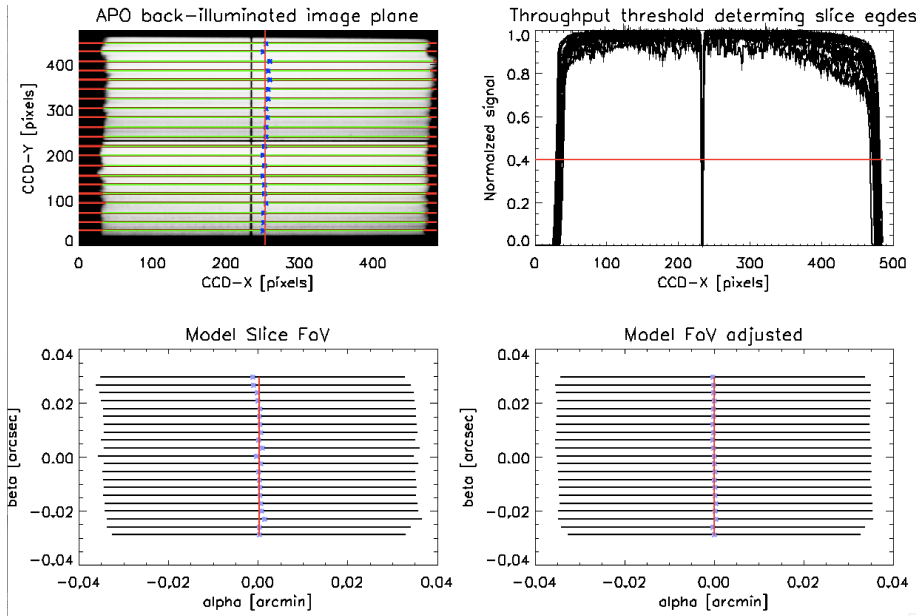


Figure 5.5 Correction of the slice-to-slice offsets of the α -coordinate: The top left panel shows the input plane of Channel 1. Along each red line the signal for each slice is extracted and normalized (right top panel). The centre of the slice (blue stars) is determined by using the relative signal strength (40%) as a discriminator for the slice. The slice centres are then compared with the slice centres of the optical model (bottom left panel) and adjusted correspondingly (bottom right).

of this chapter. Of relevance to us is that after the corrections, the resulting reconstructed PSFs were very stable all over the FOVs for all subchannels.

5.4.2 Etalon analysis

From the MRS exposures that we have described in the previous §5.3.2 we can reconstruct the image of the point source on the FOV at different wavelengths using the cube reconstruction algorithm, to obtain the 3D datacubes.

We start our analysis with the resulting datacubes, produced from from background-subtracted exposures. We use the following coordinate system for the data cube: α is the space coordinate in the along-slice direction, β is the space coordinate in the across-slice direction and λ_{model} is the wavelength. Both α and β are measured in arcseconds and are referred to the center of the FOV, while the wavelengths are in microns and their absolute value comes from the optical model. Here we will compare the optical model

5 Mid-infrared IFU spectroscopy from space: wavelength calibration of JWST-MIRI

wavelengths λ_{model} with the wavelengths resulting from our etalon and LWP measurements and analysis. We refer to the measured wavelengths as λ_{meas} , to differentiate them from the theoretical wavelengths.

The dimensions of the cube are 25 pixels in the α direction, 21 pixels in the β direction and 1225 wavelength bins. It is important to note that each of the 21 pixels in the across slice direction (β) is associated with one of the 21 slices shown in Fig. 5.3. The spatial sampling is 0.18 arcsecs in the α direction and 0.17 arcsecs in the β direction. This results in an effective FOV size of $4.48'' \times 3.56''$.

The left panel of Fig. 5.6 shows a layer of the data cube for a particular value of λ_{model} . The original exposure corresponds to a continuum 800 K blackbody exposure. The resulting image shows the point source near one of the corners of the FOV, with an elongated PSF due to the focusing problem of the MTS that we have mentioned before. The right panel of Fig. 5.6 shows a background exposure where we have indicated the pixels where we have measured the etalon lines with enough signal to noise to perform this analysis, and where we also have a good measurement of the continuum and filter spectra. These areas of the FOV correspond to two different pointings of the point source, and are intended to cover as many pixels as possible. We will use these well separated regions to study the variation of the wavelength properties and resolving power with position of the point source on the FOV.

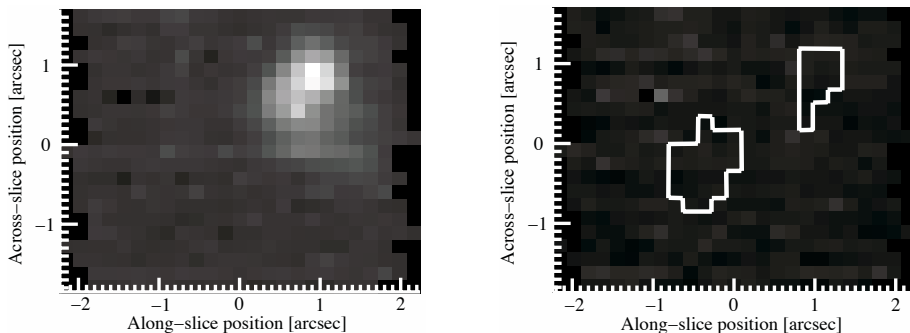


Figure 5.6 *Left*: The reconstructed point source at a particular wavelength. The elongated shape is due to focusing problems of the MTS. The horizontal axis corresponds to the along-slice spatial coordinate, α , while the vertical axis corresponds to the across-slice spatial coordinate, β . *Right*: The areas of the MRS field of view where enough signal to noise ratio was achieved for this analysis, and where LWP and continuum exposures were also taken.

The method works as follows: for each available (α, β) position we extract the spectrum of the etalon lines exposure and that of the LWP filter exposure. Provided that we know the wavelengths of the etalon lines, they provide a relative wavelength calibration along the full wavelength axis for channel 1C. On the other hand, the cutoff wavelength of the LWP spectrum provides an absolute wavelength reference for a single point in the

wavelength axis. We combine the information from this absolute reference with the relative information from the etalon lines to obtain a final wavelength scale. The uncertainty of our method depends on the accuracy with which we are able to identify the etalon line peak positions and the shape of the filter cutoff slope. This accuracy is of course a function of the signal-to-noise (S/N) ratio at which the spectra are detected. Other effects, such as line undersampling, also have to be taken into account.

The left panel of Fig. 5.7 shows a segment of the extracted etalon spectrum for ($\alpha = -0.269$ and $\beta = -0.170$). Lines are well detected with a S/N ratio of about 15, and the separation between them is well resolved, as expected for the MRS resolving power. The pixel sampling of the etalon line profiles adds an uncertainty to our determination of line peaks. Therefore, we fit Gaussian profiles to the lines in order to obtain a more accurate estimate of the peak position. We will discuss the shape of the line profile later in this paper.

The error in the line position associated with the Gaussian fit is of the order of 0.02 resolution elements. This is, as we will see later, below the instrument requirement for wavelength accuracy. However, the fact that the lines are undersampled and the presence of other sources of noise such as electronics, cosmic rays or bad pixels make the absolute determination of the line positions somewhat more uncertain than the error derived from the Gaussian fit. We expect these lines to be unresolved, and hence, while their centroid positions will provide us with a way to calibrate the wavelengths, their width will give us information about the resolving power of the instrument.

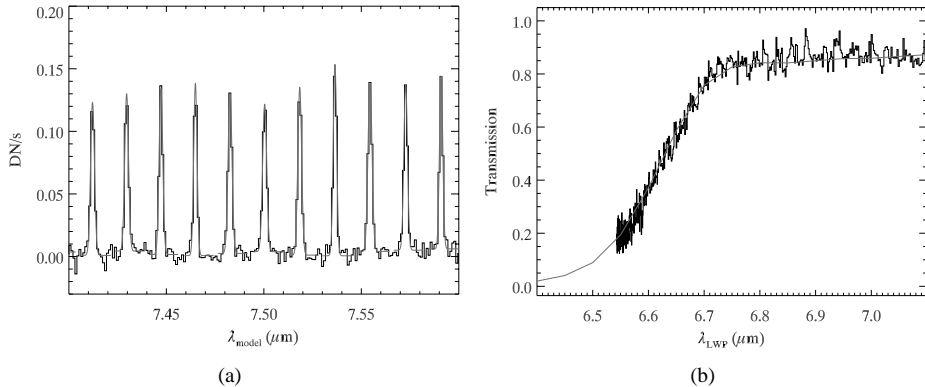


Figure 5.7 *Left*: The extracted etalon spectrum for a particular (α, β) value. Signal-to-noise ratio for the etalon lines is about 15. Lighter grey lines are Gaussian fits to the data, which is shown as a solid black line. *Right*: The transmission profile of the LWP filter. The lighter grey line is the calibrated curve, while the black line is the measured data. We fit the two curves to find an absolute reference in wavelength.

The peak positions of the etalon lines must be related to wavelengths obtained independently with high accuracy. For this purpose, we use a high resolution ($R \sim 10^5$) spectrum of the etalon transmission pattern measured independently at the Rutherford

Appleton Laboratory, in the United Kingdom. This measurement provides the relative wavelengths of the etalon lines with an accuracy of the order of 10 angstroms, i.e., far beyond our instrument requirement. Now we only need an absolute reference, and for that we use the cutoff slope of the LWP filter spectrum.

The right panel of Fig. 5.7 shows the LWP fit for a particular position in the FOV. The cutoff is clearly visible as a fading slope of the flux between 6.5 and 6.7 μm . This spectrum is the product of the continuum emission from the 800 K source and the transmission curve of the filter. To obtain an uncalibrated transmission curve from our measurements, we divide the LWP spectrum obtained with the MRS by the 800 K continuum spectrum at the same (α, β) position. We fit the resulting curve to the previously measured filter profile that samples the transmission as a function of the calibrated wavelength λ_{LWP} . It is important to note that this fit does not represent the final dispersion relation yet, but only a first order approximation to find the wavelength of a single bin. Higher orders are not so relevant at this stage, since the accuracy of the determination of the reference bin has to be lower than the separation between etalon lines only (about 0.014 μm at 6.6 μm).

In the final step we use the position of the etalon line centroids and the wavelength of the reference bin to create a grid of bin number vs. wavelength along the full range of channel 1C. We fit a second order dispersion relation to this grid and apply it to the full set of bins for each available (α, β) position. In this way we obtain a calibrated set of wavelengths for the cube bins which are illuminated. These wavelengths (λ_{meas}) are independent from the theoretical wavelengths λ_{model} .

Fig. 5.8 shows the difference between λ_{model} and λ_{meas} for different slice numbers, in units of the measured resolution element (see section 3.3). This difference increases linearly as we go to longer wavelengths, and there is a noticeable shift in the difference as we move from one slice to another. The vertical red line in the plot represents half the separation between etalon lines, and hence the minimum error we should expect from effects of line misidentification. The slice to slice variations we are observing are smaller than this minimum error, and hence must arise from different causes. The $\lambda_{\text{meas}} - \lambda_{\text{model}}$ difference spans a range of approximately 8 resolution elements for a given slice number, while the offset difference from one slice to another is about 0.2 resolution elements.

The difference plotted in Fig. 5.8 is a measure of the deviations between the designed and the built spectrometer. For instance, the zero order effect is due to alignment offsets of the detectors or the gratings. The first order effect could be partially explained by a small tilt in the detector, while the second order effects are the result of differences in the optical distortion between the as-built and the as-designed instrument. Obviously, the uncertainty in the knowledge of the LWP cutoff also adds to this difference. The first order effect seems to dominate the difference in this wavelength range.

5.4.3 Fringing

The modulation in intensity along the dispersion axis known as fringing is a common feature in infrared spectrometers and is due to the interference of wavefronts reflected by different layers of the detector. Several de-fringing algorithms have been developed

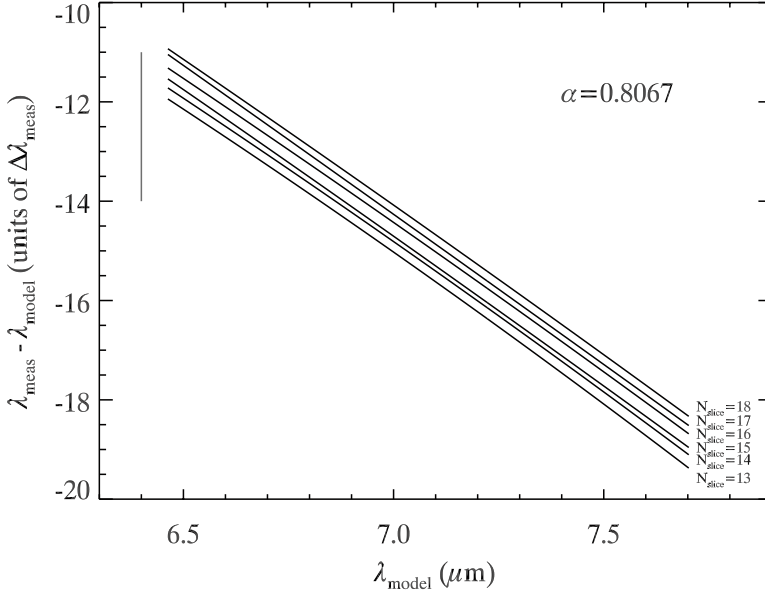


Figure 5.8 . Difference between modelled and measured wavelength for different slice numbers, for a particular along-slice position. The length of the vertical grey line is half the separation between etalon lines.

for infrared detectors of different characteristics. We can use the information contained in the fringing pattern in one of the following ways: either we use the wavelengths of the maxima and minima as compared to the predictions from the optical model to derive accurate detector features such as thickness, refractive index, etc., or we assume a model of the detector and use the distortions in the phase and period of the fringes to obtain a wavelength calibration of the instrument. Here we will attempt this latter option.

We assume that the detector has perfectly plane-parallel surfaces. Under this assumption, the period of the fringes should be constant in the wavenumber (k) domain, and deviations from this condition can be used to correct the wavelength. More specifically, if k is the *correct* wavenumber for each wavelength bin in the cube, then the frequency of the fringes is constant in k , and we should observe a linear increase of the phase ϕ with k , with proportionality factor ω :

$$\phi - \phi_0 = \omega(k - k_0) \quad (5.1)$$

We can use this relation to find the wavelength calibration for a particular spatial location in the detector:

$$k = k_0 + \frac{\phi - \phi_0}{\omega} \quad (5.2)$$

5 Mid-infrared IFU spectroscopy from space: wavelength calibration of JWST-MIRI

provided that k_0 and ω are known. From the assumed detector thickness we can obtain the separation between fringes ($k - k_0$), which corresponds to a phase difference of 2π , and hence we obtain ω . As for the absolute reference wavelength k_0 , we find it again using the LWP filter cutoff wavelength. However, unlike the etalon analysis that uses relative differences between etalon lines, in this case the absolute calibration relies completely on the fit to the cutoff slope of the filter.

The fringes are obtained from VM exposures using the MIRI calibration source, which provides uniform illumination over the full FOV. Fig. 5.9 shows the resulting fringes for a particular value of α and β . A sinusoidal function is fitted to the baseline-corrected pattern and the position of the fringes maxima is compared with the predictions from the detector model, both in frequency and phase. Deviations are translated into wavelength difference with λ_{model} , as described.

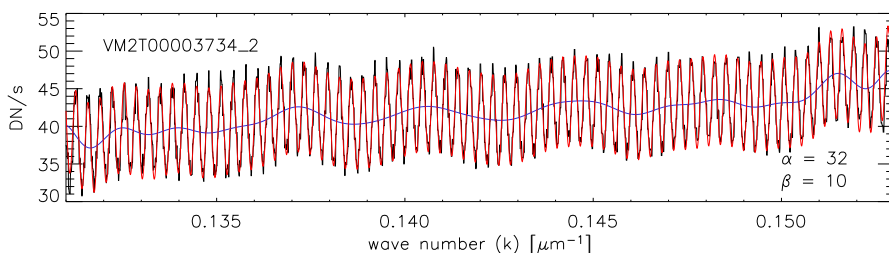


Figure 5.9 Measurement of the phase of the fringes. The black line represents the counts in the datacube as a function of wavenumber for a given α , β . The blue line is the low-frequency oscillation obtained through FFT filtering, and the red line is the cosine of the phase calculated for each k , $\cos(\phi)$, after scaling to match the amplitude of the fringes and addition of the low-frequency oscillation. Here α and β refer to the spatial bin number and the slice number, respectively.

The left panel of Fig. 5.10 shows the correction in wavelengths with respect to λ_{model} derived using the fringes for all the 21 slices. The shape of the shift varies smoothly as a function of the slice number (i.e., as a function of the slice position on the detector plane). The U-shape of the shift for some of the slices might be due to variations in the detector thickness that are not accounted for in the detector model. But they could also be due to optical distortions in the MRS itself. This result needs to be corroborated during the etalon lines calibration, once the full FOV can be illuminated with the MTS extended source.

We compare the results obtained with the two methods for two different slices in the right panel of Fig. 5.10. This comparison is only relative, since the strong dependence of the fringing method on the absolute reference makes any absolute comparison meaningless. The difference is significant. The dependence with slice position is much more dramatic when the fringes are used. Also, second order effects seem to dominate the

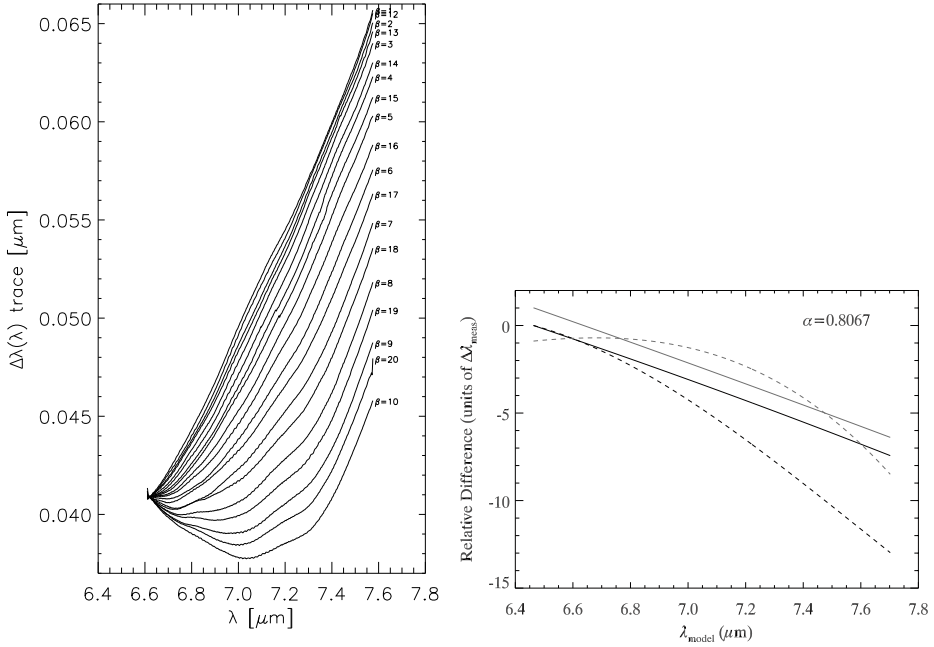


Figure 5.10 *Left*: Shift with respect to λ_{model} that needs to be applied to each slice as calculated using the fringing analysis. Here, β refers to the slice number. *Right*: Relative difference in the corrections to the model wavelengths when using the two methods described. Solid lines correspond to the etalon analysis, while dashed lines correspond to the fringing analysis. We compare two positions on the MRS FOV: $N_{\text{slice}} = 13$ (black lines), and $N_{\text{slice}} = 18$ (lighter grey lines). The origin of the y axis is arbitrary.

fringing analysis, while the difference with λ_{model} are close to linear with wavelength in the etalon analysis. The smooth variation in the shape of the curves shown in the left panel of Fig. 5.10 might be an indication that the difference between the two methods might arise from wrong assumptions about the detector properties. For instance, thickness variations (deviations from plane-parallel geometry) of the detector would produce additional distortions on the phase and frequency of the fringes. Whether this is the case, or there are other issues about the wavelength calibration that we are ignoring in the etalon analysis is a question that will have to wait until we have fully characterized FM detectors and better S/N data.

5.4.4 Line shape and resolving power

The etalon lines are not resolved by the MRS. This is shown in the left panel of Fig. 5.11, where we have plotted the high resolution measurement of one of the etalon lines together with the corresponding line as measured with the MRS during the tests. The width of the unresolved lines provides information about the resolving power of the instrument. We have determined the widths of the measured etalon lines by fitting Gaussians to the line profiles and using their full width at half maximum (FWHM). To associate the FWHM of the lines (in pixels) to the resolution element $\Delta\lambda$ (in μm), we use the derivative of the dispersion relation that we have obtained from the etalon analysis. We compute the resolution element at the positions of the lines and plot the result for a particular (α, β) in the right panel of Fig. 5.11, where we have also fitted a straight line to the set of datapoints. The linear fit gives a resolving power ($R = \lambda/\Delta\lambda$) between 2800 (at short wavelengths) and 3400 (at long wavelengths) for the derived wavelength range (6.43-7.66 μm). Deviations in R from the straight line are of about 500. The instrument requirement for resolving power states that between 5 and 10 μm , the resolving power should be greater than 2400. The goal, however, is to provide $R \sim 3000$ at these wavelengths.

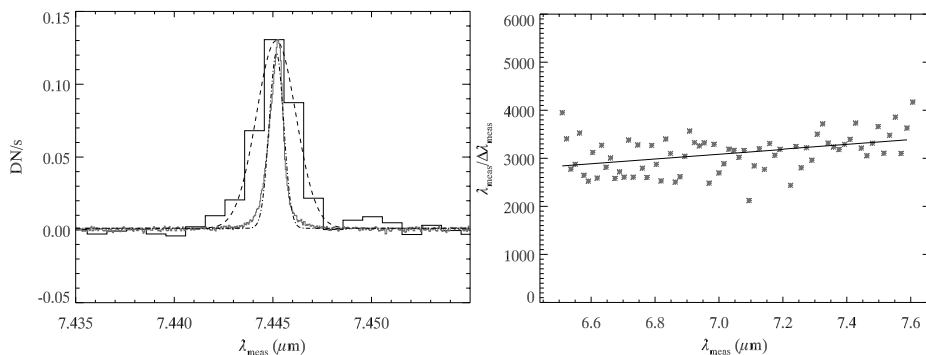


Figure 5.11 *Left*: One etalon line as seen by the MRS (solid black line) and by the high resolution measurements (solid grey line). The dotted lines are Gaussian fits to the data. *Right*: Resolving power R for the MRS subchannel 1C. The asterisks are the measured values at the line centroids, and the solid line is a linear fit to the data.

There is a spread in the measurement of the resolving power R of about 500. Insufficient S/N in the measurement of the etalon lines, which causes variations in the parameters of the Gaussian fits from line to line, may be part of the cause for this dispersion. In general, any source of noise in the original exposures can affect the shape of the lines, but we expect the flat-fielding to be the main source of error. Higher S/N again is desirable to achieve a narrower dispersion in the resolving power estimates. During FM testing, studies of the stability of the line shapes is essential to assess what is the magnitude of the variation in resolving power we should expect from one measurement to the other.

The etalon lines as measured by the MRS are the convolution of the intrinsic line shape

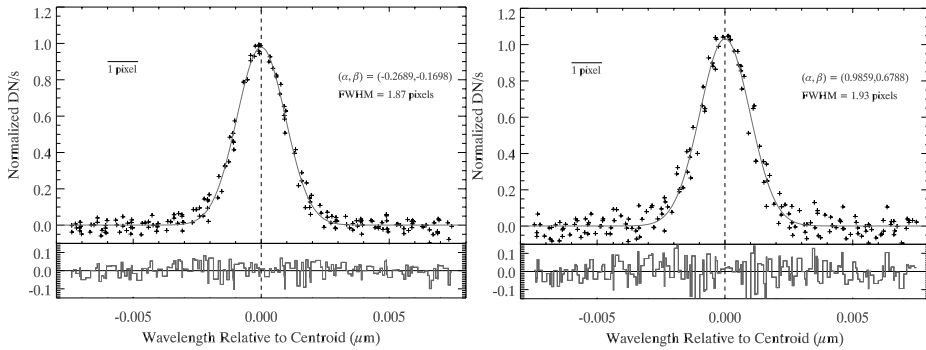


Figure 5.12 *Left*:: Overplotted etalon lines with their Gaussian centroids located at the origin, for position $(\alpha, \beta) = (-0.269, -0.170)$. The cross symbols correspond to the MRS data, while the solid grey line is a Gaussian fit to the resulting set of data. The residuals of the fit are shown at the bottom of the plot. The pixel size is also indicated. *Right*: Same as (a), but for position $(\alpha, \beta) = (0.986, 0.679)$

with the slit width of the spectrometer, which has a response that we can approximate by a Gaussian. For resolving power issues, we are more interested in getting the instrument's response unaffected by this convolution, and hence we want to deconvolve the measured profile with the intrinsic line shape. The derivation of the intrinsic line shape would require detailed modelling of the reflecting layers of the etalon device mounted on the MTS. Instead, we use the high resolution measurement of the etalon lines as a good approximation of the intrinsic line shape. Fig. 5.12 shows the Gaussian fits to the unresolved etalon line measured by MRS and the fit to the high resolution measurement for the same line. The theory of convolution of Gaussians states that the widths of two convolved Gaussian add in quadrature: $\sigma_{\text{convol}}^2 = \sigma_1^2 + \sigma_2^2$

From the two measurements we obtain with our Gaussian fits and the expression above, we obtain an estimation of the line width, once it has been deconvolved with the intrinsic shape. We find that the deconvolved widths are about 10% smaller as compared with the MRS measurements. Since the width of the Gaussian is proportional to the resolution element, this decrease in the width translates to an equivalent increase of the resolving power. This increment brings us above our goal of $R > 3000$ at these wavelengths.

Line shape

Perhaps more important than an absolute wavelength calibration at this point, the study of the unresolved line shapes across the FOV is crucial. If the line is not symmetric, future dynamical studies using spectral lines might be affected by a purely instrumental effect. For instance, near the edge of the detector, internal reflections might cause additional line peaks or bumps. It is difficult to judge the symmetry of the etalon lines given the level of

pixel sampling we have in the data. With FWHMs of between 2 and 3 pixels, the lines might appear asymmetric, but they hardly provide a definitive answer.

In Fig. 5.12 we have overplotted 12 normalized neighboring etalon lines with wavelengths near $7.4\mu\text{m}$ with their Gaussian centroids all located at the origin, for two different positions of the FOV. The plots show a statistical line shape that is well fitted by a Gaussian, within the errors shown in at the bottom of the plots. For both positions, the FWHM of the fitted Gaussians is of about 1.9 pixels.

As mentioned before, undersampling reduces the accuracy with which the line centroids can be determined. Although geometrical ray tracing predicted line widths of less than one pixel, our measurements in Fig. 5.12 show that the actual line widths are close to Nyquist sampling, at least in the wavelength range studied here.

5.5 Summary and outlook

We have studied the wavelength properties of the MIRI Medium Resolution Spectrometer. Using input from optical modelling and an analysis of the synthetic etalon lines produced with the telescope simulator, we have designed a tool to obtain a wavelength calibration from MIRI test data. The wavelength calibration of the instrument before launch is of crucial importance for the development of the reduction software and for the planning of commissioning and science observations that will require the spectroscopic capabilities of JWST.

Even though we were restricted by the quality of the data, which we expect to improve during the testing of the Flight Model of MIRI, the different methods seem to provide the necessary accuracy to verify the instrument requirements. In particular, even at a moderate S/N ratio of about 15, the etalon line analysis provides wavelength references with an accuracy below a tenth of the resolution element. An absolute wavelength calibration will require smaller uncertainties in the determination of an absolute reference using the LWP filter. But even with our S/N restrictions, the effect of a wrong matching of the etalon lines with their actual wavelengths is not bigger than the separation between two etalon lines, and this should be improved with FM data. Fringing provides an interesting way of checking the results, but it might be more useful to study variations in the detector properties such as substrate thickness. The resolution-limited line shapes are well fitted by Gaussians and have FWHM larger than one pixel, minimizing the effect of a wrong calibration due to undersampling.

The analysis has been carried out for channel 1C of the detector, where we can establish an absolute reference with the LWP filter cutoff wavelength. However, this method can be extended to other channels by finding an absolute reference for those channels where a filter cutoff is not available. This reference can be, for example, the pattern created by synthetic lines from different etalon filters that overlap in some portions of the different subchannels. In this way, once we have obtained a full set of data with the FM, an absolute wavelength calibration can be achieved for the full wavelength range of MIRI.

ACKNOWLEDGEMENTS

This chapter would not have been possible without the input from many people within the MIRI European Consortium and in particular the MIRI test team. Our colleagues in the US have also provided very helpful comments and new ideas. In particular, this work would not have been possible without the Data Handling and Analysis Software (DHAS), developed by Jane Morrison, at the University of Arizona.

CHAPTER 6

The spectral properties of JWST-MIRI: calibration of the Flight Model¹

MIRI is the mid-infrared instrument for JWST. The instrument has been fully assembled and tested in the United Kingdom by an international consortium, and now awaits integration with the rest of the JWST observatory. In this chapter we describe the functionality and the performance of the MIRI integral field spectrometer. Using the method described in 5, we obtain the wavelength calibration of the spectrometer for its full wavelength range. This is the only calibration of the instrument available before in-orbit measurements are performed. We measure the wavelength ranges of the sub-bands, estimate the resolving power of the instrument, and investigate the shape of the unresolved spectral lines. We are able to verify compliance with most of the instrument requirements. In particular, the spectral resolving power of MIRI is well above the values required to perform the planned science.

¹Partially based on MIRI FM test reports by J.R. Martínez-Galarza, A. Glauser, E. Schmalzl, F. Lahuis, J. Morrison

6.1 Introduction

The Mid-Infrared Instrument (MIRI) onboard JWST is the next milestone in space-based mid-infrared astronomy. It will provide imaging, spectroscopy and coronagraphy at wavelengths of $5\ \mu\text{m}$ to $28\ \mu\text{m}$. An international partnership between the Jet Propulsion Laboratory and a nationally funded consortium of European institutes, worked together to design, assemble, and test MIRI. Today, MIRI is the first instrument that has been fully tested and is ready to be sent to the United States for integration with the rest of the JWST observatory. MIRI will be a crucial instrument for all four of the primary science themes for JWST, namely: (a): the discovery of the “first light”; (b): the assembly of galaxies: history of star formation, growth of black holes, production of heavy elements; (c): the understanding of how stars and planetary systems form; and (d): the evolution of planetary systems and conditions for life.

During the summer 2011, the Flight Model (FM) of the MIRI instrument was thoroughly tested both in performance and functionality at the Rutherford Appleton Laboratory near Oxford, in the United Kingdom, building up on the previous experience with the Verification Model (see Chapter 5). The purpose was to verify all instrumental requirements set by the MIRI science goals using the flight software. A large portion of the test campaign was dedicated to observations with the integral field spectrometer, a crucial component of the instrument. We have obtained test MRS data of both point and extended sources and used them to perform a full calibration of the spectrometer, both spatially and spectrally, which allows for a reconstruction of the 3-dimensional information from astronomical sources. The calibration includes a measurement of the spectrometer field of view (FOV) on the sky, the measurement of the spectral ranges and resolving power for each channel, and the reconstruction of the resulting datacube. These measurements are all crucial for the verification of the instrument requirements and predictions on the science that will be possible with MIRI.

In Chapter 5 we have presented a method for the wavelength calibration of the MIRI spectrometer, and successfully applied it to VM data for one of the spectrometer subbands. In this chapter we use the method to provide a full spectral calibration of the instrument, for its entire wavelength range. This provides the only reference to the spectral properties of MIRI before any on-flight calibrations become available. We use the calibrated datacubes and our calibration method to measure important spectral properties such as wavelength coverage and spectral resolving power. We then compare the results with the instrumental requirements set by the MIRI science. In §6.2 we present a description of the observational setup, the observations performed and the reduction pipeline used. In §6.3 we present the analysis tools and methods that we have used to perform the wavelength calibration. We discuss our results in §6.4 and compare them with the instrumental requirements to verify their compliance. We finish this chapter with a summary of our main findings in §6.5.

6.2 Observations

6.2.1 The test campaign and the observational setup

The MIRI Flight Model Test Campaign was carried out in the summer of 2011. The instrument was inside a cryogenic chamber that kept it close to the operational temperature of 7 K. A revised version of the MIRI Telescope Simulator (MTS) was used to provide the incoming beam, both for extended and point sources. The improvements of the MTS with respect to the VM version included a sharper point source (using pinholes of either $25\ \mu\text{m}$ or $100\ \mu\text{m}$ in diameter) and a full illumination of the MIRI FOV with the extended source, including both the imager and MRS fields of view. MIRI is equipped with a Contamination Control Cover (CCC) that blocks any incoming light if necessary. For dark exposures, the CCC was kept closed.

On board calibration sources were employed to provide flat fields for both the MIRI imager and the MRS. The MTS was also equipped with solid state etalons and edge filters that provided the synthetic etalon lines and absolute wavelength references used for the

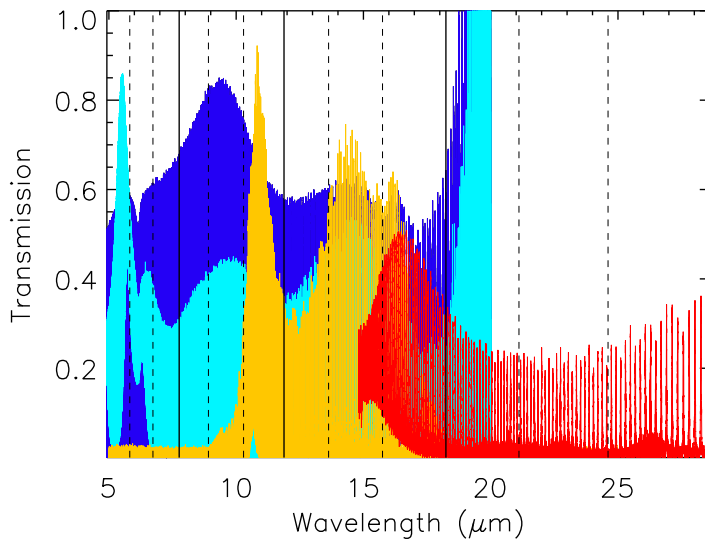


Figure 6.1 The transmission spectrum of the MTS solid state etalons, calibrated at high resolution prior to the test campaign. The color code is as follows. *Cyan*: Etalon 1A, *Blue*: Etalon 1B, *Yellow*: Etalon 2A, *Red*: Etalon 2B. The boundaries between channels are indicated by the solid lines, while sub-bands for each channel are separated by the dashed lines.

6 The spectral properties of JWST-MIRI: calibration of the Flight Model

wavelength calibration of the spectrometer. A total of 337 hours of exposure time were employed for the performance tests of MIRI, of which about 65% were dedicated to the MRS. Most of the MRS exposure time was used for 100 μm pinhole observations, and a considerable part was used for extended source observations.

For all the observations the MTS blackbody (BB) source was at a temperature of 800 K, and the 100 μm pinhole was used to produce test point sources, with a fully open Variable Aperture System (VAS). Exposures were made with the slow readout mode for the MRS detectors.

6.2.2 Test data

To perform a full wavelength calibration of the four spectrometer channels, a large amount of observations were performed, including both extended and point sources. The extended source was used to fully illuminate the MRS FOV, and used the MTS solid state etalon filters (see Chapter 5) to generate a synthetic spectrum for the full MRS range. We also took etalon exposures with the 100 μm point source, to study variations of the resolving power with position of the source in the FOV.

Extended source observations

The wavelength calibration is achieved by measuring the positions of the unresolved spectral lines produced by the MTS etalon filters on the reconstructed cube. There are four of these etalon filters (1A, 1B, 2A, 2B), each optimized for one specific MRS channel. In Fig. 6.1 we show the coverage of each etalon within the MRS wavelength range, as measured prior to the test campaign.

We have measured the full MIRI spectrum for each of the solid state etalons whose transmission is shown in Fig. 6.1. For each etalon, three exposures were taken to cover the full 5 μm -29 μm wavelength range, one exposure for each grating configuration: SHORT (A), MEDIUM (B) and LONG (C). Each exposure takes the corresponding sub-spectrum for all four channels simultaneously. The final spectrum for each etalon is thus composed of 12 sub-spectra. We have also obtained additional spectra of the long wavelength pass (LWP) and short wavelength pass (SWP) filters of the MTS Filter Wheel (FW), which provide absolute reference wavelengths for sub-bands 1C and 4B (with cutoff wavelengths at 6.6 μm and 21.5 μm respectively), as well as the spectrum of the unfiltered blackbody, which allows us to measure the instrumental response to the BB spectrum. Table 6.1 summarizes the combinations of etalons and grating positions for which we have obtained data.

To minimize the MTS FW movements, we first selected the desired etalon and then took three exposures corresponding to the three sub-spectra. Each of these exposures is followed by a background exposure. Only then we move on to the next etalon. After the etalon exposures are taken, we take the LWP, SWP and BB continuum exposures, with their respective backgrounds.

MTS Filter	Gratings A	Gratings B	Gratings C
1A	Yes	Yes	Yes
1B	Yes	Yes	Yes
2A	Yes	Yes	Yes
2B	Yes	Yes	Yes
LWP	No	No	Yes
SWP	No	Yes	No
BB Continuum	Yes	Yes	Yes

Table 6.1 Combinations of MTS filter positions and grating configurations for which we have obtained data.

Early exposures during the test campaign using etalon 1A and the dichroics set to LONG (hence, sub-band 1C), showed that our original approach for the exposure using 32 slow frames/integration and 4 integrations/exposure produced S/N ratios well beyond the necessary values, and hence for the rest of the campaign we reduced our exposures to 24 frames/integration, 4 integrations/exposure, which provided S/N above 50 for most of the MRS wavelength range. The instrument requirement associated to this measurement states that the wavelengths should be determined to an accuracy of at least 10% of the resolution element when the etalon lines are detected with a S/N of 50.

In order to investigate the temporal and mechanical wavelength stability, additional etalon exposures with the extended source were taken in different epochs of the test campaign, but given the limited test time, only etalons 1A and 2A were used. The different epochs were separated by at least one week. The first epoch is May 19, 2011, followed by epochs on June 21, and July 10. On July 21, an additional repeat of the etalon exposure was performed to check for stability after the grating mechanism had been configured.

Point source observations

For the point source etalon observations, we have performed a raster scan with the point source with five symmetric pointings with a step size of $1/4$ of the slice width across the slice for two of the slices in each channel. These two slices are identified as Field 1 and Field 2 in each case. The origin of the 5-pointing raster pattern is at the nominal dither position. Fig. 6.2 shows the scan positions for all 4 channels.

The exposure times were adjusted to guarantee a peak to base S/N ~ 100 for the reconstructed PSF. The resulting exposures were of 32 frames/integration, 2 integrations/exposure, in slow mode.

6.2.3 Data reduction

The data reduction consists on the following steps: (i): Creation of slope images from raw data registered on the two MRS detectors; (ii): Subtraction of the background and

6 The spectral properties of JWST-MIRI: calibration of the Flight Model

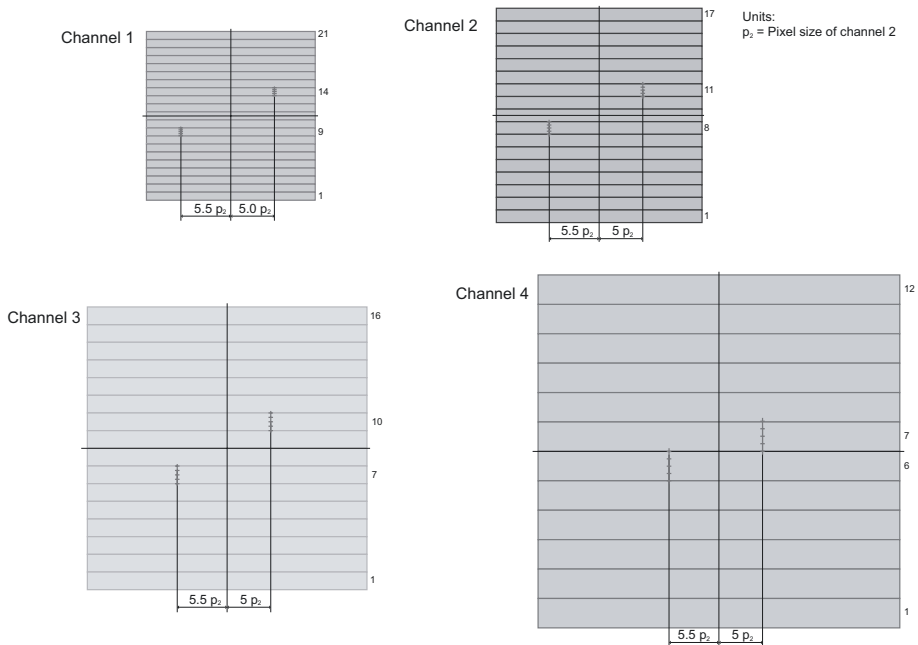


Figure 6.2 Field positions for the point source etalon exposures (small horizontal grey marks). Each channel is shown only once, but the pointings are repeated for all sub-bands.

flat-fielding of the resulting slope images, and (iii): Reconstruction of the datacube.

The following steps were performed on the raw data in preparation for the analysis. Version 5.0.7 of the *Data Handling and Analysis System* (DHAS) software¹ was used for all the datasets.

- The measured charge ramps on the detector are converted into slope values for each frame. The process involves correction of bad pixels, cosmic rays, as well as non-linearity corrections in the ramps. The average slope is calculated over multiple integrations. The resulting slope images are in counts per second (DN/s) and called level 2 data.
- Optionally, darks, pixel flats and fringe flats can be applied to the level 2 data. The fringe correction is customary in infrared detectors, because multiple reflections within the detector substrate create a Fabry-Perot fringing pattern.
- Spectral pixel flat fields are obtained from the spectrum of the BB extended source for all sub-bands. The flats are background subtracted and corrected by fringing.

¹The DHAS software has been developed by Jane Morrison, University of Arizona.

We divide our slope images by these flats.

- No fringe flats were applied to the level 2 data, since not all fringe flats were available by the time of the analysis. Our tests show that at the S/N obtained, not including the fringe flats does not affect the measured centroids of the etalon lines by more than a few percent of the resolution element. The resulting data are level 3 files.
- Data cubes are built from the resulting MRS level 3 data. The dimensions of the resulting cubes are the along-slice spatial coordinate, α , the across-slice spatial coordinate, β (related to the slice number N_{slice} shown in Figs. 6.3 and 6.4), and the wavelength derived from the optical model, λ_{model} . We discuss the details of the image reconstruction in §5.4.1.
- Background cubes are subtracted from the etalon, filter and continuum cubes, in a bin by bin basis. We perform the wavelength calibration on the resulting datacubes.

6.2.4 Reduced data

Extended source

In Figs. 6.3 and 6.4 we show slope images of the extended source MRS spectra for all four channels in sub-band 'A' (each figure shows one of the MRS detectors). We also show a zoomed view of the etalon lines for each channel in Fig. 6.5. These figures illustrate how the spectrum of an extended source looks like on the detector space, prior to the reconstruction of the datacube.

The etalon lines are detected with a signal-to-noise well above the required value of 50, over the full MRS wavelength range. An exception is sub-band 4C, which has a low throughput resulting from an inaccurate manufacturing of the grating. The low throughput for this sub-band reflects in a S/N of only a few for etalon lines on the long-wavelength end of the detector array. Nonetheless, etalon lines on the short-wavelength end of the detector (about a third of the pixels) are also detected with S/N over 50. For most of the other sub-bands the S/N is well above a value of 50 (about 900 in the middle of the spectral range). The high S/N in the etalon lines located on the regions of maximum transmission guarantees sufficient S/N in other regions of the etalon transmission range, in the overlapping regions with lines from different etalons (See Fig. 6.1). The resulting overlap pattern will be used later as an absolute reference wavelength for those sub-bands where no wave-pass filter was available.

Point source

For the point source etalon observations, the etalon lines were detected with a S/N varying from about 120 in Channel 1 to about 20 in Channel 4. The latter value is below the required S/N of 50, but for the long wavelength sub-bands where the S/N is lower, the

6 The spectral properties of JWST-MIRI: calibration of the Flight Model

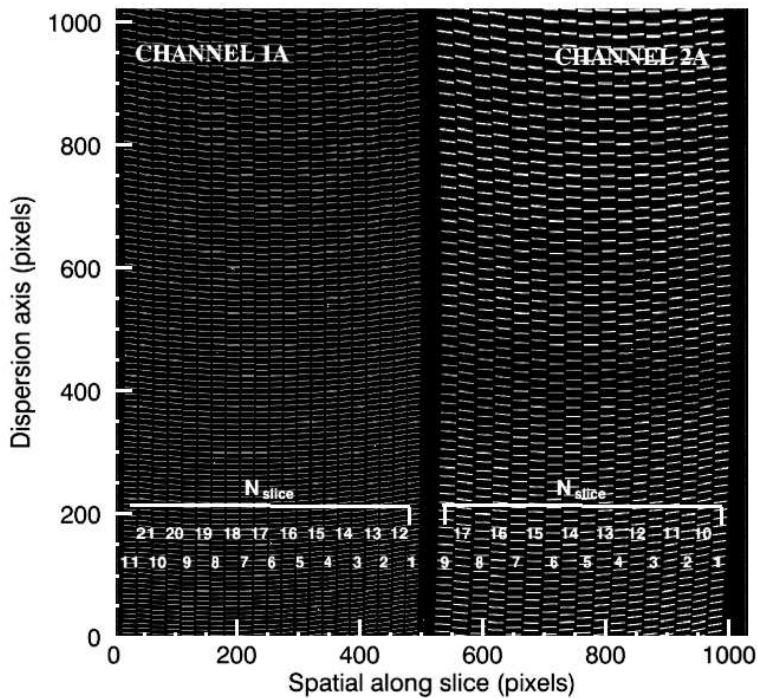


Figure 6.3 The slope image of the etalon 1A spectrum of an extended source, as registered on the SW detector for sub-bands 1A (left half of the detector) and 2A (right half of the detector).

etalon line profiles are better sampled on the detector, with FWHMs of about 3 pixels. In Fig. 6.6 we show an example of how the spectrum of a point source looks like on the detector array after the flat fielding has been applied. A comparison of this spectrum with the spectrum shown in Fig. 6.3 shows the reduced spatial extension of the point source as compared to the extended source. The etalon lines appear here as small dots, while in the case of the extended source they appear as horizontal lines. Adjacent slices on the detector do not correspond to neighbouring pixels in the FOV of the respective channel. This is the reason for the detection pattern observed on the detector.

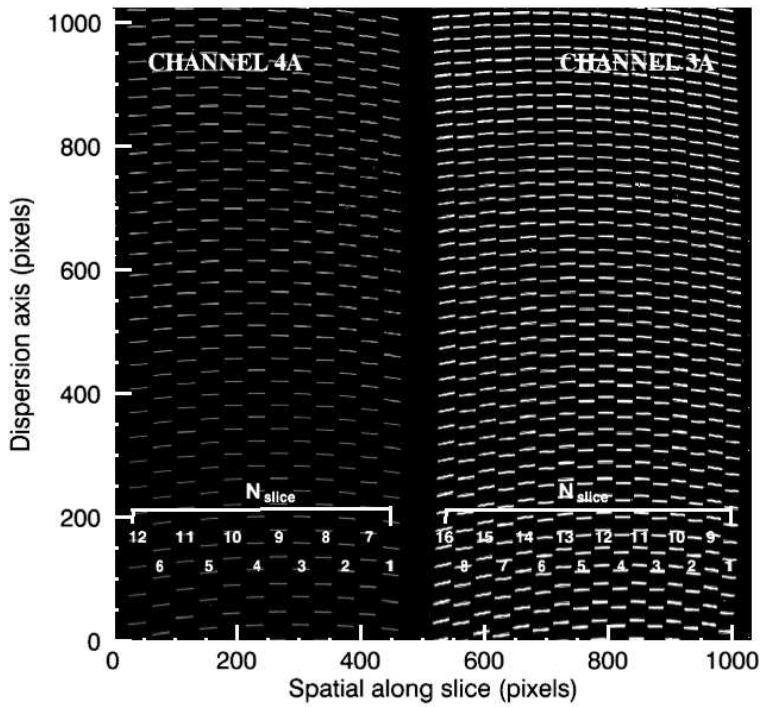


Figure 6.4 The slope image of the etalon 2A spectrum of an extended source, as registered on the LW detector for sub-bands 4A (left half of the detector) and 3A (right half of the detector).

6.3 Analysis

6.3.1 Wavelength characterisation

Up to this point, the resulting cubes have been constructed using the wavelengths resulting from the optical models, and hence these are the 'as-modelled' wavelengths. The purpose of the wavelength calibration is to update those wavelengths on the cube and detector space, to account for effects in detector and grating alignment, incidence angle of the light, and other effects in the as-built spectrometer that modify the predicted wavelengths. We now describe how this calibration was performed. The method builds on the experience obtained with VM data (see Chapter 5), but benefits from the much better data quality of the data obtained with the FM hardware.

6 The spectral properties of JWST-MIRI: calibration of the Flight Model

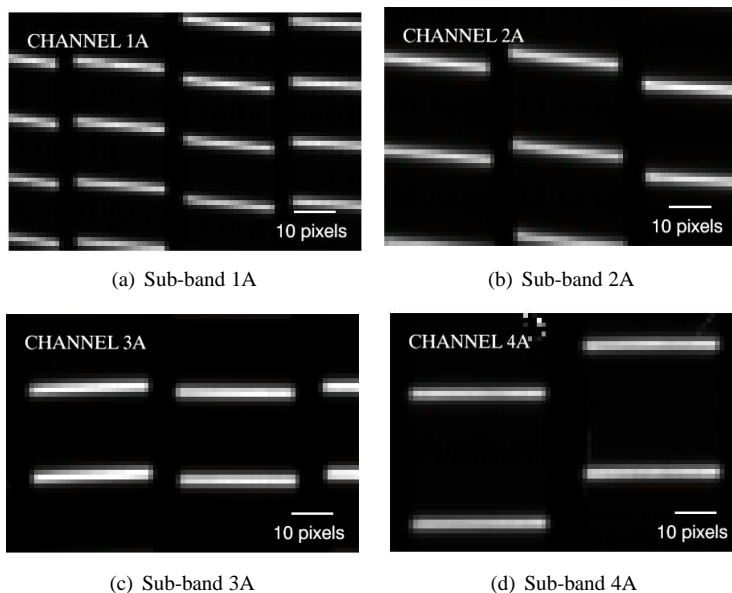


Figure 6.5 Detail of the unresolved etalon lines as registered on the detector, for the different MRS channels.

Extraction of the spectra

We extract the spectrum of each (α, β) pixel in the cube along the λ direction, for each of the 12 sub-bands. We end up with a spectrum for each spatial pixel in the FOV, and the image reconstruction algorithm relates each cube coordinate (α, β, λ) to a position (x, y) on the detector array. This is a one-to-one relation. The extraction is made using a single pixel aperture to avoid any potential smear of the line widths by combining different pixels. This is possible because we have an extended source that fully illuminates the FOV. A different approach is used for the extraction of a point source spectrum.

In Fig. 6.7 we show a single wavelength “slice” for each the four cubes resulting from an exposure with a particular grating configuration. The observed horizontal lines (particularly visible in sub-band 3A) that divide the FOV in two regions with different intensities are due to an uncorrected sky flat used in our analysis. The sky-flats are intended to correct for throughput variations in both the along-slice (α) and the across-slice (β) directions, but they were not properly measured at the time of our analysis.

Gaussian fit to the etalon lines

In Fig. 6.8 we show a part of the extracted etalon spectrum for a particular (α, β) position. Shown are two different sub-bands 1A and 4A. We fit Gaussian profiles to the registered spectral lines to measure the position of their centroids and their widths. The Gaussian fit

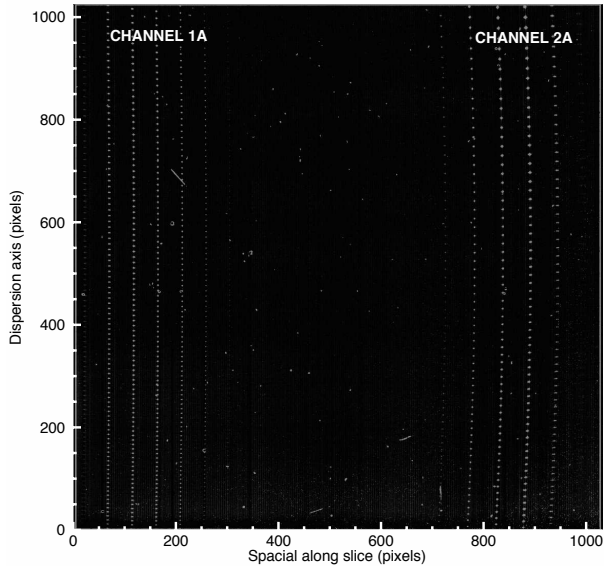


Figure 6.6 The slope image of the etalon 1A spectrum of a point source, as registered in the SW detector for sub-bands 1A (left half of the detector) and 2A (right half of the detector).

was performed in the bin space of the dispersion axis of the cube (λ), and not in wavelength space derived from the optical models, since those are precisely the wavelengths that we intend to derive and correct. By working on the bin space, we made no assumptions about the wavelengths. The fits provide a measure of the centroid of each line and their full width at half maxima (FWHM). Both quantities are measured in units of the cube bin.

The Gaussian fits provide an accurate measurement of the etalon line centroids in the cube space. Using the transformation described in §5.4.1 for the cube reconstruction, we can locate those centroids also in the detector space. With the signal to noise achieved, the accuracy in the line centroids is of the order of 2% of the resolution element for each sub-band. The wavelengths of the peaks are known to an accuracy of a few Angstroms from a previous high resolution measurement of the etalon transmission (see §6.3.2 for a discussion on the associated errors). These high resolution measurements were carried out using a IR spectrometer at the Rutherford Appleton Laboratory, at temperatures of $\sim 77 K$ (cryogenic) and $\sim 77 K$ (room), to study the centroid variations with temperature.

With the information of the line centroids and a set of relative reference wavelengths from the high resolution measurements, we only need an absolute wavelength reference in order to associate each centroid with its actual wavelength. This will be the base of a

6 The spectral properties of JWST-MIRI: calibration of the Flight Model

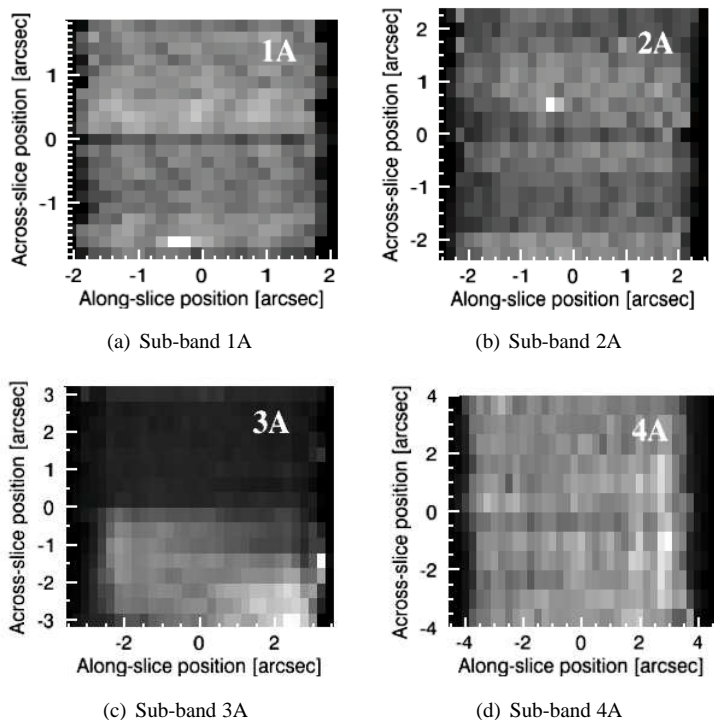


Figure 6.7 Single wavelength layers of the reconstructed images for the four MRS channels, with the gratings in 'A' configuration (short wavelengths). The pixel scale has been modified in each case to match the spatial dimensions.

dispersion relation between cube bins and wavelengths.

Absolute wavelength references

Building up on the experience from VM testing, we used the two wave-pass filters to obtain an absolute reference wavelength for those sub-bands where their cutoff wavelengths are registered. For FM testing, the much better quality of the detectors, as well as the possibility of longer integrations with the extended source resulted in a better measurement of the LWP filters response. Also, since the long-wavelength detector for channels 3 and 4 is now available, we can also measure the response of the SWP filter.

The transmission curve of both filters has been characterised prior to the test campaign at room temperature (295 K) and at a cryogenic temperature of 77 K. At this cryogenic temperature, the LWP filter has a cutoff wavelength near $6.6 \mu\text{m}$ (sub-band 1C), while the SWP has a cutoff wavelength near $21.5 \mu\text{m}$ (sub-band 4B). According to the telemetry data obtained during the test, the operating temperature of the LWP and SWP filters is

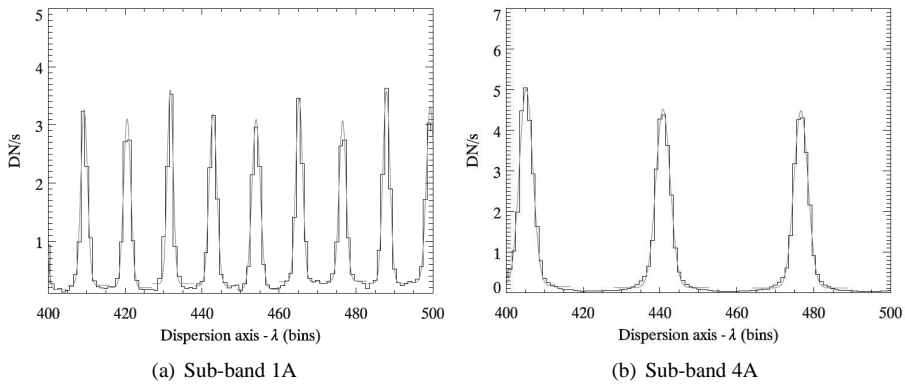


Figure 6.8 Gaussian fits to the etalon lines for two of the sub-bands. The black lines is the MRS spectrum, and the lighter grey lines are the Gaussian fits.

about 34 K. A simple extrapolation from the transmission curves at room and cryogenic temperatures allowed us to conclude that the shift in the cutoff wavelength from a further decrease in temperature (to the operational 34 K) is less than the relative separation between etalon lines. This is important, since it means that we rely on the much better accuracy of the centroid positions rather than the accuracy on the cutoff wavelength.

We obtained a measured transmission curve from the extracted spectra of the wave-pass filters and the blackbody continuum taken during the campaign. A comparison with the calibrated curves provided the absolute reference we were aiming for. The measured spectra of the LWP and SWP filters is the product of the actual filter response and the BB continuum, and hence we divide the measured spectra by the measured BB continuum. We correlate the resulting response curve with the reference transmission curve for each spatial position (α, β) in the FOVs of sub-bands 1C and 4B and in this way we obtain an absolute reference wavelength in the center of the cutoff slope. Fig. 6.9 shows the resulting correlations for a particular spatial coordinate.

For those sub-bands where no wave-pass filter is available as an absolute reference, we used a different approach to calibrate the wavelengths. The transmission of the etalon filters is optimized for but not limited to one MRS channel. That implies that for a given sub-band, etalon lines from more than one etalon filter are detected in different exposures. Therefore, for most of the sub-bands, we measure etalon lines from different etalons, that overlap with each other. The performance test was designed so that these overlapping etalon lines were detected with a S/N of at least 50. The resulting overlapping or beating pattern of the etalon lines for each sub-band is used as an absolute reference for wavelength. We use these overlaps for all remaining sub-bands.

For sub-band 4C the situation is more tricky. FM testing has revealed that the throughput for this sub-band is not optimal, and the etalon lines we detect in 4C have low S/N ratio, specially in the long wavelength end. Also, we have only detected lines from etalon 2B in this sub-band, and hence no overlap pattern was observed. We then looked for spec-

6 The spectral properties of JWST-MIRI: calibration of the Flight Model

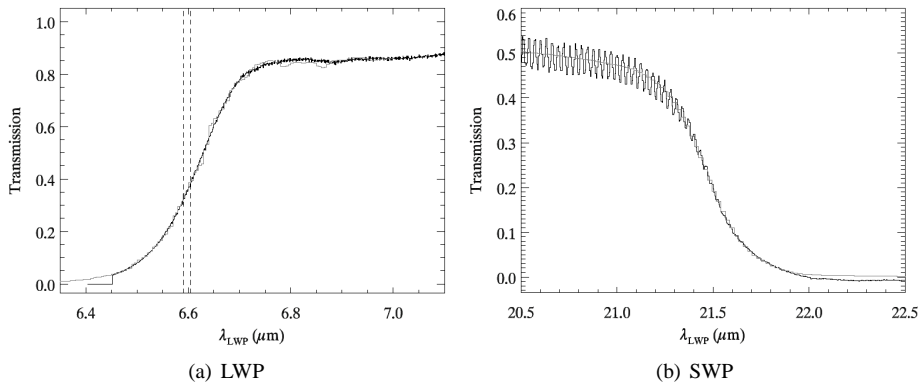


Figure 6.9 The measured transmission curves of the LWP (a) and SWP (b) filters (black lines) correlated with the reference curves (lighter grey lines). The effect of fringing is more pronounced in sub-band 4B, where the SWP cutoff falls. The dashed lines indicate the separation between two adjacent etalon lines.

tral features that could serve as wavelength references. There is a broad absorption feature near the long wavelength end of this sub-band. While this feature remains unidentified, the fringe analysis showed that the feature is internal to MIRI. If we use the wavelengths predicted by the Zemax model, this feature can be associated to a wavelength of $27.8 \mu\text{m}$ as shown in Fig. 6.10. We use this feature as our “absolute” reference, but we are aware that it is model-dependent. While this might lead to an incorrect absolute calibration, it allows for a relative calibration of this sub-band.

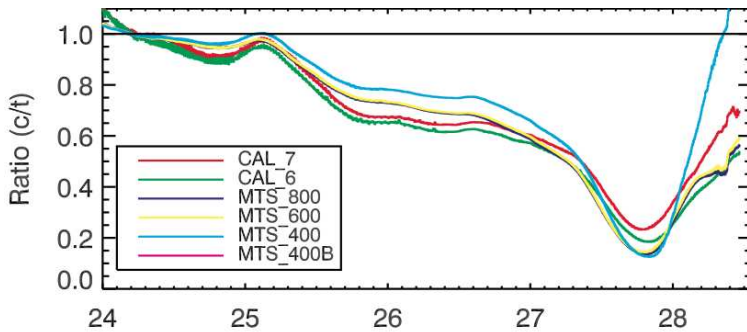


Figure 6.10 The broad absorption feature seen in sub-band 4C at approximately $28.7 \mu\text{m}$, for the calibration source and the continuum of the MTS blackbody at different temperatures. The x axis is the Zemax wavelength (in μm). We use this feature as a wavelength reference for sub-band 4C.

Dispersion relation and unresolved line widths

We have fitted a second order polynomial to the resulting array of cube bins vs. wavelength for each (α, β) position in the field of view for each of the sub-bands. Deviation of the data with respect to polynomials of higher orders would be smaller than the required precision for this measurement. In Fig. 6.11 we show the dispersion relation as derived in this way for a particular FOV position in 2 of the sub-bands. Along the y axis, instead of the absolute wavelength, we have plotted the difference between the derived wavelengths and the Zemax wavelengths, in units of the resolution element for each sub-band. The dispersion slightly deviates from linear relations.

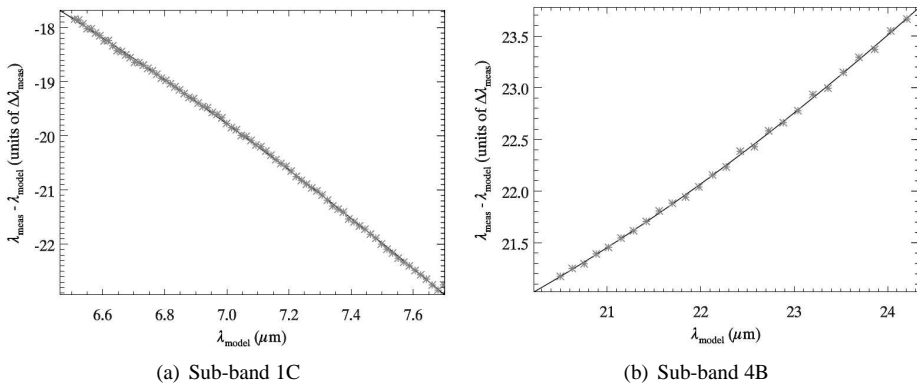


Figure 6.11 The difference between the modelled and measured spectrograph dispersion, as a function of the Zemax wavelengths. The asterisks mark the measured centroids of the etalon lines, and the solid black line is the polynomial fit.

We used the same approach as in VM testing to estimate the resolving power. The FWHM of the unresolved etalon lines is a good estimate of the size of the resolution element at the particular wavelengths of the line centroids. From the Gaussian σ parameter (the Gaussian width) in our fits, we obtained the FWHM in units of cube bins using:

$$\text{FWHM} = \Delta\lambda = 2 \sqrt{2 \ln 2} \sigma \quad (6.1)$$

Using the derivative of the polynomial dispersion relation that we have fitted, we converted the FWHM to microns, and then we calculated $R = \lambda/\Delta\lambda$ for the full MRS range and for the totality of the field of view.

The conversion from the measured FWHMs in units of cube bins into equivalent FWHMs in detector pixels is not straightforward, because the cube spectral bin size is constant in wavelength and the size of the binning corresponds approximately to the detector pixel size at the shortest wavelength of each sub-channel. That means that, for a particular sub-band, a wavelength bin projected onto the detector has approximately the same size as a detector pixel only at the short wavelength end. At the long wavelength

end, its size is smaller than the detector pixel by approximately 20%. The reason for this change has to do with the binning method used for the cube reconstruction.

To assess the impact of this effect, we adopted two different approaches to calculate the FWHMs of the unresolved lines in pixels. In the first approach, we assumed a linear conversion between cube bins and detector pixels, simply by multiplying the measured FWHMs in cube bins by $N_{\text{bin}}/N_{\text{pix}}$, the ratio between total cube bins for the respective cube and the total number of detector pixels in the array in the wavelength dimension. This will slightly overestimate the size of the pixels in the long-wavelength end of each sub-band. In the second approach, we assumed a uniform decrease in the size of the pixel relative to the bin as we move towards longer wavelengths, in such a way that at the wavelength of the first (shortest wavelength) etalon line, the pixel is 95% the size of the bin, while at the position of the last (longest wavelength) etalon line, the pixel is 85% the size of the bin.

6.3.2 Uncertainties

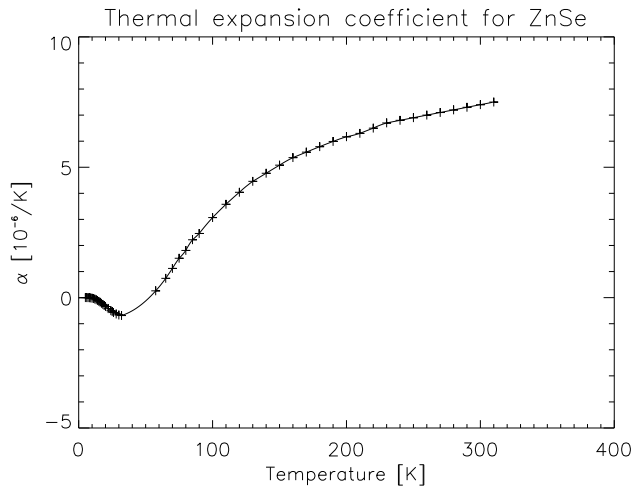
Absolute and relative centroids of the etalon peaks

There are several sources of uncertainty involved in the determination of the dispersion relation as described in the previous section. Here we evaluate their impact on our results.

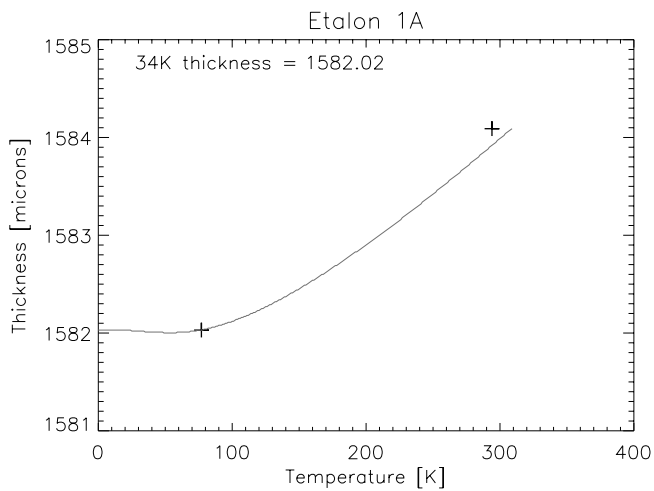
The first source of error comes from the uncertainty in the reference etalon peak positions, measured at high resolution before the testing. The positions of the peaks were measured at a resolution of $R \sim 10^5$ before testing at RAL at two different temperatures: room temperature (~ 295 K) and at a cryogenic temperature (~ 77 K). However, as revealed by the telemetry data acquired during testing, the operational temperature of the etalon filters is close to 34 K during the whole campaign. The etalon thickness and hence the positions of the etalon lines changes with temperature, due to the thermal properties of the material of which the etalons are made (ZnSe for etalons 1A, 1B and 2A and CdTe for etalon 2B). In order to estimate the shift in position of the line centroids from the measured 77 K to the 34 K operational temperature, we have extrapolated the etalon thickness at 34 K by using available literature data on the thermal expansion coefficient (α_{thermal}) of the mentioned materials (Browder & Ballard 1969, 1972, Smith & White 1975). In order to perform the extrapolation, we used the thicknesses at 295 K and 77 K, as derived from the etalon equation that gives the separation between peaks:

$$\Delta\lambda = \frac{\lambda_0^2}{2nl \cos(\eta)} \quad (6.2)$$

where n is the refractive index of vacuum ($n = 1$), l is the etalon thickness and η is the incidence angle of the light on the etalon filter (we assume $\eta = 0$). Fig. 6.12(a) shows the literature data used for the thermal expansion coefficient of ZnS, and Fig 6.12(b) shows the resulting extrapolation of the etalon thickness. We conclude that the shift in wavelengths of the peaks from 77 K to 34 K is negligible for the purposes of our analysis: a fraction of 2-4% of the resolution element for all sub-bands.



(a) Thermal expansion coefficient



(b) Etalon thickness

Figure 6.12 (a) The thermal expansion coefficient (α_{thermal}) for ZnSe, from the literature (Browder & Ballard 1969, 1972, Smith & White 1975). (b) The extrapolated value of the etalon thickness for $T < 77$ K.

The combined effect of this wavelength shift with the uncertainty introduced by fitting the etalon lines with Gaussian profiles is still $< 1\%$ of the resolution element. Although

6 The spectral properties of JWST-MIRI: calibration of the Flight Model

we have not done a similar analysis for the position of the cutoff wavelengths of the LWP and SWP filters, we do not expect a major change in their position at 34 K. Nevertheless, the accuracy needed for the cutoff wavelengths is set by the separation between neighbouring etalon lines, which is much larger than any shift due to temperature effects.

Another source of error for the wavelength calibration comes from the deviations of the measured line centroids with respect to the derived second-order polynomial dispersion relation. We have measured the standard deviation of the shift between the measured line positions and the value of the derived dispersion relation across the wavelength range, for all FOV positions in each sub-band. We then construct an histogram with the values of the measured absolute shifts, in units of microns. Fig. 6.13 shows the resulting histograms for two of the sub-bands.

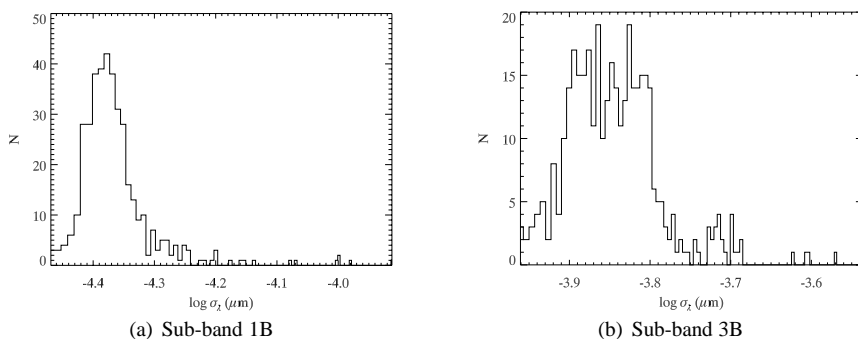


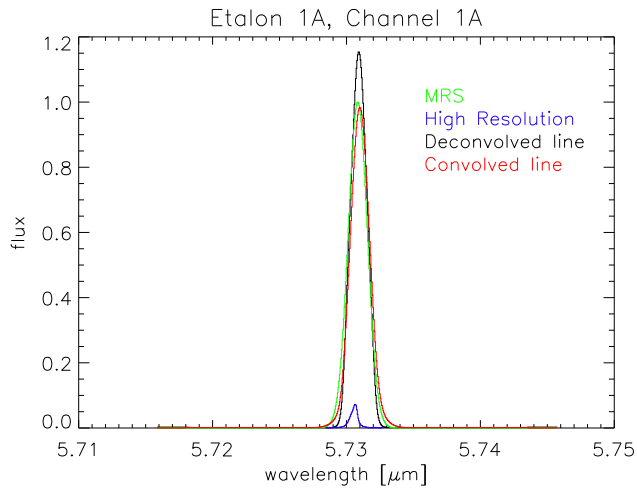
Figure 6.13 Observed standard deviations from a second-order dispersion relation across the FOV for sub-bands 1B (a) and 3B (b).

The figures imply that, on average, the deviation between the centroid positions and the derived dispersion relation is of the order of 1 \AA , or about 2% of the resolution element for all sub-bands. This is the dominant error in our analysis, and it is at least one order of magnitude larger than the errors derived from Gaussian fitting of the lines and temperature variations. We thus consider that we know the wavelengths of the derived data cubes with uncertainties of 0.02 times the spectral resolution element.

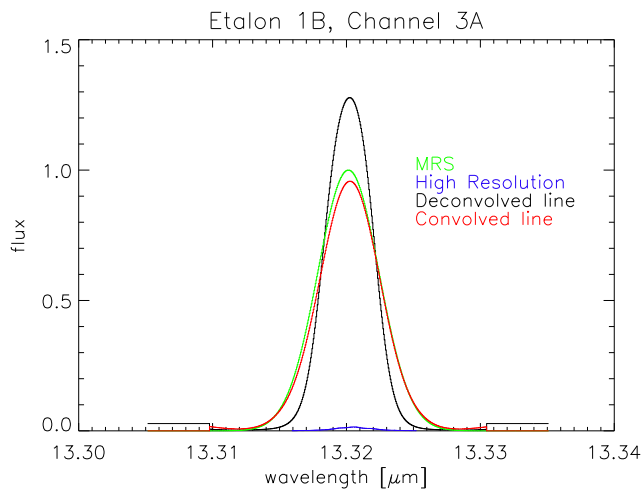
An additional source of error is the fringing pattern associated with multiple reflections within the detector. As we have stated, we did not correct for fringing for the dataset in study. Although we were not able to quantify it for all channels, a comparison between the measured line positions before and after fringe correction for channel 1 revealed that applying such correction does not change the line centroids by more than our 2% of the resolution element, and hence our uncertainties are still dominated by the polynomial fit.

Resolving power

The observed etalon line profiles are the convolution of the intrinsic line shape and the spectral response of the MRS. The resolving power calculated here using only the FWHM



(a) Sub-band 1A



(b) Sub-band 3A

Figure 6.14 Deconvolution of the observed etalon lines (green) with the intrinsic line profile obtained from the high resolution observations (blue), for sub-bands 1A (a) and 3A (b). The result is the instrument spectral response (black), which we have convolved again with the intrinsic profile to check the deconvolution. The recovered profile is shown in red.

of the unresolved etalon lines is thus jeopardized by the effect of the intrinsic line profiles. In order to estimate the errors introduced by this effect on the calculation of the resolv-

ing power, R , we have deconvolved the observed line shapes with the intrinsic shape of the lines, that we obtain from the high resolution measurements of the etalon transmission performed at RAL prior to testing. For this purpose, we used the IDL procedure `max_entropy`, which deconvolves the two profiles using the maximum entropy method. Fig. 6.14 shows the result of the deconvolution for two of the MRS channels.

The profile of the instrument spectral response, as obtained from the deconvolution, is narrower than the observed unresolved profile. This implies that the resolution calculated from the FWHM is an underestimate. We studied the effect of the deconvolution on the line widths across the full wavelength range of the MRS, using the method described. We conclude that the enhancement in resolving power resulting from the correction for the intrinsic line shape is between 10% and 20%. For a given sub-band, there is a smooth increase in this enhancement with wavelength. Also, the enhancement is larger in the long wavelength channels, where the intrinsic widths of the lines start to be comparable with the resolving power of the instrument.

6.4 Results and discussion

6.4.1 The resolving power of the MRS

In Table 6.2 we list the wavelength ranges and resolving powers that we have calculated for each of the MRS sub-bands using the methods described above. For each sub-band, we list a nominal value for the resolving power, R , corresponding to its measured value at the center of each band. We also list the size of the resolution element for each band, in detector pixels, using the two methods that we have described at the end of §6.3.1. In both methods, the uncertainties are dominated by the variation of the line width with wavelength. The second method overestimates the pixel size in the longer wavelength sub-bands, where the spectral bins are smaller. Table 6.2 also shows the approximate sizes (in detector pixels) of the overlapping regions between the corresponding sub-band and the following sub-band.

A crucial aspect of the MRS performance has to do with the sampling of unresolved spectral features. Zemax models predicted an undersampling of the unresolved etalon lines for channel 1, below the Nyquist frequency. More specifically, modelling has shown that the FWHM of an unresolved spectral line, as provided by the optical system, is sampled by less than the two required detector pixels. In the modelling, this applies to most sub-spectra. For channels 1, 2 and 3 spectral lines are predicted to have a FWHM of about 0.9 pixels for point sources, and 1.4 pixels for extended sources. Table 6.2 indicates that the lines are well sampled with at least the 2 pixels, with the exception of sub-band 1A, where the resolution element is slightly smaller than 2 pixels.

Overlapping regions of 100 pixels or larger are desirable for an optical matching of the different sub-bands during the science extraction of the spectra. Table 6.2 shows that this is the case for most of the overlapping regions, with some exceptions (sub-bands 1C, 3B, 3C), where the overlapping region is smaller. Nevertheless, the full wavelength range from 4.9 μm to 28.4 μm is fully covered and well sampled.

Sub-band	λ_{\min} [μm]	λ_{\max} [μm]	R	$\Delta\lambda_1$ [px]	$\Delta\lambda_2$ [px]	Overlap [px]
1A	4.91	5.79	3200	1.9(0.2)	1.9(0.2)	180
1B	5.60	6.62	3200	2.0(0.2)	2.0(0.2)	150
1C	6.46	7.63	3100	2.0(0.2)	2.0(0.2)	80
2A	7.55	8.91	2800	2.2(0.2)	2.2(0.2)	140
2B	8.71	10.34	2700	2.2(0.2)	2.2(0.1)	275
2C	9.89	11.71	2750	2.2(0.2)	2.3(0.2)	105
3A	11.50	13.59	2500	2.4(0.2)	2.5(0.2)	170
3B	13.19	15.58	2000	3.1(0.3)	3.4(0.4)	65
3C	15.40	18.14	2200	3.0(0.3)	3.0(0.3)	70
4A	17.88	21.34	1500	3.3(0.3)	3.7(0.3)	170
4B	20.69	24.68	1600	3.6(0.3)	4.3(0.1)	165
4C	23.83	28.43	1400	4.1(0.1)	7.2(1.1)	-

Table 6.2 The spectral properties of the MRS sub-bands. Uncertainties are indicated in parenthesis.

Fig. 6.15 shows the measured resolving power for the full wavelength range. The calibrated wavelengths are shown on the x axis, and the resolving power on the y axis. We plot these values for all the positions within the FOV. The thick black areas are the pile-up of individual black solid lines corresponding to $R(\lambda)$ calculated at different spatial (α, β) coordinates in the FOV. They give an indication of the variations of the resolving power with position on the IFU. The solid red lines are the spatially averaged values of R .

The instrumental requirement for resolving power states that MIRI shall provide integral field spectroscopy with spectral resolving power $R > 2400$ between $5 \mu\text{m}$ and $10 \mu\text{m}$, $R > 1600$ from $10 \mu\text{m}$ through $15 \mu\text{m}$ and $R > 800$ from $15 \mu\text{m}$ through $27 \mu\text{m}$. Our results indicate that we are well above these requirements.

6.4.2 Variations of R with wavelength and position in the field

In general, for a particular sub-band the resolving power increases with wavelength. There is a dispersion in the measured value of R from the widths of individual unresolved lines of the order of 10%. Noise in the data and the effect of fringing can be responsible for this dispersion. Nevertheless, we can estimate the resolving power for an extended source with 10% uncertainty. Although lines at channel 4 are detected with less S/N, they are sampled by more pixels in the detector, and hence the dispersion in the line-to-line width does not increase dramatically.

We now investigate the variation in the resolving power with the position of the point source in the field. More specifically, we want to study how R changes as we move the point source across a spatial slice in the cube, and also from slice to slice. For this we use

6 The spectral properties of JWST-MIRI: calibration of the Flight Model

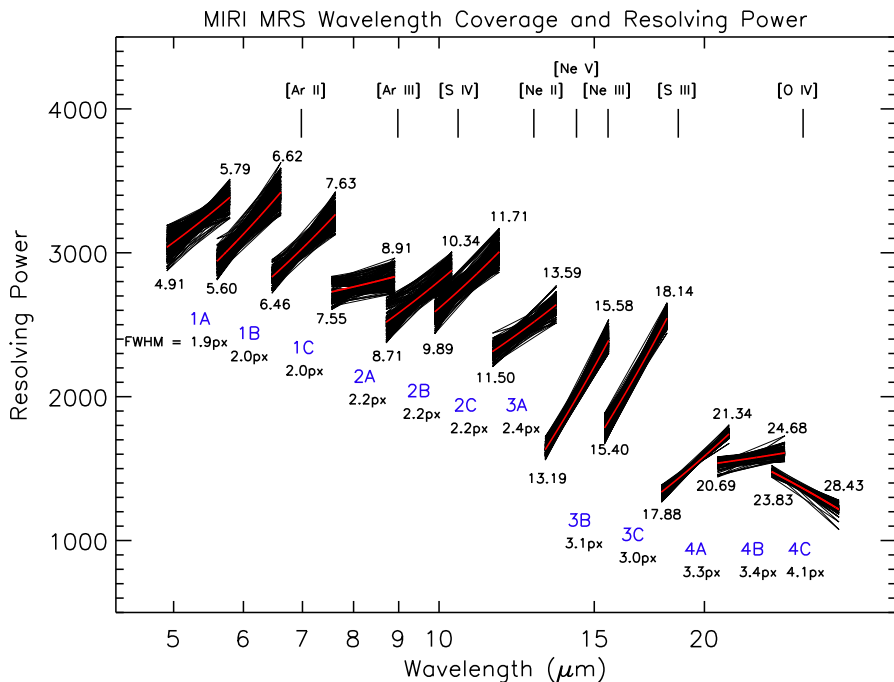


Figure 6.15 The Resolving Power of the MRS. The wavelength ranges for each sub-band are indicated. Red lines correspond to the spatially averaged values of R . Some relevant mid-IR nebular lines are indicated.

the point source observations that we have described in §6.2.2. In Fig. 6.16 we show the reconstructed image of the point source for one of the positions shown in Fig. 6.2, for two of the sub-bands: 1A and 4A. Unfortunately, the PSF of the 100 μm pinhole point source has some structure and does not allow for a detailed study of the PSF size as a function of wavelength. However, our purpose here is not the characterisation of the PSF, but the study of spatial variations of R .

Using the same method as with the extended source, we have measured the spectral resolving power as a function of position of the source. Fig. 6.17 shows the linear fit to the line widths for the three grating positions of channel 1, as the point source moves across the slice for the two different field positions shown in Fig. 6.2. Variations in resolving power when the point source moves across the slice are of the order of 1% and are within the error bars of the individual line widths. On the other hand, variations associated with placing the point source in different slices are of the order of 5% as seen in the Fig. 6.17. In sub-band 1A, the resolving power difference is larger for shorter wavelengths, while for the other sub-bands, the differences remains about the same for the sub-band range. Although close-by in the MRS FOV, the two fields are far apart in the detector space,

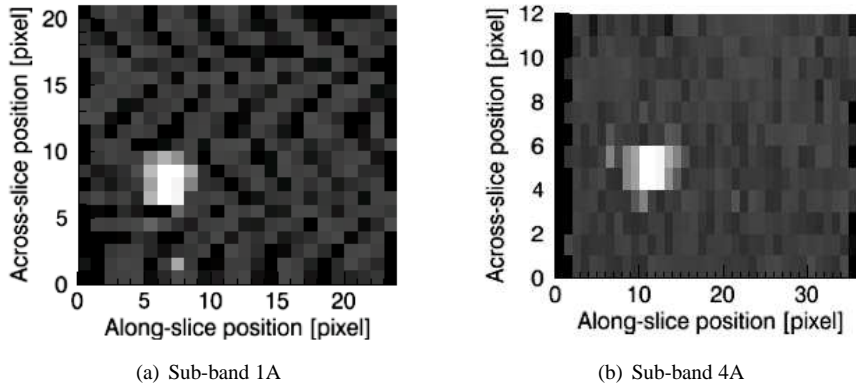


Figure 6.16 The reconstructed point source at a specific wavelength for sub-bands 1A (*a*) and 4A (*b*), for a particular position of the raster scan.

and hence the variations seen in Fig. 6.17 should give us a good estimate of the spectral resolution variations across the full FOV.

6.4.3 Line shape and spectral ghosts

We used the extended source observations to look for spectral ghosts in the spectra and to study the profile shape of the measured etalon lines. To accurately measure the average line shapes across the wavelength range of each sub-band, we shifted all lines in a given sub-spectrum using the Gaussian parameters, so that they all share the same centroid and baseline, in a similar way as we did in §5.4.4 with VM data. We have previously dubbed this method “superresolution”. For the FM data, the wavelength range used to perform the superresolution extraction equals about twice the separation between etalon lines, centered on the common line centroid for each sub-band.

Fig. 6.18 shows the superresolution data for all sub-bands. We do not detect any unexpected spectral features along the spectra, apart from the almost perfectly Gaussian profile of the etalon lines. We have performed the same procedure for several random positions in the FOV with similar results. Any spectral ghost arising in the gratings is below the rms noise of the resulting superresolution etalon line, which varies between 0.5% and 1.5% of the line peak. The plots of Fig. 6.18 also show that the line shape is very symmetric for all sub-bands, only deviating slightly from a perfect Gaussian in the wings, specially for the longer wavelength sub-bands.

6.4.4 Wavelength stability

We investigated the temporal wavelength stability of the MRS by looking for variations in time of either the etalon line centroids, or the Fabry-Perot fringing pattern over periods

6 The spectral properties of JWST-MIRI: calibration of the Flight Model

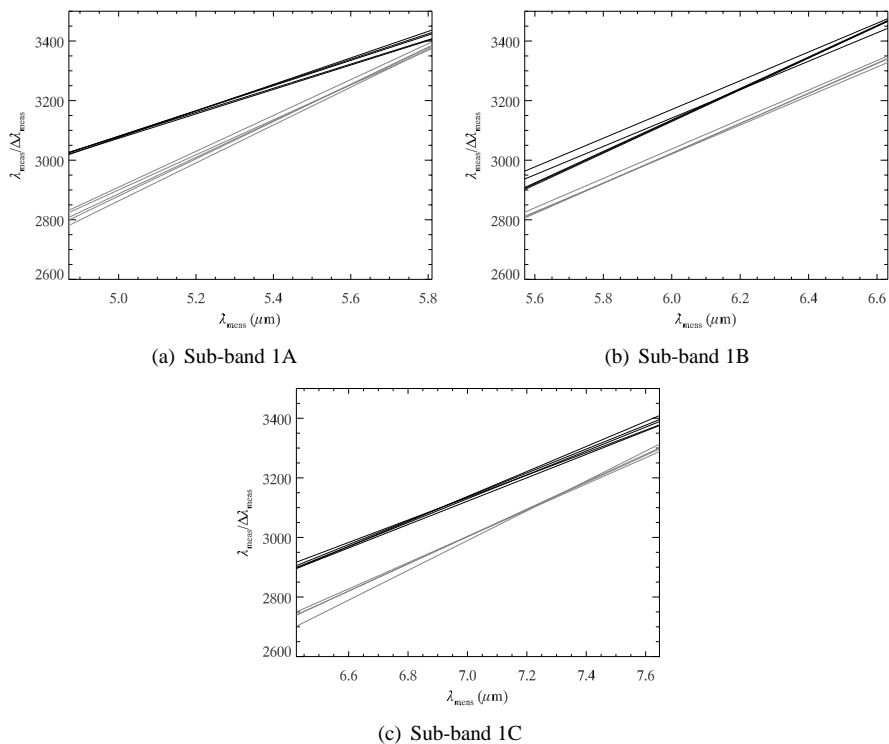


Figure 6.17 The variations in resolving power in sub-bands 1A (a), 1B (b) and 1C (c). Lines of the same color indicate the same field, or position in the FOV, as indicated in Fig. 6.2. Field 1 is in black, while Field 2 is in grey.

of time of several weeks. The science goals of MIRI require a temporal wavelength stability better than 2% of the size of the resolution element. To verify if we are within the requirements, we used the extended source etalon exposures that we have obtained at different epochs of the test campaign, as described in §6.2.2, as well as fully illuminated BB exposures, with the fringe pattern.

Time variations in wavelength

Fig. 6.19 shows the difference in sub-band 1B etalon line positions for the different epochs, with respect to the reference epoch, May 19. The result indicates that the overall shift in the etalon line positions from epoch to epoch is larger than the overall line-to-line spread. The differences are in general larger than the instrument requirement, 2% of the resolution element. In fact, for June 21 and July 10 the shift with respect to the reference positions reach about ~ 8% of the resolution element size. Some additional facts help our interpretation of this result.

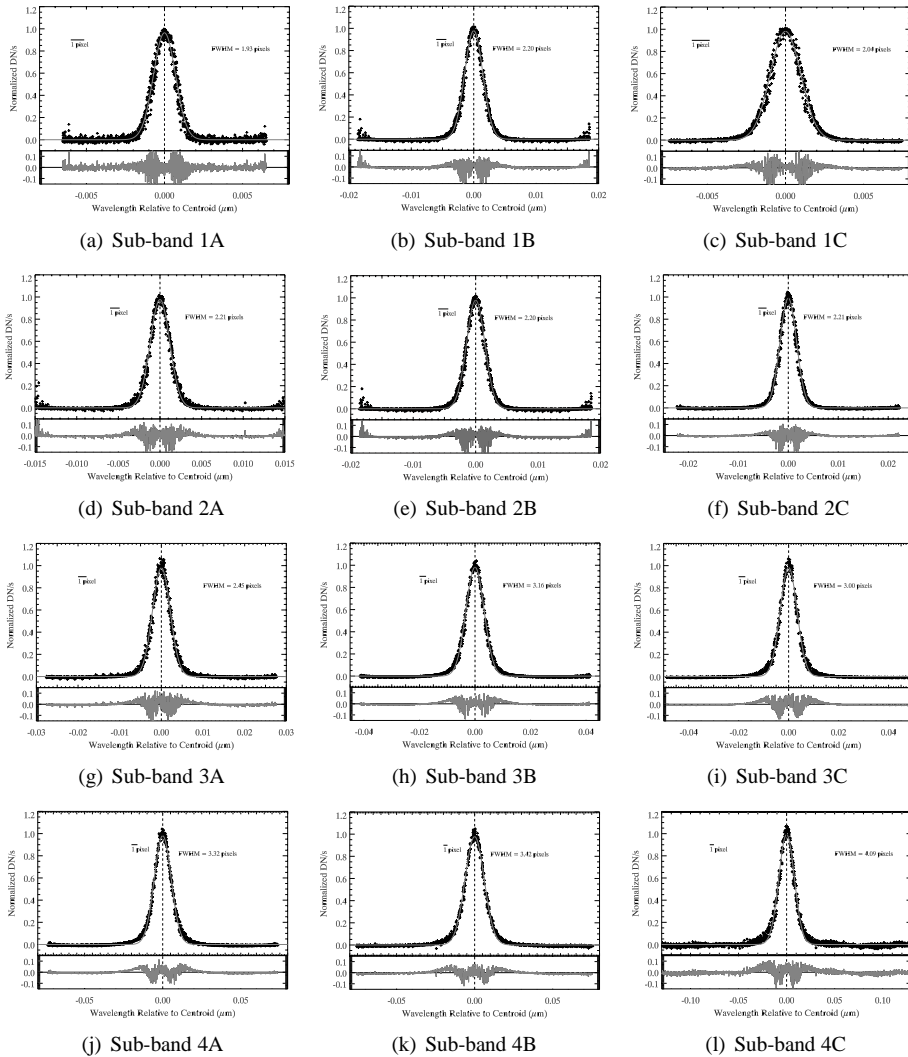


Figure 6.18 Spectral line shapes. The etalon lines in a particular field position shifted to have a common centroid. The grey line is a Gaussian fit to the resulting data. Residuals of the Gaussian fit are shown in the individual lower panels and the pixel size and FWHM of the line are indicated.

Two thermal cycles of the instrument took place between the observation epochs, on May 19 and June 21. We can not rule out that the observed shifts are the result of changes in the external conditions between these thermal cycles, rather than limitations on the stability of the spectrometer optics. Between June 21 and July 10 there were no power

6 The spectral properties of JWST-MIRI: calibration of the Flight Model

or thermal cycles of the instrument and at least one of the two exposures taken on June 21 shows differences in line positions that are within the required 2% of the resolution element. According to our results, the most dramatic shift in position within a single thermal cycle is related to the reconfiguration of the grating wheel mechanism. This shift is of about 5% of the resolution element as illustrated by the light grey and dark grey diamonds in Fig. 6.19.

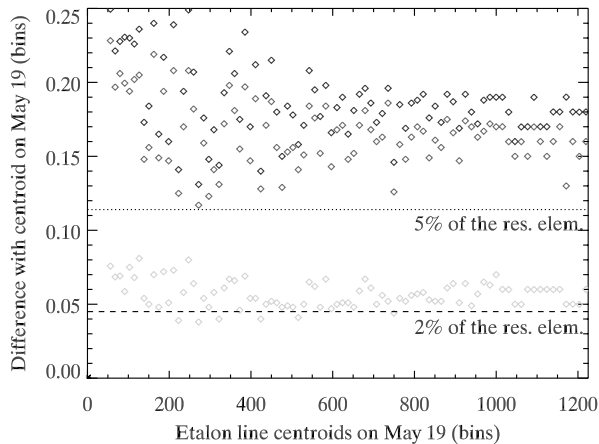


Figure 6.19 Shifts in the measured sub-band 1B line centroids with respect to the centroids on the reference epoch, May 19, in units of cube bins. Dark grey diamonds are for June 21, light gray diamonds for the same date after reconfiguring the grating mechanism and black diamonds are for July 10. The dashed line corresponds to a difference with the reference epoch of 2% of the resolution element, while the dotted line corresponds to 5% of the resolution element.

Variations with field position

Fig. 6.20 shows the variation of the shift in centroid positions for sub-band 1B, as a function of time and field position. The data points correspond to the mean value of the shift across the entire wavelength range of sub-band 1B, for three different field positions, corresponding approximately to the center of the FOV and two diagonal corners. The temporal variations in the position of the centroids is practically the same for all three field positions. This suggests that the shift is uniform across the entire field of view. The change in position for the lines measured after reconfiguration of the grating wheel on June 21 is of about 5% of the resolution element.

In particular, the shift in the etalon positions after the grating wheel mechanism is reconfigured is approximately the same across the field of view. During the period of time between the two exposures on June 21, temperature variations of the etalons did not

exceed 0.1 K, according to telemetry data. This is far too small to cause any noticeable changes in the peak positions. As a reference, our thermal models of the etalons indicate that a change of temperature in 1 K would only produce a change of 0.9% of the resolution element in the line positions.

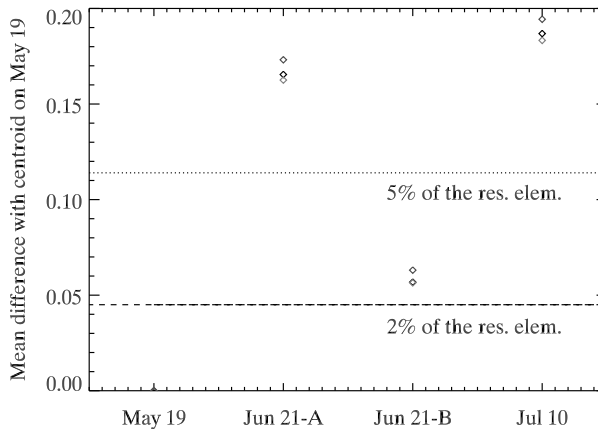


Figure 6.20 Mean shift in the line centroid positions as a function of epoch and field position. Data points correspond to the center of the FOV (black diamonds), the bottom left corner (light grey diamonds) and upper right corner (dark grey diamonds).

Variations with grating wheel configuration

If the shift in line centroids is due to mechanical reproducibility in the grating wheel, we expect a random behavior in the line shifts from sub-band to sub-band, rather than a similar behavior for all sub-bands. The reason is that the latter situation would indicate a variation on the conditions from epoch to epoch, rather than the random mechanical variations in position of the gratings after several reconfigurations.

We have used data taken for all three grating wheel positions in channel 1 to study the sub-band to sub-band variations. Additionally, we have measured the positions of the lines for the four epochs in sub-band 2A. For channel 3B, we have data available on May 19 and July 12. Fig. 6.21 shows the mean variations with respect to May 19 for the sub-bands for which we have data. The mean centroid positions were measured at a particular location in the field of view, namely the FOV center. There is no evidence of a uniform or monotone increase in the position differences with epoch. Instead, the behavior appears random from sub-band to sub-band, which favors mechanical reproducibility as the reason for the shifts.

We should expect shifts in the position of the spectra associated with hardware differences between the optics of the various gratings. However, we would not expect to

6 The spectral properties of JWST-MIRI: calibration of the Flight Model

measure a shift between two spectra obtained with the same grating, after a reconfiguration has been performed. Unless, of course, these shifts are due to mechanical reproducibility. Our measurements made on June 21 indicate that, for all measured sub-bands, reconfiguration of the wheel introduced noticeable shifts, the smallest one being for sub-band 2A, close to 2% of the resolution element. Once again, this points to mechanical reproducibility as the source of the shifts.

The relative grating-to-grating tolerances of the as-designed grating hardware when all degrees of freedom are considered (translation along the z axis and rotation about all three spatial axes) have error budgets that translate into shifts in position of spectral features of about 2.5 detector pixels. As we have mentioned, these errors are repeatable to accuracies beyond what we can measure and therefore, it is likely that differences between the positions of the lines after the grating wheel mechanism has been reconfigured are due to errors in the wheel mechanism itself.

Fringe stability

So far we have studied stability relying only on the etalon lines. However, we can not rule out that the shifts that we have measured are related to stability issues in the filters or conditions of the telescope simulator itself, rather than the MRS opto-mechanics. The Fabry-Perot fringe pattern formed due to multiple reflections within the detector substrate is independent of the MTS, and thus an ultimate diagnostic for wavelength stability. We have performed an analysis of the fringe stability to confirm if the shifts measured in the etalon line centroids are due to MIRI mechanical repeatability issues, or if they arise already in the MTS.

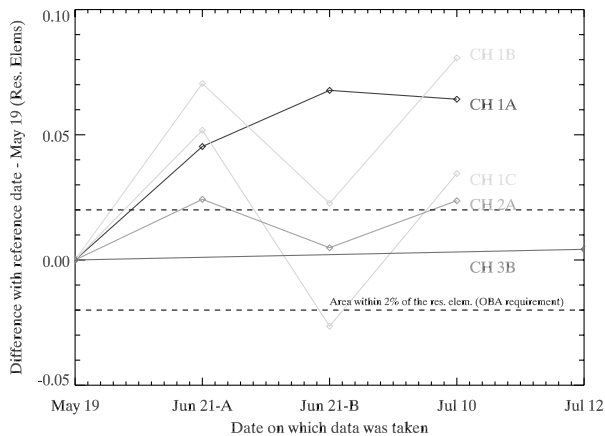


Figure 6.21 Mean shift in the line centroid positions as a function of epoch and grating wheel configuration. Data points correspond to the center of the FOV. The 2% of the resolution element requirement is shown as the two dashed lines.

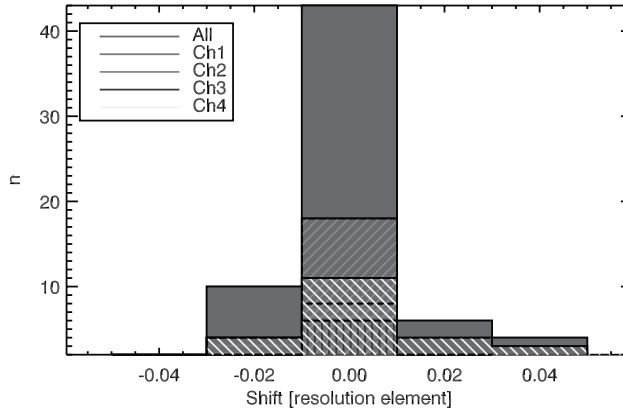


Figure 6.22 Distribution of relative shifts of the fitted fringe pattern at different epochs for all MRS channels.

We have studied the stability of the MRS over multiple epochs using fully illuminated blackbody observations. The analysis was done for a region of a particular detector slice (or a small area of the FOV), for all channels. We extract the fringe spectra at several epochs, and fit a model spectrum to each of them. We then determine relative spectral shifts from these fits using the IDL routine `CORREL_OPTIMIZE`, which finds the effective shifts (in pixels) between two arrays. Fig. 6.22 shows a distribution of the observed shifts in resolution elements (assuming a FWHM of 1.9, 2.2, 3 and 3.7 pixels for the respective MRS channels, from Table 6.2). The data show that the pixel shifts are in general less than 0.02 resolution elements), which implies compliance with the instrument requirement.

These results implies that the shifts observed in the etalon line centroids over different epochs, which are of the order of 5% of the resolution element, arise in the etalons themselves, and not in the MRS. If the shift was produced inside MIRI, then we would have observed a similar shift in the fringe pattern.

6.5 Summary

We have performed the wavelength calibration of the Flight Model Integral Field Spectrograph of the MIRI instrument, which will fly onboard the *James Webb Space Telescope* in 2018. We have described the data cube reconstruction from raw data, and used the synthetic unresolved etalon lines and wave-pass filters to calibrate the wavelength ranges and resolving powers for all 4 instrument channels. We have shown that the instrument complies with the instrumental requirements in resolving power and wavelength stability that are set by the MIRI science goals. Here is a summary of our main findings.

1. After ground data processing and application of the calibration data, we have measured the wavelengths of the MRS spectra within 2% of the size of the resolution

6 The spectral properties of JWST-MIRI: calibration of the Flight Model

element, using unresolved etalon lines that are measured with signal to noise ratios well above 100.

2. The shortest wavelength registered by the MRS is $4.91 \mu\text{m}$ and the maximum registered wavelength is $28.43 \mu\text{m}$. Within a tolerance of about 3 resolution elements, we are thus compliant of the instrumental requirement regarding wavelength coverage. Absolute calibration of sub-band 4C was made based on the Zemax model of the instrument.
3. Band overlaps between sub-bands span a range of at least 70 pixels. This allows for a smooth matching of the different sub-spectra to produce a final science result with continuous coverage of the full wavelength range.
4. The resolving power of the MRS between 5 and $10 \mu\text{m}$ is greater than 2400. From $15 \mu\text{m}$ to $28 \mu\text{m}$, the resolving power is always larger than 1200. If we account for the intrinsic shapes of the etalon lines, we see an increase in the resolving power of between 10% and 20% with respect to these values.
5. The spectral resolution element of the MRS is sampled by at least two detector pixels for the full range of the spectrometer, except for sub-band 1C, where the resolution element is 1.9 pixels wide.
6. Variations of the resolving power across an individual FOV slice are below the level of uncertainty introduced by the error in the statistical width of the etalon lines (about 1%), while changes of 5% in R are produced by moving the point source from slice to slice.
7. The MRS wavelengths are stable to a level below 2% the size of the resolution elements, both over long periods of time (~ 1 week) and after reconfiguring the grating wheel mechanism.

Bibliography

- Allen, L. E., et al. 2004, *ApJS*, 154, 363
- Alonso-Herrero, A., Rieke, G. H., Rieke, M. J., et al. 2006, *ApJ*, 650, 835
- Armus, L., Mazzarella, J. M., Evans, A. S., et al. 2009, *PASP*, 121, 559
- Asensio Ramos, A., & Ramos Almeida, C. 2009, *ApJ*, 696, 2075
- Banks, K., Larson, M., Aymergen, C., & Zhang, B. 2008, *Proc. SPIE*, 7017,
- Barbá, R. H., Maíz Apellániz, J., Pérez, E., et al. 2009, *Ap&SS*, 324, 309
- Beck, S. C., Turner, J. L., & Kloosterman, J. 2007, *AJ*, 134, 1237
- Beirão, P., Brandl, B. R., Devost, D., et al. 2006, *ApJ*, 643, L1
- Beirão, P., Appleton, P. N., Brandl, B. R., Seibert, M., Jarrett, T., & Houck, J. R. 2009, *ApJ*, 693, 1650
- Beirão, P., Armus, L., Appleton, P. N., et al. 2010, *A&A*, 518, L60
- Belenguer, T., Alcacera, M. A., Aricha, A., et al. 2008, *Proc. SPIE*, 7010,
- Bernard-Salas, J., et al. 2009, *ApJS*, 184, 230
- Bik, A., Puga, E., Waters, L. B. F. M., et al. 2010, *ApJ*, 713, 883
- Bonnell, I. A., Vine, S. G., & Bate, M. R. 2004, *MNRAS*, 349, 735
- Brandl, B. R., Devost, D., Higdon, S. J. U., et al. 2004, *ApJS*, 154, 188
- Brandl, B. R., et al. 2006, *ApJ*, 653, 1129
- Brandl, B. R., Sniijders, L., den Brok, M., et al. 2009, *ApJ*, 699, 1982
- Browder, J. S., & Ballard, S. 1969, *Appl. Opt.* 8, 793-798
- Browder, J. S., & Ballard, S. 1972, *Appl. Opt.* 11, 841-843
- Calzetti, D., Kennicutt, R. C., Jr., Bianchi, L., et al. 2005, *ApJ*, 633, 871
- Calzetti, D., Wu, S.-Y., Hong, S., et al. 2010, *ApJ*, 714, 1256
- Caputi, K. I., Lagache, G., Yan, L., et al. 2007, *ApJ*, 660, 97
- Cassinelli, J. P., & Swank, J. H. 1983, *ApJ*, 271, 681
- Castor, J., McCray, R., & Weaver, R. 1975, *ApJ*, 200, L107
- Charlot, S., & Bruzual, A. G. 1991, *ApJ*, 367, 126
- Chien, L.-H., Barnes, J. E., Kewley, L. J., & Chambers, K. C. 2007, *ApJ*, 660, L105
- Chini, R., Kruegel, E., & Kreysa, E. 1992, *A&A*, 266, 177
- Chu, Y.-H., & Kennicutt, R. C., Jr. 1994, *ApJ*, 425, 720

Bibliography

- Chu, Y.-H., & Mac Low, M.-M. 1990, *ApJ*, 365, 510
- Churchwell, E., & Goss, W. M. 1999, *ApJ*, 514, 188
- Crosthwaite, L. P., Turner, J. L., Hurt, R. L., et al. 2001, *AJ*, 122, 797
- Crowther, P. A., Schnurr, O., Hirschi, R., Yusof, N., Parker, R. J., Goodwin, S. P., & Kassim, H. A. 2010, *MNRAS*, 1103
- da Cunha, E., Charlot, S., & Elbaz, D. 2008, *MNRAS*, 388, 1595
- Decin, L., Morris, P. W., Appleton, P. N., Charmandaris, V., Armus, L., & Houck, J. R. 2004, *ApJS*, 154, 408
- Dickel, J. R., Milne, D. K., Kennicutt, R. C., Chu, Y.-H., & Schommer, R. A. 1994, *AJ*, 107, 1067
- Dole, H., Lagache, G., Puget, J.-L., et al. 2006, *A&A*, 451, 417
- Donahue, M., de Messières, G. E., O'Connell, R. W., Voit, G. M., Hoffer, A., McNamara, B. R., & Nulsen, P. E. J. 2011, *ApJ*, 732, 40
- Dopita, M. A., et al. 2005, *ApJ*, 619, 755
- Dopita, M. A., et al. 2006, *ApJ*, 639, 788
- Dopita, M. A., et al. 2006, *ApJ*, 647, 244
- Dopita, M. A., et al. 2006, *ApJS*, 167, 177
- Dors, O. L., Jr., Storchi-Bergmann, T., Riffel, R. A., & Schimdt, A. A. 2008, *A&A*, 482, 59
- Draine, B. T. 2003, *ARA&A*, 41, 241
- Draine, B. T., Dale, D. A., Bendo, G., et al. 2007, *ApJ*, 663, 866
- Draine, B. T. 2011, *EAS Publications Series*, 46, 29
- Drissen, L., Crowther, P. A., Úbeda, L., & Martin, P. 2008, *MNRAS*, 389, 1033
- Dudik, R. P., Weingartner, J. C., Satyapal, S., et al. 2007, *ApJ*, 664, 71
- Elbaz, D., & Cesarsky, C. J. 2003, *Science*, 300, 270
- Elbaz, D., Dickinson, M., Hwang, H. S., et al. 2011, *A&A*, 533, A119
- Eldridge, J. J., & Relaño, M. 2011, *MNRAS*, 411, 235
- Elfhag, T., Booth, R. S., Hoeglund, B., Johansson, L. E. B., & Sandqvist, A. 1996, *A&AS*, 115, 439
- Elmegreen, B. G., & Lada, C. J. 1977, *ApJ*, 214, 725
- Elmegreen, B. G. 2011, *EAS Publications Series*, 51, 45
- Fariña, C., Bosch, G. L., & Barbá, R. H. 2012, *AJ*, 143, 43
- Fazio, G. G., Hora, J. L., Allen, L. E., et al. 2004, *ApJS*, 154, 10
- Feast, M. W., & Catchpole, R. M. 1997, *MNRAS*, 286, L1
- Ferland, G. J., Korista, K. T., Verner, D. A., et al. 1998, *PASP*, 110, 761
- Fernández-Ontiveros, J. A., Prieto, M. A., & Acosta-Pulido, J. A. 2009, *MNRAS*, 392, L16
- Fischera, J., & Dopita, M. 2005, *ApJ*, 619, 340
- Freedman, W. L., Wilson, C. D., & Madore, B. F. 1991, *ApJ*, 372, 455
- Galliano, F., Madden, S. C., Jones, A. P., Wilson, C. D., Bernard, J.-P., & Le Peintre, F. 2003, *A&A*, 407, 159

- Galliano, F. 2004, Ph.D. Thesis,
- Gautier, T. N., III, Fink, U., Larson, H. P., & Treffers, R. R. 1976, *ApJ*, 207, L129
- Gerin, M., Combes, F., & Nakai, N. 1988, *A&A*, 203, 44
- Glauser, A. M., Glasse, A., Morrison, J. E., et al. 2010, *Proc. SPIE*, 7731,
- Gonzalez-Delgado, R. M., Perez, E., Diaz, A. I., et al. 1995, *ApJ*, 439, 604
- González Delgado, R. M., García-Vargas, M. L., Goldader, J., Leitherer, C., & Pasquali, A. 1999, *ApJ*, 513, 707
- González Delgado, R. M., & Pérez, E. 2000, *MNRAS*, 317, 64
- Gratton, R. G., Bragaglia, A., Clementini, G., Carretta, E., Di Fabrizio, L., Maio, M., & Taribello, E. 2004, *A&A*, 421, 937
- de Grijs, R., Lee, J. T., Mora Herrera, M. C., Fritze-v. Alvensleben, U., & Anders, P. 2003, *New A*, 8, 155
- Groves, B. 2004, "Dust in Photoionized Nebulae", Ph.D. Thesis, Australian National University, Australia
- Groves, B., Dopita, M. A., Sutherland, R. S., Kewley, L. J., Fischera, J., Leitherer, C., Brandl, B., & van Breugel, W. 2008, *ApJS*, 176, 438
- Groves, B., Nefs, B., & Brandl, B. 2008, *MNRAS*, 391, L113
- Groves, B. A., & Allen, M. G. 2010, *New Astronomy*, 15, 614
- Haan, S., Armus, L., Laine, S., et al. 2011, *ApJS*, 197, 27
- Haschke, R., Grebel, E. K., & Duffau, S. 2011, *AJ*, 141, 158
- Heckman, T. M. 2005, *Starbursts: From 30 Doradus to Lyman Break Galaxies*, 329, 3
- Heiner, J. S., Allen, R. J., & van der Kruit, P. C. 2009, *ApJ*, 700, 545
- Houck, J. R., et al. 2004, *ApJS*, 154, 18
- Hummel, E., van der Hulst, J. M., & Keel, W. C. 1987, *A&A*, 172, 32
- Hunter, D. A., Shaya, E. J., Scowen, P., Hester, J. J., Groth, E. J., Lynds, R., & O'Neil, E. J., Jr. 1995, *ApJ*, 444, 758
- Hunter, D. A., Baum, W. A., O'Neil, E. J., Jr., & Lynds, R. 1996, *ApJ*, 456, 174
- Indebetouw, R., et al. 2009, *ApJ*, 694, 84
- Israel, F. P., & Baas, F. 2003, *A&A*, 404, 495
- Israel, F. P., Wall, W. F., Raban, D., Reach, W. T., Bot, C., Oonk, J. B. R., Ysard, N., & Bernard, J. P. 2010, *A&A*, 519, A67
- Jonsson, P., Groves, B. A., & Cox, T. J. 2010, *MNRAS*, 403, 17
- Kaufman, M. J., Wolfire, M. G., Hollenbach, D. J., & Luhman, M. L. 1999, *ApJ*, 527, 795
- Kaufman, M. J., Wolfire, M. G., & Hollenbach, D. J. 2006, *ApJ*, 644, 283
- Kennicutt, R. C., Jr. 1984, *ApJ*, 287, 116
- Kennicutt, R. C., Jr. 1998, *ARA&A*, 36, 189
- Kennicutt, R. C., Jr., Armus, L., Bendo, G., et al. 2003, *PASP*, 115, 928
- Kilbinger, M., et al. 2010, *MNRAS*, 405, 2381
- Kim, H.-S., et al. 2007, *ApJ*, 669, 1003
- Kotilainen, J. K., Reunanen, J., Laine, S., & Ryder, S. D. 2000, *A&A*, 353, 834

Bibliography

- Kramer, C., Buchbender, C., Xilouris, E. M., et al. 2010, *A&A*, 518, L67
- Kroes, G., Oudenhuisen, A., de Haan, M., Jager, R., & Pauwels, E. 2010, *Proc. SPIE*, 7731,
- Kroupa, P. 2002, *Science*, 295, 82
- Krumholz, M. R., Matzner, C. D., & McKee, C. F. 2006, *ApJ*, 653, 36
- Lada, C. J., & Lada, E. A. 2003, *ARA&A*, 41, 57
- Lagache, G., Puget, J.-L., & Dole, H. 2005, *ARA&A*, 43, 727
- Lançon, A., Goldader, J. D., Leitherer, C., & González Delgado, R. M. 2001, *ApJ*, 552, 150
- Lawton, B., Gordon, K. D., Babler, B., et al. 2010, *ApJ*, 716, 453
- Lazendic, J. S., Dickel, J. R., & Jones, P. A. 2003, *ApJ*, 596, 287
- Lebouteiller, V., Bernard-Salas, J., Brandl, B., Whelan, D. G., Wu, Y., Charmandaris, V., Devost, D., & Houck, J. R. 2008, *ApJ*, 680, 398
- Lebouteiller, V., Bernard-Salas, J., Whelan, D. G., et al. 2011, *ApJ*, 728, 45
- Lebrón, M., Mangum, J. G., Mauersberger, R., et al. 2011, *A&A*, 534, A56
- Leitherer, C., et al. 1999, *ApJS*, 123, 3
- Levesque, E. M., Kewley, L. J., & Larson, K. L. 2010, *AJ*, 139, 712
- Maercker, M., & Burton, M. G. 2005, *A&A*, 438, 663
- Magrini, L., Vílchez, J. M., Mampaso, A., Corradi, R. L. M., & Leisy, P. 2007, *A&A*, 470, 865
- Maíz-Apellániz, J. 2001, *ApJ*, 563, 151
- Maíz-Apellániz, J., Pérez, E., & Mas-Hesse, J. M. 2004, *AJ*, 128, 1196
- Mak, D. S. Y., Pun, C. S. J., & Kong, A. K. H. 2011, *ApJ*, 728, 10
- Malhotra, S., et al. 2001, *ApJ*, 561, 766
- Maloney, P. R., Hollenbach, D. J., & Tielens, A. G. G. M. 1996, *ApJ*, 466, 561
- Maraston, C. 2005, *MNRAS*, 362, 799
- Marchesini, D., van Dokkum, P. G., Förster Schreiber, N. M., et al. 2009, *ApJ*, 701, 1765
- Martínez-Galarza, J. R., Groves, B., Brandl, B., et al. 2011, *ApJ*, 738, 176
- Mason, R. E., Levenson, N. A., Packham, C., et al. 2007, *ApJ*, 659, 241
- Mathis, J. S., Rumpl, W., & Nordsieck, K. H. 1977, *ApJ*, 217, 425
- Matsuoka, Y., Yuan, F.-T., Takeuchi, Y., & Yanagisawa, K. 2011, *arXiv:1111.4522*
- Meier, D. S., Turner, J. L., & Schinnerer, E. 2011, *AJ*, 142, 32
- Melnick, J. 1980, *A&A*, 86, 304
- Micelotta, E. R., Jones, A. P., & Tielens, A. G. G. M. 2010, *A&A*, 510, A37
- Mineo, S. 2011, Ph.D. Thesis,
- Miura, R., et al. 2010, *ApJ*, 724, 1120
- Morisset, C., Schaerer, D., Bouret, J.-C., & Martins, F. 2004, *A&A*, 415, 577
- Motte, F., Andre, P., & Neri, R. 1998, *A&A*, 336, 150
- Oey, M. S., & Clarke, C. J. 1997, *MNRAS*, 289, 570
- Peeters, E., Mattiotta, A. L., Hudgins, D. M., & Allamandola, L. J. 2004, *ApJ*, 617, L65
- Pellegrini, E. W., Baldwin, J. A., & Ferland, G. J. 2010, *ApJS*, 191, 160

- Pereira-Santaella, M., Alonso-Herrero, A., Rieke, G. H., et al. 2010, *ApJS*, 188, 447
- Petrosian, A. R., & Burenkov, A. N. 1993, *A&A*, 279, 21
- Phillips, M. M., Pagel, B. E. J., Edmunds, M. G., & Diaz, A. 1984, *MNRAS*, 210, 701
- Poglitsch, A., Waelkens, C., Geis, N., et al. 2010, *A&A*, 518, L2
- Quillen, A. C., Frogel, J. A., Kuchinski, L. E., & Terndrup, D. M. 1995, *AJ*, 110, 156
- Reach, W. T., Megeath, S. T., Cohen, M., et al. 2005, *PASP*, 117, 978
- Read, A. M. 2003, *MNRAS*, 342, 715
- Relaño, M., Lisenfeld, U., Pérez-González, P. G., Vílchez, J. M., & Battaner, E. 2007, *ApJ*, 667, L141
- Relaño, M., & Kennicutt, R. C. 2009, *ApJ*, 699, 1125
- Ressler, M. E., Cho, H., Lee, R. A. M., et al. 2008, *Proc. SPIE*, 7021,
- Rieke, G. H., Alonso-Herrero, A., Weiner, B. J., et al. 2009, *ApJ*, 692, 556
- Robitaille, T. P., & Whitney, B. A. 2010, *ApJ*, 710, L11
- Rubin, R. H., Simpson, J. P., Lord, S. D., et al. 1994, *ApJ*, 420, 772
- Russell, S. C., & Dopita, M. A. 1992, *ApJ*, 384, 508
- Sanders, D. B., & Mirabel, I. F. 1996, *ARA&A*, 34, 749
- Sandstrom, K., Krause, O., Linz, H., et al. 2010, *A&A*, 518, L59
- Sargsyan, L. A., & Weedman, D. W. 2009, *ApJ*, 701, 1398
- Schinnerer, E., Böker, T., Meier, D. S., & Calzetti, D. 2008, *ApJ*, 684, L21
- Searle, L., Sargent, W. L. W., & Bagnuolo, W. G. 1973, *ApJ*, 179, 427
- Seale, J. P., Looney, L. W., Chu, Y.-H., et al. 2009, *ApJ*, 699, 150
- Servillat, M., Dieball, A., Webb, N. A., et al. 2008, *A&A*, 490, 641
- Shields, G. A. 1990, *ARA&A*, 28, 525
- Siebenmorgen, R., & Krügel, E. 2007, *A&A*, 461, 445
- Silva, L., Granato, G. L., Bressan, A., & Danese, L. 1998, *ApJ*, 509, 103
- Smith, B. J., Struck, C., & Pogge, R. W. 1997, *ApJ*, 483, 754
- Smith, B. J., & Struck, C. 2001, *AJ*, 121, 710
- Smith, J. D. T., et al. 2007, *PASP*, 119, 1133
- Smith, J. D. T., et al. 2007, *ApJ*, 656, 770
- Smith, T. F., & White, G. K. 1975, *Journal of Physics C Solid State Physics*, 8, 2031
- Sofia, U. J., & Jenkins, E. B. 1998, *ApJ*, 499, 951
- Stiavelli, M. 2010, *American Institute of Physics Conference Series*, 1294, 158
- Storchi-Bergmann, T., Nemmen, R. S., Spinelli, P. F., et al. 2005, *ApJ*, 624, L13
- Struck, C., & Smith, B. J. 2003, *ApJ*, 589, 157
- Takagi, T., Arimoto, N., & Hanami, H. 2003, *MNRAS*, 340, 813
- Taniguchi, Y., Kawara, K., Nishida, M., Tamura, S., & Nishida, M. T. 1988, *AJ*, 95, 1378
- Terlevich, R. 1997, *Revista Mexicana de Astronomia y Astrofisica Conference Series*, 6, 1
- Tielens, A. G. G. M. 2008, *ARA&A*, 46, 289
- Toomre, A. 1977, *Evolution of Galaxies and Stellar Populations*, 401

Bibliography

- Tosaki, T., Miura, R., Sawada, T., et al. 2007, *ApJ*, 664, L27
- Townsley, L. K., Broos, P. S., Feigelson, E. D., Brandl, B. R., Chu, Y.-H., Garmire, G. P., & Pavlov, G. G. 2006, *AJ*, 131, 2140
- Tüllmann, R., et al. 2008, *ApJ*, 685, 919
- Van Kerckhoven, C., et al. 2000, *A&A*, 357, 1013
- Vázquez, G. A., & Leitherer, C. 2005, *ApJ*, 621, 695
- Walborn, N. R., & Blades, J. C. 1987, *ApJ*, 323, L65
- Walborn, N. R., & Blades, J. C. 1997, *ApJS*, 112, 457
- Walborn, N. R., Maíz-Apellániz, J., & Barbá, R. H. 2002, *AJ*, 124, 1601
- Walcher, J., Groves, B., Budavári, T., & Dale, D. 2011, *Ap&SS*, 331, 1
- Walsh, J. R., Nandy, K., Thompson, G. I., & Meaburn, J. 1986, *MNRAS*, 220, 453
- Wang, G. 1992, *Acta Astrophysica Sinica*, 11, 311
- Wang, Q. D. 1999, *ApJ*, 510, L139
- Weedman, D. W., Feldman, F. R., Balzano, V. A., et al. 1981, *ApJ*, 248, 105
- Wells, M., Hawkins, G., & Olofsson, G. 2004, *Proc. SPIE*, 5487, 794
- Wells, M., Lee, D., Oudenhuisen, A., et al. 2006, *Proc. SPIE*, 6265
- Werner, M. W., Becklin, E. E., Gatley, I., Ellis, M. J., Hyland, A. R., Robinson, G., & Thomas, J. A. 1978, *MNRAS*, 184, 365
- Westerlund, B. E. 1997, *Cambridge Astrophysics Series*, 29
- Whitney, B. A., et al. 2008, *AJ*, 136, 18
- Whitworth, A. 1979, *MNRAS*, 186, 59
- Wilson, C. D., & Scoville, N. 1992, *ApJ*, 385, 512
- Wilson, C. D., Harris, W. E., Longden, R., & Scoville, N. Z. 2006, *ApJ*, 641, 763
- Wolf, C. 2009, *MNRAS*, 397, 520
- Wright, G. S., Rieke, G., Barella, P., et al. 2008, *Proc. SPIE*, 7010,
- Yang, H., Chu, Y.-H., Skillman, E. D., & Terlevich, R. 1996, *AJ*, 112, 146
- Yun, M. S., & Hibbard, J. E. 2001, *ApJ*, 550, 104
- Zakamska, N. L. 2010, *Nature*, 465, 60
- Zinnecker, H., & Yorke, H. W. 2007, *ARA&A*, 45, 481

Nederlandse Samenvatting

Veel van de spectaculaire sterrenkundige afbeeldingen in wetenschappelijke tijdschriften en documentaires, recentelijk verkregen met professionele telescopen, vinden hun oorsprong in natuurkundige processen die betrekking hebben op het leven van sterren. Dit omvat zowel hun geboorte te midden van dichte wolken van interstellair gas en stof dat tot massieve sterclusters leidt, als ook hun spectaculaire einde in grootse explosies, supernovae genaamd, die voor korte duur zo helder als een heel melkwegstelsel kunnen worden. De fysica achter deze fenomenen zijn niet alleen visueel schitterend, maar ze bevatten ook de geheimen over hoe het leven van sterren verbonden is met de evolutie van het Universum in zijn geheel.

Dit proefschrift onderzoekt een specifiek aspect in deze complexe relatie in het bijzonder: de invloed die de straling geproduceerd door jonge massieve sterren heeft op het interstellair medium (ISM) uit waar ze zijn geboren, afgeleid uit waarnemingen gemaakt met infraroodtelescopen. In dit boekje ontwikkelen we een nauwkeurige en krachtige methode om infraroodwaarnemingen van intensieve stervormingsgebieden te combineren met theoretische voorspellingen. Het doel is om een beter begrip te krijgen van wat de interacties tussen massieve sterren en het ISM ons kan leren over de fysica achter massieve stervorming in het Universum.

Massieve sterren en hun relatie met het ISM

De meeste sterren in een melkwegstelsel vormen zich uit een gravitationele ineenstorting van een enorme moleculaire wolk (GMC; vertaald uit het Engels: giant molecular cloud). Deze ineenstorting doet zich voor op tijdschalen van honderd tot duizend jaar. Eén van de mogelijke gevolgen van dit proces, misschien wel één van de meest spectaculaire, is het ontstaan van sterclusters en associaties met een massa in de orde van honderd tot duizend keer die van onze zon. De meest massieve sterren in deze clusters kunnen ieder wel 100 keer zo zwaar zijn als onze zon. Deze massieve sterren hebben sterke stralingsvelden en sterwinden die actief wisselwerken met het overgebleven gas en stof uit de oerwolk waaruit ze zijn gevormd. Het massieve stervormingsgebied, bekend als de Tarantula nevel (ook wel als 30 Doradus), dat we in Hoofdstuk 2 bestuderen, is een indrukwekkend voorbeeld van deze wisselwerking (zie Figuur 1).

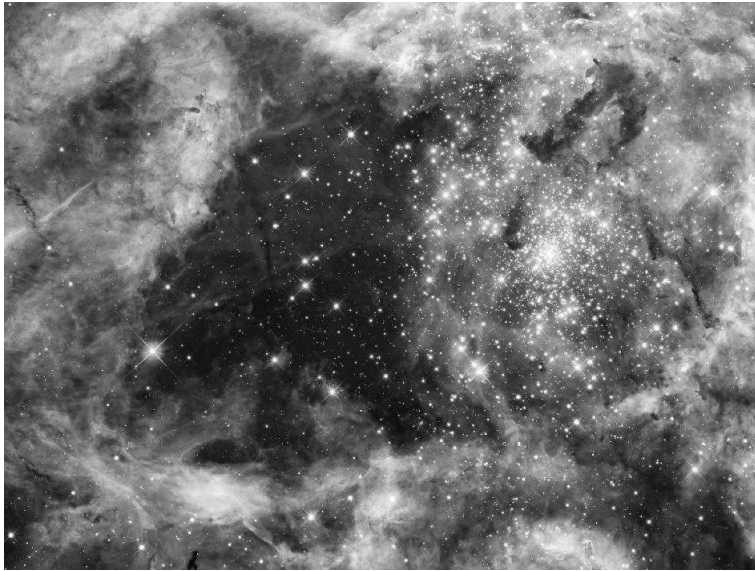


Figure 1 Het massieve stervormingsgebied 30 Doradus, in de Grote Magelhaense Wolk, gefotografeerd met de Ruimtetelescoop Hubble (Afbeelding via NASA).

Een gedeelte van de straling uitgezonden door deze sterren ioniseert het nabije gas, daarbij kleurrijke aanblikken producerend die met onze telescopen zijn vastgelegd, in zogenoemde H II gebieden die gevuld zijn met heet geïoniseerd waterstof. Een ander gedeelte van de straling wordt geabsorbeerd door stofdeeltjes in het ISM die daarbij verhit worden en in het infrarood licht beginnen te gloeien en dat met onze telescopen kan worden waargenomen. Vervolgens, drukken de mechanische druk uitgeoefend door de straling van de sterren en de heftige supernova explosies het ISM samen waardoor de ineenstorting van naburige moleculaire wolken veroorzaakt wordt, leidend tot nieuwe periodes van stervorming. Al deze processen modifieren de galactische omgeving en beïnvloeden de latere ontwikkeling van de melkwegstelsels waarin ze plaatsvinden. Eén van de grootste uitdagingen in de moderne sterrenkunde is om deze processen te begrijpen en te kwantificeren. Het is ook één van de belangrijkste doelstellingen in dit proefschrift.

Massieve sterren en recente stervorming

De sterren die stellaire associaties zoals die in Figuur 1 omvatten, zijn bijna allemaal tegelijkertijd geboren en hebben een breed bereik in individuele stellaire massa's. Niettemin, alleen die sterren met een massa gelijk aan een paar keer die van onze zon hebben een aanzienlijk effect op het ISM. In feite, in gebieden waar deze associaties gevormd worden, komt het meeste van het waargenomen licht afkomstig van deze massieve sterren; hoewel minder in aantal zijn ze wel vele malen helderder dan hun lage-massa tegen-

hangers. Het zijn deze massieve sterren die de energievoorraad in stervormingsgebieden domineren. Aan de andere kant, de meest massieve sterren zijn ook diegene met de kortste levensduur, waarbij ze al na een paar miljoen jaar door hun brandstof heen zijn, een kort leven vergeleken met de enkele miljarden jaren dat een ster zoals onze zon kan leven. Daarom, door in een afzonderlijk gebied van een melkwegstelsel het geïoniseerde gas en het stof te bestuderen dat verhit wordt door het licht van de massieve sterren, kunnen we objecten onderzoeken die minder dan 10 miljoen jaar geleden gevormd zijn (i.e. een korte tijdschaal in een kosmologisch perspectief) en zodoende kunnen we de recente stervormingsgeschiedenis in dat gebied bestuderen.

Starbursts

Het is mogelijk om kwantitatief vast te stellen hoe snel nieuwe sterren worden gevormd in specifieke gebieden. Om dit te doen kunnen we bijvoorbeeld de hoeveelheid infrarood licht meten, dat wordt uitgezonden door opgewarmd stof¹. Ook kunnen we het licht meten dat wordt uitgezonden door atomaire deeltjes die geïoniseerd zijn door het stralingsveld van jonge sterren. De hieruit voortkomende helderheden kunnen worden geïnterpreteerd als fysisch meer intuïtieve grootheden. We kunnen bijvoorbeeld de infrarode helderheid van een stervormingsgebied zien als de gemiddelde moleculaire massa die wordt omgezet in sterren per jaar. Nogmaals, aangezien deze sterren slechts een zeer korte levenscyclus hebben, kunnen we hieruit schatten hoe snel sterren worden gevormd in bepaalde gebieden van het universum *op dit moment*. We kunnen bijvoorbeeld afleiden dat in onze Melkweg sterren worden gevormd met een snelheid van ongeveer 1 zons-massa per jaar. Anders gezegd, elk jaar wordt gemiddeld genomen een enkele ster met een massa gelijk aan onze Zon geboren in ons melkwegstelsel.

We kunnen de stervormingssnelheid (star formation rate, SFR) in verscheidene gebieden van ons universum afleiden door het infrarode licht te meten dat wordt uitgezonden door nabije en verre melkwegstelsels. Astronomen hebben dit gedaan en leiden daaruit af dat niet alle melkwegstelsels sterren vormen met dezelfde snelheid. Een belangrijk deel van deze stelsels hebben SFRs die tientallen, honderden of zelfs duizenden malen groter zijn dan die van onze Melkweg. Dit betekent dat deze objecten grote infrarode helderheden hebben. Sterker nog, als we verder weg gaan van ons melkwegstelsel om verder weg gelegen gebieden in ons universum te bestuderen, dan valt op dat het aandeel van objecten met een hoge SFR, die we 'starbursts' noemen, alleen maar toeneemt. Tot op de dag van vandaag is het nog niet helemaal duidelijk waarom deze starbursts zulke hoge stervormingssnelheden hebben. We weten dat om dit mogelijk te maken, grote hoeveelheden moleculair gas verplaatst moeten worden naar relatief kleine gebieden in een melkwegstelsel binnen korte tijd. Echter, de processen die dit transport mogelijk maken, alsmede het proces waarmee opeenvolgende stervorming wordt veroorzaakt door voorafgaande stervorming, moeten nog steeds afdoende worden verklaard.

¹Aangenomen moet worden, uiteraard, dat andere warmtebronnen die niets van doen hebben met stervorming relatief onbelangrijk zijn voor dit proces.



Figure 2 De kern van het melkwegstelsel NGC 1097 heeft een intensieve starburst ring, zichtbaar op deze afbeelding genomen in het infrarood door de Spitzer Space Telescope. Dit is een van de stelsels die we bestuderen in **Hoofdstuk 4**. (Afbeelding geproduceerd door NASA.).

Spectroscopie van stervormingsgebieden in het infrarood

Om antwoorden te vinden op sommige van deze vragen rondom het fenomeen van starbursts zijn astronomen in de afgelopen twee à drie decennia het infrarode universum gaan bestuderen. Er zijn verscheidene redenen om dit golflengtegebied te kiezen. Allereerst, zoals gezegd, schijnen stervormingsgebieden sterk in infrarood licht vanwege thermische straling van opgewarmd stof. Bovendien vindt de meest intensieve stervorming plaats achter dichte lagen van gas en stof, waar zichtbaar licht dat onze ogen kunnen zien niet doorheen komt, terwijl het infrarode licht er juist wel uit komt. Dus het licht dat wordt opgevangen door onze infrarode telescopen schijnt door de compacte lagen van gas en stof en bereikt ons vanuit de zeer diepe gebieden waar nieuwe, zware sterren worden geboren. Naast de digitale afbeeldingen gemaakt door detectoren speciaal ontworpen om infrarood licht te zien, die de structuur van het stof en moleculair gas tonen, bestuderen we tegenwoordig starbursts met infrarood spectroscopie – een van meest geavanceerde technieken van dit moment.

Om te begrijpen wat infrarood spectroscopie is, kunnen we denken aan de kleuren van de regenboog. Net zoals we een prisma kunnen gebruiken om zonlicht op te breken in de kleuren van de regenboog (het spectrum van het zichtbare licht), kunnen we, met de juiste instrumenten, ook het spectrum van het infrarode licht uitgezonden door astronomische lichamen opvangen. In het specifieke geval van stervormingsgebieden zijn infrarode spectra essentieel om de energieverdeling van de verschillende bestanddelen van het interstel-

laire medium te kunnen waarnemen. Dit biedt aan degenen die dergelijke spectra kunnen interpreteren de mogelijkheid om een precieze beschrijving van de fysische toestanden van deze gebieden te geven. Sommige van deze bestanddelen die herkenbaar zijn aan hun infrarode straling zijn atomaire gas, stofdeeltjes, en een bepaald soort moleculen dat karakteristiek is voor stervormingsgebieden, genaamd polycyclische aromatische koolwaterstoffen (PAHs). De analyse van infrarode spectra maakt het mogelijk om belangrijke fysische gegevens af te leiden van deze gebieden, zoals de stervormingssnelheid, de gasdruk waartegen de straling van sterren zich voortplant, of de hoeveelheid jonge sterren die nog verborgen zijn in het dichte gas en de stofsluiers waaruit deze gevormd werden.

Infrarode spectra worden gemeten door speciale instrumenten geïnstalleerd in moderne telescopen. Om deze spectra op de juiste wijze te kunnen interpreteren en om er een fysische betekenis aan toe te kennen in de context van stervorming en hoe dit alles zich verhoudt tot het interstellair medium, moeten we deze spectra vergelijken met theoretische modellen die de sterkte en de energieverdeling van de uitgezonden straling voorspellen. Dit is verre van eenvoudig, omdat verschillende fysische omstandigheden kunnen leiden tot vergelijkbare spectra, wat leidt tot tegengestelde en misleidende conclusies. Bovendien zijn de meeste starbursts zo ver weg dat we de structuur ervan niet kunnen onderscheiden, zelfs niet met de grootste telescopen. Daardoor kunnen we de verschillende bestanddelen, zoals sterren, gas en stof, niet herleiden tot verschillende componenten van de spectra. Een nauwkeurige en robuuste methode is nodig om betrouwbare waarden toe te kennen aan de fysische parameters van verafgelegen starbursts, en om de ware toestanden van de materie in deze objecten te kunnen onderzoeken.

Een Bayesiaanse methode om infrarode spectra te interpreteren

In het eerste deel van dit proefschrift (Hoofdstukken 2, 3 en 4) ontwikkelen we een nieuwe methode om infrarode spectra van starbursts te interpreteren. Deze methode geeft nauwkeurige en betrouwbare waarden voor fysische parameters van deze objecten en berekent kwantificeerbare en statistisch-toepasselijke onzekerheden. Deze methode gebruikt Bayesiaanse statistiek² om de waarschijnlijkheid dat zekere fysische parameters bepaalde waarden hebben te schatten (bijvoorbeeld de stervormingssnelheid). Bayesiaanse statistiek maakt het mogelijk om nieuwe kennis over de parameters (observationeel of theoretisch) op te nemen in de bepaling van hun waarschijnlijkheden. Intuïtief gezien betekent dit dat de onderzoeker op elk moment de mate waarin hij of zij een zeker resultaat als betrouwbaar inschat kan bijwerken door nieuwe gegevens mee te nemen. De methode is reproduceerbaar en biedt betrouwbaardere resultaten dan wat behaald kan worden uit een directe vergelijking tussen modellen en waarnemingen. In dit proefschrift passen we deze nieuwe methode toe op spectra van starbursts genomen door de Spitzer Space Telescope. Hier volgt een korte beschrijving van de hoofdstukken.

Hoofdstuk 2

In dit hoofdstuk introduceren we onze methode en de kalibratie daarvan met het grote

²Genoemd naar Thomas Bayes (1701-1761), een Engelse priester en wiskundige die deze statistiek voor het eerst formuleerde.

ster-vorming gebied 30 Doradus (Figuur 1). Dit gebied heeft twee eigenschappen die het extra geschikt maken voor de kalibratie: 30 Doradus is (1) al vaak en in groot detail bestudeerd door andere auteurs, en (2) ligt zo dichtbij dat we het ruimtelijk op kunnen lossen met onze telescoop. Dit stelt ons in staat om de losse onderdelen van het systeem (massieve sterren, gas, stof, etcetera) van elkaar te onderscheiden en in verband te brengen met bepaalde onderdelen van het infrarode spectrum van 30 Doradus. Onze methode kan de eigenschappen van 30 Doradus goed reproduceren. We laten zien dat we de onzekerheden in het bepalen van zekere parameters significant kunnen verkleinen door het gebruik van spectrale lijnen in onze analyse. Dit zorgt ervoor dat onze methode meer robuuste resultaten oplevert in vergelijking met andere methoden. Tenslotte beschrijven we onze ontdekking dat het infrarode spectrum van 30 Doradus verklaard kan worden met de aanwezigheid van een significant aantal jonge sterren die nog steeds omsloten zijn door de stof- en gas-wolk waaruit ze geboren zijn. Dit is een aanwijzing dat 30 Doradus een actief stervormend gebied is.

Hoofdstuk 3

NGC 604 in het driehoekssterrenstelsel is het op één-na dichtbijzijnde grote stervorming gebied. In dit hoofdstuk combineren we waarnemingen in het infrarood, optisch en Röntgenstraling met onze Bayesische methode om de eigenschappen van NGC 604 te bestuderen. Ons belangrijkste resultaat is de ontdekking van massieve infrarode wolken. Deze wolken zijn erg warm en compact, en binnenin deze wolken worden massieve sterren gevormd. Een intrigerende verklaring voor deze ontdekking is dat de stervorming in deze wolken geactiveerd is door een eerdere episode van stervorming tijdens welke de meeste nu zichtbare sterren in NGC 604 gevormd zijn. Onze resultaten suggereren bovendien dat NGC 604 in een verder geëvolueerd stadium van stervorming is dan zijn grotere broer 30 Doradus, maar dat dit niet noodzakelijk het einde van actieve stervorming betekent.

Hoofdstuk 4

In dit hoofdstuk gebruiken we onze methode van interpretatie van infrarood spectra op grotere maar verder weg gelegen stervormingsgebieden. Deze gebieden liggen in het centrum van een paar sterrenstelsels in het nabije universum. Met de in hoofdstuk 2 en 3 opgedane ervaring kunnen we overeenkomsten vinden in de eigenschappen van deze relatief kleine groep stercluster vormingsgebieden. Wij vinden bijvoorbeeld aanwijzingen voor het feit dat de stervormingsgebieden met de grootste hoeveelheid aan moleculaire brandstof (en dus met de hoogste stervormingssnelheid), niet altijd de grootste sterclusters vormen. De grootste groepen lijken in tegenstelling gevormd te worden in de stervormingsgebieden met de laagste stervormingssnelheid. We concluderen ook dat de stervormingsgebieden met de grootste sterclusters een relatief grote bijdrage ondervinden van erg jonge sterren die nog door een dikke envelop van stof omgeven worden. Een meer compleet onderzoek van de spectra van stervormings gebieden is noodzakelijk om definitieve conclusies te trekken over het verband tussen de eerdere episodes van stervorming tijdens welke de ster-groepen gevormd zijn, en de huidige periodes van stervorming.



Figure 3 JWST zal stervormingsgebieden in ongekend detail gaan bestuderen. Hoofdstukken 5 en 6 zijn gewijd aan de spectrometer die gekoppeld is aan deze grote telescoop (Afbeelding via NASA).

Hoofdstukken 5 en 6

Ondanks de ontwikkeling van steeds betere analyse methoden wordt de nauwkeurigheid van onze resultaten nog steeds erg beïnvloed door de techniek en afmetingen van de telescopen die we gebruiken. Dit toont het belang aan van grotere en betere telescopen voor het verder ontwikkelen van onze kennis van stervormingsgebieden. Tegen het einde van dit decennium zullen de ruimtevaartorganisaties uit de Verenigde Staten, Europa en Canada een nieuwe grote en geavanceerde infrarood telescoop de ruimte in sturen. Deze telescoop gaat de "James Webb Space Telescope" (JWST) heten en wordt, met een spiegel van 6.5 meter in diameter, de grootste infrarood telescoop die ooit in de ruimte is geplaatst. Eén van de instrumenten die aan boord zal zijn van de JWST is het "Mid-InfraRed Instrument" (MIRI). MIRI bestaat uit een camera en een spectrometer, en hiermee kunnen we stervormingsgebieden en andere gebieden in ons heelal met een ongekend detail en gevoeligheid bestuderen.

De laatste twee hoofdstukken van dit proefschrift zijn gewijd aan MIRI. Dit instrument is gebouwd in Europa en Nederland heeft hierbij een rol van cruciaal belang gespeeld. De auteur van dit proefschrift heeft gewerkt aan de kalibratie van MIRI bij het Rutherford Appleton Laboratorium in Oxford, Engeland. In het tweede deel van dit proefschrift beschrijven we de functionaliteit van MIRI en de kalibratie processen van de spectrom-

Nederlandse Samenvatting

eter. Meer specifiek beschrijven we één van de belangrijkste kalibraties van de spectrometer - die voor de golflengte kalibratie. We passen onze kalibratiemethode ook toe op gegevens die zijn verzameld tijdens de testfase. Hieruit concluderen we dat MIRI infrarood spectra kan verzamelen met een resolutie die tenminste 10 keer hoger is dan die van zijn voorganger, de infrarood spectrometer aan boord van de Spitzer ruimte telescoop. MIRI aan boord van de JWST betekent dus een grote stap voorwaarts in de nabije toekomst voor het bestuderen van de vorming van massieve sterren.

Muchas de las espectaculares imágenes obtenidas hoy en día por los grandes telescopios profesionales, que nos deslumbran en las páginas de las revistas científicas y en los documentales de televisión, tienen su origen en procesos relacionados con las vidas de las estrellas. Desde su nacimiento en medio de densas nubes de gas y polvo interestelar que dan lugar a masivos cúmulos de estrellas, hasta sus cataclísmicos finales en explosiones colosales llamadas supernovas, que en lapsos de tiempo de tan sólo unos cuantos días pueden llegar a ser tan brillantes como galaxias enteras, los procesos físicos detrás de estos fenómenos no sólo agregan belleza a las imágenes astronómicas, sino que además esconden los secretos sobre cómo la vida de las estrellas está relacionada con la evolución del Universo como un todo.

Esta tesis indaga sobre un aspecto particular de este complejo entramado: la influencia que la radiación proveniente de jóvenes estrellas masivas tiene en el medio interestelar a partir del cual se forman, tal como se deduce de las observaciones hechas con telescopios infrarrojos. En las páginas de esta tesis, ideamos un método certero y robusto para combinar observaciones infrarrojas de regiones de formación estelar con predicciones teóricas. El objetivo es avanzar hacia la comprensión de cómo la interacción entre las estrellas y el medio interestelar puede enseñarnos acerca de la física de la formación de estrellas masivas en el Universo.

Estrellas masivas y su relación con el medio interestelar

La mayoría de las estrellas en una galaxia se forma a partir del colapso gravitacional de una gigante nube de gas molecular, que sucede en escalas de tiempo de cientos de miles de años. Uno de los posibles resultados de este proceso, y tal vez uno de los más espectaculares, es el surgimiento de asociaciones estelares cuyas masas son del orden de cientos de miles de veces la masa de nuestro Sol. Las estrellas más masivas en estas jóvenes aglomeraciones pueden contener individualmente la masa de 100 soles juntos, y emitir intensos campos de radiación y vientos estelares que interactúan notablemente con el gas y el polvo restantes en la nube primigenia de la cual se formaron. La región de formación estelar conocida como la Nebulosa Tarántula (o 30 Dorado), que estudiaremos en el **Capítulo 2**, es un ejemplo impresionante de esta interacción. (Ver Figura 1).

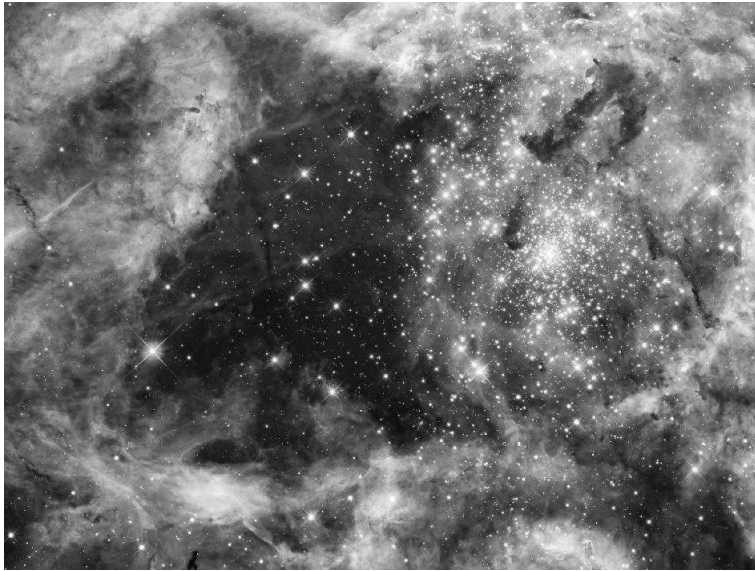


Figure 1 La región de formación estelar masiva 30 Doradus, en la Gran Nube de Magallanes, fotografiada con el Telescopio Espacial Hubble (crédito NASA).

Una parte de la radiación emitida por dichas estrellas ioniza el gas cercano, produciendo la viva gama de colores capturada por los telescopios en las llamadas regiones H II de hidrógeno ionizado. Otra parte de la radiación es absorbida por partículas de polvo en el entorno, que se calientan y brillan en luz infrarroja que podemos detectar con telescopios modernos. Además, la presión mecánica de la radiación estelar, así como las violentas explosiones en las que estrellas más grandes y menos longevas encuentran su fin, comprimen el material interestelar, y pueden incluso producir el colapso de nubes moleculares vecinas, iniciando un nuevo episodio de formación estelar. Todos estos procesos modifican el entorno galáctico, y tienen una influencia en la subsiguiente evolución de las galaxias donde tienen lugar. Entenderlos y cuantificarlos es por tanto uno de los grandes retos de la astronomía actual, y uno de los objetivos de esta tesis.

Estrellas Masivas y Formación Estelar Reciente

Las estrellas que hacen parte asociaciones estelares como la de la Figura 1, nacen todas de manera casi simultánea y con diversas masas individuales. Sin embargo, sólo aquellas estrellas cuya masa es unas cuantas veces la masa del Sol (o más), tienen una influencia notable en el medio interestelar. De hecho, en las regiones donde se forman estas asociaciones, casi toda la luz que detectamos proviene de estrellas masivas, que aunque son mucho menos numerosas que las estrellas de baja masa, son miles de veces más luminosas, y por tanto dominan el presupuesto energético. Pero estas estrellas masivas son

también las primeras en morir, pues agotan su combustible en tan sólo unos pocos millones de años, en comparación con los miles de millones de años que puede vivir una estrella de baja masa como el Sol. Por lo tanto, al estudiar el gas ionizado y el polvo calentado por la luz de estrellas masivas en una región particular de una galaxia, estamos sondeando objetos que se formaron hace menos de 10 millones de años (una etapa de tiempo corta en términos cósmicos), y por lo tanto estamos investigando la historia reciente de formación estelar en dicha región.

Starbursts

Podemos cuantificar el ritmo con el cual se forman estrellas en una región particular midiendo por ejemplo la cantidad de luz infrarroja emitida por el polvo caliente¹. También podemos medir la cantidad de luz emitida por átomos que han sido ionizados por el intenso campo de radiación de las estrellas jóvenes. Dichas cantidades de luz (o luminosidades) pueden ser interpretadas en términos de cantidades físicamente más intuitivas. Por ejemplo, podemos interpretar la luminosidad infrarroja de una región de formación estelar en términos de la cantidad promedio de gas molecular que ha sido convertida en estrellas cada año. Puesto que las estrellas masivas responsables del calentamiento del polvo tienen períodos de vida muy cortos, esta medida nos da una idea del ritmo *actual* con el que se forman estrellas en una región del Universo. Por ejemplo, nuestra galaxia, la Vía Láctea, forma estrellas a un ritmo aproximado de 1 masa solar por año. En otras palabras cada año, en promedio nace una nueva estrella con la masa del Sol en nuestra galaxia.

Podemos inferir esta *Rata de Formación Estelar* (RFE) en varias regiones del Universo midiendo la luz infrarroja emitida por distintas galaxias. Al hacerlo, rápidamente notamos que no todas las galaxias forman estrellas al mismo ritmo. Una considerable cantidad de objetos tienen RFE de decenas, cientos, e incluso miles de veces la RFE de nuestra galaxia, lo cual se traduce en altísimas luminosidades infrarrojas. De hecho, a medida que nos alejamos de nuestra galaxia, y estudiamos regiones más distantes del Universo, vemos que la fracción de objetos con alta formación estelar, que llamamos *starbursts*, es cada vez mayor. En la actualidad no está totalmente claro por qué estos *starbursts* forman estrellas a ritmos tan altos. Sabemos que para que esto suceda, grandes cantidades de gas deben ser transportadas, en períodos de tiempo cortos, a regiones relativamente pequeñas de una galaxia. Sin embargo, los procesos que hacen posible este transporte no tienen una explicación definitiva, como tampoco la tienen las etapas de formación estelar sucesivas que pueden desencadenarse por la interacción de estrellas jóvenes con el medio interestelar.

Espectroscopia Infrarroja de Regiones de Formación Estelar

Para intentar encontrar algunas respuestas al fenómeno de los *starbursts*, en las últimas dos o tres décadas los astrónomos han comenzado a estudiar el Universo en longitudes de onda infrarrojas. Son varias las razones por las cuales estudiamos regiones de formación estelar usando este tipo de luz. Primero, dichas regiones son brillantes en el infrarrojo

¹Asumiendo, por supuesto, que otros procesos que pueden calentar el polvo, y que no están relacionados con formación estelar, son marginales.



Figure 2 El núcleo de la galaxia NGC 1097 contiene un intenso anillo starburst, visible en esta fotografía infrarroja obtenida con el Telescopio Espacial Spitzer. Este es uno de los objetos que estudiamos en el **Capítulo 4**. (crédito NASA).

debido a la emisión térmica del polvo, como hemos discutido. Pero además, las densas regiones de polvo y gas detrás de las cuales ocurre el proceso de formación estelar, opacas para la luz normal, son transparentes para la luz infrarroja. Por lo tanto, la luz detectada por nuestros telescopios infrarrojos logra atravesar las compactas cortinas de gas y polvo, y alcanzarnos desde las zonas profundas donde nacen nuevas estrellas. Además de las fotografías digitales obtenidas con detectores especialmente diseñados para registrar luz infrarroja, y que revelan la estructura física de la distribución de polvo y material molecular (ver Figura 2), una de las técnicas más sofisticadas usadas por los astrónomos hoy en día es la espectroscopía infrarroja.

Para entender de qué se trata, podemos imaginar los colores del arcoiris. De la misma manera en que podemos tomar un prisma y descomponer la luz del Sol en los colores del arcoiris (el espectro de la luz visible), es posible también obtener un espectro de la luz infrarroja proveniente de los cuerpos astronómicos, usando instrumentos apropiados. En el caso particular de las zonas de formación estelar, los espectros infrarrojos son de gran utilidad, ya que revelan la distribución de energía con la cual los componentes del medio interestelar emiten su radiación, ofreciendo, para quien pueda interpretarlos, una descripción de las condiciones físicas en dichas regiones. Algunos de los componentes que emiten luz infrarroja y pueden ser identificados en el espectro son el gas atómico, las partículas de polvo y algunas moléculas basadas en carbono, típicas de estos ambientes, llamadas hidrocarburos aromáticos policíclicos (PAHs). El análisis de estos espectros permite derivar importantes parámetros físicos de la región, tales como la RFE, la presión

del gas contra la cual trata de abrirse paso la radiación estelar, o la cantidad de estrellas jóvenes que aún están cubiertas por los gruesos envoltorios de gas de los cuales se formaron.

Los espectros infrarrojos son obtenidos con instrumentos especiales abordo de los telescopios. Para interpretarlos correctamente y asignarles un significado físico en el contexto de la formación estelar y su relación con el medio interestelar, los espectros deben ser comparados con modelos teóricos que predicen su intensidad y distribución de energía. La labor no es fácil, pues condiciones físicas diferentes pueden dar lugar a espectros muy semejantes, generando interpretaciones confusas o contradictorias. Además, la mayoría de starburst son objetos lejanos en cuya estructura no podemos diferenciar las estrellas masivas del gas ionizado y el polvo, pues todo aparece muy junto en las imágenes obtenidas. Un método robusto y preciso es necesario para asignar valores confiables a los parámetros físicos de starburst lejanos, y así investigar las verdaderas condiciones de la materia en estos objetos.

Un método Bayesiano para interpretar espectros infrarrojos

En la primera parte de esta tesis (Capítulos 2, 3 y 4) desarrollamos un nuevo método para la interpretación de espectros infrarrojos de starbursts, que arroja resultados inequívocos para los parámetros físicos de estos objetos, y les asigna incertidumbres cuantificables y estadísticamente apropiadas. El método usa estadística Bayesiana² para estimar la probabilidad de que ciertos parámetros (el ritmo de formación estelar, por ejemplo), tengan un valor determinado. El método Bayesiano permite incluir en la evaluación de las probabilidades cualquier nueva evidencia obtenida (experimental o teóricamente) sobre los parámetros físicos. Intuitivamente, lo que esto quiere decir es que el investigador puede actualizar en cualquier momento el nivel de convicción con que cree en el resultado de un modelo, al incluir nueva evidencia en su análisis. El método ofrece resultados reproducibles y muchos menos confusos que aquellos obtenidos por comparación directa del espectro con las predicciones. En esta tesis aplicamos el método a espectros obtenidos principalmente con el Telescopio Espacial Spitzer. A continuación describimos brevemente los capítulos del presente trabajo.

Capítulo 2

Presentamos nuestro método y lo calibramos usando una región gigante de formación estelar: 30 Dorado, en la cercana Gran Nube de Magallanes (Figura 1). Esta región ofrece dos ventajas: ha sido estudiada en detalle por varios autores y además está lo suficientemente cercana para identificar componentes individuales del sistema (estrellas masivas, gas, polvo, etc.) y relacionarlas con características particulares del espectro infrarrojo. Este primer capítulo arroja varios resultados. Primero, reportamos el éxito de nuestro método en reproducir las condiciones físicas en 30 Dorado. Además, mostramos que al incluir en nuestro análisis las líneas espectrales generadas a causa de la absorción de luz estelar por gases atómicos en el medio interestelar, reducimos las incertidumbres de

²Nombrada en honor de Thomas Bayes (1701-1761), un clérigo y matemático inglés que la formuló por primera vez.

varios parámetros, logrando resultados más precisos que con otros métodos. Finalmente, también descubrimos que el espectro de 30 Dorado es compatible con la presencia de una componente considerable de jóvenes estrellas aún envueltas en sus nubes primigenias. Esto indica una gran cantidad de formación estelar sucediendo actualmente en esta región.

Capítulo 3

Luego de 30 Dorado, la más cercana región gigante de formación estelar es NGC 604, localizada en la galaxia del Triángulo. En este capítulo estudiamos sus condiciones físicas usando nuestro método, combinado con varias observaciones infrarrojas, ópticas, y de rayos-X. El resultado principal es el descubrimiento de masivos cúmulos infrarrojos compactos y calientes, donde se están formando actualmente nuevas estrellas, lo cual sugiere que episodios anteriores de formación estelar han desencadenado nuevos eventos en épocas muy recientes. Además nuestro método indica que el starburst NGC 604 está en un estado evolutivo más avanzado que su hermana mayor, 30 Dorado, lo cual no es impedimento para que siga formando estrellas activamente.

Capítulo 4

En este capítulo usamos nuestro método en la interpretación de los espectros infrarrojos de starbursts más grandes y lejanos, ubicados en las zonas nucleares de algunas galaxias en el Universo Local, como el de la Figura 2. La experiencia obtenida en los capítulos precedentes nos permite identificar ciertas tendencias en las condiciones físicas de estos starbursts. Por ejemplo, encontramos evidencia preliminar de que los starburst con mayor combustible de gas molecular, y que por tanto tienen RFE más altas, no son necesariamente los que forman las aglomeraciones estelares más masivas. Por el contrario, estas últimas parecen formarse en zonas con baja RFE. Encontramos también que los starbursts con aglomeraciones estelares más grandes tienden a contener una mayor contribución por parte de estrellas muy jóvenes, aún envueltas en densas capas de polvo. Sin embargo, sólo con un estudio más extenso sería posible inferir una relación entre episodios anteriores de formación estelar, y estos eventos recientes.

Capítulos 5 y 6

Aún cuando nuestros métodos de análisis se hacen cada vez mejores, seguimos limitados en este tipo de investigaciones por la sofisticación y el tamaño de nuestros telescopios. Por lo tanto, sólo mejores observatorios nos permitirán seguir avanzando en la comprensión de la formación de estrellas masivas en el Universo. Al final de esta década, un nuevo y poderoso telescopio infrarrojo será enviado al espacio por las agencias espaciales de Estados Unidos, Europa y Canadá. El Telescopio Espacial James Webb tendrá un espejo principal de 6.5 m de diámetro, y será por lo tanto el más grande telescopio infrarrojo construido hasta la fecha. Uno de los instrumentos que llevará a bordo será el espectrómetro del infrarrojo medio, o MIRI, que se compone de una cámara y un espectrómetro. MIRI estudiará los starbursts y otras regiones de formación estelar con un detalle y sensibilidad nunca vistas.

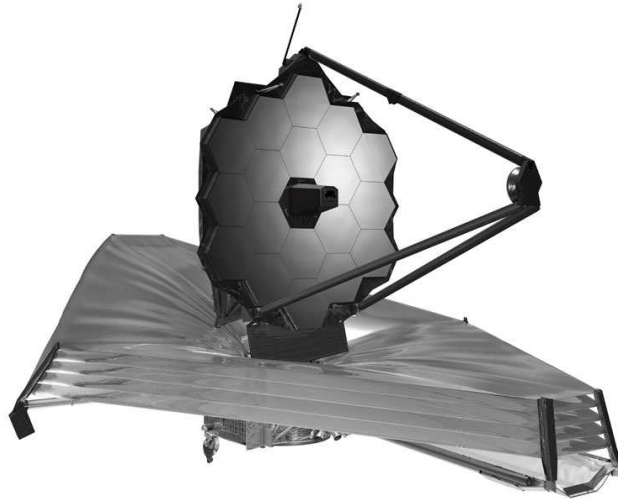


Figure 3 El Telescopio Espacial James Webb (JWST) estudiará regiones de formación estelar con un detalle nunca visto. Los **Capítulos 5 y 6** están dedicados al espectrómetro infrarrojo abordo de JWST. (crédito NASA).

La segunda parte de esta tesis, que contiene los dos últimos capítulos, está dedicada a MIRI. Este instrumento ha sido construido en Europa, con una participación crucial de los Países Bajos. El autor tomó parte activa en la calibración final del instrumento, que fue realizada en el Laboratorio Rutherford Appleton, en Oxford, Reino Unido. En esta parte de la tesis se describe el funcionamiento del instrumento y la calibración del espectrómetro. Específicamente, se describe el método utilizado para la calibración de la longitud de onda y se aplica este método a los datos obtenidos durante las pruebas realizadas al instrumento. Los resultados indican que MIRI logrará una resolución espectral al menos diez veces mejor que su predecesor, el espectrómetro abordo de Spitzer. Esto significa un gran avance en nuestras capacidades observacionales, y una nueva ventana para estudiar la formación de estrellas masivas en un futuro cercano.

Curriculum Vitae

I was born in the capital of Colombia on September 13, 1981, the same year in which personal computers were introduced to the market, the AIDS virus was first reported, and Pope John Paul II was shot in the middle of a crowded St. Peter's Square in Rome. I spent my early years playing with my brother David and my little cousins in the corridors of the big family house in Soacha, near Bogotá, from where I witnessed with similar astonishment the difficult years of a country subjugated by the intolerance and violence of the drug trafficking lords, and the beauty of the sky decorated with the majestic tail of comet Halley.

In 1990 my parents, Fanny and Ricardo, took us to live in a pretty house in the outskirts of Bogotá, and after a few years at the Colegio Champagnat, I started high school at the Centro Educativo Integral Colsubsidio, from where I graduated in 1998 with the highest score in my class for the state exams. By that time I was already convinced that I wanted to do astronomy, with the only problem that I was also convinced that I wanted to become a writer. It was only my math professor who tipped the scales in favor of science, and so I enlisted to study physics at the National University in Bogotá, a place that is famous for having a square named after “Che Guevara”, but also for producing the best professionals in the country. There, I obtained my degree in physics in 2005.

Shortly before, when I was about to give up my astronomical aspirations due to the lack of research done on this field in Colombia, I was lucky to meet Dr. David Ardila, under whose advice I enrolled in the Summer Student Program at the *Space Telescope Science Institute* (STScI) in Baltimore, where I worked with Dr. Inga Kamp on optical spectroscopy of chemically peculiar stellar atmospheres. This work evolved into a project that took me to the dry mountains of the Atacama desert in Chile and to the hot plains of southern Arizona, where I worked for a few months with Prof. Dr. George Rieke and Dr. Kate Su in what was going to become my first scientific publication: a study of the mid-infrared excess around λ Bootis stars. It was then that infrared light first shone for me.

I landed in the Netherlands in early 2006, and over the last six years living here, I have learned a lot about astronomy and also about life. At the Leiden Observatory I obtained my MSc degree in 2007 with a thesis on observational aspects of filamentary star formation in Ophiuchus, supervised by Dr. Michiel Hogerheijde. Afterwards, my interest

Curriculum Vitae

in both star formation and infrared observations and instruments were met by a kind offer by Dr. Bernhard Brandl to do a PhD thesis on infrared spectroscopy of starbursts and the calibration of the next generation space-based infrared spectrometer, to fly onboard the *James Webb Space Telescope* in 2018. The booklet that you are holding now is the result of this PhD work.

I have presented my work at several international institutions and academic events, including the Far Infrared Meeting at the University College in London, the SPIE instrumentation meeting in San Diego, California, and the General Assembly of the International Astronomical Union in Rio de Janeiro, Brazil. I have also spent some time working with my collaborators at the Lowell Observatory, in Flagstaff and at the Max-Planck Institut für Astronomie in Heidelberg. I have combined my research work with an active participation in outreach activities to bring astronomy closer to people in Colombia, and to professionalize the exercise of this field in the region of the world where I was lucky to be born.

In the summer 2012 I will move back to the United States to start a post-doctoral research position at the Harvard-Smithsonian Center for Astrophysics. Now that I look back, but more importantly, now that I look ahead, I am happy to have chosen astronomy as my profession for life.

Acknowledgements

Over the last six years in Leiden, as a master student first, and later on as a promovendus, I was extremely fortunate to have met wonderful colleagues and friends, and to have enriched this exciting academic challenge with very satisfactory personal experiences. First of all, I am grateful to this country, the Netherlands, for having received me and given me the opportunity to pursue a career in astronomy, and to the Netherlands Research School for Astronomy (NOVA) for providing the funding for this research. That said, there is a lot of people that made my life better (and happier) here.

I would not have made it to Leiden without the support of David Ardila and Inga Kamp. My first research experience in Leiden with Michiel Hogerheijde taught me many useful lessons, and I am grateful to him too. I also want to acknowledge the postdocs that accompanied my research and provided very useful advice and comments on my work, but also relaxing moments over a drink or just nice chats: so thank you Brent Groves, Sarah Kendrew and Eva Schmalzl (née Meyer). Additional excellent advice and good Spanish tapas came from Fred Lahuis, to whom I am very grateful too. As I am to other Sterrewacht members that made my research more exciting: Marissa, Mayuresh, Ainil, and all the Local Universe and Instrumentation people.

I was very lucky to be part of the MIRI Test Team, a very productive but also a very fun group that helped to get the Mid-Infrared Instrument in shape to fly. I will never forget the excellent nights spent at the EGSE room testing MIRI while the whole of England was sleeping, and the dinners of the Consortium Meetings. In particular, I want to thank Alistair Glasse for teaching me a lot about the instrument, Adrian Glauser for being a good partner and guide in the wavelength calibration, and some team members that made it all enjoyable: Gillian, Jane, Scott, Thodori, Cyrine, Ruymán, Antonio, Bart, the other Eva (Bauwens), Karl, Sebastian, Tim, Paul, Helen. I keep my hopes high that we will get that Margarita machine before JWST flies!

Sergio, caro mio, sai che sei stato per me quasi come il fratello italiano che non ho mai avuto! Grazie per essere lí, per la tua amicizia sincera, per la tua cortesia e il tuo cibo; per essere il mio confidente e il vero amico di cui tante volte ho avuto bisogno. Spero di vederti spesso negli Stati Uniti! and, of course, you you! Kalle, you were one of the first sterrewachters with whom I had a drink in Leiden, and one of the last ones too, shortly after my PhD colloquium. Thank you for all the great Swedish food and above all for you

Acknowledgements

for your friendship. Jeanette, you are my other great Swedish friend, a person on whom I could always count, and a good heart that taught me good things about life. Thank you for that! Beste Jordy, you were a great officemate, a good friend and the best HFC Haarlem supporter I have ever met! Thank you for the relaxing moments at the office! Carina and Karoliina, you both arrived from Finland and brought excellent moments with you. It was nice to run by your side.

Some old-school sterrewachters made my life happier before they left. Thank you Niruj, Carolina, Elisabetta, Hendrik, Mario, Olja, Olmo, Ann-Marie, Thibaut. And thank you also to the new wave of sterrewachters that lately have made me the honor of taking me for lunch and call me their friend: Matteo, Irene, Mattia, Berenice, Nicola, Silvia. I always enjoyed a coffee-time chat with Franco, Giorgia, Markus, Bernardetta, Joseph and Christian.

My friends in the Netherlands know how special they are for me. I do not think I need to say more. They were my life beyond astronomy. Thank you Iberia, Andrea, Justin, Angelica, Eric, Carmen, Eva, Asmara, Luca, Giulia, Giovanni, Jorge, Petra, Haavar, Soledad, Kathrine, Dalia, Julia, Julio, Lin, Franz, Maria Helena, Hugo. Some of them are gone but not forgotten. Thank you Juanes, Cata, Germán, Magdoula, Robert Max, Gerrit, Joey, y mi paisita preferido, Esteban, el primero que tuvo el honor de cocinarme y de sacarme a pasear por el mundo, y a quien por fortuna espero encontrar pronto en la tundra de Quebec.

Simone y Tiziana, ustedes (tres) fueron nuestra familia en la última parte de éste viaje. Su compañía hizo que nunca me sintiera lejos de casa y sus alegrías fueron mías también. Nos vemos en Boston.

A mis amigos de Colombia, muchas gracias por no olvidarme. Gracias por estar ahí, siempre. Gracias a Juanita, Diego, Daniel Camilo, Eduardo, Julián, Marcela, Daniel, Carito, Mónica. Gracias a mis tías, tíos, primos y primas, a la bonita familia en Colombia, por estar siempre atentos a mis asuntos.

Madre, padre, hermano: gracias por creer en mí. Gracias por convencerme de que se puede estar a la altura de los propios sueños, siempre, y por ser la familia incondicional que me inspiraba a seguir en cada momento difícil. Éste logro es de ustedes también.

Lara, mi amor, tal vez podría haber llegado a ser doctor, pero no habría sido un doctor feliz si no te hubiera encontrado. Tu amor, y tu inmensa paciencia en los meses difíciles hicieron esta tesis posible, y la hicieron mejor. Poder seguir el camino a tu lado es el más feliz suceso de mi vida en Leiden, y el comienzo de mejores días.

J. R. Martínez Galarza,
Leiden, April 2012.

Notes:

